Controlling the Carbon-Bio Interface: *ex-situ* and *in-situ* Studies of Fundamental Biomolecule-Carbon Interactions

A thesis presented to the University of Dublin, Trinity College for the degree of Doctor of Philosophy in Chemistry

by

Federico Zen

Under the supervision of Prof. Paula E. Colavita

School of Chemistry & CRANN

Trinity College Dublin

2017

Declaration

I declare that the work in this thesis it has not been submitted as an exercise for a degree at this or any other University and it is entirely the my own work Due acknowledgement and references are given to others were appropriate.

I agree that the TCD Library may lend or copy the thesis upon request, subject to the Irish Copyright Legislation.

Federico Zen, April 2017

_____

Acknowledgments

First and foremost I would like to express my very great appreciation to my supervisor Prof. Paula Colavita, for her constant help and support of my research. Her immense knowledge, guidance, intense dedication and contagious enthusiasm have helped me develop as a scientist immeasurably over the past four years.

I would also like to express my gratitude to the people, who have collaborated in this thesis work. Miss Joana Vasconcelos who worked with me during this four years at the same project: she has been not only an exemplary coworker but also a great friend. Mr. James Behan, Mr. Guido Ciapetti, Mr. Khairul Hoque and Dr. Daniela Angione who carried out several experiments with me. Prof. Eoin Scanlan, Mr Adam Myles and Dr. Thomas Duff for the compound synthesis. Dr. Vasilios Karanikolas and Prof. Louise Bradley for their contribution in model simulations. Dr. Dilushan Jayasundara, Mr. Ronan Cullen and Dr. Deirdre Murphy for their help and suggestions and for the training me when I arrived in the group.

A special thank goes to the Insplorion company for the access to NPS instrumentation; in particular to Mr. Patrik Bjöörn, Ms. Jenny Andersson and Dr. Olof Andersson for their generous support and fantastic welcome in Gothenburg.

Moreover I would like to thanks Dr. Cormac.McGuinness, Dr. Elisabetta Arca, Dr. Karsten Fleischer and Miss. Emma Norton for their training and constant help at the XPS instrument. I'm very grateful to Prof. John Boland for the access to AFM instrumentation and Dr. Shaun Mills for his precious assistance; and to Dr. Babu Ramesh and Dr. Trevor Woods for access to contact angle instrumentation. I also would like to express my gratitude to Prof. María J. Santos-Martínez for the access to the QCM-D instrument.

Furthermore, I would like to thank all the past and present group members, including the people that I mentioned above, also Dr. Carlota Fernandez, Dr. Leticia Esteban, Dr. Michelle Browne, Dr. Suoyuan Lian, Dr Serban Stamatin and

all the visiting researchers for making this work a thoroughly enjoyable experience. A special thank goes to the people that spent time proof reading this thesis: thanks so much James, Adam, Carlota and Jojo!! Finally thanks to all the staff and postgraduate students in the chemistry department.

Last but not least my gratitude goes to my parents and my brother who, despite the distance, never stopped supporting me during all these years.

Summary

Amorphous carbon has emerged as a promising material for biological applications. The widespread interest in using disordered carbon coatings in orthopaedic and biomedical devices is due to their desirable physical/chemical properties, such as chemical inertness, low frictional coefficient, wear resistance and excellent smoothness. However, the functionality and durability of carbon-coated devices *in vivo* are mainly governed by their interfacial interactions with blood and tissues. These interactions are thought to be determined by molecular events occurring at short times after implantation, such as adsorption of protein and lipids. The control of biomolecules-carbon reactions through the modulation of carbon surface properties should potentially improve the biocompatibility of this family of biomaterials even further. This thesis aims at the understanding of carbon interfacial interactions with biological fluids and how these interactions may impact host response towards amorphous carbon coatings.

In Chapter 1 an introduction to the properties, applications and biomedical impact of disordered carbon materials is given. Moreover the description of the fundamental forces involved in the adsorption of biomolecules (*i.e.* proteins) at solid surfaces is presented. Surface modifications are able to modulate these interfacial events by tuning the surface properties of biomaterials. A particular interest is dedicated to hydrophilic coatings that are capable of preventing protein adsorption. A new class of synthetic antifouling polymers is represented by saccharide coatings, which aim at mimicking the glycoprotein envelope present in the antiadhesive glycocalyx. In our lab simple mono- and disaccharides are functionalized on to carbon surfaces using aryl diazonium chemistry. In this thesis the ability of preventing protein adsorption of these coatings is tested using a combination of *ex-situ* and *in-situ* techniques. The methods adopted for the determination of protein adsorption at carbon surfaces are described in Chapter 2. In this chapter the sputtering method utilized for amorphous carbon deposition is also illustrated along with the description of the characterization techniques used at bare and modified carbon surfaces.

The results obtained from the characterization of bare surfaces are reported in Chapter 3. Two different carbon surfaces were produced using DC magnetron spattering: amorphous carbon (a-C), with high graphitic content and high optical absorptivity, and hydrogenated amorphous carbon (a-C:H), with low graphitic content and high optical transparency. A third type of film was produced by exposing a-C surfaces to UV/ozone treatment, giving a highly hydrophilic oxidized amorphous carbon (ox-C) layer.

Protein adsorption studies at bare and carbohydrate coated surfaces are reported in Chapter 4. *Ex-situ* results show that glycan layers are able to prevent unspecific protein adsorption with enhanced rejection observed in the case of the tested di-saccharide vs. simple mono-saccharides for near-physiological protein concentration values. Antifouling properties at phenylglycoside layers correlate positively with wetting behaviour and Lewis basicity.

Following that, further *in-situ* studies of protein adsorption at bare and modified carbon surfaces are reported. In chapter 5, the adsorption of two plasma proteins (albumin and fibrinogen) at a-C and a-C:H surfaces were investigated using a combination of nanoplasmonic sensing (NPS) and simulation methods: results show that the methodology proposed is well suited to investigating and comparing protein adsorption at carbons, even in the case of carbon materials with highly dissimilar dielectric properties. In Chapter 6, the NPS technology, in combination with quartz crystal microbalance (QCM) methods, was used to investigate the dynamic of albumin adsorption at bare and modified carbon surfaces. *In-situ* results confirmed *ex-situ* observations. Moreover the macroscopic roughness of sensor chips was found to effect protein adsorption at surfaces. Finally, QCM experiments indicate that protein conformation at carbohydrate layers likely differs from that at bare carbon.

In the last chapter the interest in exploring the competitive adsorption of protein and lipids is explained as a continuation of this thesis work.

CONTENTS

Abbreviations

A	Absorbance
a-C	Amorphous carbon
a-C:H	Hydrogen-doped carbon
AFM	Atomic force microscopy
ATR	Attenuated total reflectance
BE	Binding energy
BML	Buried metal layer
BSA	Bovine serum albumin
CA	Contact angle
DC	Direct current
DLC	Diamond like carbon
DLS	Dynamic light scattering
DOS	Density of states
EO	Ethylene oxide
FA	Fatty acid
FDTD	Finite difference time domain
Fib	Fibrinogen
FL	Fermi level
FTIR	Fourier transform infrared
G	Gibbs free energy
Gal	Galactose
Glc	Glucose
H	Enthalpy
HEELS	High energy electron loss spectroscopy
HOPG	Highly ordered pyrolytic graphite
IR	Infrared
IRRAS	Infrared reflectance absorption spectroscopy
KE	Kinetic energies
Lac	Lactose
LSPR	Localised surface plasmon resonance
Lyz	Lysozyme
Man	Mannose
MCT	Mercury cadmium telluride
MSSR	Metal surface selection rule
NEXAEFS	Near-edge x-ray-adsorption spectroscopy
NMR	Nuclear magnetic resonance
NPS	Nanoplasmonic sensing
OWRK	Owen, Went, Rabel and Kaelble
ox-C	Oxidized amorphous carbon
PBS	Phosphate buffer saline
PC	Phosphatidylcholine
PECVD	Plasma-enhanced chemical vapour deposition
PEG	Poly(ethylene glycol)
PEO	Poly(ethylene oxide)

PMMA	Poly(methyl methacrylate)
PS	Phosphatidylserine
PTEF	Polytetrafluoroethylene
PVD	Physical vapour deposition
QCM	Quartz crystal microbalance
QCM-D	Quartz crystal microbalance with dissipation
R	Reflectance
Rha	Rhamnose
RF	Radio frequency
RMS	Root mean square
S	Entropy
SAM	Self-assembled monolayers
SE	Spectroscopic ellipsometry
SFE	Surface free energy
SP	Surface plasmon
SPR	Surface plasmon resonance
ta-C	Tetrahedral amorphous carbon
ta-C:H	Hydrogenated tetrahedral amorphous carbon
TIR	Total internal reflection
TL	Tauc-Lorentz
TSM	Thickness shear mode
UHMWPE	Ultra-high molecular weight polyethylene
UV	Ultraviolet
VL	Vacuum level
vOCG	van Oss, Chaudhury and Good
XPS	X-ray photoelectron spectroscopy

List of Figures

CHAPTER 3:

CHAPTER 5:

CHAPTER 6:

List of Tables

CHAPTER 1:

CHAPTER 2:

CHAPTER 3:

CHAPTER 4:

CHAPTER 5:

List of Schemes

1 Introduction

The following chapter provides an overview of the applications of carbon materials, specifically of amorphous carbon coatings, in the biological field. Disordered carbon films are presented as very versatile materials with properties which may be tuned by varying deposition parameters, doping or via surface modifications. Surface properties are of great importance in the determination of the bioresponse of carbon-coated devices because they regulate carbon-biomolecule interactions, such as adsorption of proteins and lipids. The fundamental forces involved in protein-solid interactions are discussed, along with a description of the modification methodology for the prevention of protein adsorption at surfaces.

1.1 Carbon materials for biological applications

Carbon materials have attracted great interest in the biological field due to their excellent biocompatibility profile and chemical inertness. Moreover the possibility of robust surface functionalization allows for the optimization of bio-carbon interactions [1-3] and modulation of optical and surface properties [4, 5]. The research activity relating to carbon-based materials, which has seen a recent spike in interest for therapeutic and diagnostic purposes, is fuelled by the wide variety of forms in which carbon allotropes can be found: from thin films and surface coatings to micro- and nanoparticles. In the last decade, carbon nanomaterials based on trigonal planar bounding configurations, such as fullerenes [6], nanotubes [3, 7] and graphene [8], have been widely studied as drug delivery materials, for imaging within diagnostic devices and as scaffolds for cell culture growth. More recently, carbon dots [5] have emerged as novel nanomaterials for biosensors and bioimaging applications due to their low cytotoxicity and tunable optical properties. Porous carbon [4, 9] in the form of micro- and nanoparticles, which possesses high specific surface area and small pore size, holds great promise as cellular delivery and imaging agents. Among the members of the nanocarbon family, nanoscale diamond [2, 10-12] has received considerable attention due to potential applications in fields such as luminescent bio-imaging, drug delivery, quantum engineering, surface coatings, seeding *etc*. Other forms of diamond, namely microcrystalline and the bulk material, as well as diamond films have a long history of use for these purposes [10, 13, 14]. In parallel to the development of the chemical vapour deposition of diamond, and the discovery of new carbon nanoparticles, there has been substantial advancement in the use of disordered carbons for orthopaedic and medical devices [15]. Pyrolytic carbon is one of the early biomaterials of which formulation and physiochemical properties were studied and tuned specifically for medical applications, and one example of which is its use for over 40 years in coating components of mechanical heart valves [16, 17]. Similarly, diamond-like carbon (DLC) has been integrated into catheters, stents, joint replacements, sensors and even contact lenses, owing to high wear resistance, low friction coefficients and chemical inertness [18-20]. The expansive literature and the numerous applications mentioned above underline the tremendous success of carbon

materials in the biological field. However there are still many open questions to resolve and a clear understanding of the reason for carbon biocompatibility has not yet been found. The following sections are dedicated to the description of properties and applications of DLC coatings, with a specific emphasis on the biological field. Surface modification of amorphous carbons is described in relation to the control of surface properties and carbon-bio interactions; of particular consideration is the case of surfaces capable of minimizing unspecific adsorption of plasma proteins.

1.2 Diamond-like carbon (DLC) coatings

DLC refers to a broad range of forms of amorphous carbon containing various fractions of sp^2 and sp^3 bonds with differing concentrations of molecular hydrogen [15]. DLC coatings are well known for their outstanding properties such as chemical inertness, low friction coefficient, high hardness, wear resistance and optical transparency in the IR spectral range [15, 21]. The first report on hard amorphous carbon films was published in the early 1950's [22], but it didn't attract much attention until about two decades later, when the research activity on DLC started increasing exponentially, reaching the maximum output in the 2000's with almost 500 publications per year [21]. Today DLC materials are used worldwide on an industrial scale, particularly for automotive applications with more than 100 million parts coated per year with a market value of several hundred million euro [21]. Various forms of DLC coatings, such as amorphous carbon (a-C), tetrahedral amorphous carbon (ta-C), hydrogen-doped carbon (a-C:H) and hydrogenated tetrahedral amorphous carbon (ta-C:H), have found widespread applications in areas of optical windows, magnetic storage disks, car parts, biomedical coatings and micro-electromechanical devices [15]. The properties of the carbon coating can be adjusted according to application requirements by doping with metals, (*e.g.* silver or titanium), or with other elements, such as silicon, oxygen, fluorine or nitrogen [21, 23]. The term DLC describes a large variety of carbon-based materials. As such in order to provide a classification of the different types of carbon coating, DLC structures and properties are described in detail within the following section.

1.2.1 DLC: properties and classification

The versatility of disordered carbon materials is due in part to the great variety of crystalline and disordered structures that carbon can form. Diamond and graphite can be considered the two extreme forms, in which carbon displays a structure with long-range order. In the case of diamond, carbon atoms adopt a tetrahedral coordination with strong σ bonds between adjacent atoms. This configuration is commonly referred to as sp^3 hybridisation. The physical properties of diamond are derived from its strong σ bonding. Diamond has a wide 5.5 eV band gap and the highest atom density of any solid. This makes diamond a good electrical insulator, and an extremely hard material [20]. At the other extreme, with the sp^2 configuration of graphite, each atom is trigonally coordinated to three other atoms by σ bonds in a plane, with π orbitals orientated parallel to the σ bonding plane. The electron delocalization due to the π orbitals coupling on a single graphite plane makes it a zero band gap semiconductor and a very soft material due to the weak interactions among planes. The combination of these two bonding configurations in an amorphous medium imparts several properties similar to diamond, such as the hardness, elastic modules and chemical inertness, and several of those similar to graphite, such as the conductivity, to DLC materials. These properties are present in an isotropic disordered thin film, which has no grain boundaries, good coverage and is cheap to produce [15]. Despite the definition “diamond-like”, DLC is in fact not like crystalline diamond. It is not as hard and is virtually amorphous , therefore it shows better adhesion and tribological properties due to the higher smoothness and lack of polycrystalline growth morphology [18].

A comparison between DLC materials and crystalline carbon is provided in Table 1.1 below, showing some properties of a-C, ta-C, a-C:H and ta-C:H with diamond, graphite and other forms of carbon are summarized.

Table 1.1. Comparison of some main properties of some form of DLC with those of reference materials (diamond, graphite, polyethylene) [15].

	sp^3 (%)	H (%)	Bandgap (eV)	Hardness (GPa)	Reference
Diamond	100	0	5.5	100	[24]
Graphite	0	0	0		[25]
Glassy carbon	0	0	0.01		[26]
a-C	5-20	0	0.5		[27]
a-C:H	20-60	30-50	1-4	10-20	[28]
ta-Ct	80-88	0	2.5	80	[28-30]
ta-C:H	70	30	2.0-2.5	50	[31]
Polyethylene	100	67	6	0.01	[32]

DLCs have been characterised in great detail and their growth mechanism is now broadly understood [15]. A number of techniques have been developed to produce DLC films; the most common of which are physical vapour deposition (PVD), *i.e.* sputtering or arc evaporation, and plasma-enhanced chemical vapour deposition (PECVD), which is the most popular laboratory method [15, 21, 23]. Sputtering, however is preferred for industrial processes due to its versatility, widespread use with many materials and its easy scalability [15]; this is, also, the method used in our laboratory [33-35] (see Chapter 2 for experimental setting).

Each of the above methods can be used to deposit DLC coatings that can be easily doped and/or alloyed with different materials. This leads to a wide range of properties depending on its sp^3, sp^2 and hydrogen content together with incorporation of other hetero-elements [20]. The family of disordered carbon is schematically presented in Figure 1.1, wherein the compositions of the various forms of amorphous carbon and C-H alloys are displayed in a ternary phase diagram[15], first used by Jacob and Moller[36]. Disordered carbon materials with graphitic ordering, such as soot, char, glassy carbon or evaporated carbon, lie in the lower left corner. In the right hand corner, the hydrocarbon polymers define the limits of the triangle, beyond which it is not possible to form interconnecting C-C networks and, therefore, solid films. The deposition methods listed above can produce carbon films with increasing degrees of sp^3 bonding. Sputtered carbon is

generally defined as a-C and it is a highly graphitic film (~20 % of sp^2). With this method the hydrogen content can be increased by using a H_2 enriched atmosphere, producing a-C:H films. These types of films are produced using a sputtering chamber in our lab and full characterization is presented in Chapter 3. Films with higher fractions of sp^3 bonding are defined as ta-C, according to the convention by McKenzie [29]. A range of techniques, *e.g*. PECVD, is able to reach the interior of the triangle, producing a-C:H or hydrogenated amorphous carbon (ta-C:H) films, depending on the sp^3 content.

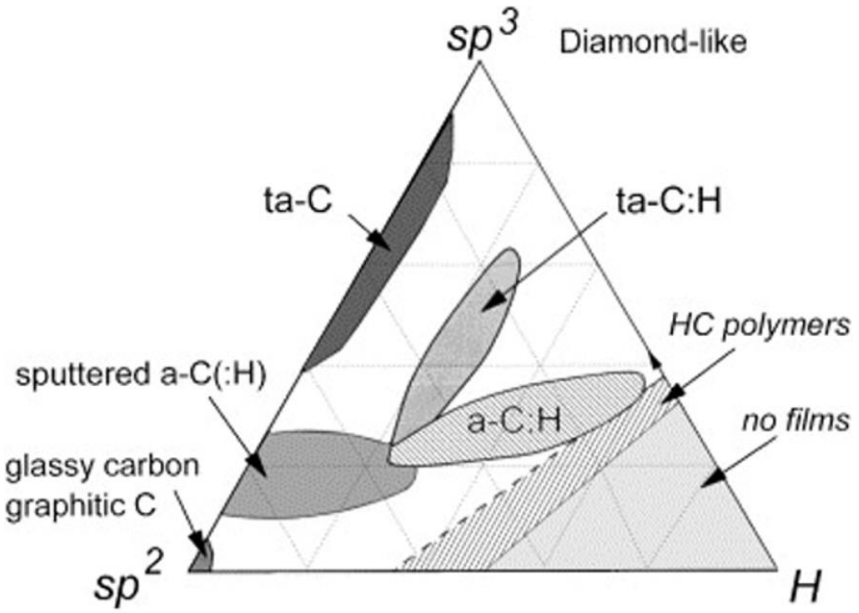

Figure 1.1. Ternary phase diagram of bonding in amorphous carbon-hydrogen alloys [15].

In addition to the type of films presented above, DLC is an excellent starting point for doping with different elements. Thanks to its amorphous nature, it is possible to introduce small amounts of additional elements into the DLC matrix, and still maintain the amorphous phase of the film [37]. Metal doped DLC, for instance, can be deposited *via* reactive sputtering by use of a pure metal target in hydrocarbon-argon atmosphere, or alternatively, a metal-carbon target [21]. Other heteroatoms, such as nitrogen and fluorine, can be incorporated in the DLC coating by deposition under diethylamine (or in nitrogen rich atmosphere) and fluorocarbon vapour, respectively [38]. Doping DLCs with metals and other heteroatoms is a well-known method to tune bulk and surface properties of disordered carbon coatings. Si, F, N, O, W, V, Co, Mo, Ti and their combinations are

common doping elements that are beneficial as they can increase adhesion and electrical conductivity and reduce residual stresses in the coating, without compromising the wear performances [21, 23]. Since the addition of these elements into the DLC matrix can also continuously adjust the surface properties (see Section 1.4), it should be possible to improve the excellent biocompatibility of DLC even further [37]. Other strategies to tune biological properties of carbon coatings are surface modifications, which are described in the next section.

1.2.2 Surface modification at DLC

The advantages of using surface modification strategies stem from the possibility of controlling the interfacial structures, properties and reactivity of surfaces without affecting the properties of the bulk materials. Disordered carbon surfaces can be easily modified by formation of very stable molecular coatings, which can be attached through strong C-C, C-N or C-O-X covalent bonds [39]. Many methods for the modification of disordered carbon surfaces have been developed and some of the main approaches are described below. Electrochemical methods have been largely used for the grafting of carbon surfaces and their mechanism is now well-established [40, 41]: for instance, in the aryldiazonium reaction the formation of covalent bonds to the carbon surface is obtained through radical generation, or in the case of oxidation of amines the reaction goes through cation radical formation. However, the increasingly available access to a greater number of molecular groups, due to the commercial availability and synthetic advancements, has encouraged the development of new methods for the covalent modification of carbon surfaces. Non-electrochemical approaches are less rapid, but they are more practical when the dimension or shape of the sample impedes electrochemical treatment, or in the absence of satisfactory electrical contact, as in the case of particle suspensions or relatively insulating carbons. These methods involve reactions that are either spontaneous at room temperature or that are promoted by UV irradiation, heat or chemical reduction agents. The reactive group forming the covalent bond with the carbon surfaces are typically aryldiazonium salts, primary amines, ammonia, alkenes, alkynes, azides or diazirines. The thickness of the layer typically ranges from approximately 1 nm (one monolayer) to over 20 nm, whereas electrochemical grafting often leads to multilayers or

polymeric films and it can be difficult to limit grafting to one monolayer [42, 43]. The relevant review from Barriére and Downard [39] reports a detailed overview of those non-electrochemical strategies for the functionalization at graphitic carbon.

Among those methods, the most studied reaction involves aryldiazonum salts. The spontaneous grafting of aryldiazonium salts is an effectual strategy for surface modifications, and it is widely used to display a range of functionalities or to provide anchoring groups for further functionalization [33]. In Figure 1.2 we present a schematic of the typical *in-situ* aryldiazonium reaction happening at the surface. Originally the first substrate grafted via diazonium salts was glassy carbon, but the method was soon extended to many other types of material: from carbon (*i.e.* diamond, HOPG, graphene, carbon nanotubes, carbon fibers, carbon black and porous carbon) to metals and polymers [44]. The possibility of using different functional groups (R group in Figure 1.2) results in a wide range of molecules that can be attached to the carbon surface [45].

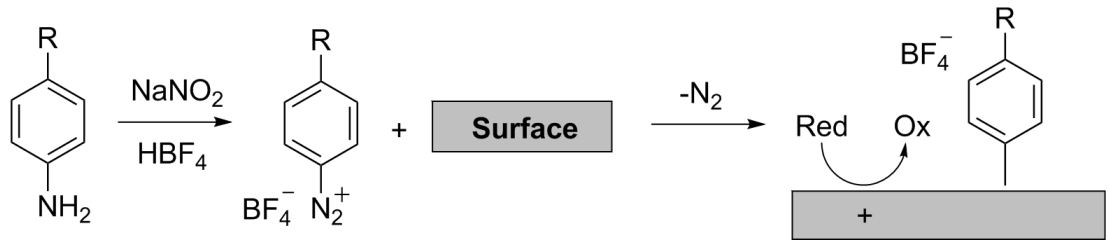

Figure 1.2. Chemisorption reaction for aryldiazonium salts.

In our group the spontaneous chemisorption of aryldiazonium salts at amorphous carbon surfaces was investigated using first small molecules, such as nitrobenzene [33] and nitronaphthalene [35] diazonium salts, and then larger functional group, such as mono- and di-saccharides, for bio applications [1, 46]. As is the case with metal substrates, the spontaneous reaction is facilitated by the reducing potential of the carbon material and its rate improves as the density of occupied states near the Fermi level of the material increases; *i.e.* reaction rates are higher for increase metallic character in the carbon substrate. This was shown first for nanotubes [47, 48] and graphene nanoribbons [49] and was shown to be valid in the case of amorphous materials in works from our group [34, 50].

Other strategies for the modification of amorphous carbon substrates were explored by use of UV light to promote grafting of fluorinated terminal alkenes at a-C surfaces [51].

1.3 DLC as biomaterial

The research on biomaterials has been expanding rapidly over the last 60-70 years over a broad multidisciplinary area, including human health, economy and many scientific fields [16, 52]. The growing interest for biomaterials is explained by the increasing demand for long lasting implants tied to the aging population, the higher standard of living in developed countries and the growing ability to address previously untreatable medical conditions [16, 23]. In fact, the number of implantation of man-made medical devices, such as hip joints, heart valves, dental roots, intraocular lenses, etc., is increasing every year [23, 52]. However, very few materials are functional and compatible enough with the human body, which represents a corrosive environment for many implanted devices [19, 37]. In order to avoid the failure of the implant, biomaterials should be chemically and biochemically inert to surrounding cells and tissue, wear and corrosion resistant, with low friction coefficient required for some applications and, importantly, resistant to leaching of any toxic or carcinogenic elements within the human body [20]. Materials regularly used for implants and biomedical devices are metallic alloys (*i.e.:* CrCo, stainless steel, Ti-6Al-4V) ceramics (alumina and zirconia), ultra-high molecular weight polyethylene (UHMWPE) and other polymers [19, 23, 37]. These materials suffer, however, from some drawbacks of long-term use [20]: the corrosion and wear, debris at the surface of the artificial material can induce release of metal ions and other particles leading to cellular damage, infections, blood coagulation and failure of the implant.

With the purpose of preventing (or alleviating) these problems and extending the average life time of implants, the development of adhesive, protective and biocompatible films as coating for prosthetics and biomedical devices has been proposed as a viable solution [19, 20]. DLC coatings have emerged as a promising material, owing to their high hardness, low frictional coefficient, high wear and corrosive resistance, chemical inertness, and excellent smoothness [20, 53].

Moreover their chemical composition, containing principally carbon and hydrogen, may facilitate the biocompatibility of these materials. DLC materials have been tested already for orthopaedic applications: a-C:H, used as coating for CoCr hip joints, has shown excellent tribological properties and better wear resistance than UHMWPE and alumina, but without the risks associated with fracture of ceramic components [18-20]. DLC coatings can also improve durability of implants in cardiovascular applications. An example can be seen in the case of arterial stents; these are metal tubes inserted permanently in the human body and are exposed to corrosion and wear: uncoated stents tend to release metals such as Ni, Cr, Mo and Mn within 4 days of contact with human plasma [20], but no metal release has been observed for DLC-coated stents, which were also found to reduce platelet adhesion and thrombogenicity, even after long term implantations [18, 20, 54]. Another application for DLC materials are stainless steel guidewires, which are used to introduce catheters, stents and other medical devices in the human body. Medical guidewires are thus required to possess properties of inertness, flexibility, very low frictional coefficients and short term biocompatibility and hemocompatibility; a-C:H coated guidewires satisfied all these requirements exhibiting better performances than other coatings like polytetrafluoroethylene (PTFE) [20, 55]. Many other applications are reported: for soft contact lenses DLC coatings appear to reduce the problem of biofilm formation; catheters have been coated with mixtures of silver and DLC, to prevent bacterial infection; in microsurgery DLC coatings increase the sharpness of surgical needles with the advantage of reducing reflection due to the dark colour of carbon [18]. The topic is amply discussed in the literature with many reviews published [18-20, 37, 52], including the most recent from Love *et. al.* [23]: all of which underline the need for further studies and *in vivo* testing. However, all the excellent chemical/physical properties, that underpin the good performance of DLC in the biomedical field, are not sufficient to explain the biocompatibility of carbon-coated devices. The development and optimization of carbon for biomedical applications has been and largely remains the result of an empirical process. The interaction occurring between carbon and biological media is still not understood in detail [53]; greater predictive tools and material design guidelines could be developed by improving our knowledge of the interfacial properties of

carbon at the molecular level [16, 56, 57]. This thesis aims to contribute to the understanding of carbon interfacial interactions with biological fluids and how these interactions may impact host response towards this family of biomaterials.

1.4 Interaction of solid surfaces with biological fluids

While the load bearing properties of implants are mainly controlled by the bulk characteristics of the biomaterials, the interaction with the surrounding environment is governed by the surface properties [37]. In fact, durability and performance of an artificial material *in vivo* is strongly correlated to its interaction with blood and tissue [16, 53, 56]. Specifically, the host response is thought to be determined by molecular events occurring at short times after implantation [16, 56-59]. Upon contact with a biological fluid, biomaterials are exposed to water, solvated ions, biomolecules and cells. All these entities enter in a dynamic competition for surface sites, dominated by their diffusion coefficient in solution. The first molecules that reach the surface are the small ones that are transported faster than larger objects like cells. Biomolecules, such as proteins and lipids, are thought to form an initial conditioning film that control subsequent cell-surface events. Therefore, when we talk about cell-surface interaction, it is ultimately an interaction between cells and surface-bound biomolecules [56]. Hence, much effort in the field of carbon biocompatibility has been devoted to understanding biomolecule-carbon interactions. The majority of the works have been dedicated to elucidating the protein-carbon interactions, due to protein abundance in bodily fluids and their importance for cell recognition [16, 60-69]. However, despite the intense attention devoted to this type of interaction, there is still great controversy regarding the structure of protein-adsorbed layers and the dynamics of their formation [16, 65]. Several works have shown that plasma proteins adsorb at a carbon surface without any denaturation, revealing a possible explanation of carbon biocompatibility. Other studies, on the contrary, found that proteins denature at the carbon surface; in these cases, carbon biocompatibility was ascribed to a specific sequence in which proteins adsorb [65]. In summary, no straightforward correlation between protein adsorption and carbon biocompatibility has emerged so far [68]. The main focus of this thesis is centred on the investigation of protein-carbon interaction in relation to the surface

properties. However, because of the complexity and composition variety of bodily fluids, other molecules might play an equally important role in the determination of bioresponse to carbon materials. In the next section we will address the discussion to these contributions, while the role of proteins at the solid-liquid interface will be described in depth in Section 1.5

1.4.1 Role of lipids

Since a direct correlation between protein adsorption and cell adhesion properties has not been found [59, 70], it is likely that other interfacial interactions at the early stages after contact between carbon and a biological environment might have an impact on carbon bioresponse. One hypothesis is to consider other macromolecules present in biological fluids that play a critical role in cell adhesion, and therefore in determining carbon biocompatibility. Good candidates for this are lipids, due to their abundance in biological fluids and tissue that is often comparable to that of proteins [71]. In Table 1.2 the concentration of some of the most relevant proteins, triglycerides and fatty acids in human plasma are reported.

Table 1.2. Concentration of some relevant biomolecules in human plasma [71].

Biomolecule	**Concentration (mmol/liter)**	**Concentration (mg/mL)**
Albumin	0.52-0.82	35-55
Fibrinogen	0.004-0.012	1.50-4.00
Triglycerides	<1.8	1.6
Free fatty acids	0.28-0.89	<0.08-0.25

Evidence of a potential role of lipids in defining the biocompatibility of a material was given in early studies by Baier and Dutton. They discovered that significant amounts of lipids co-adsorb with proteins at the initial stages of immersion after a solid comes in contact with blood [72]. Moreover, lipids are known to modulate surface-protein interaction [73, 74], and critically determine the performance of biomaterials [75, 76].

Nevertheless, very little is known about lipid-carbon interactions. A parallel part of this project is, therefore, focused on investigating lipid adsorption at carbon surfaces. Lipid-carbon and protein-carbon interaction studies were carried out separately over the past four years. These results will be merged for the investigation of competitive adsorption of protein and lipid at carbon surfaces, with the purpose of identifying the origin of carbon coating biocompatibility and in identification of factors leading to desirable host response to these materials. An introduction to this final part will be included in Chapter 7, where some preliminary data are also reported. The results presented in this thesis, instead, will focus mainly on protein adsorption studies and on the modulation of adsorption via surface modification of a-C with carbohydrates. The background related to protein adsorption on bare and surface modified substrates will be discussed in detail in the next sections.

1.5 Proteins at solid-liquid interface

The adsorption of proteins at the solid-liquid interface is a process that has resulted in many applications in addition to many problems in biotechnology. For instance, the biocompatibility of implants can be improved by preadsorption of albumin. This is the case, for example, of low temperature isotropic carbon, whose high biocompatibility was demonstrated by Feng [65] due to a formation of a protein layer on the surface that is strongly adsorbed and consists of completely denatured proteins. This tenacious, proteinaceous film seems to prevent subsequent collision of other biomolecules and cells, thereby minimizing interfacial activated processes [77]. However, protein adsorption causes mostly undesirable effects in many areas including biomaterials (e.g. blood-contacting biomaterials and contact lenses), bioassays (e.g. immunoassays and biosensors), bioseparations and chromatography. Many reports in the literature [77-82] have been dedicated to the understanding of protein adsorption phenomena, with the aim of controlling or preventing its occurrence. Yet, a general mechanism for this process has not been identified and theoretical descriptions often fail to explain experimental observations due to many reasons [77, 83]. The first complication is given by the intricacy of describing protein molecules. Proteins are complex

macromolecules with high molecular weights, ranging from thousands to millions of Daltons that possess surface domains variable in hydrophobicity and charge. Such protein surface heterogeneity presents difficulties in describing molecule-surface interactions and in modelling conformation changes that are known to occur after adsorption [77, 83]. An additional difficulty arises from the influence of water structuring in protein-surface interactions. Solvation interactions are known to play a major role in protein adsorption at most surfaces and they have to be considered in theoretical calculations of adsorption energy [83]. Finally, many solid surfaces, such as synthetic polymers, possess heterogeneity that add further variables to the modelling [77].

In this chapter we will discuss general aspects of the mechanism of protein adsorption, including consideration of solvation interactions that provide a crucial driving force for this process. Moreover, we will discuss some of the approaches used for preventing protein adsorption on biomaterials. In particular poly(ethylene oxide) (PEO) modified surfaces will be described and compared with carbohydrate coated carbon surfaces.

1.5.1 Thermodynamic Approach

Protein adsorption from aqueous solution onto solid surfaces is the net result of various types of interactions that simultaneously occur among all the components in the system, such as protein, surface, water and small molecules and ions [83]. Adsorption of protein at the surface takes place spontaneously, at constant temperature and pressure, only if

$$\Delta_{ads}G = (\Delta_{ads}H - T\Delta_{ads}S) < 0 \qquad (1)$$

where G, H and S are, respectively, Gibbs free energy, enthalpy and entropy; and where Δ_{ads} indicates the change in thermodynamic state functions due to the adsorption process. As we can see from the equation above, the negative Gibbs energy change can be achieved by a decrease in enthalpy and/or increase in entropy. Due to the huge difference in size between protein and water molecules, the adsorption of a single protein produces a substantially large release of water molecules that are associated to the protein. This increases the total entropy of the system, and thus results in a decrease of the Gibbs free energy [83]. The thermodynamic analysis is useful in explaining protein adsorption but it doesn't

provide any detail or quantification on how water structuring specifically influences protein adsorption. Molecular approaches are necessary for a better understanding of the role of water molecules.

1.5.2 Forces involved in Protein Adsorption

The interactions that are involved in protein adsorption to solid surfaces include van der Waals forces, electrostatic "double layer" forces, solvation (hydration and hydrophobic) forces and entropic (steric or fluctuation) forces. The extent of adsorbed proteins is determined by the competition between attractive and non-specific repulsion interactions, as shown in Table 1.3 [83].

Table 1.3. Types of attractive and repulsive forces [83].

Attractive force	**Repulsive force**
Electrostatic attractions	Electrostatic repulsion
Hydrophobic interactions	Hydration forces
Specific interactions	Steric repulsion (non-specific)
Van der Waals forces	

Among these, van der Waals and electrostatic forces are intrinsic of protein-substrate interactions, while others are the result of structural or conformational change. Electrostatic interactions are not likely to be very significant, since most biomaterials in use are neutrally charged at physiological pH. In addition, the Debye length is less than 10 Å at physiological ionic strengths [83], while most proteins are larger than 20 to 30 Å [77]. Therefore, electrostatic interactions might play a role only at very close range and be involved in the development of local contact between the macromolecule and the surface. Specific interactions are generally highly attractive, however they can usually be neglected since typical biomaterials do not possess structures that can be recognized by biomolecules with specific tertiary structures. Hence, van der Waals forces and hydrophobic interactions are the most important forces [83] that need to be considered in order to rationalise adsorption behaviour.

Repulsive forces play a crucial role in the case of surfaces capable of resisting protein adsorption. For instance, hydration forces arise whenever water molecules bind to a surface containing hydrophilic groups, while steric repulsion

is provided by the thickness of a grafted layer of hydrophilic molecules. However, it is often not easy to distinguish between these two contributions, as we will see later in this section.

1.5.3 Solvation interactions

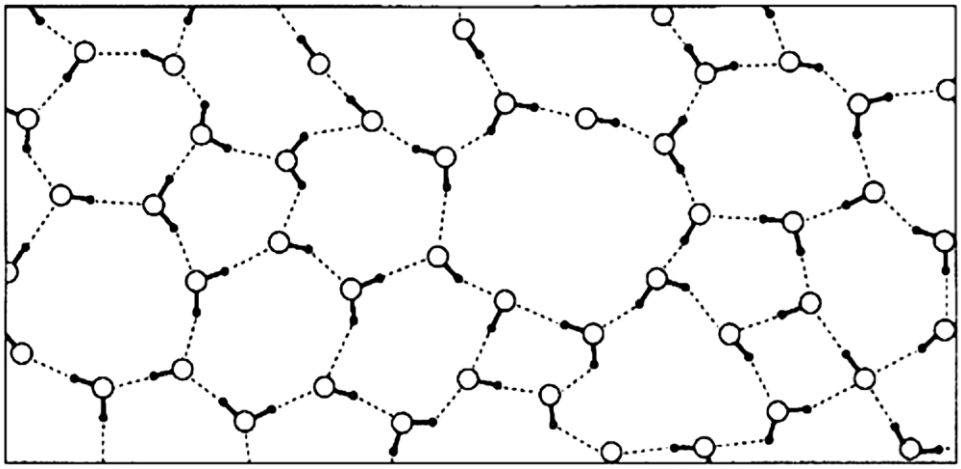

Figure 1.3. Two-dimensional representation of the structuring of bulk water [83].

Water is a highly structured liquid, where individual water molecules are linked to each other through hydrogen bonds to form a locally tetrahedral arrangement (Figure 1.3). When a solute is dissolved in water, this type of arrangement is disrupted and solvation interactions are determined by the structuring of water molecules around the solute [83]. Solvation interactions play a key role in the case of proteins, with which water can interact and bind in different ways, depending on the surface properties of each specific protein [56]. This surface water "shell" strongly influences the protein adsorption process, that can be considered to occur through disruption of the water molecules network at the surface by the protein approaching to the substrate [83]. Water, in fact, will change its structural arrangement facing to proteins as well as to biomaterials. Thus the total energy for protein adsorption in water includes not only the direct protein-surface interaction energy, but also any change in the protein-water and water-biomaterial interaction energy [83]. A schematic representation of the process is reported in Figure 1.4.

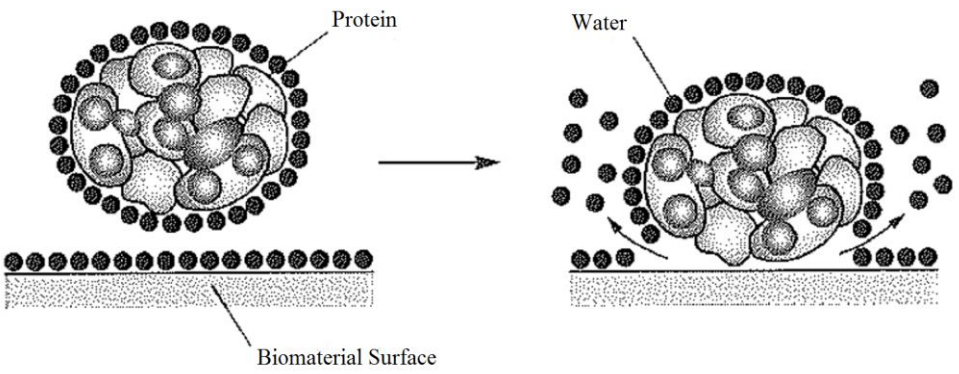

Figure 1.4. Schematic description of protein adsorption on biomaterial surface. Water molecules are removed from contact sites between the amino acids residues and the biomaterial. Some of water molecules can remain trapped in certain space between the protein and the surface if the void sizes are larger than water molecules [83].

To understand the solvation interactions occurring at the biomaterial surface, we distinguish between the two limit cases of hydrophilic and hydrophobic surfaces.

Water molecules facing the hydrophilic surface form a networked structure through hydrogen bonding to the surface (Figure 1.5). Proteins approaching the surface, therefore, need to displace the water molecules by breaking hydrogen bonds. Unless the work necessary for this displacement is smaller than that gained by adsorption of protein to the surface, the protein adsorption is, in general, energetically unfavourable. For this reason, hydration forces are classified as repulsive [83].

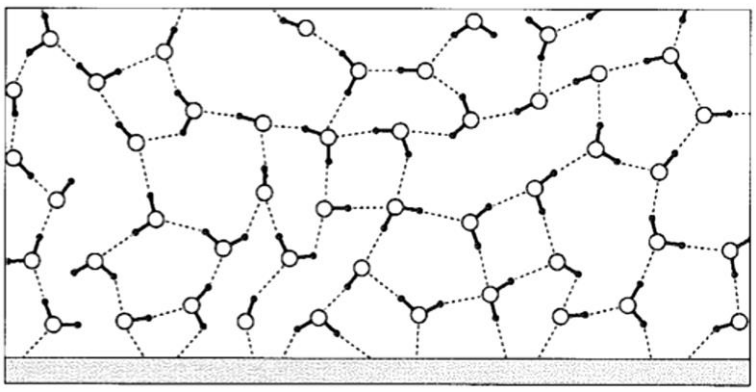

Figure 1.5. Water structuring on a hydrophilic surface. Molecules of the surface can participate in the formation of networked water structure [83].

Water molecules facing hydrophobic surfaces, on the contrary, do not form hydrogen bonds with the surface, but they form a self-assembled structure with its own hydrogen-bonding network (Figure 1.6). This restructuring of water on hydrophobic surfaces is claimed to be more ordered than in the bulk liquid, even though their hydrogen bonds are weaker than in pure water. It is, therefore, entropically unfavourable due to the imposition of a new, more ordered, structure. Without any specific bond the hydrophobic interaction is mainly an entropic phenomenon. Following this approach, protein adsorption on hydrophobic surfaces releases structured water into the bulk liquid water, and thus increases the system entropy contributing to a reduction in free energy. This is seen as the reason why hydrophobic interactions are associated with strong attractive forces between surfaces and proteins [83].

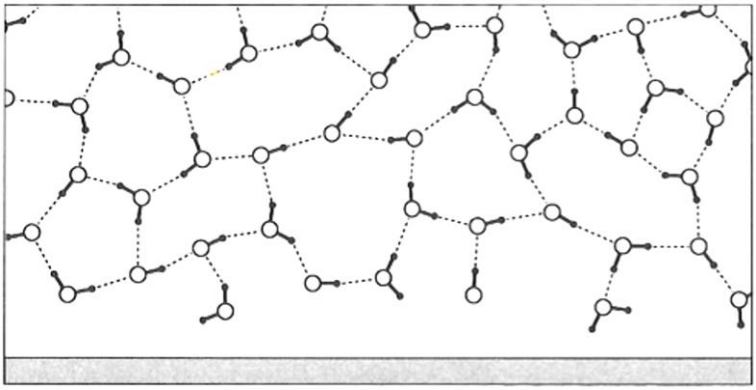

Figure 1.6. Water structuring on a hydrophobic surface. Molecules of the surface cannot participate in self-association of water molecules near the surface [83].

1.5.4 Inert surfaces

As mentioned at the beginning of Section 1.5, a number of approaches have been developed to prevent or control protein adsorption, due to the problems arising from this process in numerous fields of biotechnology. Surfaces that do not adsorb proteins are commonly referred to as “nonadsorbing”, “antifouling” or “inert” and are usually obtained by surface modifications that make the surface more hydrophilic [16, 78]. High hydrophilic surfaces have almost zero interfacial free energy in aqueous media and they are not readily contaminated in water [83]. At the molecular level, this behaviour arises from the arrangement at the solid-liquid interface of water molecules, which form a hydrogen binding-network at the surface (see section 1.5.3). As listed in Table 1.3, the other driving repulsive

force that can hinder protein adsorption is steric repulsion. The steric repulsion force is also called repulsive entropic or fluctuation force, and it arises from the thermal motion of protruding surface groups or from the thermal fluctuation of flexible fluid-like interfaces [83]. As mentioned at the end of section 1.5.2, it is currently not clear how to separate hydration forces from steric repulsion. Guidelines were drawn up for the designing of nonadsorbing surfaces; for instance, after examination of almost 60 mixed self-assembled monolayers (SAMs) presenting a range of functional groups, Whitesides and others proposed that groups that made surfaces inert have four common features: (i) hydrophilic, (ii) hydrogen bond acceptors, (iii) not hydrogen bond donors and (iv) overall electrically neutral [78, 79]. For a better understanding of the mechanisms involved in preventing protein adsorption, we are now presenting the case of PEG coated surfaces that are probably one of the most successful and most studied types of inert surface in the literature.

1.5.4.1 PEO coated surfaces

The polymer composed of -CH_2CH_2O- repeating units is generally known as poly(ethylene oxide) PEO or poly(ethylene glycol) PEG. Interestingly, this polymer is extremely soluble in water, even though it is neither ionised nor very polar; in fact, closely related polyethers, such as polymethylene oxide (-CH_2O-) and polypropylene oxide (-$CH_2CH_2CH_2O$-) are instead water insoluble under ordinary conditions. It is suggested that the high water solubility of PEO is the result of a good structural fit between water molecules and polymer: the ethylene segments seem to fill voids in the water structure, minimally perturbing its network [83]. The conformation assumed by the PEO chains in water appears to be crucial to imparting its antifouling properties when it is coated on surfaces. It has been demonstrated that helical and amorphous conformers, assembled on polycrystalline gold surfaces, are inert toward protein adsorption, whilst planar, all-trans conformers on silver substrates are not [80, 83]. Grunze and collaborators showed that the configuration of PEO molecules attached on surfaces is extremely dependent on the polarity of the solvent at the interface and it changes drastically through air, water and tetrachloromethane. In particular, it was found that in water different conformations coexist in the film [80].

The models developed to explain the inertness of long chain PEG covered surfaces are based mostly on steric repulsions arising from the osmotic pressure and elastic restored forces that are created when you attempt to compress this layer made of flexible, hydrated chains [82]. These models however are inadequate to explain the numerous observations of antifouling behaviour of surfaces modified with very short PEG chains [83]. For instance, studies by Prime and Whitesides on PEG-terminated SAMs, showed that short-chain PEGs (even with only three ethylene oxide, EO, units) are effectively able to prevent protein adsorption as long as the surface coverage is high [84]. This means that chemical effects must also play a role in determining the antifouling effect of PEGs and they must be incorporated into theoretical models that explain inertness of PEG surfaces. Van Oss and co-workers discussed the role of Lewis acid-base interactions in the properties of PEO-coated surfaces [83]. Despite the quantitative limits emphasized by Della Volpe and Siboni [85], there is some interest in considering fouling-resistant behaviour from the point of view of Van Oss approach. Because of the PEO Lewis base character, the PEO-water interaction is strong and involves the orientation of interfacial water with the oxygen atoms pointing away from PEO. The Lewis acid-base interaction at the aqueous interface, propagated by the orientational distribution of neighbouring water molecules, is the source of high hydration forces. In this respect, PEO is superior to other water-soluble polymers because of its Lewis base character. What we need to keep in mind from these considerations is that the role of water structure at the surface is the basis of the "chemical view" of protein resistance. Non-steric theories, necessarily, can arise if only hydrogen bond chemistry is considered, as much as allowed by the theoretical and computational limits and difficulties [83].

1.5.4.2 Carbohydrate coated surfaces

Even though PEO coating have been shown to successfully minimize protein adsorption at surfaces [70, 86]; its polymeric chains can easily oxidize, losing their antifouling properties [87]. Many surface modification methods have been developed as alternative to PEO functionalization for preventing protein adsorption, often inspired by biological systems [88]. Some of the strategies proposed involve cationic polymers, enzymes or peptides, which are effective but

costly and often present problems of leaching and durability [87]. A source of inspiration was found in the glycocalyx present in certain cell membranes, which consists of an ensemble of glycosylated molecules that can direct specific cell-cell interactions and biological recognition events as well as inhibit nonspecific undesirable adhesion of other cells and molecules at the cell surface [89, 90]. Saccharide coatings represents a new class of synthetic antifouling polymers [91] that have been recently studied in several works [91-94] and that aim at mimicking the glycoprotein envelope present in the antiadhesive glycocalyx, The use of polysaccharides for antifouling is actually relatively popular: oligosaccharides [94] and sugar-terminated polymers [78, 91-93] exhibit excellent capability in preventing protein, bacteria and cell adsorption at solid surfaces, while being extremely stable to oxidation [95-101]. As in the case of PEGs, it is surprising that even short monosaccharides are capable of preventing/minimising fouling of biomolecules; for instance our group showed evidence of albumin resistance of aryl galactoside coatings via fluorescence experiments [46]. A special effort in this thesis will be dedicated on the understanding of the mechanism involved in the protein antifouling properties emerging for mono- and di-saccharide coated carbon surfaces.

1.6 Aim of this study

As described in Section 1.3, disordered carbon is emerging as a promising material for many biological applications: DLC has been utilized to provide a protective and biocompatible coating for orthopaedic and biomedical devices. Moreover the possibility of tuning carbon surface properties, *via* molecular grafting or atom doping, might improve the biological properties of DLC coatings even further. Much effort have been devoted to the understanding of carbon-bio interactions, with particular focus on the role of protein adsorption effects on host response towards this family of biomaterials. This thesis contributes to the fundamental understanding of the correlation between protein fouling and interfacial properties of carbon surfaces.

In Chapter 3 the bare amorphous carbon surfaces used in this thesis are fully characterized to provide a description of surface and bulk properties, which can affect the adsorption of proteins at surfaces.

Chapter 4 presents a detailed study of protein adsorption at carbohydrate-modified carbon surfaces. The adsorption of three proteins at different concentrations was investigated *via ex-situ* methods at bare and modified amorphous carbon surfaces. The amount of protein adsorbed at the surfaces were correlated with changes in surface properties due to the carbohydrate coating. This work has been published in Scientific Report (see Appendix).

Finally, in Chapter 5 and 6 the dynamic of protein adsorption were investigated using a combinations of *in-situ* techniques at both bare and modified carbon surfaces. The work presented in Chapter 5 has been published in Langmuir (see Appendix).

The results summarized in this thesis contribute to the understanding on how surface properties can affect carbon-protein interactions and open the path to further studies of carbon interfacial interactions with other biomolecules as introduced in Chapter 7.

1.7 References

1. Zen, F., M.D. Angione, J.A. Behan, R.J. Cullen, T. Duff, J.M. Vasconcelos, E.M. Scanlan, and P.E. Colavita, *Modulation of Protein Fouling and Interfacial Properties at Carbon Surfaces via Immobilization of Glycans Using Aryldiazonium Chemistry.* Scientific Reports, 2016. **6**: p. 24840.
2. Rehor, I., H. Mackova, S.K. Filippov, J. Kucka, V. Proks, J. Slegerova, S. Turner, G. Van Tendeloo, M. Ledvina, M. Hruby, and P. Cigler, *Fluorescent Nanodiamonds with Bioorthogonally Reactive Protein-Resistant Polymeric Coatings.* ChemPlusChem, 2014. **79**(1): p. 21-24.
3. Vardharajula, S., S.Z. Ali, P.M. Tiwari, E. Eroğlu, K. Vig, V.A. Dennis, and S.R. Singh, *Functionalized carbon nanotubes: biomedical applications.* International Journal of Nanomedicine, 2012. **7**: p. 5361-5374.
4. Duffy, P., L.M. Magno, R.B. Yadav, S.K. Roberts, A.D. Ward, S.W. Botchway, P.E. Colavita, and S.J. Quinn, *Incandescent porous carbon microspheres to light up cells: solution phenomena and cellular uptake.* Journal of Materials Chemistry, 2012. **22**(2): p. 432-439.
5. Wang, J. and J. Qiu, *A review of carbon dots in biological applications.* Journal of Materials Science, 2016. **51**(10): p. 4728-4738.
6. Krishna, V., N. Stevens, B. Koopman, and B. Moudgil, *Optical heating and rapid transformation of functionalized fullerenes.* Nature Nanotechnology, 2010. **5**(5): p. 330-334.
7. Liang, F. and B. Chen, *A Review on Biomedical Applications of Single-Walled Carbon Nanotubes.* Current Medicinal Chemistry, 2010. **17**(1): p. 10-24.
8. Wang, Y., Z. Li, J. Wang, J. Li, and Y. Lin, *Graphene and graphene oxide: biofunctionalization and applications in biotechnology.* Trends in Biotechnology, 2011. **29**(5): p. 205-212.
9. Fang, Y., D. Gu, Y. Zou, Z. Wu, F. Li, R. Che, Y. Deng, B. Tu, and D. Zhao, *A Low-Concentration Hydrothermal Synthesis of Biocompatible Ordered Mesoporous Carbon Nanospheres with Tunable and Uniform Size.* Angewandte Chemie International Edition, 2010. **49**(43): p. 7987-7991.
10. Krueger, A. and D. Lang, *Functionality is Key: Recent Progress in the Surface Modification of Nanodiamond.* Advanced Functional Materials, 2012. **22**(5): p. 890-906.
11. Faklaris, O., V. Joshi, T. Irinopoulou, P. Tauc, M. Sennour, H. Girard, C. Gesset, J.C. Arnault, A. Thorel, J.P. Boudou, P.A. Curmi, and F. Treussart, *Photoluminescent Diamond Nanoparticles for Cell Labeling: Study of the Uptake Mechanism in Mammalian Cells.* ACS Nano, 2009. **3**(12): p. 3955-3962.
12. Chen, M., E.D. Pierstorff, R. Lam, S.-Y. Li, H. Huang, E. Osawa, and D. Ho, *Nanodiamond-Mediated Delivery of Water-Insoluble Therapeutics.* ACS Nano, 2009. **3**(7): p. 2016-2022.
13. Williams, O.A., *Nanocrystalline diamond.* Diamond and Related Materials, 2011. **20**(5–6): p. 621-640.
14. Auciello, O. and A.V. Sumant, *Status review of the science and technology of ultrananocrystalline diamond (UNCD™) films and application to multifunctional devices.* Diamond and Related Materials, 2010. **19**(7–9): p. 699-718.

15. Robertson, J., *Diamond-like amorphous carbon.* Materials Science and Engineering Reports, 2002. **37**(4-6): p. 129-281.
16. Ratner, B.D., A.S. Hoffman, F.J. Schoen, and J.E. Lemons, *Biomaterials Science*. 2nd ed. 2004, London: Elsevier Academic Press.
17. Gott, V.L., D.E. Alejo, and D.E. Cameron, *Mechanical heart valves: 50 years of evolution.* Annals of Thoracic Surgery, 2003. **76**(6): p. S2230-9.
18. Dearnaley, G. and J.H. Arps, *Biomedical applications of diamond-like carbon (DLC) coatings: A review.* Surface and Coatings Technology, 2005. **200**(7): p. 2518-2524.
19. Grill, A., *Diamond-like carbon coatings as biocompatible materials—an overview.* Diamond and Related Materials, 2003. **12**(2): p. 166-170.
20. Roy, R.K. and K.R. Lee, *Biomedical applications of diamond-like carbon coatings: A review.* Journal of Biomedical Materials Research Part B-Applied Biomaterials, 2007. **83B**(1): p. 72-84.
21. Bewilogua, K. and D. Hofmann, *History of diamond-like carbon films — From first experiments to worldwide applications.* Surface and Coatings Technology, 2014. **242**: p. 214-225.
22. Schmellenmeier, H., *Die Beeinflussung von festen Oberflächen durch eine ionisierte Gasatmosphäre.* Experimentelle Technik der Physik, 1953. **1**: p. 49-68.
23. Love, C.A., R.B. Cook, T.J. Harvey, P.A. Dearnley, and R.J.K. Wood, *Diamond like carbon coatings for potential application in biological implants—a review.* Tribology International, 2013. **63**: p. 141-150.
24. Field, J.E., *Properties of Diamond*. 1993, London: Academic Press.
25. Kelly, B.T., *Physics of graphite*. 1981, London: Applied Science.
26. Robertson, J., *Amorphous carbon.* Advances in Physics, 1986. **35**(4): p. 317-374.
27. Pharr, G.M., D.L. Callahan, S.D. McAdams, T.Y. Tsui, S. Anders, A. Anders, J.W.A. III, I.G. Brown, C.S. Bhatia, S.R.P. Silva, and J. Robertson, *Hardness, elastic modulus, and structure of very hard carbon films produced by cathodic-arc deposition with substrate pulse biasing.* Applied Physics Letters, 1996. **68**(6): p. 779-781.
28. P. Koidl, C.W., B. Dischler, J. Wagner, M. Ramsteiner, *Plasma Deposition, Properties and Structure of Amorphous Hydrogenated Carbon Films.* Materials Science Forum, 1990. **52-53**: p. 41-70.
29. McKenzie, D.R., *Tetrahedral bonding in amorphous carbon.* Reports on Progress in Physics, 1996. **59**(12): p. 1611.
30. Fallon, P.J., V.S. Veerasamy, C.A. Davis, J. Robertson, G.A.J. Amaratunga, W.I. Milne, and J. Koskinen, *Properties of filtered-ion-beam-deposited diamondlike carbon as a function of ion energy.* Physical Review B, 1993. **48**(7): p. 4777-4782.
31. Weiler, M., S. Sattel, K. Jung, H. Ehrhardt, V.S. Veerasamy, and J. Robertson, *Highly tetrahedral, diamond-like amorphous hydrogenated carbon prepared from a plasma beam source.* Applied Physics Letters, 1994. **64**(21): p. 2797-2799.
32. Ashby, M.F. and D.R.H. Jones, *Engineering Materials*. 1980, Oxford: Pergamon Press.
33. Cullen, R.J., D. Jayasundara, L. Soldi, J. Cheng, G. Dufaure, and P.E. Colavita, *Spontaneous grafting of nitrophenyl groups on amorphous carbon thin films:*

A structure-reactivity investigation. Chemistry of Materials, 2012. **24**(6): p. 1031-1040.
34. Murphy, D., R.J. Cullen, D. Jayasundara, E.M. Scanlan, and P.E. Colavita, *Study of the spontaneous attachment of polycyclic aryldiazonium salts on amorphous carbon substrates.* RSC Advances, 2012. **2**(16): p. 6527-6534.
35. Murphy, D.M., R.J. Cullen, D. Jayasundara, R.L. Doyle, M.E.G. Lyons, and P.E. Colavita, *Heterogeneous charge transfer at the amorphous carbon/solution interface: effect on the spontaneous attachment of aryldiazonium salts.* Journal of Physical Chemistry C, 2013. **117**(44): p. 22768–22777.
36. Jacob, W. and W. Möller, *On the structure of thin hydrocarbon films.* Applied Physics Letters, 1993. **63**(13): p. 1771-1773.
37. Hauert, R., *A review of modified DLC coatings for biological applications.* Diamond and Related Materials, 2003. **12**(3-7): p. 583-589.
38. Leezenberg, P.B., W.H. Johnston, and G.W. Tyndall, *Chemical modification of sputtered amorphous-carbon surfaces.* Journal of Applied Physics, 2001. **89**(6): p. 3498-3507.
39. Barrière, F. and A.J. Downard, *Covalent modification of graphitic carbon substrates by non-electrochemical methods.* Journal of Solid State Electrochemistry, 2008. **12**(10): p. 1231-1244.
40. Pinson, J. and F. Podvorica, *Attachment of organic layers to conductive or semiconductive surfaces by reduction of diazonium salts.* Chemical Society Reviews, 2005. **34**(5): p. 429-439.
41. Downard, A.J., *Electrochemically Assisted Covalent Modification of Carbon Electrodes.* Electroanalysis, 2000. **12**(14): p. 1085-1096.
42. Menanteau, T., E. Levillain, A.J. Downard, and T. Breton, *Evidence of monolayer formation via diazonium grafting with a radical scavenger: electrochemical, AFM and XPS monitoring.* Physical Chemistry Chemical Physics, 2015. **17**(19): p. 13137-13142.
43. Ceccato, M., L.T. Nielsen, J. Iruthayaraj, M. Hinge, S.U. Pedersen, and K. Daasbjerg, *Nitrophenyl Groups in Diazonium-Generated Multilayered Films: Which are Electrochemically Responsive?* Langmuir, 2010. **26**(13): p. 10812-10821.
44. Pinson, J., *Attachment of Organic Layers to Materials Surfaces by Reduction of Diazonium Salts*, in *Aryl Diazonium Salts*. 2012, Wiley-VCH Verlag GmbH & Co. KGaA. p. 1-35.
45. Mahouche-Chergui, S., S. Gam-Derouich, C. Mangeney, and M.M. Chehimi, *Aryl diazonium salts: a new class of coupling agents for bonding polymers, biomacromolecules and nanoparticles to surfaces.* Chemical Society Reviews, 2011. **40**(7): p. 4143-4166.
46. Jayasundara, D.R., T. Duff, M.D. Angione, J. Bourke, D.M. Murphy, E.M. Scanlan, and P.E. Colavita, *Carbohydrate Coatings via Aryldiazonium Chemistry for Surface Biomimicry.* Chemistry of Materials, 2013. **25**(20): p. 4122-4128.
47. Baik, S., M. Usrey, L. Rotkina, and M. Strano, *Using the Selective Functionalization of Metallic Single-Walled Carbon Nanotubes to Control Dielectrophoretic Mobility.* The Journal of Physical Chemistry B, 2004. **108**(40): p. 15560-15564.
48. Strano, M.S., C.A. Dyke, M.L. Usrey, P.W. Barone, M.J. Allen, H. Shan, C. Kittrell, R.H. Hauge, J.M. Tour, and R.E. Smalley, *Electronic Structure Control*

of Single-Walled Carbon Nanotube Functionalization. Science, 2003. **301**(5639): p. 1519-1522.
49. Sharma, R., N. Nair, and M.S. Strano, *Structure–Reactivity Relationships for Graphene Nanoribbons.* The Journal of Physical Chemistry C, 2009. **113**(33): p. 14771-14777.
50. Cullen, R.J., D.R. Jayasundara, L. Soldi, J.J. Cheng, G. Dufaure, and P.E. Colavita, *Spontaneous Grafting of Nitrophenyl Groups on Amorphous Carbon Thin Films: A Structure–Reactivity Investigation.* Chemistry of Materials, 2012. **24**(6): p. 1031-1040.
51. Cullen, R.J., D.R. Jayasundara, R.J. Baker, G. O' Connell, T. Donnelly, K.E. Ballantine, J.G. Lunney, and P.E. Colavita, *Laser-driven rapid functionalization of carbon surfaces and its application to the fabrication of fluorinated adsorbers.* RSC Advances, 2016. **6**(86): p. 82924-82932.
52. Cui, F.Z. and D.J. Li, *A review of investigations on biocompatibility of diamond-like carbon and carbon nitride films.* Surface and Coatings Technology, 2000. **131**(1–3): p. 481-487.
53. Stueber, M., L. Niederberger, F. Danneil, H. Leiste, S. Ulrich, A. Welle, M. Marin, and H. Fischer, *Surface topography, surface energy and wettability of magnetron-sputtered amorphous carbon (a-c) films and their relevance for platelet adhesion.* Advanced Engineering Materials, 2007. **9**(12): p. 1114-1122.
54. Gutensohn, K., C. Beythien, J. Bau, T. Fenner, P. Grewe, R. Koester, K. Padmanaban, and P. Kuehnl, *In Vitro Analyses of Diamond-like Carbon Coated Stents: Reduction of Metal Ion Release, Platelet Activation, and Thrombogenicity.* Thrombosis Research, 2000. **99**(6): p. 577-585.
55. McLaughlin, J.A., B. Meenan, P. Maguire, and N. Jamieson, *Properties of diamond like carbon thin film coatings on stainless steel medical guidewires.* Diamond and Related Materials, 1996. **5**(3): p. 486-491.
56. Kasemo, B., *Biological surface science.* Surface Science, 2002. **500**(1-3): p. 656-677.
57. Kasemo, B. and J. Lausmaa, *Surface properties and processes of the biomaterial-tissue interface.* Materials Science and Engineering: C, 1994. **1**(3): p. 115-119.
58. Schwartz, Z. and B.D. Boyan, *Underlying mechanisms at the bone–biomaterial interface.* Journal of Cellular Biochemistry, 1994. **56**(3): p. 340-347.
59. Thevenot, P., W. Hu, and L. Tang, *Surface Chemistry Influences Implant Biocompatibility.* Current Topics in Medicinal Chemistry, 2008. **8**(4): p. 270-280.
60. Takeda, A., H. Akasaka, S. Ohshio, I. Toda, M. Nakano, and H. Saitoh, *Adsorption ability comparison of plasma proteins on amorphous carbon surface.* Journal of Physics and Chemistry of Solids, 2012. **73**(11): p. 1331-1334.
61. Jones, M.I., I.R. McColl, D.M. Grant, K.G. Parker, and T.L. Parker, *Protein adsorption and platelet attachment and activation, on TiN, TiC, and DLC coatings on titanium for cardiovascular applications.* Journal of Biomedical Materials Research, 2000. **52**(2): p. 413-421.
62. Lousinian, S. and S. Logothetidis, *Optical properties of proteins and protein adsorption study.* Microelectronic Engineering, 2007. **84**(3): p. 479-485.

63. Berlind, T., P. Tengvall, L. Hultman, and H. Arwin, *Protein adsorption on thin films of carbon and carbon nitride monitored with in situ ellipsometry.* Acta Biomaterialia, 2011. **7**(3): p. 1369-1378.
64. Yadav, P.K., F. McKavanagh, P.D. Maguire, and P. Lemoine, *Adsorption of bovine serum albumin on amorphous carbon surfaces studied with dip pen nanolithography.* Applied Surface Science, 2011. **258**(1): p. 361-369.
65. Feng, L. and J.D. Andrade, *Protein adsorption on low temperature isotropic carbon. I. Protein conformational change probed by differential scanning calorimetry.* Journal of Biomedical Materials Research, 1994. **28**(6): p. 735-743.
66. Feng, L. and J.D. Andrade, *Protein Adsorption on Low-Temperature Isotropic Carbon: II. Effects of Surface Charge of Solids.* Journal of Colloid and Interface Science, 1994. **166**(2): p. 419-426.
67. Feng, L. and J.D. Andrade, *Protein adsorption on low temperature isotropic carbon: III. Isotherms, competitivity, desorption and exchange of human albumin and fibrinogen.* Biomaterials, 1994. **15**(5): p. 323-333.
68. Forti, S., L. Lunelli, C.D. Volpe, S. Siboni, L. Pasquardini, A. Lui, R. Canteri, L. Vanzetti, C. Potrich, M. Vinante, C. Pederzolli, and M. Anderle, *Hemocompatibility of pyrolytic carbon in comparison with other biomaterials.* Diamond and Related Materials, 2011. **20**(5-6): p. 762-769.
69. Yang, P., N. Huang, Y.X. Leng, J.Y. Chen, R.K.Y. Fu, S.C.H. Kwok, Y. Leng, and P.K. Chu, *Activation of platelets adhered on amorphous hydrogenated carbon (a-C:H) films synthesized by plasma immersion ion implantation-deposition (PIII-D).* Biomaterials, 2003. **24**(17): p. 2821-2829.
70. Ostuni, E., R.G. Chapman, M.N. Liang, G. Meluleni, G. Pier, D.E. Ingber, and G.M. Whitesides, *Self-assembled monolayers that resist the adsorption of proteins and the adhesion of bacterial and mammalian cells.* Langmuir, 2001. **17**(20): p. 6336-6343.
71. Kratz, A., M. Ferraro, P.M. Sluss, and K.B. Lewandrowski, *Laboratory reference values.* New England Journal of Medicine, 2004. **351**(15): p. 1548-1563.
72. Baier, R.E. and R.C. Dutton, *Initial events in interactions of blood with a foreign surface.* Journal of Biomedical Materials Research, 1969. **3**(1): p. 191-206.
73. Malmsten, M., *Ellipsometry Studies of Protein Adsorption at Lipid Surfaces.* Journal of Colloid and Interface Science, 1994. **168**(1): p. 247-254.
74. Malmsten, M. and B. Lassen, *Competitive protein adsorption at phospholipid surfaces.* Colloids and Surfaces B: Biointerfaces, 1995. **4**(3): p. 173-184.
75. Lorentz, H. and L. Jones, *Lipid deposition on hydrogel contact lenses: How history can help us today.* Optometry and Vision Science, 2007. **84**(4): p. 286-295.
76. McHenry, M.M., E.A. Smeloff, W.Y. Fong, G.E. Miller Jr, and P.M. Ryan, *Critical obstruction of prosthetic heart valves due to lipid absorption by Silastic.* Journal of Thoracic and Cardiovascular Surgery, 1970. **59**(3): p. 413-425.
77. Brash, J., *Interfacial Phenomena and Bioproducts*. 1996: Taylor & Francis.
78. Ostuni, E., R.G. Chapman, R.E. Holmlin, S. Takayama, and G.M. Whitesides, *A survey of structure-property relationships of surfaces that resist the adsorption of protein.* Langmuir, 2001. **17**(18): p. 5605-5620.

79. Ostuni, E., B.A. Grzybowski, M. Mrksich, C.S. Roberts, and G.M. Whitesides, *Adsorption of proteins to hydrophobic sites on mixed self-assembled monolayers.* Langmuir, 2003. **19**(5): p. 1861-1872.
80. Zolk, M., F. Eisert, J. Pipper, S. Herrwerth, W. Eck, M. Buck, and M. Grunze, *Solvation of oligo(ethylene glycol)-terminated self-assembled monolayers studied by vibrational sum frequency spectroscopy.* Langmuir, 2000. **16**(14): p. 5849-5852.
81. Jeon, S.I. and J.D. Andrade, *Protein—surface interactions in the presence of polyethylene oxide: II. Effect of protein size.* Journal of Colloid and Interface Science, 1991. **142**(1): p. 159-166.
82. Jeon, S.I., J.H. Lee, J.D. Andrade, and P.G. De Gennes, *Protein—surface interactions in the presence of polyethylene oxide: I. Simplified theory.* Journal of Colloid and Interface Science, 1991. **142**(1): p. 149-158.
83. Morra, M., *Water in Biomaterials Surface Science*. 2001: John Wiley & Sons.
84. Prime, K.L. and G.M. Whitesides, *Adsorption of proteins onto surfaces containing end-attached oligo(ethylene oxide): a model system using self-assembled monolayers.* Journal of the American Chemical Society, 1993. **115**(23): p. 10714-10721.
85. Della Volpe, C., D. Maniglio, M. Brugnara, S. Siboni, and M. Morra, *The solid surface free energy calculation: I. In defense of the multicomponent approach.* Journal of Colloid and Interface Science, 2004. **271**(2): p. 434-453.
86. Clare, T.L., B.H. Clare, B.M. Nichols, N.L. Abbott, and R.J. Hamers, *Functional Monolayers for Improved Resistance to Protein Adsorption: Oligo(ethylene glycol)-Modified Silicon and Diamond Surfaces.* Langmuir, 2005. **21**(14): p. 6344-6355.
87. Banerjee, I., R.C. Pangule, and R.S. Kane, *Antifouling Coatings: Recent Developments in the Design of Surfaces That Prevent Fouling by Proteins, Bacteria, and Marine Organisms.* Advanced Materials, 2011. **23**(6): p. 690-718.
88. Kirschner, C.M. and A.B. Brennan, *Bio-Inspired Antifouling Strategies.* Annual Review of Materials Research, 2012. **42**(1): p. 211-229.
89. Hilkens, J., M.J.L. Ligtenberg, H.L. Vos, and S.V. Litvinov, *Cell membrane-associated mucins and their adhesion-modulating property.* Trends in Biochemical Sciences, 1992. **17**(9): p. 359-363.
90. Sumiyoshi, M., J. Ricciuto, A. Tisdale, I.K. Gipson, F. Mantelli, and P. Argüeso, *Antiadhesive Character of Mucin O-glycans at the Apical Surface of Corneal Epithelial Cells.* Investigative Ophthalmology & Visual Science, 2008. **49**(1): p. 197-203.
91. Ham, H.O., S.H. Park, J.W. Kurutz, I.G. Szleifer, and P.B. Messersmith, *Antifouling Glycocalyx-Mimetic Peptoids.* Journal of the American Chemical Society, 2013. **135**(35): p. 13015-13022.
92. Ederth, T., T. Ekblad, M.E. Pettitt, S.L. Conlan, C.X. Du, M.E. Callow, J.A. Callow, R. Mutton, A.S. Clare, F. D'Souza, G. Donnelly, A. Bruin, P.R. Willemsen, X.J. Su, S. Wang, Q. Zhao, M. Hederos, P. Konradsson, and B. Liedberg, *Resistance of galactoside-terminated alkanethiol self-assembled monolayers to marine fouling organisms.* ACS Applied Materials and Interfaces, 2011. **3**(10): p. 3890-3901.

93. Hederos, M., P. Konradsson, and B. Liedberg, *Synthesis and self-assembly of galactose-terminated alkanethiols and their ability to resist proteins.* Langmuir, 2005. **21**(7): p. 2971-2980.
94. Holland, N.B., Y. Qiu, M. Ruegsegger, and R.E. Marchant, *Biomimetic engineering of non-adhesive glycocalyx-like surfaces using oligosaccharide surfactant polymers.* Nature, 1998. **392**(6678): p. 799-801.
95. Angione, M.D., T. Duff, A.P. Bell, S.N. Stamatin, C. Fay, D. Diamond, E.M. Scanlan, and P.E. Colavita, *Enhanced Antifouling Properties of Carbohydrate Coated Poly(ether sulfone) Membranes.* ACS Applied Materials & Interfaces, 2015. **7**(31): p. 17238-17246.
96. Ederth, T., T. Ekblad, M.E. Pettitt, S.L. Conlan, C.-X. Du, M.E. Callow, J.A. Callow, R. Mutton, A.S. Clare, F. D'Souza, G. Donnelly, A. Bruin, P.R. Willemsen, X.J. Su, S. Wang, Q. Zhao, M. Hederos, P. Konradsson, and B. Liedberg, *Resistance of Galactoside-Terminated Alkanethiol Self-Assembled Monolayers to Marine Fouling Organisms.* ACS Applied Materials & Interfaces, 2011. **3**(10): p. 3890-3901.
97. Österberg, E., K. Bergström, K. Holmberg, J.A. Riggs, J.M. Van Alstine, T.P. Schuman, N.L. Burns, and J.M. Harris, *Comparison of polysaccharide and poly(ethylene glycol) coatings for reduction of protein adsorption on polystyrene surfaces.* Colloids and Surfaces A: Physicochemical and Engineering Aspects, 1993. **77**(2): p. 159-169.
98. Holland, N.B., Y.X. Qiu, M. Ruegsegger, and R.E. Marchant, *Biomimetic engineering of non-adhesive glycocalyx-like surfaces using oligosaccharide surfactant polymers.* Nature, 1998. **392**(6678): p. 799-801.
99. Perrino, C., S. Lee, S.W. Choi, A. Maruyama, and N.D. Spencer, *A Biomimetic Alternative to Poly(ethylene glycol) as an Antifouling Coating: Resistance to Nonspecific Protein Adsorption of Poly(l-lysine)-graft-dextran.* Langmuir, 2008. **24**(16): p. 8850-8856.
100. Lord, M.S., D. Pasqui, R. Barbucci, and B.K. Milthorpe, *Protein Adsorption on Derivatives of Hyaluronan.* Macromolecular Symposia, 2008. **266**(1): p. 17-22.
101. Mussard, W., N. Kebir, I. Kriegel, M. Estève, and V. Semetey, *Facile and Efficient Control of Bioadhesion on Poly(dimethylsiloxane) by Using a Biomimetic Approach.* Angewandte Chemie International Edition, 2011. **50**(46): p. 10871-10874.

2 Instrumental Methodology

The experimental settings and theory of the techniques used are reported in this chapter. The sputtering method for the deposition of amorphous carbon films is described. Characterizations of the films were carried out via x-ray photoelectron spectroscopy (XPS) and surface free energy (SFE) determination. For the study of protein adsorption at carbon surfaces, three label-free techniques were utilized: infrared reflection adsorption spectroscopy (IRRAS) provides a semi-quantitative method for the ex-situ measurement of proteins adsorbed at surfaces; nanoplasmonic sensing (NPS) and quartz crystal microbalance (QCM) were used for in-situ experiments.

2.1 Sputtering Method

Amorphous carbon films can be produced by physical vapour deposition, which consists of the formation of a condensable vapour by physical means and subsequent deposition of a thin layer from this vapour [1]. In sputtering deposition, this condensable vapour is produced via the bombardment of a solid material source, commonly referred to as a 'target', with energetic ions. This technique involves the generation of an Ar plasma that is created and supported by a high voltage DC or RF source. The argon ions comprising the plasma are accelerated towards a cathodic target causing an atomic collision cascade and the resulting ejection or 'sputtering' of target atoms. The sputtered atoms constitute a condensable vapour that forms a thin film of the target material at the desired substrate [1]. In the case of carbon deposition a graphite target electrode is used [2]; however, because of the low sputtering yield of graphite, a magnet is usually placed behind the target to increase the deposition rate. In magnetron sputtering the coupling of the electric field, due to the voltage supplier, and the orthogonal magnetic field causes the electrons to spiral and increase their path length and thus to increase the degree of ionization of the plasma (Figure 2.1). The magnetron effect results in enhanced ion bombardment and sputtering rate [1, 2].

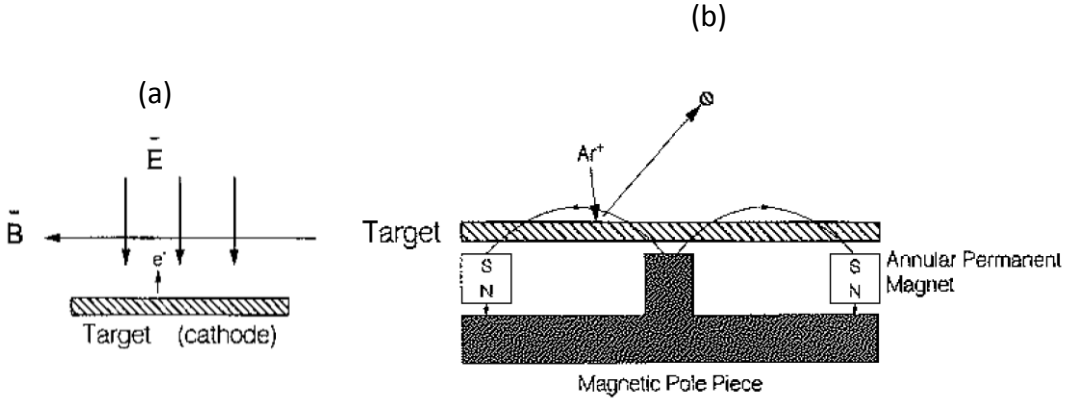

Figure 2.1. The magnetron: (a) a static magnetic field is created parallel to the surface of the target to retain electrons in the region and (b) an annular design, such as the one employed in our lab [1].

Sputtering is commonly used for depositing a-C in industrial applications because of its efficiency and versatility [2]. The deposition conditions are, in fact, reasonably independent of the surface geometry, but film properties can be controlled by the plasma power and gas pressure. Higher sputtering power

generates a more graphitic film and, thus, a softer and more conductive material [3, 4]. On the other hand, the sp^3 content of a-C can be increased by applying a substrate bias voltage, which increases the ion energy and produces a film with higher hardness and electrical resistivity[5]. This technique is performed under moderate to low vacuum (10^{-4} to 10^{-1} mbar, depending on the sputtering arrangement), in order to obtain a desired level of purity of the film [1]. Ar is the common gas used for a-C deposition, but reactive sputtering can produce also a-C:H and a-C:N by using an Ar/H_2 and Ar/N_2 plasma respectively [2].

In our laboratory, amorphous carbon films (a-C) were prepared via DC-magnetron sputtering (Torr International, Inc.) at a base pressure ≤ 2×10^{-6} mbar and a deposition argon pressure of 7×10^{-3} mbar. Changing the deposition time, it is possible to control the thickness of the sputtered carbon on various types of substrates, to satisfy experimental requirements. The specifications of carbon preparations for the samples used in different techniques are described in details in the experimental section of the following chapters. Films of different composition can be prepared by varying the H_2/Ar gas content while sputtering; hydrogen doped films were obtained via H_2 introduction at the concentration of 10% and shall be referred to as a-C:H. A picture of the sputtering system used is reported in Figure 2.2. The setup is equipped with an additional sputtering gun where a Ti target is placed. Ti deposition is performed *via* DC magnetron sputtering under the same conditions prior to a-C deposition, either to improve carbon films adhesion or in the case of infrared reflectance absorption spectroscopy (IRRAS) samples.

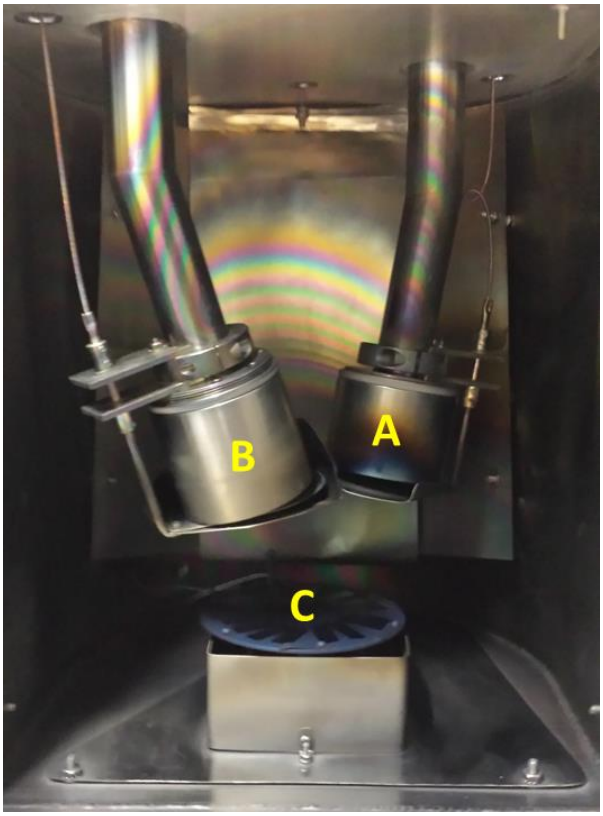

Figure 2.2. Sputtering chamber used in our lab. The plasma is generated at the two sputtering guns with the graphite (A) and titanium (B) targets, located above the rotating stage (C), where samples are placed.

2.2 Surface Characterization

2.2.1 X-ray Photoelectron Spectroscopy

Photoelectron spectroscopy involves the energy analysis of electrons ejected from matter by incident radiations. X-ray photoelectron spectroscopy (XPS) uses an x-ray incident radiation to probe core electrons, which have very characteristic energies and thus allows elemental analysis and gives information on the chemical state[6]. Moreover XPS probes only the surface region of solid materials (with a penetration depth of 1-10 nm) and, therefore, it is widely used to study adsorption phenomena.

X-ray sources for XPS use characteristic emission lines from an anodic metal target, bombarded by high energy electrons. The bombarding electrons can eject

electrons from the inner shells of the atoms of the metal target. Those vacancies will be quickly filled by electrons dropping down from higher levels, emitting X-rays with sharply defined frequencies. Most common instruments utilize the $K\alpha_{1,2}$ emission lines resulting from 2p→1s transitions of Al or Mg targets, which has line widths of 0.85 eV and 0.70 eV and energies of 1486.6 eV and 1253.6 eV, respectively[6]. $K\alpha_{1,2}$ lines are accompanied by 'satellite' lines due to similar transitions. In addition, a continuous spectrum is also produced, called Bremsstrahlung, due to the primary electrons energy. When a higher resolution is required, 'satellite' lines and Bremsstrahlung can be removed using a monochromatic x-ray source. Monochromatic XPS instruments are based on diffraction at a quartz crystal of Al Kα x-rays, with an improvement of the line widths up to 0.2 – 0.3 eV [6].

The x-rays irradiate the sample causing the electrons from core level shells to be emitted by the photoelectric effect. Emitted electrons possess a measured kinetic energies (KE), which is correlated to the original binding energy (BE) according to the following equation:

$$hv = KE + BE + \phi_{SP} \tag{2.1}$$

where hv is the energy of the incident X-ray photon and ϕ_{SP} is the spectrometer work function. An energy level diagram for a conductive sample in contact with an electron spectrometer is shown in Figure 2.3, from which the Equation (2.1) follows. The BE is implicitly defined as the energy separation between the core level and the Fermi level (FL) [6].

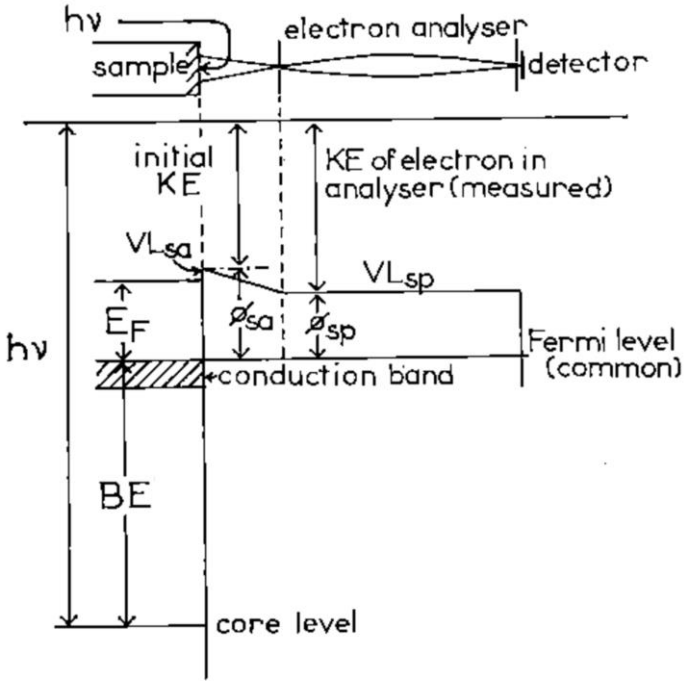

Figure 2.3. Energy level scheme for a conducting (metallic) sample in electrical equilibrium with the spectrometer, where E_F is the Fermi energy and VL is the vacuum level. The work function (ϕ) and the Fermi energy are not identical because the work function includes not only a bulk term, but also a surface term. The subscripts "sa" and "sp" stand for sample and spectrometer, respectively [6].

The determination of the BE of core level electrons and their spectral profile can give much information about the material in a sample. XPS can be used for the determination of the composition and the element concentration at the sample surface, owing to the unique set of BEs typical of each element. Moreover, small but measurable changes in the element BEs are correlated with the chemical environment of the atom. These differences in BEs, called chemical shifts, can be used to identify the chemical state of the material measured. Other peaks in XPS spectra are correlated with Auger electrons, which may be emitted because of the relaxation of the excited ions remaining after photoemission.

In this thesis, results obtained from two different XPS instruments are presented. In chapter 3 a monochromatized XPS instrument was used for the determination of sp^2 and sp^3 content in amorphous carbon films, for which the peak to peak separation is 0.7-0.9 eV. In these cases, XPS characterization was performed on an ultrahigh vacuum system (Omicron) at 1×10^{-10} mbar base

pressure, equipped with a monochromatized Al Kα source (1486.6 eV) and a multichannel array detector. When only an elementary analysis was required and the high resolution spectra was not needed, XPS measurement were carried out with a not monochromatized instrument: in Chapter 5 and 6 we used a VG Scientific ESCAlab Mk II system (<2 ×10-8 mbar) with an Al Kα X-rays (1486.6 eV) source.

2.2.2 Surface Free Energy

Surface free energy, or surface tension, is defined as the free energy change γ when the surface area of a medium is increased by unit area [7]. The process of creating a unit area of surface is equivalent to separating two half-unit areas from contact, so that we can write:

$$\gamma_1 = \frac{1}{2} W_{11} \tag{2.2}$$

where γ_1 is the surface energy of medium 1 and W_{11} is the reversible work done to separate unit areas of two surfaces of identical media from contact to infinity in a vacuum, known as work of cohesion. For two different media ($1 \neq 2$), instead, this energy is referred to as the work of adhesion W_{12} (see Figure 2.4) that is described by Dupree's equation:

$$W_{12} = \gamma_1 + \gamma_2 - \gamma_{12} \tag{2.3}$$

where γ_1 and γ_2 are the surface energy of media 1 and 2, respectively, and γ_{12} is the interfacial free energy (or interfacial tension).

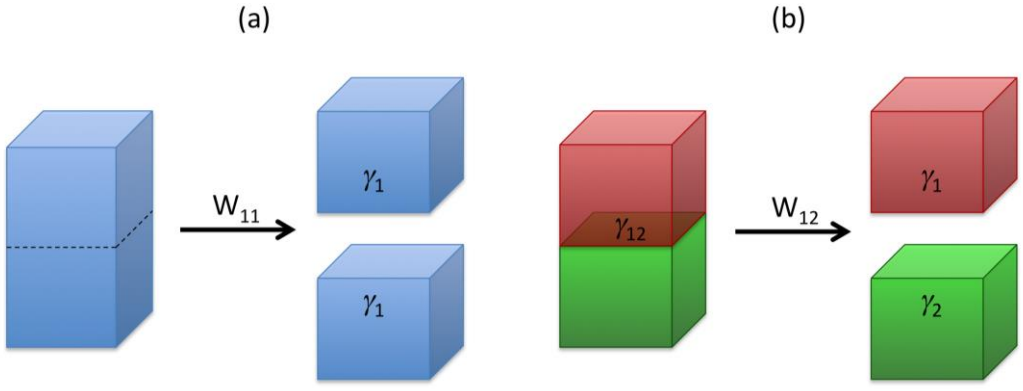

Figure 2.4. Definition of energy terms associated with the separation of two surfaces of (a) identical medium and (b) two different media from contact to infinity in vacuum. In (a) the work done, $\boldsymbol{W_{11}}$, is called work of cohesion, while in (b) $\boldsymbol{W_{12}}$ is called work of adhesion.

Generally, in the case of solids, γ is denoted by γ_S and is given in units of energy per unit area (mJ m^{-2}), while for liquids, γ is denoted by γ_L expressed in units of tension per unit length (mN m^{-1}). The two units are numerically and dimensionally the same [7].

In surface science the estimation of the SFE of a material can be extremely useful for determining its interfacial properties and interactions with other media [8]. The main technique used to calculate the SFE of a substrate is Contact Angle (CA) analysis, in which the deformation of macroscopic liquid droplets when they adhere to a surface is determined. Models require the use of more than one liquid for deriving SFE from CA measurements, however many studies report only water CA in order to evaluate the wettability of substrates [9, 10]. Interaction with water is particularly interesting in the case of biomaterials, since all the biological processes occur in aqueous solutions. For instance, as mentioned in the introduction, inert surfaces are generally very hydrophilic, since it is thought that wettability plays an important role in defining the extent to which a surface can resist biofouling [11-15].

With the purpose of obtaining information about intermolecular interactions at the interface and their influence on wetting, adsorption and adhesion behaviour, the SFE of a-C, a-C:H, ox-C and sugar coated a-C substrates were determined via CA measurements using the sessile drop method.

2.2.2.1 Contact Angle Measurements

Provided that the roughness effects at the solid surface and chemical reaction at the solid/liquid interface are negligible [8], the contact angle (θ), made by a drop of a liquid deposit on a solid surface (see Figure 2.5), contains information about the surface tension of the solid and liquid through Young's equation:

$$\gamma_S = \gamma_{SL} + \gamma_L \cos\theta \qquad (2.4)$$

where γ_S and γ_L are the surface tension of the solid and liquid, respectively, and γ_{SL} is the interfacial tension of the solid-liquid interface [16].

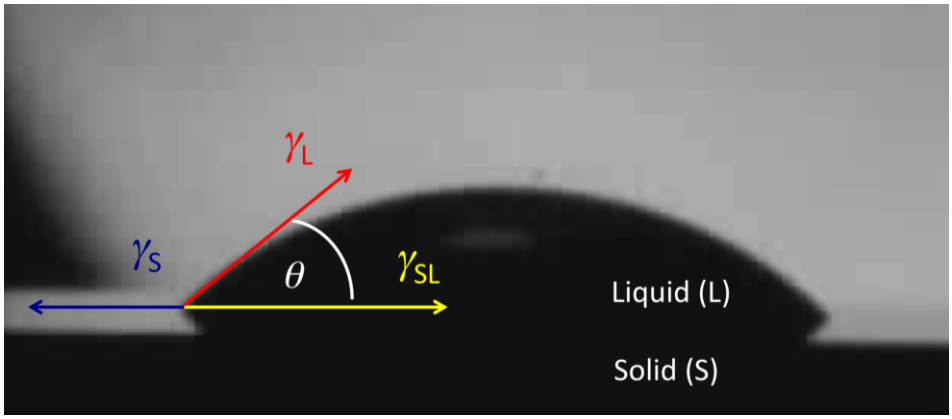

Figure 2.5. Drop of water (liquid) deposit on a-C surface (solid). The CA ($\boldsymbol{\theta}$) and vectors that describe the solid ($\boldsymbol{\gamma_S}$) and liquid ($\boldsymbol{\gamma_L}$) surface tension and the interfacial tension ($\boldsymbol{\gamma_{SL}}$) are shown in the picture.

In the results presented in this thesis, static CA was measured on a CA analyser (B/W camera from Appro, FTA Video software). In order to remove adventitious contamination, measurements were taken on surfaces after methanol rinsing immediately prior to CA characterization [8]; a minimum of three CA measurements were obtained for each surface.

2.2.2.2 SFE modelling

Equation (2.4) reflects the equilibrium between the cohesive forces in the liquid drop and adhesive forces at the liquid-solid interface. In order to derive the solid surface tension (γ_S) from the experimental values of γ_L and θ, an estimation of γ_{SL} has to be obtained [8]. Alternatively, most of the theories propose an expression for the thermodynamic work of adhesion for a solid and a liquid in contact (W_{SL}), combining equations (3) and (4) [16]

$$W_{SL} = \gamma_L(1 + \cos\theta) \tag{2.5}$$

known as the Young-Dupré equation. In order to derive the SFE from the experimental values of θ it is necessary to describe the work of adhesion W_{SL} as a function of γ_S and γ_L. One of the widely used approach is the model of Owen, Went, Rabel and Kaelble (OWRK-theory) [17], which makes two fundamental assumptions. First, surface tension can be broken down in separate components, since the free energy of cohesion is made up of contributions from a number of independent forces [16]. Thus, the total SFE is divided in two components: a

dispersive part, due to London forces, and a polar part due to all the non-London forces, as proposed by Fowkes in 1962 [18]:

$$\gamma = \gamma^d + \gamma^p \tag{2.6}$$

where γ^d and γ^p are respectively the dispersive and the polar component of the surface free energy. Second, Owens and Wendt implemented the Fowkes model using a geometric mean approximation to express the work of adhesion at the solid-liquid interface as combination of the dispersive and the polar components:

$$W_{SL} = 2\sqrt{\gamma_S^d \gamma_L^d} + 2\sqrt{\gamma_S^p \gamma_L^p} \tag{2.7}$$

From the Young-Dupree equation, it follows that

$$\gamma_L(1 + \cos\theta) = 2\sqrt{\gamma_S^d \gamma_L^d} + 2\sqrt{\gamma_S^p \gamma_L^p} \tag{2.8}$$

Therefore, to obtain γ_S^d and γ_S^p of a solid, the CA of at least two liquids with known surface tension components ($\gamma_L, \gamma_L^d, \gamma_L^p$) on the solid must be determined [18]. Multisolvent analysis was carried out using three polar (glycerol, formamide and distilled water) and two nonpolar (diiodomethane and 1-bromonaphthalene) liquids, as described in details in Chapter 3. Surface tension components of the test liquids at 20 °C are reported in Table 2.1 [19].

Table 2.1. Total surface tensions and their dispersive and polar components (in mJ m^{-2}) of test liquids [19].

Test liquids	γ_L	γ_L^d	γ_L^p
Water	72.8	21.8	51.0
Glycerol	63.3	33.6	29.7
Formamide	57.3	28.0	29.3
Diiodomethane	50.8	50.4	0.38
1-Bromonaphthalene	44.4	44.4	0

Another widely used model was developed by van Oss, Chaudhury and Good (vOCG) [19, 20]. Similarly to the OWRK approach, the vOCG assumes that the surface tension results from additive contribution of apolar, or Lifshitz-van der Waals (γ^{LW}), and polar, or Lewis acid-base (γ^{AB}) interactions:

$$\gamma = \gamma^{LW} + \gamma^{AB} \tag{2.9}$$

The work of adhesion for the apolar, W_{SL}^{LW}, forces are approximated by geometric means, as treated in the OWRK model:

$$W_{SL}^{LW} = 2\sqrt{\gamma_S^{LW}\gamma_L^{LW}} \tag{2.10}$$

On the other hand, the Lewis acid-base interactions are essentially asymmetrical, since electron-acceptor and electron-donor parameters are usually quite different in a given polar substance. Moreover one parameter cannot manifest without its opposite [19]. Therefore the work of adhesion for the polar interaction W_{SL}^{AB} is not expressed by a simple geometric mean, but it includes the asymmetrical contributions γ^- and γ^+ from electron donor-acceptor interactions, respectively, between two different substances, as below:

$$W_{SL}^{AB} = 2\left(\sqrt{\gamma_S^-\gamma_L^+} + \sqrt{\gamma_S^+\gamma_L^-}\right) \tag{2.11}$$

The total work of adhesion at the solid-liquid interface, W_{SL}, is then given by:

$$W_{SL} = 2\left(\sqrt{\gamma_S^{LW}\gamma_L^{LW}} + \sqrt{\gamma_S^-\gamma_L^+} + \sqrt{\gamma_S^+\gamma_L^-}\right) \tag{2.12}$$

Equation (2.12), in combination with the Young-Dupre equation results in:

$$\gamma_L(1+\cos\theta) = 2\sqrt{\gamma_S^{LW}\gamma_L^{LW}} + 2\sqrt{\gamma_S^-\gamma_L^+} + 2\sqrt{\gamma_S^+\gamma_L^-} \tag{2.13}$$

which can be used to obtain γ_S^{LW}, γ_S^- and γ_S^+ by measuring the CA of three liquids with known surface tension components γ_L^{LW}, γ_L^- and γ_L^+. The choice of the three liquids for the multisolvent analysis was based on the work done by Della Volpe *et al.* [21], who evaluated the readability of SFE determination from vOCG model for different triplets of solvents. The test liquids used in this work are water, glycerol and diiodomethane: they correspond, according to Della Volpe's paper, to a complete and well-balanced set of liquids, in which dispersive, acidic and basic liquids are present. The data for the surface tension components of the test liquids at 20 °C are given in Table 2.2 [8].

Table 2.2. Total surface tensions and their dispersive and acid-base components (in mJ m^{-2}) of test liquids, at T=20 °C [8].

Test liquids	γ_L	γ_L^{LW}	γ_L^+	γ_L^-
Water	72.8	21.8	25.5	25.5
Glycerol	63.3	34	3.92	57.4
Diiodomethane	50.8	50.8	0	0

2.3 Label-Free Techniques for Protein Detection

2.3.1 Infrared Reflection Adsorption Spectroscopy

Infrared reflectance absorption spectroscopy (IRRAS) is a method for measuring infrared (IR) spectra of thin layers on bulk substrates, including metals, semiconductors and insulators [22]. In IRRAS, the IR active vibrations of molecules adsorbed on a planar surface are obtained in reflection mode. Optimal experimental conditions in IRRAS studies of ultrathin films on metals are achieved using p-polarized light on the surface at a grazing angle. Under these conditions, high sensitivity is reached thanks to the enhancement of the signal that is, in part, due to the conductive properties of metallic surface.

According to Fermi's golden rule, the intensity of an optical absorption is proportional to the transition dipole projection along the direction of the electric field polarization and to the intensity of the electric field. Therefore, the rate at which the radiation energy is absorbed is strongly dependent upon the electric field intensity at the place where absorption occurs. A qualitative description of electric field at the metal surface can help to understand the enhancement mechanism in grazing-angle reflection spectra of thin films on metals [22]. The nomenclature presented in Figure 2.6 for describing the optical parameters of layered systems is used.

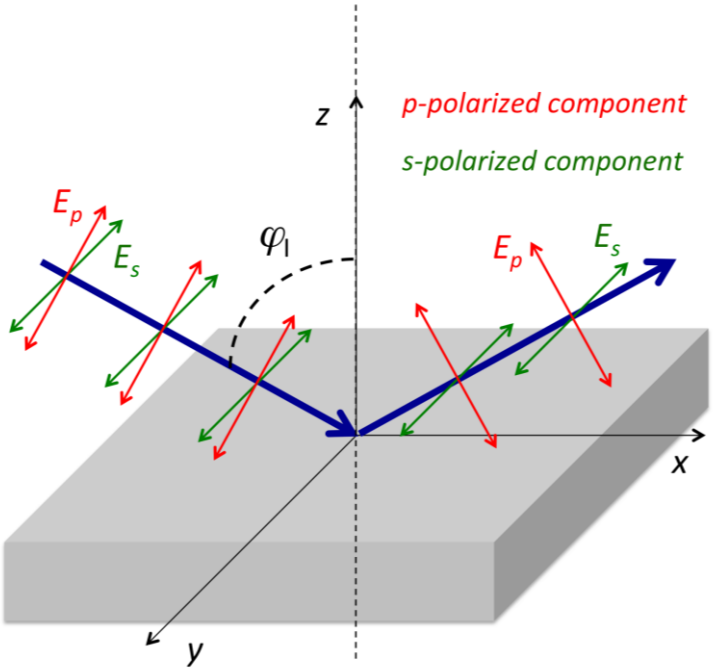

Figure 2.6. Incident and reflected electric field vectors in two-phase system.

The laws of electrostatics state that at any point outside a conductor near its surface the electric field is always perpendicular to the surface, while at any point inside the conductor the net electric field is always zero. Therefore, in the case of the tangential electric field, the induced electric field is equal and opposite to the external field on both sides of the metal, which results in the vanishing of the *x*- and *y*-components of electric field. On the contrary, if the external electric field is perpendicular to the surface, the induced dipole moment has an electric field parallel to the source field outside the metal. As a result, the *z*-component of the electric field near a metal surface does not vanish, but it is enhanced (Figure 2.7) [22]. Thus, only vibrational modes with a transition dipole component normal to the surface will be excited. This is known as metal surface selection rule (MSSR).

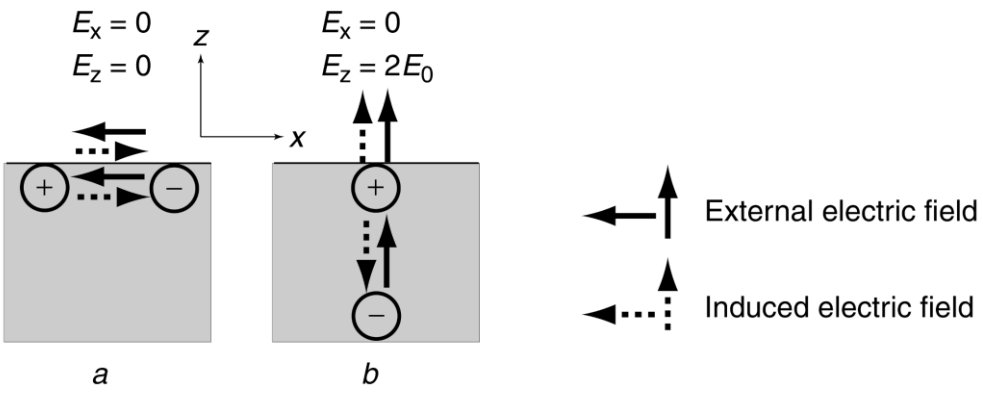

Figure 2.7. Graphic representation of instantaneous electric fields appearing at the metal interface and in the bulk. Dashed narrows illustrate induced field and solid narrows correspond to external field [22].

The enhancement of IRRAS spectral sensitivity depends not only on the intensity of the electric field, but also on the geometric factor. In fact, the induced electric field at metal surfaces can justify an increment of the signal only by a factor 2, whereas the maximum enhancement can increase up to a factor ~30 at grazing angles of incidence [22]. The other origin of the enhancement is that spectra are represented in units of absorbance, $A = -\log\frac{R}{R_0}$, or reflectivity, $\Delta R/R_0$ (that is the first approximation in Taylor series of the absorbance); where R_0 and R are the reflectance of the bare substrate and the substrate with the layer, respectively, and $\Delta R = R_0 - R$ is called absorption depth. According to these units, IRRAS sensitivity is maximized at the angle at which a thin layer will cause the greatest change in reflectance (highest value of ΔR). This happens where the metal (or semiconductor) is close to its minimum in reflectance, R_0. Of course, a balance must be reached between obtaining a signal and detecting measureable differences in reflectance; in a metal this is not a problem, but optimal conditions are reached at a pseudo-Brewster angle. In dielectric materials this means that measurements need to be taken at incident angles which differ slightly from the proper Brewster angle. The case of Ti, used as a sub-layer in our samples, is showed in Figure 2.8; the *p*-polarized reflectance ($R_{0,p}$) decreases significantly at grazing angles of incidence, causing the absorption depth to increase.

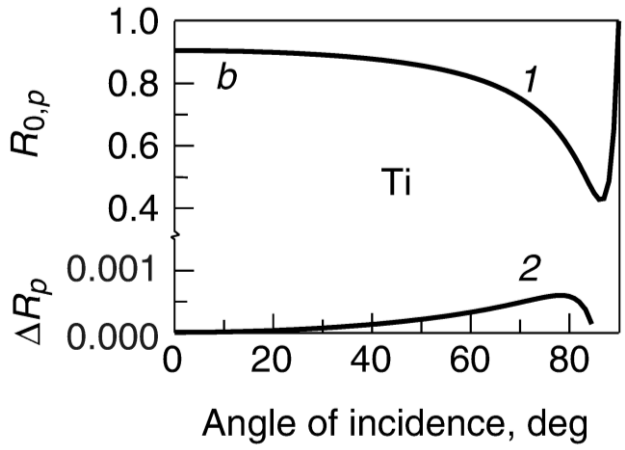

Figure 2.8. Dependence on angle of incidence of (1) reflectance $\boldsymbol{R_{0,p}}$ of a bare substrate and (2) adsorption depth $\Delta\boldsymbol{R_p}$ for 1-nm layer ($\hat{\boldsymbol{n}} = \boldsymbol{18.6 - 77i}$) at Ti ($\hat{\boldsymbol{n}} = \boldsymbol{1.564 - 0.384i}$) substrate; $\boldsymbol{\nu}$ = 1200cm^{-1}; *p*-polarization [22].

That is why *p*-polarized light and grazing angles close to Brewster or pseudo-Brewster angles are typically used in IRRAS experiments.

The IRRAS method can be used to study ultrathin layers not only on metals but also on semiconductors and dielectrics (including liquid) [22]. Even though sensitivity is much lower than when metallic surfaces are used, the waiving of MSSR allows both *s*- and *p*-polarized spectra to be measured. Characteristic of dielectrics and semiconductors in the range of their transparency is the existence of the polarizing Brewster angle φ_B at which the intensity of the reflected component of *p*-polarized light is equal to zero. Carbon materials have features inherent to both transparent and metallic substrates, since their absorption index typically does not exceed 1-3; values which are between those characteristic for transparent media and metals. Figure 2.9 shows the *p*- and *s*-components of the reflectance for three different substrates: a typical metal (Au), a semi-metal (HOPG, chosen as example for a carbon material) and a transparent material (Si) [23]. Considering the case of HOPG, we can see that its reflectance of *s*-polarized radiation is not constant as in the case of metal substrates, but increases with the angle of incidence. On the other hand, the *p*-component shows a minimum that is close, but not equal, to 0 at the "pseudo-Brewster" angle.

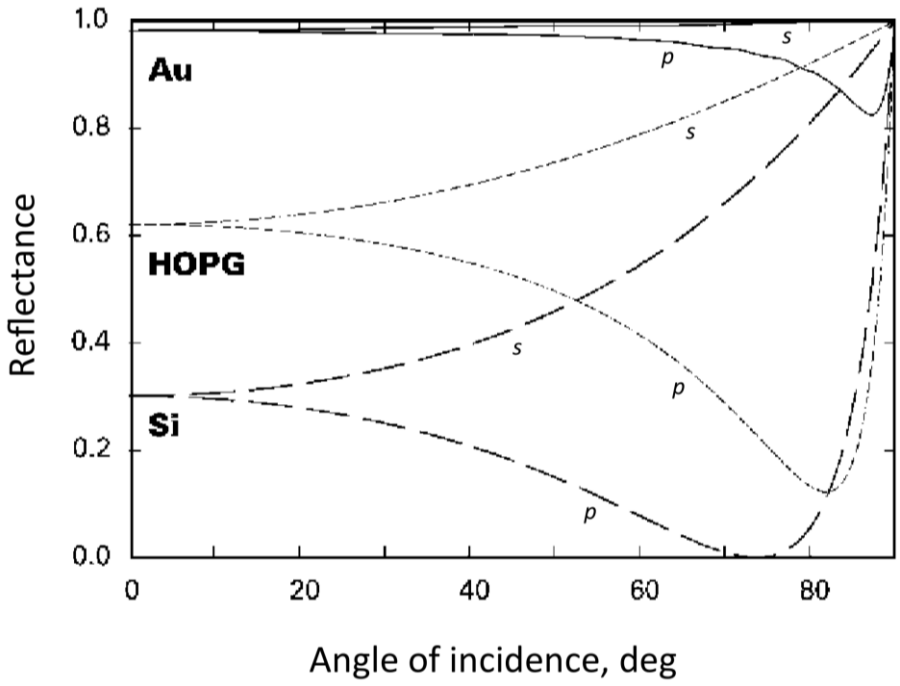

Figure 2.9. Dependence on angle of incident of reflectance for *s*- and *p*-polarization radiations for three different substrate: Au ($\hat{\boldsymbol{n}} = \mathbf{2.1} - \mathbf{21.33}\boldsymbol{i}$), HOPG ($\hat{\boldsymbol{n}} = \mathbf{5.044} - \mathbf{4.09}\boldsymbol{i}$) and Si ($\hat{\boldsymbol{n}} = \mathbf{3.433} - \mathbf{0}\boldsymbol{i}$); $\boldsymbol{\nu}$ = 2900cm^{-1} [23].

Even though IRRAS is a well-established method for studying ultrathin layers on transparent substrates, its sensitivity is almost one order of magnitude lower than on metals. However, it is possible to combine the advantage of metal and transparent IRRAS by using a complex-substrate of transparent layer on a metal [22]. This technique is knows as buried metal layer (BML)-IRRAS and is adopted in this study where the substrate consists of a layer of a-C on the top of a metallic layer of Ti [24].

In this report IRRAS spectra were collected on a Fourier Transform Infrared (FTIR) Spectrometer (Tensor 27, Bruker) equipped with a Mercury Cadmium Telluride (MCT) detector, a specular reflectance accessory (VeeMax II), and a ZnSe polarizer. Spectra were taken at 80° incidence using p-polarized light; 100 spectra were collected at 4 cm^{-1} resolution using a bare substrate as a background sample; IRRAS data were obtained in triplicates as a minimum. All spectra reported in this work were baseline corrected using commercial software (WinFIRST).

2.3.2 Localized Surface Plasmon Resonance

Surface plasmons (SPs), also called surface plasmon polarizations, are surface electromagnetic waves that propagate parallel to metal/dielectric interfaces [25]. Materials that are capable of supporting SP generation at air or water interphase are typically noble metals like gold and silver, but also copper, titanium or chromium. SP phenomena is used in surface plasmon resonance (SPR) spectroscopy where a glass prism is coated with a thin film (~50 nm) of noble metal (commonly gold or silver) that works as a sensing platform. In this technique, the light beam is reflected at metal/prism interface under total internal reflection (TIR) conditions. In TIR, the reflected photons create an evanescent wave that has its maximum intensity at the interface and decays exponentially away from the phase boundary to a penetration depth on the order of 200 nm [25]. At the right frequency, this evanescent wave enters in resonance with the SPs at the metal/dielectric interphase, producing a SP absorption band that is collected in reflectance. The resonance frequency is dependent on change in the dielectric refractive index that can arise from interfacial events such as adsorption and interactions with organic molecules. SPR spectroscopy has become widely used in the fields of chemistry and biochemistry to characterize biological surfaces and to monitor binding events, due to its high sensitivity and ability to measure in real time [25, 26].

SP phenomena changes markedly when the metal is separated into particles that are smaller than the wavelength of light [27]. The light incident on noble metal nanoparticles induces the conductive electrons in them to oscillate collectively with a resonance frequency (Figure 2.10), generating an intense light scattering with the appearance of an intense SP adsorption band and an enhancement of the local electromagnetic field [27, 28]. The resonance frequency are characteristic of the type of the material (typically gold or silver) and highly sensitive to the size, distribution and shape of the nanoparticles, as well as the environment which surrounds them [27, 28]. The phenomenon is known as localised surface plasmon resonance (LSPR) and manifestation of it has been reported historically and has fascinated people for centuries. The intense red colour of aqueous dispersions of colloidal gold particles is an example [28].

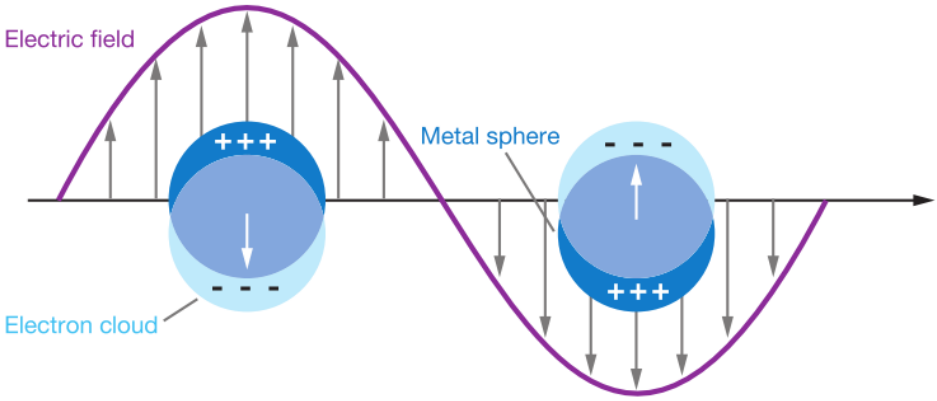

Figure 2.10. Schematic diagrams illustrating a localized surface plasmon [29].

Recent advances in colloidal chemical preparations of metallic nanoparticles and lithographic techniques for the nanofabrication of periodic array allowed the exploitation of the LSPR in the field of optical sensors [27-29]. Nanoplasmonic sensing (NPS) techniques has reached a significant level of recognition in this millennium and have been already extensively used for studying many chemical and biological relevant interfacial events [26-34]. Similarly to SPR, the NPS instrumentations monitor the wavelength shift of the characteristic LSPR that take place in response to change in the local refractive index [26, 29]. The use of NPS systems provides numerous advantages compared to the SPR instrument, without considerably affecting the sensitivity of the measurement [27-29]: (i) lower sensitivity to bulk changes; (ii) the ability to modulate the optical operating range through careful nanostructure design; (iii) greater hardware flexibility and simplicity, which considerably decreases the price of the instruments and allows much more straightforward approaches, such as transmission UV-vis spectroscopy.

The setup used in this thesis is an XNano instrument (Insplorion AB, Gothenburg, Sweden) and reported in Figure 2.11. The instrument was kindly provided by the Insplorion company. Ensemble-averaged recordings of plasmonic resonance peak were collected in optical transmission mode. Glass sensor chips (Insplorion AB) with deposited gold nanodisks (50 nm radius, 20 nm thickness, 8% surface coverage) fabricated by hole-mask colloidal lithography, were mounted in an optical flow cell for *in-situ* measurements. Sample solutions were

flowed through the measurement chamber via peristaltic pump at a continuous rate.

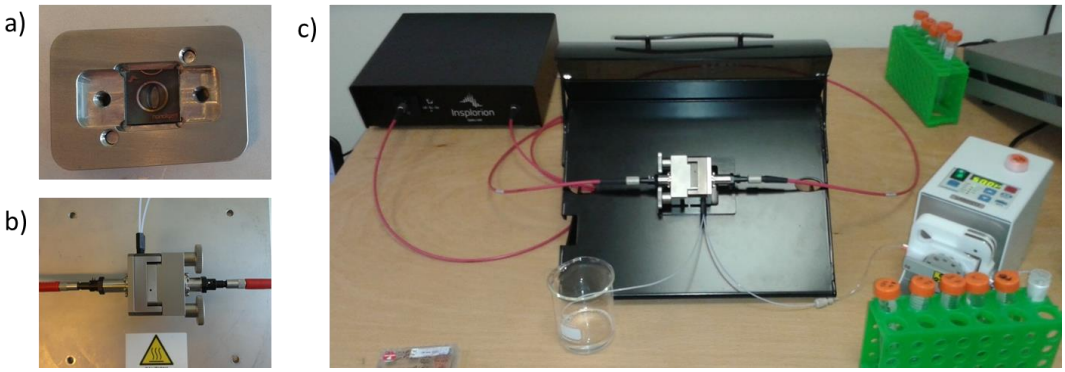

Figure 2.11. XNano instrument: (a) a-C coated NPS chips mounted in the flow cell, (b) the flow cell and (c) complete NPS setup.

2.3.3 Quartz Crystal Microbalance

Quartz crystal microbalance (QCM), or thickness shear mode (TSM), resonators are acoustic wave sensors based on the so called piezoelectric effect. According to this phenomenon, the application of a voltage across a crystal induces a reorientation of the acentric material, resulting in a latter strain and a mechanical strain deformation. QCM sensors consist of a thin disk of single crystal quartz with metal electrodes deposited on each side of the disk (see Figure 2.12a). The crystal can made to oscillate by connecting it to an external driving oscillating system. At a resonance frequency, the alternating electric field across the crystal causes a vibrational motion in share mode [35, 36], as reported in Figure 2.12b and c.

Figure 2.12. (a) Picture of a 10 MHz QCM sensor and a schematic representation of the quartz crystal with the gold electrodes on each side (b) before and (c) after applying the external driving oscillating circuit.

The sensing principle is that any change in mass, added or removed from the electrode induces a frequency shift, *Δf*. Sauerbrey [37] developed an equation to correlate the measured *Δf* with the relative change in mass *Δm*

$$\Delta f = -\frac{2f_0^2}{A\sqrt{\mu\rho}}\Delta m, \tag{2.14}$$

where f_0 is the resonance frequency in the measurement medium, A is the effective surface area of the electrode and μ and ρ are the density and the shear modulus, respectively, of the quartz. This equation is valid only when the added mass is evenly distributed over the electrode, much smaller than the weight of quartz disk and rigidly attached at the electrode surface with no slip or deformation due to the oscillation motion. These conditions are generally satisfied for adsorption measurements of small molecules in vacuum or gaseous environment. Traditionally the first QCM measurements were limited to these conditions until Nomra *et al.* showed that crystals completely immersed in liquid can also be driven to oscillate in a stable manner [36]. QCM suddenly became a powerful technique for *in-situ* interfacial study in liquid. However, the registered *Δf* results affected by additional contributions:

$$\Delta f = \Delta f_m + \Delta f_y + \Delta f_a + \Delta f_x, \tag{2.15}$$

where Δf_m is due to the absorbed mass, Δf_y is due to viscous damping, Δf_a is due to surface stress and Δf_x arise from nonshear coupling [38]. While for small molecules the contribution from Δf_y is negligible, in the case of organic layer, such as proteins, the viscous damping has a considerable effect. On the other hand, Δf_a and Δf_x contribution are usually time independent during adsorption processes from solution, although they can slightly vary between experimental runs [38]. The contribution from the viscous damping can be estimated by measuring the energy dissipated during the crystal oscillation in liquid environment. Two main methods are developed for this type of measurements and are described in the following sections.

2.3.3.1 QCM with impedance analysis

Electroacoustic devices such as QCM resonators can be described by a network of electrical parameters. The common electrical equivalence of a quartz crystal unit near resonance is reported in Figure 2.13, consisting of a branch with a capacitor C_1, a resistance R_1 and an inductor L_1 in series (which defines the

electromechanical characteristic of the quartz resonator) in parallel with a second capacitor C_0 (which is the static capacitance of the quartz resonator with the electrodes) [35].

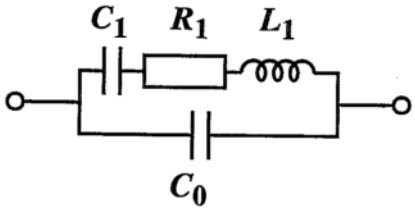

Figure 2.13. Equivalent electrical representation of a QCM crystal.

The advantage of expressing the mechanical properties of the QCM crystal in electrical equivalents is that it is possible to determine the equivalent circuit components using a network analyser. Thus the properties and the interaction of the crystal with the contacting medium can be derived from impedance analysis, which involves the measurement of a current at a known applied voltage over a specified range of frequency [35]. From the determination of R_1 and L_1 it is possible to obtain the quality factor Q from the relation:

$$Q = \frac{\omega L_1}{R_1}, \tag{2.16}$$

where ω is the angular frequency at the resonance. The quality factor Q, which is defined as the ratio of the energy stored to the energy lost during the oscillation, is an inverse absolute measure of the energy dissipated and it can be correlated with viscous damping contribution mention above.

Unfortunately the QCM setup in our lab doesn't possess a network analyser and no impedance analysis was processed. Our instrument consists of an impedance-scanning EQCM (Gamry Instruments), which acquires the relative impedance spectrum near resonance. The typical response is an S-shape curve, represented in Figure 2.14. The frequency at the minimum and maximum of the curve correspond to the serial (f_s) and parallel (f_p) resonance frequency, respectively, and they are recorded in real time from fitting extrapolations.

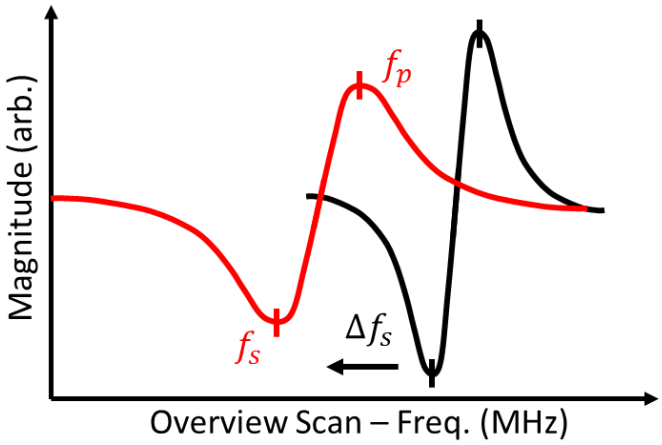

Figure 2.14. Cartoon of a relative impedance spectrum obtained by QCM measurements. The two curves represent the acquisition before (black line) and after (red line) mass adsorption at the QCM electrode. The red curve is broader due to energy losses correlated with the adsorbed mass.

The shift of the serial resonance frequency Δf_s is usually correlated to the mass adsorbed at the electrode, if assuming that the other contributions are negligible. The combination of f_s and f_p are, instead, used for the determination of the relative quality factor Q_r

$$Q_r = \frac{(f_s+f_p)}{2(f_p-f_s)}, \tag{2.17}$$

which gives an idea of the contribution due to the viscous damping.

The impedance QCM measurements were carried out using a static reaction cell with a home-built temperature-controlled box equipped with Peltier cooling and a mobile mixer system. The setup is reported in Figure 2.15

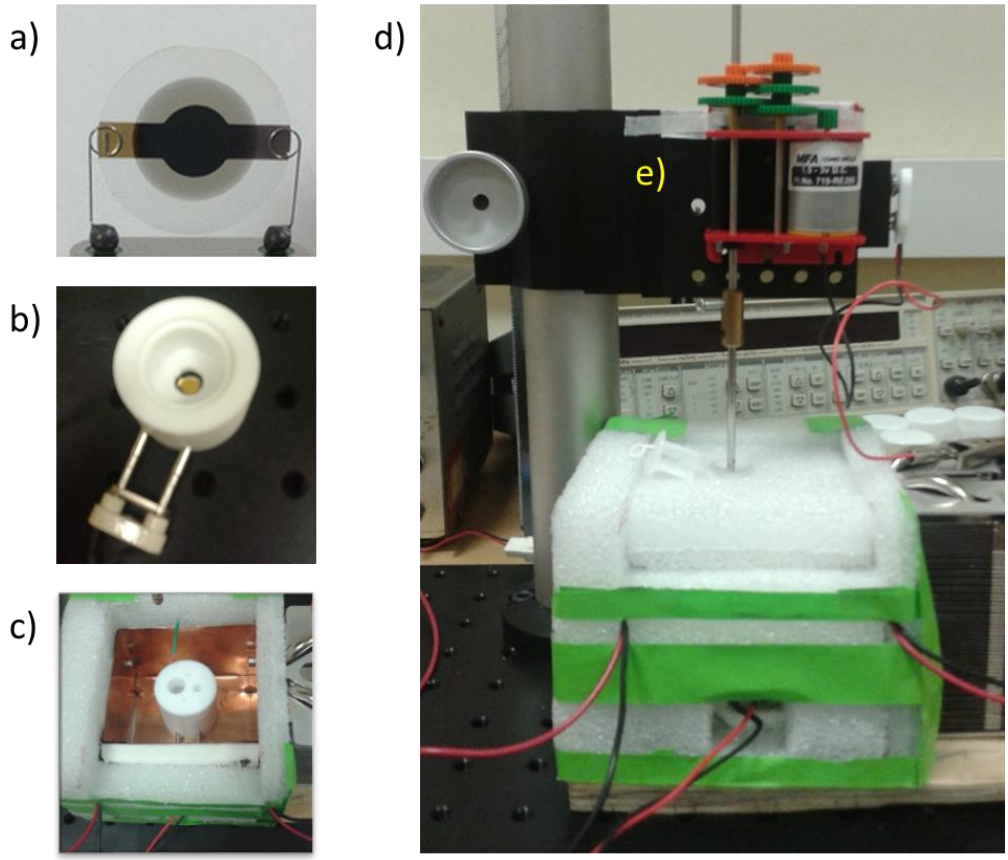

Figure 2.15. Instrumentals of the impedance QCM setup: (a) a-C coated QCM crystal, (b) static Teflon cell, (c) temperature-controlled box and (d) complete setup with the (e) mixer.

2.3.3.2 QCM with dissipation (QCM-D)

An alternative method for the simultaneous determination of the resonance frequency and the absolute *Q* factor was introduced by Rodahl *et. al*. [36] and it is referred as QCM-D. These instruments are now extremely popular and are widely used in many *in-situ* studies of biomolecule interactions at solid surfaces [39-44]. In the QCM-D setup the quartz crystal is exited at the resonance frequency by an external signal generator that can be separated from the resonator by means of a computer controlled relay [45]. When the voltage source connected to the QCM is switched off, the amplitude of the oscillation, *A*, decay as an exponentially damped sinusoid

$$A(t) = A_0 e^{-t/\tau} \sin(\omega t + \varphi) + constant, \qquad (2.18)$$

where τ is the decay time constant, φ is the phase, and the *constant* is the dc offset. The decay time is related to the dissipation factor *D* by

$$D = \frac{2}{\omega\tau} \qquad (2.19)$$

The dissipation factor is indicative of the energy dissipation and is equivalent to the inverse of the quality factor [36]. The entire process is continuously repeated, yielding both characteristic oscillation parameters with a time resolution of less than 10 s [45].

The QCM-D measurements carried out in this thesis were obtained thanks to the collaboration with Prof. María J. Santos-Martínez from the School of Pharmacy. The setup consisting in Q-Sense® E4 QCM-D system (Q-Sense AB, Vastra Frolunda, Sweden) is reported in Figure 2.16.

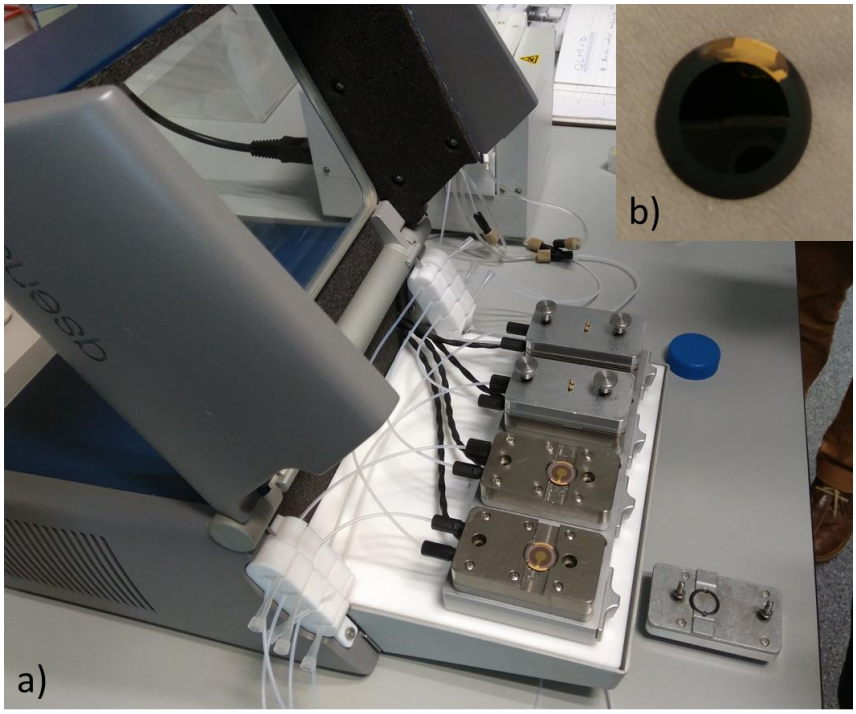

Figure 2.16. Q-Sense® E4 QCM-D system: (a) the four temperature and flow-controlled modules with two crystals mounted and (b) a-C coated QCM-D crystal.

2.4 References

1. Mahan, J.E., *Physical Vapor Deposition of Thin Films*. 2000: Wiley.
2. Robertson, J., *Diamond-like amorphous carbon.* Materials Science and Engineering Reports, 2002. **37**(4-6): p. 129-281.
3. Savvides, N. and B. Window, *Diamondlike amorphous carbon films prepared by magnetron sputtering of graphite.* Journal of Vacuum Science & Technology A: Vacuum, Surfaces, and Films, 1985. **3**(6): p. 2386-2390.
4. Cho, N.H., K.M. Krishnan, D.K. Veirs, M.D. Rubin, C.B. Hopper, and B. Bhushan, *Chemical structure and physical properties of diamond-like amorphous carbon films prepared by magnetron sputtering.* Journal of Materials Research, 1990. **5**(11): p. 2543-2554.
5. Logothetidis, S., *Sputtered amorphous carbon films: Micro-structure, density, optical and mechanical properties.* International Journal of Modern Physics B, 2000. **14**(2-3): p. 113-124.
6. Briggs, D., *Handbook of x-ray and ultraviolet photoelectron spectroscopy*. 1977: Heyden.
7. Israelachvili, J.N., *Intermolecular and Surface Forces*. 2010: Elsevier Science.
8. Zebda, A., H. Sabbah, S. Ababou-Girard, F. Solal, and C. Godet, *Surface energy and hybridization studies of amorphous carbon surfaces.* Applied Surface Science, 2008. **254**(16): p. 4980-4991.
9. Ham, H.O., S.H. Park, J.W. Kurutz, I.G. Szleifer, and P.B. Messersmith, *Antifouling Glycocalyx-Mimetic Peptoids.* Journal of the American Chemical Society, 2013. **135**(35): p. 13015-13022.
10. Ostuni, E., R.G. Chapman, R.E. Holmlin, S. Takayama, and G.M. Whitesides, *A survey of structure-property relationships of surfaces that resist the adsorption of protein.* Langmuir, 2001. **17**(18): p. 5605-5620.
11. Kasemo, B., *Biological surface science.* Surface Science, 2002. **500**(1-3): p. 656-677.
12. Ratner, B.D., A.S. Hoffman, F.J. Schoen, and J.E. Lemons, *Biomaterials Science*. 2nd ed. 2004, London: Elsevier Academic Press.
13. Stueber, M., L. Niederberger, F. Danneil, H. Leiste, S. Ulrich, A. Welle, M. Marin, and H. Fischer, *Surface topography, surface energy and wettability of magnetron-sputtered amorphous carbon (a-c) films and their relevance for platelet adhesion.* Advanced Engineering Materials, 2007. **9**(12): p. 1114-1122.
14. Kirschner, C.M. and A.B. Brennan, *Bio-Inspired Antifouling Strategies.* Annual Review of Materials Research, 2012. **42**(1): p. 211-229.
15. Morra, M., *Water in Biomaterials Surface Science*. 2001: John Wiley & Sons.
16. van Oss, C.J., *Interfacial Forces in Aqueous Media*. 1994: Taylor & Francis.
17. Owens, D.K. and R.C. Wendt, *Estimation of the surface free energy of polymers.* Journal of Applied Polymer Science, 1969. **13**(8): p. 1741-1747.
18. Zhao, Q., Y. Liu, and E.W. Abel, *Effect of temperature on the surface free energy of amorphous carbon films.* Journal of Colloid and Interface Science, 2004. **280**(1): p. 174-183.
19. van Oss, J.C., *Interfacial Forces in Aqueous Media*. 1st ed. 1994, New York: Marcel Dekker.

20. Van Oss, C.J., M.K. Chaudhury, and R.J. Good, *Interfacial Lifshitz-van der Waals and polar interactions in macroscopic systems.* Chemical Reviews, 1988. **88**(6): p. 927-941.
21. Della Volpe, C., D. Maniglio, M. Brugnara, S. Siboni, and M. Morra, *The solid surface free energy calculation: I. In defense of the multicomponent approach.* Journal of Colloid and Interface Science, 2004. **271**(2): p. 434-453.
22. Tolstoy, V.P., I. Chernyshova, and V.A. Skryshevsky, *Handbook of Infrared Spectroscopy of Ultrathin Films*. 2003: Wiley.
23. Leitner, T., J. Kattner, and H. Hoffmann, *Infrared reflection spectroscopy of thin films on highly oriented pyrolytic graphite.* Applied Spectroscopy, 2003. **57**(12): p. 1502-1509.
24. Sun, B., P.E. Colavita, H. Kim, M. Lockett, M.S. Marcus, L.M. Smith, and R.J. Hamers, *Covalent Photochemical Functionalization of Amorphous Carbon Thin Films for Integrated Real-Time Biosensing.* Langmuir, 2006. **22**(23): p. 9598-9605.
25. Brockman, J.M., B.P. Nelson, and R.M. Corn, *Surface Plasmon Resonance Imaging Measurements of Ultrathin Organic Films.* Annual Review of Physical Chemistry, 2000. **51**: p. 41-63.
26. Yonzon, C.R., E. Jeoung, S. Zou, G.C. Schatz, M. Mrksich, and R.P. Van Duyne, *A Comparative Analysis of Localized and Propagating Surface Plasmon Resonance Sensors: The Binding of Concanavalin A to a Monosaccharide Functionalized Self-Assembled Monolayer.* Journal of the American Chemical Society, 2004. **126**(39): p. 12669-12676.
27. Anker, J.N., W.P. Hall, O. Lyandres, N.C. Shah, J. Zhao, and R.P. Van Duyne, *Biosensing with plasmonic nanosensors.* Nat Mater, 2008. **7**(6): p. 442-453.
28. Hutter, E. and J.H. Fendler, *Exploitation of Localized Surface Plasmon Resonance.* Advanced Materials, 2004. **16**(19): p. 1685-1706.
29. Willets, K.A. and R.P.V. Duyne, *Localized Surface Plasmon Resonance Spectroscopy and Sensing.* Annual Review of Physical Chemistry, 2007. **58**(1): p. 267-297.
30. Haes, A.J., C.L. Haynes, A.D. McFarland, G.C. Schatz, R.P. Van Duyne, and S. Zou, *Plasmonic materials for surface-enhanced sensing and spectroscopy.* MRS Bulletin, 2005. **30**(5): p. 368-375.
31. Haes, A.J. and R.P. Van Duyne, *A unified view of propagating and localized surface plasmon resonance biosensors.* Analytical and Bioanalytical Chemistry, 2004. **379**(7): p. 920-930.
32. Jackman, J.A., B. Spackova, E. Linardy, M.C. Kim, B.K. Yoon, J. Homola, and N.-J. Cho, *Nanoplasmonic ruler to measure lipid vesicle deformation.* Chemical Communications, 2016. **52**(1): p. 76-79.
33. Zan, G.H., J.A. Jackman, S.-O. Kim, and N.-J. Cho, *Biosensors: Controlling Lipid Membrane Architecture for Tunable Nanoplasmonic Biosensing (Small 23/2014).* Small, 2014. **10**(23): p. 4827-4827.
34. Larsson, E.M., C. Langhammer, I. Zorić, and B. Kasemo, *Nanoplasmonic Probes of Catalytic Reactions.* Science, 2009.
35. Buttry, D.A. and M.D. Ward, *Measurement of interfacial processes at electrode surfaces with the electrochemical quartz crystal microbalance.* Chemical Reviews, 1992. **92**(6): p. 1355-1379.

36. Rodahl, M., F. Höök, A. Krozer, P. Brzezinski, and B. Kasemo, *Quartz crystal microbalance setup for frequency and Q ‐factor measurements in gaseous and liquid environments.* Review of Scientific Instruments, 1995. **66**(7): p. 3924-3930.
37. Sauerbrey, G.Z., *Use of quartz vibration for weighing thin films on a microbalance.* J. Physik, 1959. **155**: p. 206-212.
38. Jayasundara, D.R., R.J. Cullen, L. Soldi, and P.E. Colavita, *In Situ Studies of the Adsorption Kinetics of 4-Nitrobenzenediazonium Salt on Gold.* Langmuir, 2011. **27**(21): p. 13029–13036.
39. Dolatshahi-Pirouz, A., K. Rechendorff, M.B. Hovgaard, M. Foss, J. Chevallier, and F. Besenbacher, *Bovine serum albumin adsorption on nano-rough platinum surfaces studied by QCM-D.* Colloids and Surfaces B: Biointerfaces, 2008. **66**(1): p. 53-59.
40. Macakova, L., E. Blomberg, and P.M. Claesson, *Effect of Adsorbed Layer Surface Roughness on the QCM-D Response: Focus on Trapped Water.* Langmuir, 2007. **23**(24): p. 12436-12444.
41. Santos-Martinez, M.J., I. Inkielewicz-Stepniak, C. Medina, K. Rahme, D. Arcy, D. Fox, J.D. Holmes, H. Zhang, and M.W. Radomski, *The use of quartz crystal microbalance with dissipation (QCM-D) for studying nanoparticle-induced platelet aggregation.* International Journal of Nanomedicine, 2012. **7**: p. 243-255.
42. Su, X., Y.-J. Wu, and W. Knoll, *Comparison of surface plasmon resonance spectroscopy and quartz crystal microbalance techniques for studying DNA assembly and hybridization.* Biosensors and Bioelectronics, 2005. **21**(5): p. 719-726.
43. Wang, X., G. Herting, I. Odnevall Wallinder, and E. Blomberg, *Adsorption of bovine serum albumin on silver surfaces enhances the release of silver at pH neutral conditions.* Physical Chemistry Chemical Physics, 2015. **17**(28): p. 18524-18534.
44. Esmeryan, K.D., C.E. Castano, M. Abolghasemibizaki, and R. Mohammadi, *An artful method for in-situ assessment of the anti-biofouling potential of various functional coatings using a quartz crystal microbalance.* Sensors and Actuators B: Chemical, 2017. **243**: p. 910-918.
45. Eike, L., H. Alexander, K. Katja, S. Claudia, R. Björn, W. Joachim, P. Bruno, and J. Andreas, *Adhesion of liposomes: a quartz crystal microbalance study.* Measurement Science and Technology, 2003. **14**(11): p. 1865.

3 Amorphous Carbon Characterization

This chapter reports a full characterization of amorphous carbon films produced in our lab via DC magnetron sputtering deposition. Chemical composition, optical and electrical properties, morphology and surface free energy of three types of films were determined: amorphous carbon (a-C) is a highly graphitic film with high optical absorptivity; hydrogenated amorphous carbon (a-C:H) has a low graphitic content and high optical transparency; and oxidised amorphous carbon (ox-C) obtained from UV/ozone exposition is a very hydrophilic surface.

This chapter includes contributions from my co-workers, as noted in the text. Specifically, James Behan contributed with the validation of the model used for ellipsometry data, while data fitting and analysis leading to the reported values were carried out by myself; Joana Vasconcelos generated the AFM images reported. Regarding the XPS data, I collected the XPS spectra presented in the chapter; the values reported are the combined result of the data analysis carried out by Joana Vasconcelos Ronan Cullen and myself.

3.1 Introduction

In the first chapter we gave a quick overview of the numerous applications of carbon materials and coatings: from charge storage to catalytic support, structural components, and medical implantable devices. Such a variability and adaptability, typical of DLC coatings, is due to the wide range of outstanding properties that this family of material can display. Depending on the type of deposition, preparation parameters and doping materials, the physical and structural properties of carbon coatings can change markedly [1] and, therefore, they have been the subject of experimental and theoretical research for several decades [1-6]. Nevertheless the variety of deposition systems and the diversity of carbon films have generated, in the past, some confusions in the nomenclature, where sometimes the same name was used for different types of film or different names were used for similar films [1]. It is essential to understand which type of DLC coating possess the best properties for the various application for the rational design of carbon-based devices. For this reason in this chapter we are going to provide a full characterization of the films produced in our lab.

One of the main properties to consider is the chemical composition of the film. DLC is a disordered phase of carbon without long-range order, containing carbon atoms manly in graphite-like sp^2 and diamond-like sp^3 [4] centres. Therefore the determination of the sp^2/sp^3 hybridization ratio is one of the principal aspects of the film characterization. Many mechanical properties, such us hardness and atomic density are, in fact, dependent from this ratio: films with higher sp^3 content tend to be less conductive, harder and of higher density than those rich in sp^2 centres; while hydrogen doping produces softer carbon materials, accompanied by a decreasing of sp^3 content [2]. A number of techniques have been used for determinations of the sp^2/sp^3 ratio in disordered carbon films: high energy electron loss spectroscopy (HEELS) and near-edge X-ray-adsorption spectroscopy (NEXAFS) are considered the most reliable measurements; ^{13}C nuclear magnetic resonance (NMR) is also rather common; while Raman is less direct, but provides a relatively fast and non disruptive method [3, 4, 7]. In this thesis we used X-ray photoemission spectroscopy (XPS) [4, 7], which is recognized as a useful tool for the investigation of local binding in materials science. Because of the localized nature of the core-level state, XPS shows in the C 1s envelope the contribution of

the carbon atoms in the sp^2 and sp^3 configurations; in addition to other minor components, mostly due to oxidized carbon centres. Moreover XPS has the advantage of identifying impurities of heteroatoms incorporated in the film, which can arise from leaks or post deposition saturation in the sputtering chamber. Therefore XPS measurements are carried out periodically to test the quality of our films.

Optical transparency and good conductivity also underpin the success of carbon materials in applications such as optical windows and micro-electrochemical devices [2]. One of the main parameters to classify carbon materials is the optical bandgap and many studies have been dedicated to find a correlation with the film composition [6, 8, 9]. Now it is generally accepted that the collective behaviour of sp^2 sites, embedded in the amorphous sp^3 matrix, are responsible for the optical and electrical properties [8]. The optical bandgap can be calculated from UV-Vis measurements [8, 10] or spectroscopic ellipsometry (SE) [11, 12] analysis, which provides also the optical constants by fitting the experimental data with the appropriate model. SE is also used in our lab as a diagnostic tool to check the quality of deposited films, thanks to its high sensitivity to bulk properties; furthermore the speed of analysis makes it suitable for periodic monitoring of film quality.

Chemical composition and optical properties are both part of the bulk characterization, whereas the interactions between carbon based devices and the surrounding environment are governed by the surface properties [6, 13, 14]. Morphology and surface free energy (SFE) are two of the main aspects in the determination of these interactions. The former is important for many applications where a smooth film is required. The SFE (together with the wettability), instead, is a common parameter used to predict the response of biological fluids to biomedical and implantable devices.

Herein we present a detailed characterization of three types of carbon: amorphous carbon (a-C) that is highly graphitic; hydrogenated amorphous carbon (a-C:H), a hydrogen-doped, sp^3-rich carbon; and oxidized amorphous carbon (ox-C), obtained from the surface oxidation of a-C substrates. Film composition and sp^2/sp^3 ratio were determined via XPS. Optical constants and film thickness were obtained from modelling of SE results. The morphology of the coatings was

studied via atomic force microscopy (AFM) roughness measurements. Moreover, the thickness values obtained from SE were confirmed by AFM using a more direct method. Finally the wettability and SFE of carbon coatings were determined using the vOGC method from multisolvent contact angle (CA) analysis.

3.2 Experimental

Chemicals and Materials. Diiodomethane (99%), glycerol (≥99.5%), sulfuric acid (95-97%), hydrochloric acid (37%), hydrogen peroxide (30%) and methanol (semiconductor grade) were purchased from Sigma and used without further purification. B-doped Si wafers were purchased from MicroChemicals (5-10 Ohms). Millipore water was used for all experiments.

Substrate Preparation. Amorphous carbon films were prepared via DC magnetron sputtering (Torr International, Inc.) at a base pressure ≤2×10^{-6} mbar and a deposition pressure of 7×10^{-3} mbar, as described in Chapter 2 (page 33). Two distinct films were prepared by varying the H_2/Ar gas ratio: one type of film was sputtered using Ar and shall be referred to as a-C from here onwards, the second type of film was sputtered using 10% H_2 in Ar resulting in a hydrogen doped material which is referred to as a-C:H. Silicon wafers were cleaned in piranha solution prior to deposition (H_2SO_4 : H_2O_2 in a 3:1 ratio – *WARNING: Piranha solution is a strong oxidant and reacts violently with organic materials and presents an explosion danger; all work should be performed under a fume hood*). For preparation of the oxidised a-C (ox-C), a-C substrates were exposed to UV light for 2 h under air. The process produces the oxidation of the carbon sites due to the formation of ozone under UV irradiation.

Characterization Methods. X-ray photoelectron spectroscopy (XPS) characterization was performed on an ultrahigh vacuum system (Omicron) at 1×10^{-10} mbar base pressure, equipped with a monochromatized Al Kα source (1486.6 eV) and a multichannel array detector, as described in Chapter 2 (page 37). Spectra were recorded with an analyzer resolution of 0.5 eV at 45° takeoff angle. Peaks were fitted to Voigt functions after Shirley background correction[15, 16] using commercial software (CasaXPS); atomic ratios were obtained from area ratios using sensitivity factors (C = 0.296; O = 0.711). Static contact angles (CA) were measured on a CA analyser (FTA) under ambient conditions of temperature

and humidity; samples were rinsed in methanol immediately prior to CA characterization [17] and a minimum of three CA measurements were obtained for each surface. Spectroscopic ellipsometry (SE) was carried out using an alpha-SETM ellipsometer (J.A. Woolam Co.). Carbon films were deposited on clean Si wafers and measured at 65°, 70°, 75° incidence angle over the 370–900 nm range; SE data was then fitted using the CompleteEASE® software package using a three layer model to account for Si, carbon and air phases. Thickness and surface roughness measurements were carried out via AFM (Asylum Research) using Au-coated silicon cantilevers (NT-MDT) in tapping mode (1 Hz and 512 scan lines).

3.3 Result and Discussion

Amorphous carbon presents heterogeneous bulk structure, typically described as a mixture of sp^2 clusters embedded in an sp^3 matrix, with electronic properties ranging from semimetallic to semiconducting [2, 18]. Depending on the conditions of deposition the ratio of sp^2 to sp^3 centres may be altered, resulting in different properties [2]. Effects of bulk composition on surface reactivity were already observed by our group: the rate of the spontaneous reaction of aryldiazonium salts on a-C were found to be strongly depended on the sp^2 content [10, 19].

XPS was used to characterize the composition of a-C, a-C:H and ox-C. [10, 20]. Even though XPS is generally considered a surface technique, the probing depth in carbon is 8-10 nm, enough to provide information on the carbon bulk composition. Survey scans (see Figure 3.1a) show the presence of carbon (at 284 eV) and oxygen (at 532 eV) in all the three samples, whereas the absence of any peaks around 400 eV indicates that no nitrogen is incorporated into the film during deposition. A more intense oxygen peak was observed for the ox-C sample, in respect to the other two films, indicating a higher content of oxygen in the oxidised carbon. XPS spectra in the C 1s region for a-C, a-C:H and ox-C films are shown in Figure 3.1b. The three samples display a main asymmetric peak that is characteristic of amorphous carbons. Peak asymmetry arises from the presence of carbon atoms in sp^2 and sp^3 bonding configurations at binding energies separated

by 0.7-0.9 eV, from energy losses and from the presence of small amounts of surface oxides [4, 7, 10]. Fit of the C 1s peak of a-C and ox-C samples yielded two main contributions at 284.4 and 285.1 eV that is assigned to sp^2 and sp^3 carbon centres, respectively. Differently, the spectrum of a-C:H was satisfactorily fitted with only one main contribution at 285.1 eV assigned to sp^3 carbons, thus confirming that this surface is rich in sp^3 centres as previously reported [10, 20]. Minor contributions at higher binding energy (286-288 eV) attributed to oxidized groups were observed for a-C, a-C:H and, to a greater extent for ox-C. In the case of ox-C, an additional contribution at 288.7 eV indicates the presence of carboxylic groups as a result of the oxidation process [20, 21].

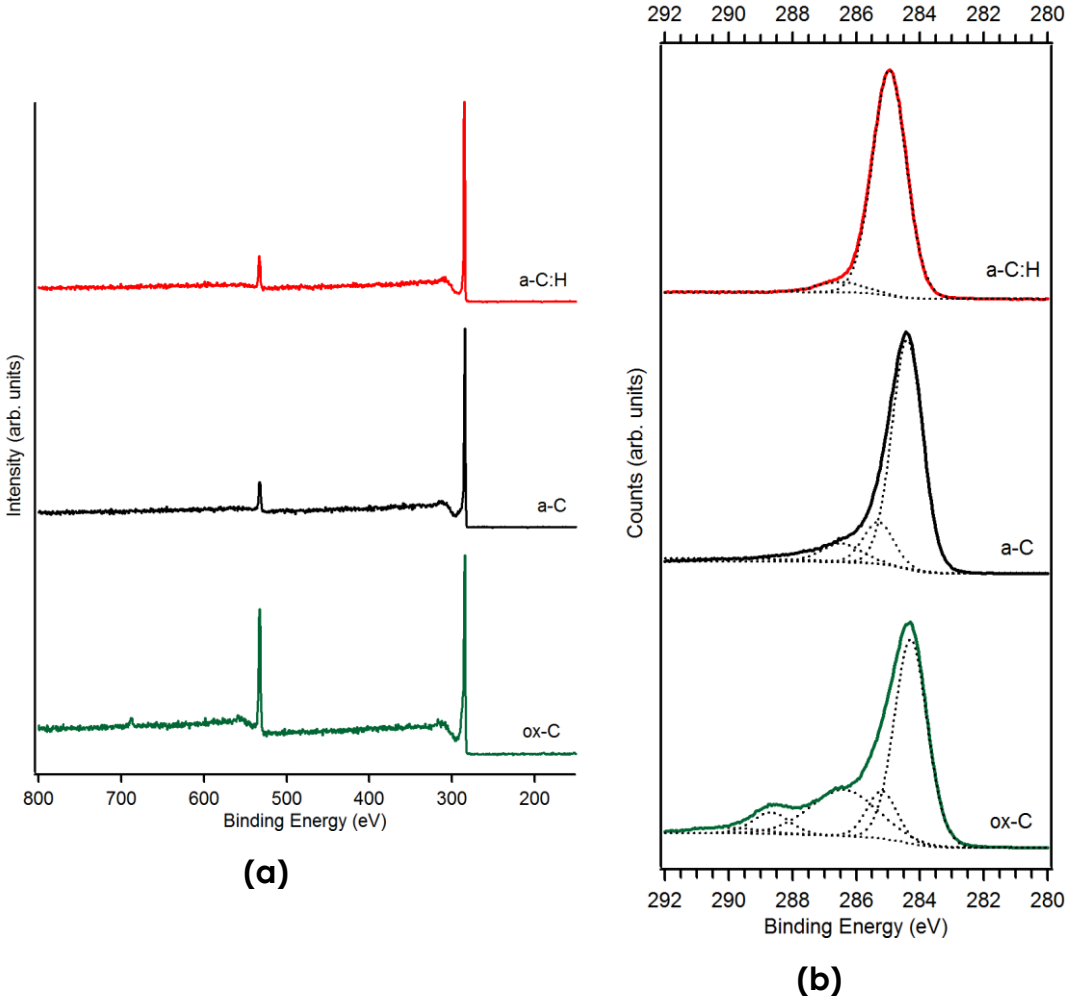

Figure 3.1. XPS spectra of (a) survey scan and (b) the C 1s region for a-C:H (red line, top), a-C (black line, middle) and ox-C (green line, bottom). Shirley background and individual contributions obtained from the best fits are show under each curve.

The relative area contribution of the sp^2 peak has been used for estimating the bulk concentrations of sp^2 centres. The relative peak area $A_{(284.4)}/A_{(284.4+285.1)}$ was found to be very similar for a-C and ox-C, with values ranging between 80% and 85%. In the case of a-C:H, only the sp^3 contribution was needed for the fitting of the C 1s peak, thus the sp^2/sp^3 ratio was approximated to 0% [20]. Increase in H content is, in fact, accompanied by a decrease in the sp^2 content in amorphous carbons due to the saturation of sp^2 centres via formation of C-H bonds [10]. The oxygen content of the three carbon materials was obtained from fits of the O 1s peak at 532 eV (data not shown). The peak area ratio A_{O1s}/A_{C1s}, corrected by relative sensitivity factors, yielded similar values of O/C ratio for a-C and a-C:H films, with values ranging between 5 and 9%. Much higher O/C ratio was found for the ox-C sample, which is consistent with the sample having undergone oxidative treatment, as already observed in the survey scan (Figure 3.1a). The O/C content in the ox-C film was estimated to 20%.

The bulk optoelectronic properties of amorphous carbon films were investigated via SE measurements. James Behan contributed to these measurements with the validation of the model used for the data fitting. The Si substrate was first characterised separately via SE using optical constants for the Si and SiO_2 layers taken from Herzinger *et al.*;[22] the experimentally determined thickness of the native oxide (1.9 nm) was kept constant in all models. In the case of a-C films, the resulting data were fitted using a 3-layer model which takes into account the substrate (Si), the a-C layer and the air phase. The a-C layer in the model stack was the only one allowed to vary and its optical constants were fitted using B-Splines while enforcing Kramers-Kronig consistency [23]. This model represents a purely mathematical parameterization (*i.e.* it requires no knowledge of the film's properties), but still results in optical constants that are physically meaningful. In the case of a-C:H films, the best fits were obtained with a similar 3-layer modelling procedure using the Tauc-Lorentz (TL) model to describe the a-C:H layer. The TL model is an empirical model which has been successfully applied to describe the optical properties of amorphous carbon films with a high degree of sp^3 bonding by other groups [24, 25]. Briefly, the Tauc-Lorentz model expresses the imaginary part of the complex dielectric function, $\varepsilon_2(E)$, as a product of the Tauc Joint Density of States (DOS) and $\varepsilon_2(E)$ obtained from the Lorentz oscillator:

$$\varepsilon_2(E) = \frac{AE_0\Gamma(E-E_g)^2}{E\left[(E^2-E_0^2)^2+\Gamma^2E^2\right]}\Theta(E-E_g) \tag{3.1}$$

With $\Theta(E < E_g) = 0$ and $\Theta(E \geq E_g) = 1$. The expression utilises 4-parameters: a prefactor, *A*, broadening parameter Γ, the peak in the joint DOS E_0 and the band gap, E_g. The real part of the dielectric function, $\varepsilon_1(E)$ is then obtained via Kramers-Kronig integration of $\varepsilon_2(E)$[25]:

$$\varepsilon_1(E) = \varepsilon_1(\infty) + \frac{2}{\pi}P\int_{E_g}^{\infty}\frac{\xi\varepsilon_2(E)}{\xi^2-E^2}d\xi \tag{3.2}$$

Fits of multiple a-C and a-C:H films obtained from 40 min long depositions were carried out using this procedure, yielding an average thickness of (73.6 ± 0.6) nm (C.I. 95%) for a-C and of (81.6 ± 0.5) nm (C.I. 95%) for a-C:H. The real (*n*) and imaginary (*k*) part of the refractive index of both types of carbon film are plotted in Figure 3.2.

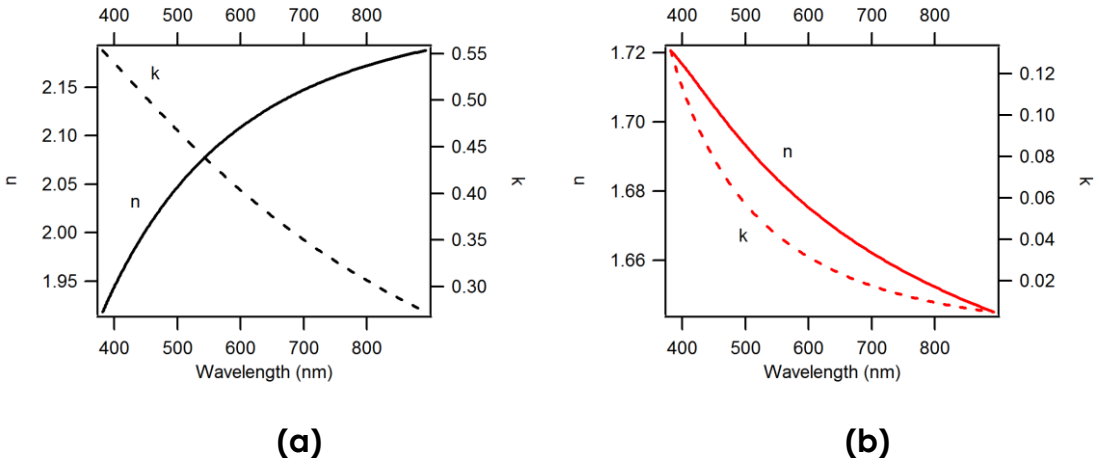

(a) **(b)**

Figure 3.2. Graphs of optical constants, *n* (solid line) and *k* (dotted line), of a-C (a) and a-C:H (b) films obtained via SE measurements. Figure adapted with permission from Zen, F., V.D. Karanikolas, J.A. Behan, J. Andersson, G. Ciapetti, A.L. Bradley, and P.E. Colavita, Langmuir, 2017. 33(17): p. 4198-4206. Copyright 2017 American Chemical Society.

These optical constants are used for the optical bandgap determination. The optical bandgap, usually known as Tauc gap (E_T) in amorphous semiconducting materials, can be extracted from the so-called Tauc formula, which is the most common in literature [8]. According to this formalism the adsorption coefficient α obeys the following relationship [26].

$$(\alpha h\nu)^{1/2} = B(h\nu - E_T) \tag{3.3}$$

where B is a constant known as disorder parameter and $h\nu$ is the photon energy. The imaginary part of the refractive index was used to calculate the absorption coefficient as a function of wavelength according to the expression $\alpha = \frac{4\pi k}{\lambda}$. Thus a Tauc plot of $(\alpha h\nu)^{1/2}$ vs. photon energy ($h\nu$) was used to carry out a fit of the linear region to Equation (3.3). The intercept on the x-axis yields the E_T value which relates to the metallic/semiconducting nature of the amorphous carbon material. In Figure 3.3 are reported the typical Tauc plots for a-C and a-C:H; the figure shows that the E_T value is larger for a-C:H thus confirming that this is a more semiconducting material than the graphitic a-C films, in agreement with similarly prepared films from our group [10]. The average E_T values calculated were found to be (0.66 ± 0.01) eV and (1.77 ± 0.01) eV for a-C and a-C:H, respectively (95% C.I.).

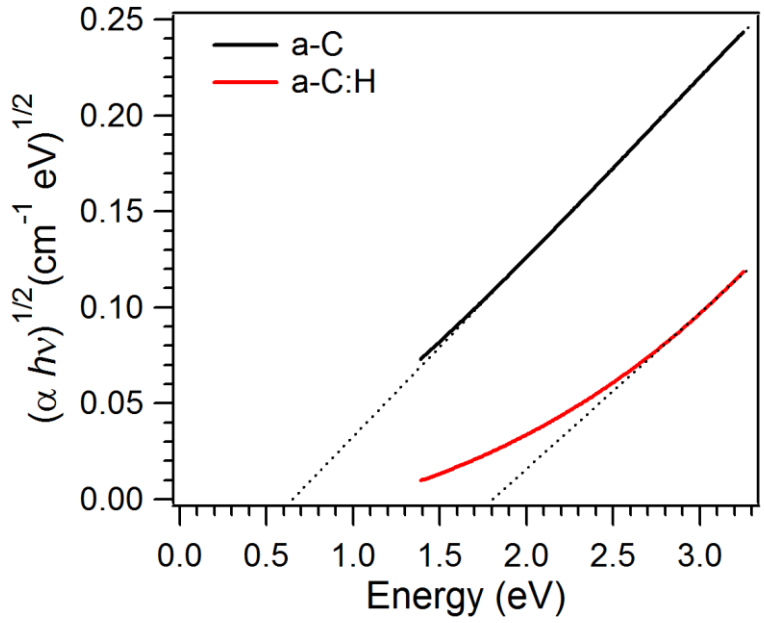

Figure 3.3. Tauc plots for a-C (black) and a-C:H (red) films. Extrapolation of the linear fit (dot line) to the X-axis results in Tauc Gap values for both carbon surfaces.

In the case of ox-C films, the UV/ozone oxidation of a-C films is a surface treatment that yields a graphitic surface with an overlayer of oxidised material. SE was used to determine the thickness of this oxide layer. For this purpose the data obtained from SE measurements were fitted using the same model utilized for the a-C film, with the addition of an oxidised surface on top of the a-C layer, modelled as a transparent Cauchy layer [27]. The thickness of both the a-C and the oxidised

overlayer were allowed to vary yielding a thickness for the oxidised overlayer of (2.8 ± 0.2) nm.

The morphology of three types of film were characterized via AFM imaging. All amorphous carbon surfaces were found to be relatively smooth and featureless (see Figure 3.4), with rms roughness of (0.94 ± 0.03) nm, (1.16 ± 0.08) nm and (0.86 ± 0.07) nm, for a-C, a-C:H and ox-C, respectively, (95% C.I.).

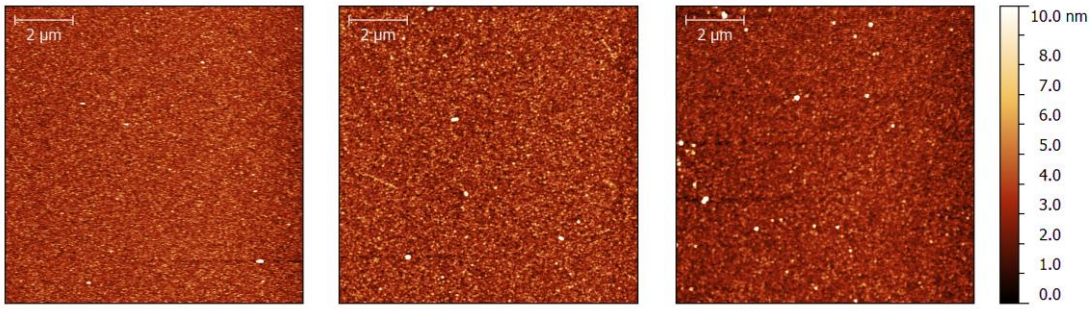

Figure 3.4. AFM topography images of a-C (a), a-C:H (b) and ox-C (c) surfaces; with the courtesy of J. M. Vasconcelos [20].

Finally SFEs of the three substrates were determined via CA measurements using multisolvent analysis. Liquid CAs can be considered independent from the surface morphology, owing to the low and very similar roughness obtained for the three carbon films [17]. For the SFE determination we used two methods: the model developed by Owen, Went, Rabel and Kaelble (OWRK) [28] and the one by van Oss, Chaudhury and Good (vOCG) [29, 30], which were described in detail in the previous chapter (see pages 39-41). Briefly, the OWRK model assumes that (i) the surface tension is the result of additive contributions from independent dispersive (γ^d) and polar forces (γ^p):

$$\gamma = \gamma^d + \gamma^p \tag{3.4}$$

and (ii) that the dispersive and polar components of the solid-liquid work of adhesion, W_{SL} can be approximated by a geometric mean as below:

$$W_{SL} = W_{SL}^d + W_{SL}^p = 2\left(\sqrt{\gamma_S^d \gamma_L^d} - \sqrt{\gamma_S^p \gamma_L^p}\right) \tag{3.5}$$

where the subscripts "*S*" and "*L*" stand for solid and liquid, respectively.

Combining Young-Dupre's equation[30] with equation (3.4) we obtain:

$$\frac{\gamma_L(1+\cos\theta)}{2\sqrt{\gamma_L^d}} = \sqrt{\gamma_S^d} + \frac{\sqrt{\gamma_L^p}}{\sqrt{\gamma_L^d}}\sqrt{\gamma_S^p} \tag{3.6}$$

Eq. (6) can be used to obtain γ_S^d and γ_S^p of a solid by measuring the CA of a series of liquids with known surface tension components (γ_L, γ_L^d, γ_L^p) [31]. Multisolvent analysis was carried out using two nonpolar and three polar test liquids: diiodomethane, 1-bromonaphthalene, glycerol, formamide and distilled water, as reported in Chapter 2. A linear fit of the lhs of eq.(8) vs. $\sqrt{\gamma_L^p}/\sqrt{\gamma_L^d}$ yields the polar and dispersive components of the unknown SFE[17] (see Figure 3.5): the intercept and slope were used to calculate γ_S^d and γ_S^p values, which are summarized in Table 3.1.

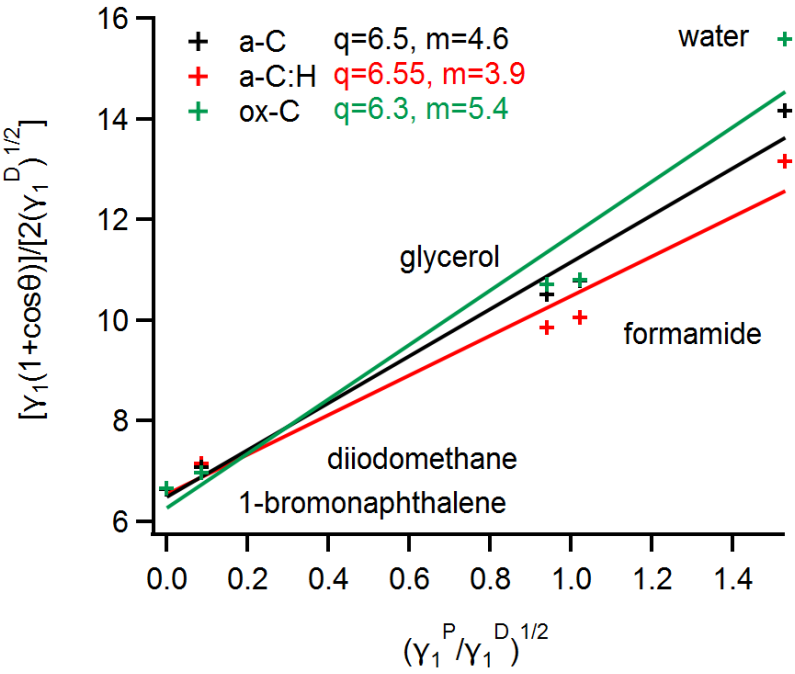

Figure 3.5. OWRK plots for a-C (black line), a-C:H (red line) and ox-C (green line) constructed using multisolvent CA data according to equation (3.6). The intercept (q) and the slope (m) of the linear fits, reported on the top left side of the graphs, were used to calculate the polar and dispersive components of the total surface tension of the solid reported in Table 3.1.

Table 3.1. Surface free energy or total surface tension (γ_S), and dispersive (γ_S^d) and polar (γ_S^p) components (mJ m^{-2}) of a-C, a-C:H and ox-C surfaces obtained from OWRK model.

Surface	γ_S (mJ m^{-2})	γ_S^d (mJ m^{-2})	γ_S^p (mJ m^{-2})
a-C	63.9	42.2	21.7
a-C:H	58.4	42.9	15.5
ox-C	68.5	39.4	29.1

The second model used for the calculation of the SFEs of a-C, a-C:H and ox-C surfaces is the vOGC model. By analogy with the OWRK, the vOGC model assumes that the total surface tension can be split into an apolar, or Lifshitz-van der Waals (γ^{LW}), and a polar (γ^{AB}) component. Additionally, the latter includes contributions γ^- and γ^+ from electron donor-acceptor interactions, respectively, also called Lewis base-acid interactions. As described in Chapter 2, the SFE (γ_{tot}) and its apolar (γ^{LW}) and polar (γ^{AB}) components of a solid can be estimated from the CAs (θ) of three tested liquids with known surface tension components γ_L^{LW}, γ_L^- and γ_L^+ using the following equation [29, 30].

$$\sqrt{\gamma_S^{LW}\gamma_L^{LW}} + \sqrt{\gamma_S^-\gamma_L^+} + \sqrt{\gamma_S^+\gamma_L^-} = \frac{\gamma_L}{2}(1+\cos\theta) \qquad (3.7)$$

where the subscripts "*S*" and "*L*" stand for solid and liquid, respectively. Water (W), glycerol (G) and diiodomethane (DIM) were the three liquids chosen to be used, accordingly to the results provided by Della Volpe et al. [32]. First γ_S^{LW} was calculated using eq. (3.7) and the CA of diiodomethane, for which $\gamma_L^+ = \gamma_L^- = 0$. CAs of water and glycerol were then used to set a system of two linear equations that were solved for $\sqrt{\gamma_S^+}$ and $\sqrt{\gamma_S^-}$. Thus γ_S^{AB} can be obtained using the correlation $\gamma_S^{AB} = 2\sqrt{\gamma_S^-\gamma_S^+}$. The resulted SFEs with the measured CAs are reported in Table 3.2 for the three a-C, a-C:H and ox-C films.

Table 3.2. Summary of SFE determination for a-C, a-C:H and ox-C surfaces: measured contact angles using water (θ_W), glycerol (θ_G) and diiodomethane (θ_{DM}); surface free energy or total surface tension (γ_{tot}), its dispersive (γ^{LW}), electron accepting (γ^+), donating (γ^-) and polar (γ^{AB}) components determined from vOCG analysis.

Surface	Contact Angle (degrees)			SFE components (mJ m^{-2})				
	θ_W	θ_G	θ_{DM}	γ^{LW}	γ^+	γ^-	γ^{AB}	γ_{tot}
a-C	35.3 ± 1.4	22.2 ± 1.4	11.9 ± 0.9	49.7	1.79	27.4	14.0	63.7
a-C:H	46.6 ± 2.6	36.6 ± 1.4	3.9 ± 1.3	50.7	0.84	21.8	8.5	59.2
ox-C	3.2 ± 0.4	16.1 ± 1.5	19 ± 4	48.0	1.34	46.7	15.8	63.9

Water CA provides a direct measurement of the wettability of carbon surfaces, which is particular important for biological applications where water is the main medium of interest (see Section 1.5). For a-C we obtained a water CA of 35.3º, while the a-C:H was found to be more hydrophobic with a water CA of 46.6º. These results are in good agreement with Leezenberg *et. al.* [33], who observed an increment of the hydrophobicity for hydrogenated amorphous carbon materials. On the other hand, ox-C has a very low water CA (θ_W < 5º) as a result of the hydrophilic oxidized layer formed during the exposure to the UV lamp. The OWRK and vOGC models are given consistent results for the calculated SFEs: the total surface tensions are very similar among the three carbon films; while a larger difference is observed for the polar component which follows the trend a-C:H < a-C < ox-C, in agreement with the increase of hydrophilicity among the surfaces.

3.4 Conclusion

In this chapter we utilized a number of techniques for the characterization of three different amorphous carbon films: a-C and a-C:H were produced by DC sputtering deposition, while ox-C is obtained from surface oxidation of a-C substrates. A combination of XPS, SE, AFM and CA methods where used for the determinations of bulk and surface properties of the films. XPS measured different sp^2/sp^3 hybridization ratio for a-C and a-C:H films, at which corresponds also diverse optical and electrical properties obtained from SE analysis: a-C was found

being highly graphitic and with small optical bandgap, whereas a-C:H, mainly present in the sp^3 configuration, possesses a more semiconducting behaviour. Sensitive change in wettability was observed upon the oxidative treatment: ox-C films resulted in an extremely hydrophilic material compared to both a-C and a-C:H surfaces, while morphology remained unchanged. To facilitate comparison of amorphous carbon properties, our results are summarised in Table 3.3.

Table 3.3. Summary of measured properties for a-C, a-C:H and ox-C films.

Surface	sp^2/sp^3 ratio	*O/C ratio*	E_T (eV)	RMS roughness (nm)	wCA (degrees)	SFE_{vOCG} (mJ m^{-2})
a-C	85%	7%	0.66 ± 0.01	0.94 ± 0.03	35.3 ± 1.4	63.7
a-C:H	0%	7%	1.77 ± 0.01	1.16 ± 0.08	46.6 ± 2.6	59.2
ox-C	82%	20%	-	0.86 ± 0.07	3.2 ± 0.4	63.9

The characterization presented above underlines the versatility of amorphous carbon materials, whose properties can be tuned through doping or surface modifications, based on the application's purposes. The description and understanding of these properties is an indispensable step for the rational design of new carbon-based material.

3.5 References

1. Lifshitz, Y., *Hydrogen-free amorphous carbon films: correlation between growth conditions and properties.* Diamond and Related Materials, 1996. **5**(3): p. 388-400.
2. Robertson, J., *Diamond-like amorphous carbon.* Materials Science and Engineering Reports, 2002. **37**(4-6): p. 129-281.
3. Ferrari, A.C. and J. Robertson, *Interpretation of Raman spectra of disordered and amorphous carbon.* Physical Review B, 2000. **61**(20): p. 14095-14107.
4. Haerle, R., E. Riedo, A. Pasquarello, and A. Baldereschi, *sp(2)/sp(3) hybridization ratio in amorphous carbon from C 1s core-level shifts: X-ray photoelectron spectroscopy and first-principles calculation.* Physical Review B, 2002. **65**(4): p. 045101.
5. Lifshitz, Y., *Diamond-like carbon — present status.* Diamond and Related Materials, 1999. **8**(8–9): p. 1659-1676.
6. Popescu, A., G. Stan, L. Duta, C. Nita, C. Popescu, V.-A. Surdu, M.-A. Husanu, B. Bita, R. Ghisleni, C. Himcinschi, and V. Craciun, *The Role of Ambient Gas and Pressure on the Structuring of Hard Diamond-Like Carbon Films Synthesized by Pulsed Laser Deposition.* Materials, 2015. **8**(6): p. 3284.
7. Jackson, S.T. and R.G. Nuzzo, *Determining hybridization differences for amorphous carbon from the XPS C 1s envelope.* Applied Surface Science, 1995. **90**(2): p. 195-203.
8. Foulani, A., *Annealing effects on optical and photoluminescence properties of a-C : H films.* Journal of Physics D: Applied Physics, 2003. **36**(4): p. 394.
9. Bewilogua, K. and D. Hofmann, *History of diamond-like carbon films — From first experiments to worldwide applications.* Surface and Coatings Technology, 2014. **242**: p. 214-225.
10. Cullen, R.J., D. Jayasundara, L. Soldi, J. Cheng, G. Dufaure, and P.E. Colavita, *Spontaneous grafting of nitrophenyl groups on amorphous carbon thin films: A structure-reactivity investigation.* Chemistry of Materials, 2012. **24**(6): p. 1031-1040.
11. Weber, J.W., T.A.R. Hansen, M.C.M. van de Sanden, and R. Engeln, *B-spline parametrization of the dielectric function applied to spectroscopic ellipsometry on amorphous carbon.* Journal of Applied Physics, 2009. **106**(12): p. 123503.
12. Behan, J.A., S.N. Stamatin, M.K. Hoque, G. Ciapetti, F. Zen, L. Esteban-Tejeda, and P.E. Colavita, *Combined Optoelectronic and Electrochemical Study of Nitrogenated Carbon Electrodes.* The Journal of Physical Chemistry C, 2017. **121**(12): p. 6596-6604.
13. Hauert, R., *A review of modified DLC coatings for biological applications.* Diamond and Related Materials, 2003. **12**(3-7): p. 583-589.
14. Stueber, M., L. Niederberger, F. Danneil, H. Leiste, S. Ulrich, A. Welle, M. Marin, and H. Fischer, *Surface topography, surface energy and wettability of magnetron-sputtered amorphous carbon (a-c) films and their relevance for platelet adhesion.* Advanced Engineering Materials, 2007. **9**(12): p. 1114-1122.
15. Shirley, D.A., *High-Resolution X-Ray Photoemission Spectrum of the Valence Bands of Gold.* Physical Review B, 1972. **5**(12): p. 4709-4714.

16. Proctor, A. and P.M.A. Sherwood, *Data analysis techniques in x-ray photoelectron spectroscopy.* Analytical Chemistry, 1982. **54**(1): p. 13-19.
17. Zebda, A., H. Sabbah, S. Ababou-Girard, F. Solal, and C. Godet, *Surface energy and hybridization studies of amorphous carbon surfaces.* Applied Surface Science, 2008. **254**(16): p. 4980-4991.
18. Pierson, H.O., *14 - Diamond-Like Carbon (DLC)*, in *Handbook of Carbon, Graphite, Diamonds and Fullerenes*. 1993, William Andrew Publishing: Oxford. p. 337-355.
19. Murphy, D.M., R.J. Cullen, D. Jayasundara, R.L. Doyle, M.E.G. Lyons, and P.E. Colavita, *Heterogeneous charge transfer at the amorphous carbon/solution interface: effect on the spontaneous attachment of aryldiazonium salts.* Journal of Physical Chemistry C, 2013. **117**(44): p. 22768–22777.
20. Vasconcelos, J.M., F. Zen, S.N. Stamatin, J.A. Behan, and P.E. Colavita, *Determination of surface ζ-potential and isoelectric point of carbon surfaces using tracer particle suspensions.* Surface and Interface Analysis, 2017. **49**(8): p. 781-787.
21. Johansson, E. and L. Nyborg, *XPS study of carboxylic acid layers on oxidized metals with reference to particulate materials.* Surface and Interface Analysis, 2003. **35**(4): p. 375-381.
22. Herzinger, C.M., B. Johs, W.A. McGahan, J.A. Woollam, and W. Paulson, *Ellipsometric determination of optical constants for silicon and thermally grown silicon dioxide via a multi-sample, multi-wavelength, multi-angle investigation.* Journal of Applied Physics, 1998. **83**(6): p. 3323-3336.
23. Weber, J.W., T.A.R. Hansen, M.C.M.v.d. Sanden, and R. Engeln, *B-spline parametrization of the dielectric function applied to spectroscopic ellipsometry on amorphous carbon.* Journal of Applied Physics, 2009. **106**(12): p. 123503.
24. Logothetidis, S., *Optical and electronic properties of amorphous carbon materials.* Diamond and Related Materials, 2003. **12**(2): p. 141-150.
25. Jellison Jr, G.E., V.I. Merkulov, A.A. Puretzky, D.B. Geohegan, G. Eres, D.H. Lowndes, and J.B. Caughman, *Characterization of thin-film amorphous semiconductors using spectroscopic ellipsometry.* Thin Solid Films, 2000. **377–378**(0): p. 68-73.
26. Tauc, J., R. Grigorovici, and A. Vancu, *Optical Properties and Electronic Structure of Amorphous Germanium.* physica status solidi (b), 1966. **15**(2): p. 627-637.
27. Franquet, A., J. De Laet, T. Schram, H. Terryn, V. Subramanian, W.J. van Ooij, and J. Vereecken, *Determination of the thickness of thin silane films on aluminium surfaces by means of spectroscopic ellipsometry.* Thin Solid Films, 2001. **384**(1): p. 37-45.
28. Owens, D.K. and R.C. Wendt, *Estimation of the surface free energy of polymers.* Journal of Applied Polymer Science, 1969. **13**(8): p. 1741-1747.
29. Van Oss, C.J., M.K. Chaudhury, and R.J. Good, *Interfacial Lifshitz-van der Waals and polar interactions in macroscopic systems.* Chemical Reviews, 1988. **88**(6): p. 927-941.
30. van Oss, J.C., *Interfacial Forces in Aqueous Media*. 1st ed. 1994, New York: Marcel Dekker.

31. Zhao, Q., Y. Liu, and E.W. Abel, *Effect of temperature on the surface free energy of amorphous carbon films.* Journal of Colloid and Interface Science, 2004. **280**(1): p. 174-183.
32. Della Volpe, C., D. Maniglio, M. Brugnara, S. Siboni, and M. Morra, *The solid surface free energy calculation: I. In defense of the multicomponent approach.* Journal of Colloid and Interface Science, 2004. **271**(2): p. 434-453.
33. Leezenberg, P.B., W.H. Johnston, and G.W. Tyndall, *Chemical modification of sputtered amorphous-carbon surfaces.* Journal of Applied Physics, 2001. **89**(6): p. 3498-3507.

4 Modulation of Protein Fouling and Interfacial Properties at Carbon Surfaces via Grafting of Glycans

Carbon materials are of great interest for biological applications such as implantable devices. However, to realize their potential it is critical to control formation and composition of the protein corona in biological media. In this chapter, protein adsorption studies were carried out at carbon surfaces functionalized with aryldiazonium layers bearing mono- and di-saccharide glycosides. Surface IR reflectance absorption spectroscopy and quartz crystal microbalance were used to study adsorption of albumin, lysozyme and fibrinogen. Protein adsorption was found to decrease by 30-90% with respect to bare carbon surfaces; notably, enhanced rejection was observed in the case of the tested di-saccharide vs. simple mono-saccharides for near-physiological protein concentration values. ζ-potential measurements revealed that aryldiazonium chemistry results in the immobilization of phenylglycosides without a change in surface charge density, which is known to be important for protein adsorption. Multisolvent contact angle measurements were used to calculate surface free energy and acid-base polar components of bare and modified surfaces based on the van Oss-Chaudhury-Good model: results indicate that protein resistance in these phenylglycoside layers correlates positively with wetting behaviour and Lewis basicity.

F. Zen, M. D. Angione, J. A. Behan, R. J. Cullen, T. Duff, J. M. Vasconcelos, E. M. Scanlan, P. E. Colavita;

Modulation of Protein Fouling and Interfacial Properties at Carbon Surfaces via Immobilization of Glycans Using Aryldiazonium Chemistry

Scientific Reports, **2016**, 24 (6), 1031-1040

This chapter is the final version of the paper of which I am first author. I carried out the investigation described (except where noted), prepared the first draft of the paper and subsequent revised drafts with my advisor. The contributions of the other coauthors are the follows: M.D.A. contributed with backup fluorescence measurements; T.D. synthesized compounds; J.A.B. and R.J.C. contributed with ellipsometry and AFM measurements; J.M.V. developed protocols for electrokinetic measurements. E.M.S. and P.E.C. led the work contributed to experimental design and the drafting of the manuscript.

4.1 Introduction

Much effort towards the design and fabrication of biomaterials and medical devices is dedicated to the attainment of desirable surface chemistry and surface physical properties, as these can often determine the biological response to materials in vivo [1]. There is therefore a strong interest in investigating surface modification strategies that enable a degree of control over interfacial biointeractions. Protein-surface interactions are thought to be of particular importance due to the abundance of these molecules in tissues and biological fluids and due to the central role of peptides and proteins in cell adhesion and signalling. Depending on the specific biomaterial and its application (*e.g.* biosensor, implant) it might be desirable to either promote protein adsorption or repel protein build-up in order to modulate performance [2-5]. Therefore, much effort has been devoted to developing surface modification strategies to modulate protein-surface interactions.

Various forms of carbon find multiple applications as biomaterials; coatings such as pyrocarbon and amorphous carbons (*e.g.* a-C, a-C:Si, a-C:H, ta-C) [6, 7], are promising for biomedical applications because of their frictional and mechanical properties, their corrosion resistance and chemical inertness, and their bio- and hemocompatibility. Carbon nanomaterials, such as nanotubes and nanodiamonds, have also received much attention as delivery agents for in vivo imaging and sensing [8, 9]. Finally, materials such as diamond electrodes, carbon coatings and carbon nanofibers are routinely used for in vivo and in vitro bioanalytical chemistry [10, 11]. For all of these applications it is critical to achieve control over interfacial interactions of the carbon solid surface with proteins in solution, to avoid unspecific adsorption that might result in undesirable cell-surface events, or in blocking of sensing/binding sites [12-15].

Several surface modification methods have been investigated in order to control and minimize protein fouling at surfaces: cationic polymers, enzymes or peptides are effective but costly and often present problems of leaching and durability [16]. Poly and oligo(ethylene glycol) (PEG, OEG) coatings have been shown to successfully minimize protein adsorption [12, 17]; however, PEG/OEGs can easily oxidize, losing their antifouling properties [16]. This problem has prompted a search for alternative antifouling coatings with enhanced chemical

stability. In an effort to mimic biological antifouling strategies, work has focused on the use of immobilized carbohydrates, given the presence of these molecules in the antiadhesive glycocalyx that surrounds certain cells [18, 19]. Research shows, in fact, that oligo- and polysaccharide coatings can control fouling and protein adsorption, while being extremely stable to oxidation.[20-26]

The use of aryldiazonium salt chemistry for the immobilization of simple carbohydrates on carbon surfaces was recently reported by our group [27]. Aryldiazonium chemistry offers a versatile route for surface immobilization with key advantages for carbon applications: (a) functionalization can be carried out from solution, (b) it occurs under mild conditions without the use of multistep reactions, and (c) it leads to the formation of robust functional layers via formation of strong C—C covalent bonds between R-Ph groups and carbon substrates [28]. This is a desirable property that imparts chemical and thermal stability to carbohydrate adlayers under a variety of conditions thus preventing interfacial exchange between the layer and biomolecules in solution. The ability to solution process surfaces also makes it intrinsically scalable and thus relevant for widespread applications. We have recently shown that immobilized phenylglycosides bearing mono-saccharide groups obtained via aryldiazonium chemistry can reduce the unspecific adsorption of Bovine Serum Albumin (BSA) at carbon surfaces [27]. However, it remains unclear whether antifouling properties can be observed with other proteins and whether specific carbohydrate structural properties are responsible for the antifouling behavior. Interestingly, we have also identified that phenyl-lactosides are more effective than mono-saccharide glycosides at preventing adsorption on polymer surfaces [29].

Herein, we report a study of protein adsorption at phenylglycoside-modified and bare amorphous carbon surfaces using five different glycosides, four bearing mono-saccharide moieties and one being a phenyl-lactoside. We use three proteins with different levels of structural complexity and isoelectric points to understand the generality of protein adsorption trends. Importantly, we investigate the relationship between protein adsorption at phenylglycoside layers and surface free energy, charge and glycoside structure with the aim of improving

our current understanding of key properties that result in antifouling activity of aryldiazonium carbohydrate layers.

4.2 Experimental Section

Chemicals and Materials. Diiodomethane (99%), glycerol (≥99.5%), sulfuric acid (95-97%), hydrochloric acid (37%), hydrogen peroxide (30%), fluoroboric acid (48 wt.% in H_2O), sodium nitrite (≥99.0%), acetonitrile (HPLC grade) and methanol (semiconductor grade) were purchased from Sigma and used without further purification. B-doped Si wafers were purchased from MicroChemicals and 10 MHz quartz crystals were purchased from International Crystal Manufacturing. Bovine Serum Albumin (BSA, ≥96%), Lysozyme from chicken egg white (Lyz), Fibrinogen from bovine plasma (Fib, 65-85% protein) and phosphate saline buffer tablets (PBS, 0.01 M, 0.0027 KCl and 0.137 NaCl pH 7.4) were purchased from Sigma. Millipore water was used for all experiments. Precursors 4-aminophenol-β-D-glucoopyranose (**1**), 4-aminophenol-β-D-galactopyranose (**2**), 4-aminophenol-α-D-mannopyranose (**3**), 4-aminophenol-α-L-rhamnopyranose (**4**) and 4-aminophenol-β-D-lactopyranose (**5**) (see Figure 4.1) were synthesized as previously reported [20, 27].

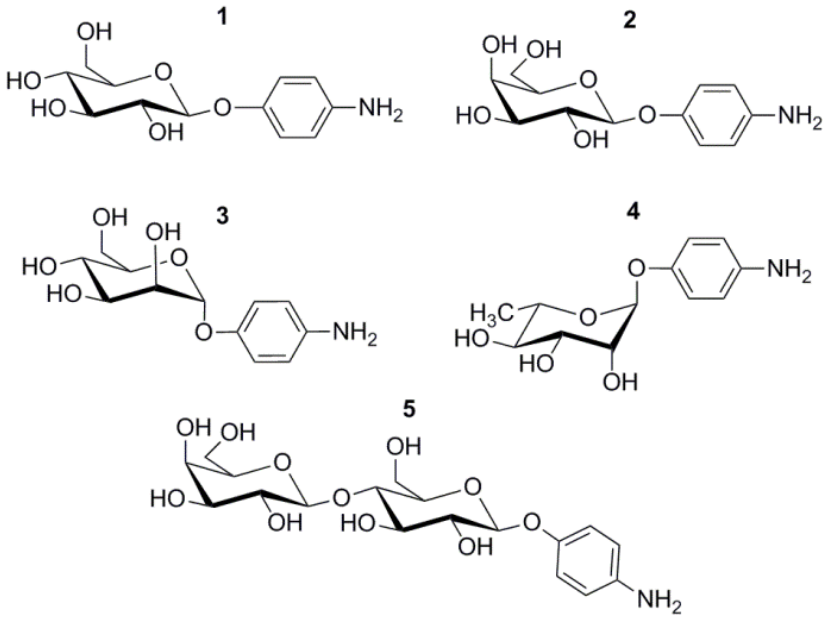

Figure 4.1. 4-aminophenyl glycosides synthesized as precursors for the preparation of carbohydrate layers *via* aryldiazonium chemistry: 4-aminophenol-β-D-glucopyranose (**1**), 4-aminophenol-β-D-galactopyranose (**2**), 4-aminophenol-α-D-mannopyranose (**3**), 4-aminophenol-α-L-rhamnopyranose (**4**) and 4-aminophenol-β-D-lactopyranose (**5**).

Substrate preparation. Amorphous carbon films (a-C) with thickness (73.6 ± 0.6) nm (C.I. 95%) were deposited via DC magnetron sputtering (Torr International, Inc.) on clean silicon wafers, as described in Chapter 3 (page 62). For infrared reflectance absorbance spectroscopy (IRRAS) measurements, Si wafers were coated prior to a-C deposition, with an optically thick (449 ± 29) nm (C.I. 95%) Ti layer via DC magnetron sputtering. The thickness of Ti underlayers was determined via Atomic Force Microscopy (AFM) in contact mode: prior to Ti deposition the wafer was coated for half of its surface with a 2% solution of PMMA in anisole; after sputtering the PMMA was dissolved in acetone, thus creating a step edge on which AFM measurements were carried out, as shown in Figure 4.2.

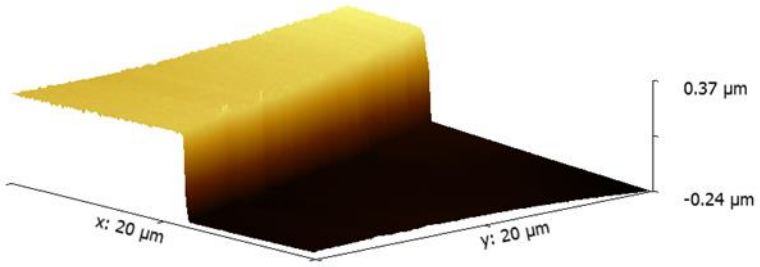

Figure 4.2. Step edge in a sputtered Ti layer used to measure the thickness of Ti underlayers.

Surface modification with carbohydrate moieties was carried out as previously reported [27], and following a protocol summarized in Scheme 1. Briefly, 4-aminophenyl glycosides were dissolved in acid; while keeping the solution in an ice bath, $NaNO_2$ was added yielding the corresponding aryldiazonium salt *in-situ* at a final concentration of 1.0 mM. Carbon samples were immersed in the aryldiazonium salt solution for 1 h, rinsed in acetonitrile and methanol and dried under argon prior to further use.

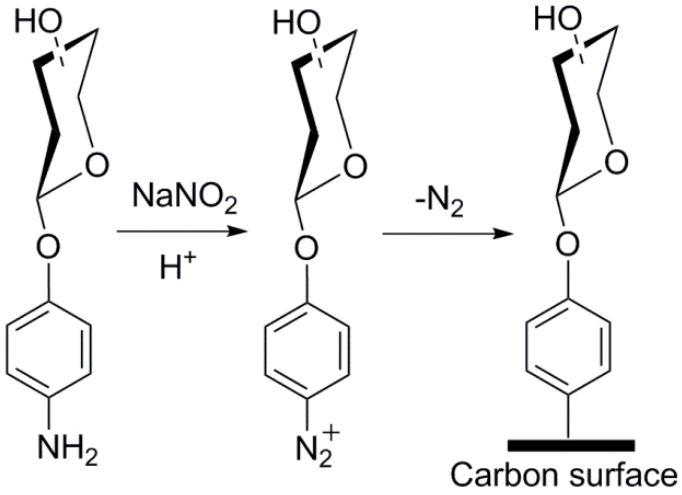

Scheme 4.1. Surface modification reaction for carbon surfaces via *in-situ* generation of aryldiazonium salts.

Characterization Methods. Static contact angles (CA) were measured on a CA analyzer (FTA) and Spectroscopic Ellipsometry (SE) was carried out using an alpha-SETM ellipsometer (J.A. Woolam Co.), following the same procedure described in details in Chapter 3 (page 63). ζ-potential measurements were carried out using a Malvern Zetasizer Nano-ZS equipped with a surface ζ-potential cell; standard 300 nm latex tracer particle suspensions, NaCl 1 mM, at pH 9.2 (Malvern, DTS1235) were used in all experiments. IRRAS was carried out on a Fourier Transform Infrared (FTIR) spectrometer (Tensor 27, Bruker) equipped with a Mercury Cadmium Telluride (MCT) detector, a specular reflectance accessory (VeeMax II), and a ZnSe polarizer. This technique was accurately described in Chapter 2 (see section 2.3.1, page 42). Spectra were taken at 80° incidence using p-polarized light; 100 spectra were collected at 4 cm^{-1} resolution using a bare substrate as background. All spectra reported in this work were baseline corrected using commercial FTIR software (WinFIRST). Quartz Crystal Microbalance (QCM) measurements were carried out *ex-situ* following a previously reported procedure [27]. The resonant frequency of a carbon coated QCM crystal was measured in air before and after protein adsorption, and the difference was used to calculate the mass change at the crystal *via* the Sauerbrey equation [30]. Measurements were carried out in a home-built chamber at the same temperature before and after modification; in the case of lactose-modified surfaces it was necessary to introduce a dessicant (Drierite®) in the measurement

chamber in order to achieve frequency stability, likely due to water adsorption by surface-bound disaccharide units. Thickness and surface roughness measurements were carried out *via* AFM (Asylum Research) using silicon cantilevers. 512 line images were collected and analysed using commercial software (Gwyddion).

Protein adsorption experiments. BSA, Lyz and Fib were dissolved in 0.01 M PBS buffer (pH 7.4) at different concentrations for each protein: 0.5 and 20 mg/mL for BSA, 0.1 and 4.3 mg/mL for Lyz and 2.5 mg/mL for Fib. Carbohydrate-coated and bare a-C surfaces were incubated in buffered protein solutions for 1 h at ambient temperature (20 ºC). Substrates were rinsed, immersed for 10 min in water, and finally dried under argon prior to characterization.

4.3 Results

4.3.1 Protein adsorption studies

Amorphous carbon (a-C) films used in our experiments were deposited *via* magnetron sputtering. These films had previously been characterized *via* a combination of spectroscopic methods [31]. Briefly, they consist of approximately 80% trigonally bonded carbon (sp^2 centers), as estimated *via* X-ray photoelectron spectroscopy (XPS) and Raman spectroscopy. The films also contain oxidized groups resulting in a 7-9% O/C atomic ratio as determined *via* XPS.

Modification of a-C with aryldiazonium salts was carried out as in our previous work (Scheme 1), *via* diazoniation of 4-aminophenyl glycoside precursors *in-situ*. Precursor glycosides bearing glucose (Glc), galactose (Gal), mannose (Man), rhamnose (Rha) and lactose (Lac) groups (compounds **1-5**, Figure 4.1), yielded surfaces from here onwards referred to as Glc-C, Gal-C, Man-C, Rha-C and Lac-C, respectively. Figure 4.3 shows examples of IR reflectance absorption spectroscopy (IRRAS) of Gal-C, a monosaccharide-modified surface, and of Lac-C, a disaccharide-modified surface, obtained from precursors **2** and **5**, respectively. Both IRRAS spectra show the characteristic infrared absorbances of glycosides in the region 1290–950 cm^{-1} due to C–O stretching modes arising from the carbohydrate ring [27, 32]. Peaks in the region 1550–1500 cm^{-1} arise from C–C skeletal vibrations of phenyl rings [32]; in particular, it was possible to observe

in all spectra the presence of a peak at 1508 cm^{-1} which can be attributed to the strong 19a stretching mode of phenyl rings [27]. Similar IRRAS spectra were obtained for Glc-C, Man-C and Rha-C surfaces.

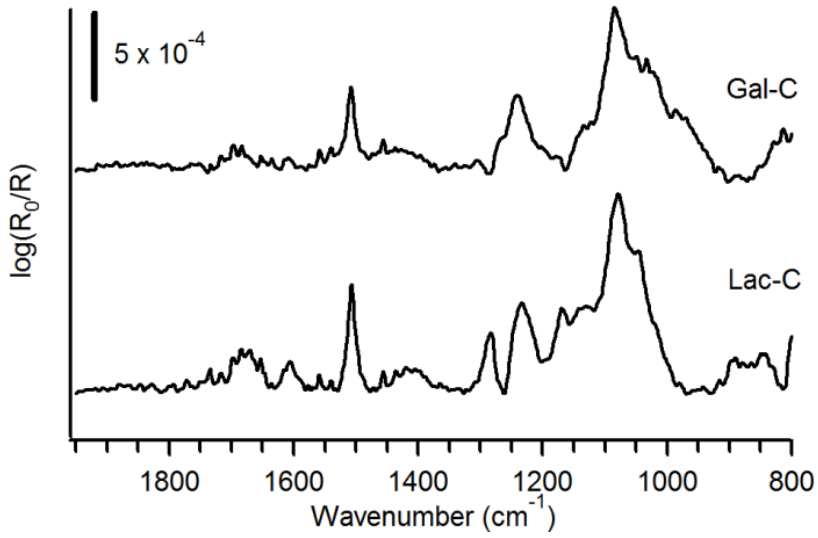

Figure 4.3. IRRAS spectra of a-C surfaces after modification with Gal (Gal-C) and Lac monosaccharides (Lac-C).

Roughness determinations were carried out *via* AFM for all the bare and modified surfaces. Topography images were collected in tapping mode and analysed by defining a 10 × 10 μm^2 box in different regions of the sample surface. Figure 4.4 shows examples of AFM images for bare and monosaccharide modified surfaces. Table 4.1 shows a summary of RMS roughness values obtained *via* AFM which were found to be lower than 1.4 nm over 100 μm^2.

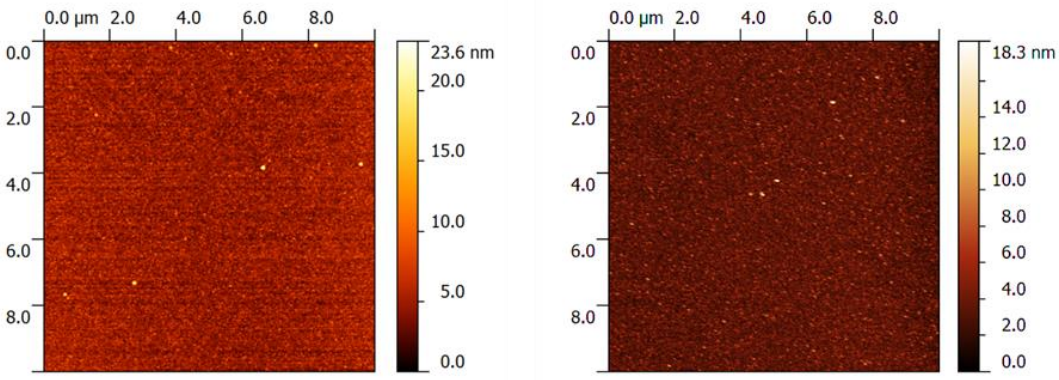

Figure 4.4. AFM topography images of bare a-C (left) and Lac-C (right) surfaces.

Table 4.1. Average RMS roughness measured for bare and modified surfaces using tapping mode AFM.

Surface	RMS roughness (nm)
a-C	0.94 ± 0.03
Gal-C	1.17 ± 0.07
Rha-C	1.10 ± 0.12
Man-C	1.35 ± 0.05
Glc-C	1.02 ± 0.04
Lac-C	1.21 ± 0.03

The thickness of phenylglycoside layers was also characterized *via* atomic force microscopy (AFM) using previously reported methods [33, 34]. Briefly, phenylglycoside-modified surfaces were first imaged in tapping mode; subsequently, a section of the film was removed by scratching the sample with the AFM tip in contact mode; finally, the step created in the organic film was imaged in tapping mode. Figure 4.5 shows an example of a Lac-C surface imaged after the scratching process and of a height profile across the step. Height profiles were used to obtain an average thickness which was found to be 0.8 ± 0.1 nm in the case of both Gal-C and Lac-C layers. These thickness values are slightly lower than

estimates of molecular length of 1.0 nm and 1.5 nm for phenyl-β-galactoside and benzyl-β-lactoside conformers, respectively, obtained from optimized glycoside geometries [35, 36]. Thickness results therefore indicate that layers prepared *via* aryldiazonium chemistry using both mono- and di-saccharide groups reach a surface coverage of at most 1 ML, as expected based on the presence of bulky terminal groups such as Lac and Gal glycans [37].

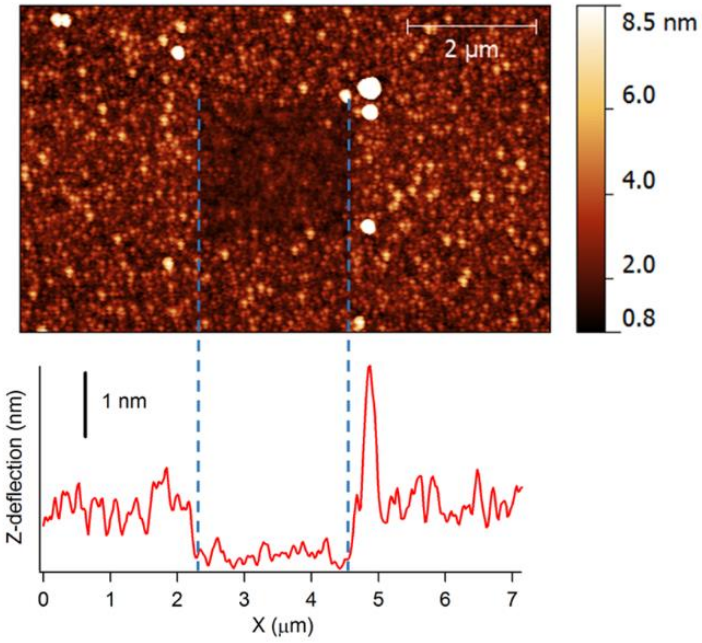

Figure 4.5. AFM topographic image of a Lac-C surface (top) after removal of a portion of the film with the AFM tip. The height profile (bottom) shows a step edge with a height equivalent to the thickness of the phenyl-lactoside layer.

In order to evaluate the antifouling properties of glycosylated interfaces, both unmodified and modified a-C substrates were incubated in buffered protein solutions for 1 h and analyzed by IRRAS *ex-situ*. Three proteins with different properties were chosen for our studies: BSA, lysozyme (Lyz) and fibrinogen (Fib); a summary of their main physical properties is reported in Table 4.2. Figure 4.6 shows IRRAS spectra in the region 1900-1300 cm^{-1} of bare a-C, Gal-C and Lac-C surfaces after incubation in BSA, Lyz and Fib solutions at two different concentrations; dotted lines in the central and right hand panel show the IRRAS spectra of Gal-C and Lac-C surfaces prior to protein adsorption in the same spectral region. After adsorption, spectra exhibit the characteristic bands of amide

groups in polypeptides: the two strong, broad peaks at ~1675 cm^{-1} and ~1540 cm^{-1} are assigned to the amide I and II modes, respectively [32]. Noticeably, the sharp peak at ~1510 cm^{-1} assigned to the aromatic ring appears in all of the spectra, thus confirming that the phenyl groups used for surface modification are strongly bound to the surface and are not displaced by adsorbed proteins. Similar results were obtained in the case of Man-C, Glc-C and Rha-C surfaces.

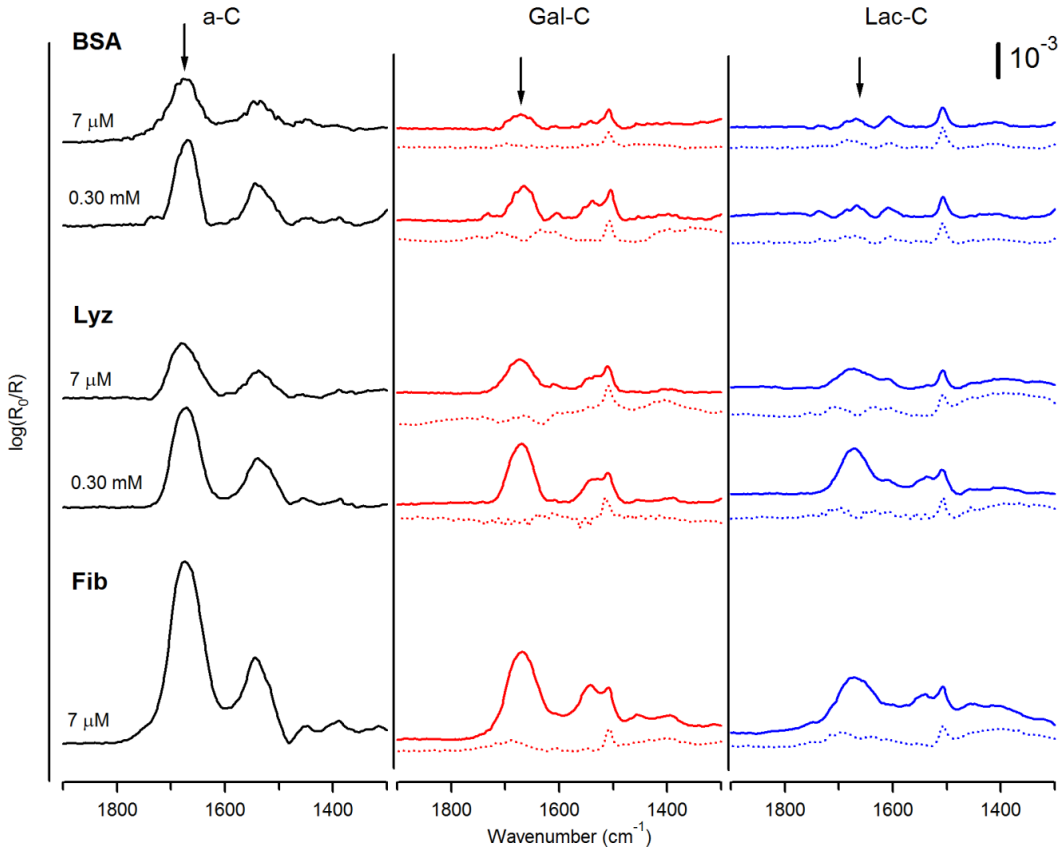

Figure 4.6. IRRAS spectra in the amide I/II region of bare a-C (black), Gal-C (red) and Lac-C (blue) surfaces after functionalization (dotted lines) and after incubation in buffered solutions of BSA, Lyz and Fib at different concentrations (solid lines). The position of the amide I band is indicated with an arrow.

Table 4.2. Main properties of proteins used for adsorption studies; molar mass, number of amino acids and isoelectric point are provided by the manufacturer, except for the isoelectric point of Fib which is taken from ref.[38] and sizes which are taken from ref. [39, 40].

	Mass (kDa)	Amino acids	Size (nm^3)	Isoelectric point
BSA	66	583	8 x 8.7 x 6	4.7 - 4.9
Lyz	14	129	4.5 x 3 x 3	11.35
Fib	340	3620	45 x 9 x 6	5.8

The relative amounts of protein adsorbed at bare and saccharide-modified surfaces can be estimated from the net absorbance of amide bands in IRRAS spectra, under the assumption of no preferential orientation of peptide bonds at the carbon surface. Net absorbance values of amide I peaks at bare a-C, and phenylglycoside-modified carbon are reported in Figure 4.7, where the inset shows the same results as percentage adsorption with respect to the bare surface. Values in Figure 4.7 were obtained from adsorption experiments carried out at two different molar concentrations: 7 μM, equivalent to 0.5, 0.1 and 2.5 g L^{-1} for BSA, Lyz and Fib, respectively, and 0.30 mM, equivalent to 20 and 4.3 g L^{-1} for BSA and Lyz, respectively. These two concentrations are relevant for understanding the behavior of surfaces in physiological conditions since molar concentrations of 7 μM are in the normal range for Fib in plasma, while a 0.30 mM concentration is close to that of albumin in serum [41]. Fib could not be studied at the higher concentration because it falls beyond its solubility limit [42].

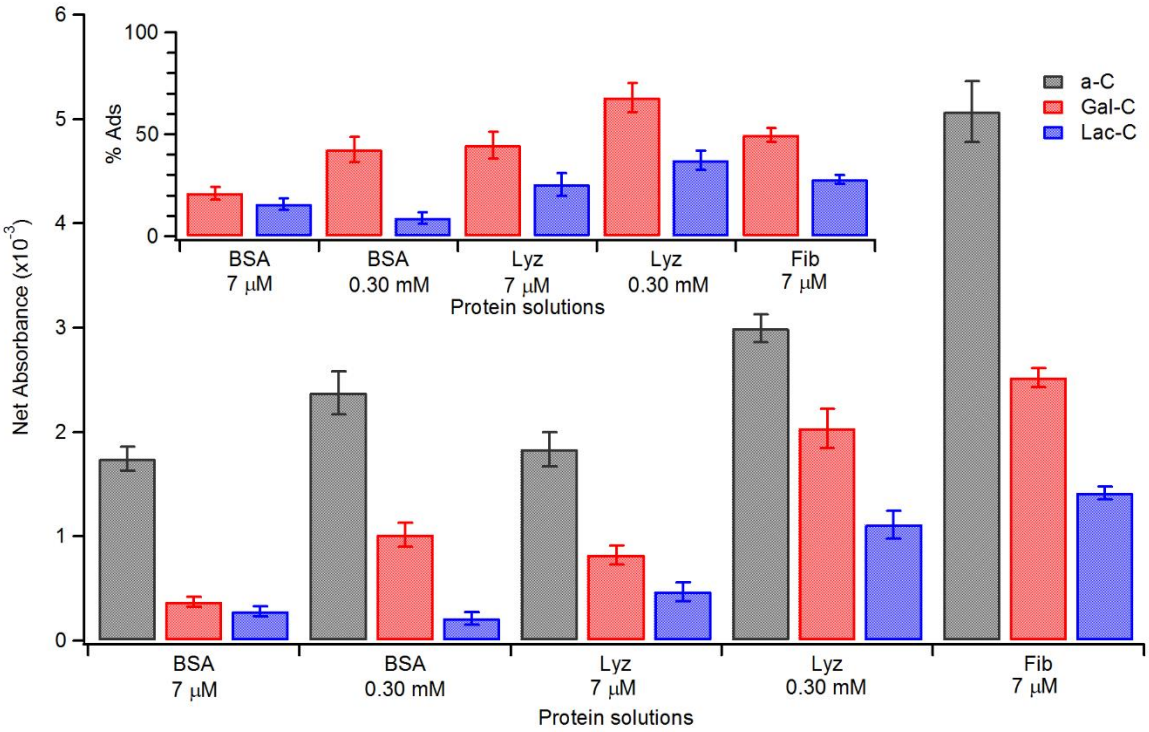

Figure 4.7. Comparison of amide I net absorbance values at a-C, Gal-C and Lac-C surfaces after incubation in solutions of BSA, Lyz and Fib. Inset shows adsorbed amounts relative to bare a-C surfaces.

IRRAS results indicate that at bare a-C surfaces, adsorption increases with increasing molar concentration for the same protein. Fib solutions yielded the strongest adsorption among all protein solutions tested. These observed trends are in general agreement with previous reports of adsorption isotherms of human albumin and fibrinogen at isotropic carbon surfaces by Feng and Andrade [43]. Adsorption values on monosaccharide-modified surfaces were significantly lower than at bare a-C for all three proteins at all concentrations studied. Similar results were obtained for surfaces modified with Glc, Man and Rha units: only small differences were observed in protein resistance among the four monosaccharides used in our studies. The amount of protein adsorbed at Lac-C was however found to be significantly lower than at either bare a-C, or monosaccharide-modified surfaces, thus indicating that Lac-C surfaces are better at resisting protein adsorption.

In order to obtain quantitative estimates of protein adsorption at mono- and di-saccharide modified surfaces, Quartz Crystal Microbalance (QCM) measurements of protein mass were also carried out *ex-situ*. Upon incubation in 7 μM BSA for 1 h, bare a-C surfaces reported a mass increase of 1.02 ± 0.27 μg cm^{-2}, whereas Gal-C and Lac-C surfaces yielded increases of only (0.35 ± 0.22) and (0.10 ± 0.11) μg cm^{-2} (C.I. 95%), respectively. The above estimates likely constitute upper boundaries for BSA adsorption at the three surfaces, given that *ex-situ* QCM also measures contributions from the mass of water trapped within the BSA layer. Table 4.3 summarizes BSA mass densities and relative adsorption mass values measured *via ex-situ* QCM, together with the corresponding adsorption estimates obtained from amide I peak absorptions in IRRAS spectra. The comparison between the spectroscopic and gravimetric determination of protein adsorption was found to be satisfactory, thus indicating that amide I peak intensities are proportional to surface mass density of proteins on these surfaces. Also, gravimetric analysis confirms that Lac-C layers perform better than Gal-C layers in terms of protein rejection.

Table 4.3. BSA adsorption measurements at a-C, Gal-C and Lac-C surfaces, carried out using 7 μM solutions. The table reports absolute adsorbed mass values determined *via ex-situ* QCM, relative adsorbed masses calculated with respect to adsorption at bare a-C and relative adsorbed values determined *via* IRRAS under the same experimental conditions.

Surface	Adsorbed BSA (μg cm^{-2})	Relative BSA Mass	Relative Amide I peak absorbance
a-C	1.02 ± 0.27	-	-
Gal-C	0.35 ± 0.22	34%	21%
Lac-C	0.10 ± 0.11	9.8%	16%

4.3.2 Surface contact angle and surface free energy studies

Surface free energy (SFE) and wettability play an important role in defining the extent to which a surface can resist biofouling. The SFE of unmodified and modified a-C substrates was determined *via* contact angle (CA) measurements of multiple solvents using the sessile drop method. In order to obtain the SFE, we used the model of van Oss, Chaudhury and Good (vOCG) [44, 45], which was described in details in Chapter 2 (pages 40-41) and Chapter 3 (page 70). Briefly, this model assumes that the total surface tension results from additive contributions of apolar, or Lifshitz-van der Waals (γ^{LW}), and polar forces (γ^{AB}):

$$\gamma = \gamma^{LW} + \gamma^{AB} \tag{4.1}$$

where γ^{AB} includes contributions γ^- and γ^+ from electron donor-acceptor interactions, respectively, also called Lewis base-acid interactions. The model assumes that the work of adhesion at the solid-liquid interface, W_{SL} , can be approximated by geometric means as below:

$$W_{SL} = 2\left(\sqrt{\gamma_S^{LW}\gamma_L^{LW}} + \sqrt{\gamma_S^-\gamma_L^+} + \sqrt{\gamma_S^+\gamma_L^-}\right) \tag{4.2}$$

where the subscripts "*L*" and "*S*" indicate components of the liquid and solid, respectively. vOCG is considered to be a suitable model for describing the asymmetric nature of polar interactions when hydrogen bonding contributions are present [44, 45]: electron donating and accepting groups must interact "reciprocally" to contribute to surface tension, as reflected by mixed donating/accepting products in Equation (4.2). Equation (4.2), in combination with the Young-Dupre equation results in:

$$\sqrt{\gamma_S^{LW}\gamma_L^{LW}} + \sqrt{\gamma_S^-\gamma_L^+} + \sqrt{\gamma_S^+\gamma_L^-} = \frac{\gamma_L}{2}(1 + \cos\theta) \tag{4.3}$$

which can be used to obtain γ_S^{LW}, γ_S^- and γ_S^+ by measuring the CA of three liquids with known surface tension components γ_L^{LW}, γ_L^- and γ_L^+.

Carbon films used for CA measurements were deposited on Si wafers and were found to display low RMS roughness before and after modification, as confirmed by AFM analysis (see Table 4.1). Surface tension components of the three test liquids at 20 °C are taken from van Oss's data compilation [45] and are reported in Table 4.4; the choice of liquids was based on the analysis of solvent triplets by Della Volpe et al. [46] $\gamma_S^{LW}$was first calculated using eq. (3) and the CA of diiodomethane, a liquid with $\gamma_L^+ = \gamma_L^- = 0$. CAs of water and glycerol were then

used to set a system of two linear equations that were solved for $\sqrt{\gamma_S^+}$ and $\sqrt{\gamma_S^-}$ [47]; positive values were obtained from our calculations thus confirming that all surfaces yield physical solutions for γ_S^+ and γ_S^-.

Table 4.4. Total surface tensions (γ_L), dispersive (γ_L^{LW}), electron donating γ_L^- and accepting (γ_L^+) components (mJ m^{-2}) of test liquids used for contact angle measurements and vOCG analysis.[45, 47].

Test liquids	γ_L	γ_L^{LW}	γ_L^+	γ_L^-
Water	72.8	21.8	25.5	25.5
Glycerol	63.3	34	3.92	57.4
Diiodomethane	50.8	50.8	0	0

CA values and surface tension components for all surfaces examined in this work are reported in Table 4.5. Bare a-C displayed a water CA of 35.3°, total SFE $\gamma_S = 63.7$ mJ m^{-2} and components $\gamma_S^{LW} = 49.7$ mJ m^{-2} and $\gamma_S^{AB} = 14.0$ mJ m^{-2}. These values are in good agreement with those reported by Leezenberg et al. [48] for sputtered a-C films, but the polar component and total surface energy are higher than those obtained by Zebda et al. [47] *via* vOCG analysis. Differences in components and total SFE could arise due to variations in material properties (*e.g.* sp^2/sp^3 or O-content) or film history [48]. Surface modification with saccharides leads to a significant decrease in water CA for all saccharide units tested, with the lowest CA observed for Lac-C surfaces. The total SFEs of phenylglycoside layers are slightly higher than that of bare a-C (<3% difference), with negligible differences observed among saccharides. Similarly, the apolar γ^{LW} contribution does not change significantly with surface treatment, remaining approximately constant across all surfaces (<3% difference).

Table 4.5. Summary of experimentally determined properties of bare and modified carbon surfaces: measured contact angles using water (θ_W), glycerol (θ_G) and diiodomethane (θ_{DM}); surface free energy or total surface tension (γ_{tot}), its dispersive (γ^{LW}), electron accepting (γ^+) and donating (γ^-) components determined from vOCG analysis; surface ζ-potential values obtained using polystyrene tracer particles in 1 mM NaCl at pH 9.2.

	Contact Angles (degrees)			SFE components (mJ m^{-2})				
Surface	θ_W	θ_G	θ_{DM}	γ^{LW}	γ^+	γ^-	γ_{tot}	**ζ-potential (mV)**
a-C	35.3 ± 1.4	22.2 ± 1.4	11.9 ± 0.9	49.7	1.79	27.4	63.7	-55 ± 3
Glc-C	20.2 ± 0.3	16.4 ± 1.2	5.4 ± 0.4	50.6	1.38	38.7	65.2	-
Gal-C	26.1 ± 1.1	17.1 ± 0.4	7.5 ± 0.4	50.4	1.61	34.2	65.2	-56.3± 1.9
Man-C	22.9 ± 0.6	15.9 ± 1.3	4.9 ± 0.1	50.6	1.52	36.5	65.5	-
Rha-C	25.0 ± 0.5	20.3 ± 0.6	6.2 ± 0.2	50.4	1.30	36.3	64.2	-
Lac-C	11.8 ± 0.4	16.9 ± 0.7	4.2 ± 0.3	50.7	1.11	43.9	64.6	-58.0± 2.6

The most striking differences among surface modifications were observed in the acid-base components. The vOCG model does not permit to directly compare the solid acid/base contributions of a solid surface [46]; however, as discussed by Della Volpe et al. [46], using the same solvent triplet it is possible to examine relative changes in acid and basic character brought upon by the surface modifications studied. Bare a-C displays the minimum γ_S^- value; modification with monosaccharides increases surface basicity by 30-40%, and a further and significant increase is observed when the disaccharide Lac is used. This result is surprising as carbohydrate units are typically classified as hydrogen bond donors and thus would not be expected to increase the Lewis basicity of a surface; possible explanations for these findings are discussed in Discussion section.

4.3.3 Surface charge density at bare and modified carbon surfaces

Electrostatic interactions can play an important role in protein adsorption phenomena given that proteins and most surfaces possess ionizable groups whose

charge is dependent on pH. To investigate whether electrostatic interactions could contribute to observed changes in protein adsorption upon carbon modification, we carried out ζ-potential measurements using standard solutions of tracer particles. Table 4.5 summarizes ζ-potential results obtained for a-C, Gal-C and Lac-C surfaces in 1 mM NaCl solutions at pH 9.2. The ζ-potential of a-C was found to be (-55 ± 3) mV, whereas surface modification with phenylglycosides led to ζ-potential values for Gal-C and Lac-C of (-56.3 ± 1.9) mV and (-58.0 ± 2.6) mV, respectively.

These results indicate that surface modification *via* aryldiazonium chemistry results in negligible changes in ζ-potential with respect to that of the bare a-C substrate. This indicates that functionalisation with phenylglycosides *via* this methodology offers a route for increasing the wettability of carbon surfaces without the introduction of significant changes in electrostatic charge, as is often the case with other modifications (e.g. oxidation). The implications of these results for understanding the origin of protein antifouling properties of aryldiazonium carbohydrate layers and for the design of carbohydrate coatings with enhanced antifouling properties will be discussed in the following section.

4.4 Discussion

Protein adsorption studies on phenylglycoside layers obtained *via* aryldiazonium chemistry show that this functionalisation strategy leads to the formation of glycoside adlayers that impart resistance to protein adsorption. Spectroscopic and gravimetric studies carried out *ex-situ*, all indicate that coated surfaces adsorb less protein than the unmodified carbon, with phenyl-lactoside groups appearing to be particularly effective at reducing unspecific adsorption.

Solvation/hydration forces have been identified as important for determining protein adsorption trends, given that solvation and desolvation processes play a key role in protein adsorption [49]. Many studies [1, 7, 21, 49-52] have in fact concluded that highly hydrophilic surfaces tend to prevent unspecific protein adsorption, whereas hydrophobic surfaces are more likely to favour protein adsorption because they are easier to dehydrate and because they can maximize their interactions with protein hydrophobic groups through changes in protein

secondary structure upon adsorption [53]. In the case of aryldiazonium carbohydrate layers, CA measurements indicate that modification results in greater hydrophilicity; this correlates well with the reduction in protein adsorption that was observed in general, for all the three proteins at both concentration ranges examined. Lac-C surfaces were found to be the most effective carbohydrate-modified surfaces in terms of repelling protein fouling, and the ones with the lowest water CA in agreement with trends that positively correlate wettability with protein resistance.

The contributions of polar and dispersive interactions resulting in the observed wettability were obtained from a multisolvent determination and analysis of Surface Free Energies (SFE). Carbohydrate surfaces obtained *via* aryldiazonium chemistry possess SFEs that are <3% higher than that of a-C. However the analysis based on the vOCG model suggests that large differences are introduced in the polar contributions to the total SFE, *via* modification of carbon with phenylglycosides. The solid-water interfacial SFE can be estimated from the data in Table 4.5, according to $\gamma_{SL} = \gamma_S + \gamma_L - 2\left(\sqrt{\gamma_S^{LW}\gamma_L^{LW}} + \sqrt{\gamma_S^-\gamma_L^+} + \sqrt{\gamma_S^+\gamma_L^-}\right)$, which yields values of 4.3, -0.2 and -6.6 mJ m^{-2} for a-C, Gal-C and Lac-C surfaces, respectively. The observation of decreasing fouling in the order a-C > Gal-C > Lac-C is therefore consistent with expectations based on values of γ_{SL} calculated from CA results.

Analysis of SFE components also indicates that surface modification *via* aryldiazonium phenyl-glycosides increases the Lewis basicity of the carbon surface: Glc-C, Man-C, Gal-C and Rha-C have 30-40% greater γ_S^- values than that of bare a-C, while phenyl-lactoside immobilization leads to a 60% increase. This is somewhat surprising as carbohydrate units are typically classified as hydrogen bond donors and, thus, would not be expected to increase the Lewis basicity of a surface. Evidence from studies on alkylthiols indicates that the presence of groups that are polar, neutral and hydrogen-bond acceptors promotes fouling resistance [21, 54]. Carbohydrates have been identified as exceptions to the hydrogen-acceptor requirement, however vOCG results suggest that this might not be the case and that once carbohydrates are immobilized they can actually enhance the hydrogen-acceptor character of surfaces. We speculate that saccharide-saccharide and saccharide-water intermolecular bonding within a dense glycan

layer, might result in the basicity displayed by phenylglycoside layers. It is likely that engagement of hydroxyl groups in intra-layer hydrogen bonding modulates the hydrogen bonding properties displayed by the saccharide layer at the solid-air interface.

Çarçabal et al. [35] carried out experimental and computational work on Man, Gal and Glc phenylglycosides and on benzyl-β-lactoside in the gas phase, showing that hydration leads to the formation of extended intra- and inter-molecular hydrogen bond networks. The effect of hydration was greater in the case of benzyl-β-lactoside which was found to effectively lock into conformation through cooperative hydrogen bonding. It appears therefore likely that the water shroud associated with saccharide units would create a barrier to dehydration, and contributes to the protein resistance of carbohydrate aryldiazonium coatings. Further studies that directly probe hydrogen bonding within aryldiazonium layers would be desirable, to determine whether trends observed for phenylglycosides in the gas phase also translate to thin films of surface-immobilized groups.

Finally, the surface-blocking effect and the steric hindrance of the saccharide moiety in phenylglycoside layers is likely to also contribute to preventing adsorption of proteins, given that coatings displaying bulky groups can screen protein-substrate interactions. Molecular density however might play a role beyond blocking access to the carbon surface, by also regulating the observed basicity of saccharide layers through intermolecular interactions within the adlayer. Thus it would be important in future studies to identify whether the observed basicity and protein resistance behavior vary significantly with molecular surface density, given the same carbohydrate motif. Conversely, carbohydrate structure might be leveraged to enhance or reduce hydrogen bonding by selecting units with different propensity to engage in inter/intra molecular hydrogen bonding. Studies of layers prepared with oligosaccharide moieties that display predominantly inter- or intra-chain bonding might reveal more about the role of inter and intra-chain interactions in determining basicity and protein fouling resistance in phenylglycoside layers.

4.5 Conclusions

We have investigated the adsorption of three proteins at carbon surfaces modified with phenylglycoside layers prepared *via* aryldiazonium chemistry; layers bearing both monosaccharides and a di-saccharide, lactose, were prepared and compared in their properties and protein resistance to bare carbon surfaces. Results indicate that these coatings display good protein resistance and that judicious choice of synthetic phenylglycosides can be used to optimize resistance. This is an important finding from a practical standpoint because aryldiazonium covalent immobilization is a versatile method for the functionalization of carbons and nanocarbons. Furthermore, it is known to work with a wide range of substrate materials beyond carbon and it is applicable under mild conditions from dip, spray and contact deposition methods. Thus, the methodology offers a versatile route to imparting antifouling properties onto surfaces of complex, mixed material devices, e.g. for biosensing, implantation, blood contacting applications.

A study of interfacial physical properties revealed that the protein resistance of these layers correlates well with their hydrophilic character when compared to the bare carbon material. An increase in wettability with respect to bare carbon is achieved without a significant change in surface charge density. Interestingly, we notice that mono and di-saccharides increase the Lewis basicity of the surface, contrary to expectations from typical reactivity patterns of carbohydrates in solution. This finding is consistent with empirical rules on the type of properties that lead to protein fouling resistance of thin-organic layers. We propose that the observed basicity might arise from inter- and intra- molecular hydrogen bonding networks, which could alter the acid-base properties of units exposed at the surface. Further studies would be desirable for understanding the correlation between Lewis basicity and inter- and intra-molecular hydrogen bonding in the phenylglycoside layer. The vast number of existing carbohydrate structural motifs offers an exciting landscape for exploring the potential of these layers to leverage structural variability and achieve tunable fouling resistance.

4.6 References

1. Ratner, B.D., A.S. Hoffman, F.J. Schoen, and J.E. Lemons, *Biomaterials Science*. 2nd ed. 2004, London: Elsevier Academic Press.
2. Andrade, J.D., V. Hlady, L. Feng, and K. Tingey, *Proteins at interfaces: Principles, problems and potential*, in *Interfacial phenomena and bioproducts*, J.L. Brash and P.W. Wojciechowski, Editors. 1996, Marcel Dekker: New York. p. 19-55.
3. Monopoli, M.P., C. Aberg, A. Salvati, and K.A. Dawson, *Biomolecular coronas provide the biological identity of nanosized materials.* Nat Nano, 2012. **7**(12): p. 779-786.
4. Aggarwal, P., J.B. Hall, C.B. McLeland, M.A. Dobrovolskaia, and S.E. McNeil, *Nanoparticle interaction with plasma proteins as it relates to particle biodistribution, biocompatibility and therapeutic efficacy.* Advanced Drug Delivery Reviews, 2009. **61**(6): p. 428-437.
5. Cifuentes-Rius, A., H. de Puig, J.C.Y. Kah, S. Borros, and K. Hamad-Schifferli, *Optimizing the Properties of the Protein Corona Surrounding Nanoparticles for Tuning Payload Release.* ACS Nano, 2013. **7**(11): p. 10066-10074.
6. Roy, D., *Surface Plasmon Resonance Spectroscopy of Dielectric Coated Gold and Silver Films on Supporting Metal Layers: Reflectivity Formulas in the Kretschmann Formalism.* Applied Spectroscopy, 2001. **55**(8): p. 1046-1052.
7. Stueber, M., L. Niederberger, F. Danneil, H. Leiste, S. Ulrich, A. Welle, M. Marin, and H. Fischer, *Surface topography, surface energy and wettability of magnetron-sputtered amorphous carbon (a-c) films and their relevance for platelet adhesion.* Advanced Engineering Materials, 2007. **9**(12): p. 1114-1122.
8. Lu, F., L. Gu, M.J. Meziani, X. Wang, P.G. Luo, L.M. Veca, L. Cao, and Y.-P. Sun, *Advances in Bioapplications of Carbon Nanotubes.* Advanced Materials, 2009. **21**(2): p. 139-152.
9. Mochalin, V.N., O. Shenderova, D. Ho, and Y. Gogotsi, *The properties and applications of nanodiamonds.* Nat Nano, 2012. **7**(1): p. 11-23.
10. McCreery, R.L., *Advanced Carbon Electrode Materials for Molecular Electrochemistry.* Chemical Reviews, 2008. **108**(7): p. 2646-2687.
11. Lockett, M.R. and L.M. Smith, *Carbon Substrates: A Stable Foundation for Biological Arrays.* Annual Review of Analytical Chemistry, 2015. **8**(1): p. 17.1-17.23.
12. Clare, T.L., B.H. Clare, B.M. Nichols, N.L. Abbott, and R.J. Hamers, *Functional Monolayers for Improved Resistance to Protein Adsorption: Oligo(ethylene glycol)-Modified Silicon and Diamond Surfaces.* Langmuir, 2005. **21**(14): p. 6344-6355.
13. Trouillon, R., D. O'Hare, and Y. Einaga, *Effect of the doping level on the biological stability of hydrogenated boron doped diamond electrodes.* Physical Chemistry Chemical Physics, 2011. **13**(12): p. 5422-5429.
14. Mu, Q., G. Jiang, L. Chen, H. Zhou, D. Fourches, A. Tropsha, and B. Yan, *Chemical Basis of Interactions Between Engineered Nanoparticles and Biological Systems.* Chemical Reviews, 2014. **114**(15): p. 7740-7781.

15. Harrison, C., *Nanotechnology: Biological proteins knock nanoparticles off target.* Nat Rev Drug Discov, 2013. **12**(4): p. 264-264.
16. Banerjee, I., R.C. Pangule, and R.S. Kane, *Antifouling Coatings: Recent Developments in the Design of Surfaces That Prevent Fouling by Proteins, Bacteria, and Marine Organisms.* Advanced Materials, 2011. **23**(6): p. 690-718.
17. Ostuni, E., R.G. Chapman, M.N. Liang, G. Meluleni, G. Pier, D.E. Ingber, and G.M. Whitesides, *Self-assembled monolayers that resist the adsorption of proteins and the adhesion of bacterial and mammalian cells.* Langmuir, 2001. **17**(20): p. 6336-6343.
18. Hilkens, J., M.J.L. Ligtenberg, H.L. Vos, and S.V. Litvinov, *Cell membrane-associated mucins and their adhesion-modulating property.* Trends in Biochemical Sciences, 1992. **17**(9): p. 359-363.
19. Sumiyoshi, M., J. Ricciuto, A. Tisdale, I.K. Gipson, F. Mantelli, and P. Argüeso, *Antiadhesive Character of Mucin O-glycans at the Apical Surface of Corneal Epithelial Cells.* Investigative Ophthalmology & Visual Science, 2008. **49**(1): p. 197-203.
20. Angione, M.D., T. Duff, A.P. Bell, S.N. Stamatin, C. Fay, D. Diamond, E.M. Scanlan, and P.E. Colavita, *Enhanced Antifouling Properties of Carbohydrate Coated Poly(ether sulfone) Membranes.* ACS Applied Materials & Interfaces, 2015. **7**(31): p. 17238-17246.
21. Ederth, T., T. Ekblad, M.E. Pettitt, S.L. Conlan, C.-X. Du, M.E. Callow, J.A. Callow, R. Mutton, A.S. Clare, F. D'Souza, G. Donnelly, A. Bruin, P.R. Willemsen, X.J. Su, S. Wang, Q. Zhao, M. Hederos, P. Konradsson, and B. Liedberg, *Resistance of Galactoside-Terminated Alkanethiol Self-Assembled Monolayers to Marine Fouling Organisms.* ACS Applied Materials & Interfaces, 2011. **3**(10): p. 3890-3901.
22. Österberg, E., K. Bergström, K. Holmberg, J.A. Riggs, J.M. Van Alstine, T.P. Schuman, N.L. Burns, and J.M. Harris, *Comparison of polysaccharide and poly(ethylene glycol) coatings for reduction of protein adsorption on polystyrene surfaces.* Colloids and Surfaces A: Physicochemical and Engineering Aspects, 1993. **77**(2): p. 159-169.
23. Holland, N.B., Y.X. Qiu, M. Ruegsegger, and R.E. Marchant, *Biomimetic engineering of non-adhesive glycocalyx-like surfaces using oligosaccharide surfactant polymers.* Nature, 1998. **392**(6678): p. 799-801.
24. Perrino, C., S. Lee, S.W. Choi, A. Maruyama, and N.D. Spencer, *A Biomimetic Alternative to Poly(ethylene glycol) as an Antifouling Coating: Resistance to Nonspecific Protein Adsorption of Poly(l-lysine)-graft-dextran.* Langmuir, 2008. **24**(16): p. 8850-8856.
25. Lord, M.S., D. Pasqui, R. Barbucci, and B.K. Milthorpe, *Protein Adsorption on Derivatives of Hyaluronan.* Macromolecular Symposia, 2008. **266**(1): p. 17-22.
26. Mussard, W., N. Kebir, I. Kriegel, M. Estève, and V. Semetey, *Facile and Efficient Control of Bioadhesion on Poly(dimethylsiloxane) by Using a Biomimetic Approach.* Angewandte Chemie International Edition, 2011. **50**(46): p. 10871-10874.
27. Jayasundara, D.R., T. Duff, M.D. Angione, J. Bourke, D.M. Murphy, E.M. Scanlan, and P.E. Colavita, *Carbohydrate Coatings via Aryldiazonium*

Chemistry for Surface Biomimicry. Chemistry of Materials, 2013. **25**(20): p. 4122-4128.
28. Barriere, F. and A.J. Downard, *Covalent modification of graphitic carbon substrates by non-electrochemical methods.* Journal of Solid State Electrochemistry, 2008. **12**(10): p. 1231-1244.
29. Angione, M.D., T. Duff, A. Bell, C. Fay, D. Diamond, E.M. Scanlan, and P.E. Colavita, *submitted.* 2015.
30. Zebda, A., H. Sabbah, S. Ababou-Girard, F. Solal, and C. Godet, *Surface energy and hybridization studies of amorphous carbon surfaces.* Applied Surface Science, 2008. **254**(16): p. 4980-4991.
31. Sauerbrey, G.Z., *Use of quartz vibration for weighing thin films on a microbalance.* J. Physik, 1959. **155**: p. 206-212.
32. Cullen, R.J., D. Jayasundara, L. Soldi, J. Cheng, G. Dufaure, and P.E. Colavita, *Spontaneous grafting of nitrophenyl groups on amorphous carbon thin films: A structure-reactivity investigation.* Chemistry of Materials, 2012. **24**(6): p. 1031-1040.
33. Socrates, G., *Infrared and Raman Characteristic Group Frequencies: Tables and Charts*. 2001: John Wiley & Sons.
34. Brooksby, P.A. and A.J. Downard, *Electrochemical and Atomic Force Microscopy Study of Carbon Surface Modification via Diazonium Reduction in Aqueous and Acetonitrile Solutions.* Langmuir, 2004. **20**(12): p. 5038-5045.
35. Anariba, F., S.H. DuVall, and R.L. McCreery, *Mono- and Multilayer Formation by Diazonium Reduction on Carbon Surfaces Monitored with Atomic Force Microscopy "Scratching".* Analytical Chemistry, 2003. **75**(15): p. 3837-3844.
36. Çarçabal, P., R.A. Jockusch, I. Hünig, L.C. Snoek, R.T. Kroemer, B.G. Davis, D.P. Gamblin, I. Compagnon, J. Oomens, and J.P. Simons, *Hydrogen Bonding and Cooperativity in Isolated and Hydrated Sugars: Mannose, Galactose, Glucose, and Lactose.* Journal of the American Chemical Society, 2005. **127**(32): p. 11414-11425.
37. Jockusch, R.A., R.T. Kroemer, F.O. Talbot, L.C. Snoek, P. Çarçabal, J.P. Simons, M. Havenith, J.M. Bakker, I. Compagnon, G. Meijer, and G. von Helden, *Probing the Glycosidic Linkage: UV and IR Ion-Dip Spectroscopy of a Lactoside.* Journal of the American Chemical Society, 2004. **126**(18): p. 5709-5714.
38. Combellas, C., D.-e. Jiang, F. Kanoufi, J. Pinson, and F.I. Podvorica, *Steric Effects in the Reaction of Aryl Radicals on Surfaces.* Langmuir, 2009. **25**(1): p. 286-293.
39. Wasilewska, M., Z. Adamczyk, and B. Jachimska, *Structure of Fibrinogen in Electrolyte Solutions Derived from Dynamic Light Scattering (DLS) and Viscosity Measurements.* Langmuir, 2009. **25**(6): p. 3698-3704.
40. Höök, F., J. Vörös, M. Rodahl, R. Kurrat, P. Böni, J.J. Ramsden, M. Textor, N.D. Spencer, P. Tengvall, J. Gold, and B. Kasemo, *A comparative study of protein adsorption on titanium oxide surfaces using in situ ellipsometry, optical waveguide lightmode spectroscopy, and quartz crystal microbalance/dissipation.* Colloids and Surfaces B: Biointerfaces, 2002. **24**(2): p. 155-170.

41. Pasche, S., J. Vörös, H.J. Griesser, N.D. Spencer, and M. Textor, *Effects of Ionic Strength and Surface Charge on Protein Adsorption at PEGylated Surfaces.* Journal of Physical Chemistry B, 2005. **109**(37): p. 17545-17552.
42. Kratz, A., M. Ferraro, P.M. Sluss, and K.B. Lewandrowski, *Normal Reference Laboratory Values.* New England Journal of Medicine, 2004. **351**(15): p. 1548-1563.
43. Rampling, M.W., *The solubility of fibrinogen in solutions containing dextrans of various molecular weights.* Biochemical Journal, 1974. **143**(3): p. 767-769.
44. Feng, L. and J.D. Andrade, *Protein adsorption on low temperature isotropic carbon: III. Isotherms, competitivity, desorption and exchange of human albumin and fibrinogen.* Biomaterials, 1994. **15**(5): p. 323-333.
45. Van Oss, C.J., M.K. Chaudhury, and R.J. Good, *Interfacial Lifshitz-van der Waals and polar interactions in macroscopic systems.* Chemical Reviews, 1988. **88**(6): p. 927-941.
46. van Oss, J.C., *Interfacial Forces in Aqueous Media*. 1st ed. 1994, New York: Marcel Dekker.
47. Della Volpe, C., D. Maniglio, M. Brugnara, S. Siboni, and M. Morra, *The solid surface free energy calculation: I. In defense of the multicomponent approach.* Journal of Colloid and Interface Science, 2004. **271**(2): p. 434-453.
48. Leezenberg, P.B., W.H. Johnston, and G.W. Tyndall, *Chemical modification of sputtered amorphous-carbon surfaces.* Journal of Applied Physics, 2001. **89**(6): p. 3498-3507.
49. Kasemo, B., *Biological surface science.* Surface Science, 2002. **500**(1-3): p. 656-677.
50. Kirschner, C.M. and A.B. Brennan, *Bio-Inspired Antifouling Strategies.* Annual Review of Materials Research, 2012. **42**(1): p. 211-229.
51. Morra, M., ed. *Water in Biomaterials Surface Science*. 2001, John Wiley & Sons: Baffins Lane, Chichester.
52. Ham, H.O., S.H. Park, J.W. Kurutz, I.G. Szleifer, and P.B. Messersmith, *Antifouling Glycocalyx-Mimetic Peptoids.* Journal of the American Chemical Society, 2013. **135**(35): p. 13015-13022.
53. Feng, L. and J.D. Andrade, *Protein adsorption on low temperature isotropic carbon. I. Protein conformational change probed by differential scanning calorimetry.* Journal of Biomedical Materials Research, 1994. **28**(6): p. 735-743.
54. Ostuni, E., R.G. Chapman, R.E. Holmlin, S. Takayama, and G.M. Whitesides, *A Survey of Structure–Property Relationships of Surfaces that Resist the Adsorption of Protein.* Langmuir, 2001. **17**(18): p. 5605-5620.

5 Nanoplasmonic Sensors for Protein Detection at Graphitic and Hydrogenated Carbon Surfaces

Various forms of carbon are known to perform well as biomaterials in a variety of applications and an improved understanding of their interactions with biomolecules, cells and tissues is of interest for improving and tailoring their performance. Nanoplasmonic sensing (NSP) has emerged as a powerful technique for studying the thermodynamics and kinetics of interfacial reactions. In this chapter, the in-situ adsorption of two proteins, bovine serum albumin and fibrinogen, were studied at carbon surfaces with differing chemical and optical properties using NPS sensors. The carbon material was deposited as a thin film onto sensing surfaces consisting of 100 nm Au nanodisks with a localized plasmon absorption peak in the visible region. Two types of material investigated were amorphous carbon (a-C), with high graphitic content and high optical absorptivity, and hydrogenated amorphous carbon (a-C:H), with low graphitic content and high optical transparency. The optical response of the Au/carbon NPS elements was modelled using the finite difference time domain (FDTD) method, yielding simulated analytical sensitivities that compare well with those observed experimentally at the two carbon surfaces. Protein adsorption was investigated on a-C and a-C:H and the protein layer thicknesses were obtained from FDTD simulations of the expected response, yielding values in the 1.8-3.3 nm range.

F. Zen, V. D. Karanikolas, J. A. Behan, J. Andersson, G. Ciapetti, A. L. Bradley, P. E. Colavita;

Nanoplasmonic Sensing Studies of Protein Adsorption at Graphitic and Hydrogenated Carbon Surfaces

Langmuir, **2017**, 33 (17), 4198-4206

This chapter is the final-accepted version of the paper of which I am first author. I carried out the investigation described (except where noted), prepared the first draft and revised drafts together with my advisor. The contributions of the other coauthors are as follows: J.A. assisted with initial NPS experimental work; J.A.B. validated the model used for ellipsometric determinations; G.C. contributed with XPS data collection; A.L.B. and V.K. contributed the FDTD simulations. and P.E.C. led the work and contributed to experimental design and manuscript drafting.

5.1 Introduction

Carbon coatings, such as amorphous carbon (a-C) and hydrogen-doped carbon (a-C:H), have emerged as good biomaterials and been integrated into several biodevices like catheters, stents, sensors, medical guidewires, surgical needles, orthopaedic implants and prostheses [1-3]. The success of carbon coatings in biological applications is partially due to their chemical inertness, low frictional coefficient, high wear resistance and many more physical/chemical properties that underpin their good performance [4, 5]. However, the durability, functionality and bioresponse of artificial materials *in vivo* are limited by their interaction with blood and tissue [2, 6] and the mechanism of blood coagulation on amorphous carbon is not yet fully understood. The competitive adsorption of plasma proteins (such as albumin and fibrinogen), occurring at the early stage after implantation, is considered to have a crucial effect in determining the host response of blood systems in contact with biomaterials [6-10]. For this reason, much effort has been dedicated to the description of protein adsorption and/or binding at carbon surfaces with different physical and chemical properties, by using both *in-situ* and *ex-situ* methods [11-16]. However, only few of the techniques applied to these studies are able to monitor dynamic interactions *in-situ*, within a fluid environment that may be tailored to model likely conditions encountered *in vivo* [17].

Surface plasmon resonance (SPR) [14, 17-19] has been recognized as a powerful and advantageous label-less method for studying the thermodynamics and kinetics of interfacial interactions *in-situ* [17]. SPR modes are hybrid modes of the free electrons of a metal and the electromagnetic field. These modes are confined at a metal-dielectric interface, propagate along it, and are extremely sensitive to interfacial changes in dielectric properties, such as those that arise from adsorption, binding or cell-adhesion events. Thin metal films are necessary to support surface plasmons in sensing applications and the majority of commercial instruments currently used for quantitative analysis and screening rely on this type of sensing elements. More recently, NPS, based on the physical phenomenon localised surface plasmon resonance (LSPR), has emerged as a valuable alternative. In LSPR modes light interacts with particles much smaller than the incident wavelength leading to a hybrid confined mode with a

characteristic resonant frequency that depends on optical properties of metal and dielectric, and on nanoparticle geometry [20-23]. LSPR can be leveraged for biological and chemical sensing by monitoring the wavelength shifts of the characteristic resonance, which take place in response to changes in the local refractive index [20, 21]. Compared to conventional SPR, NPS offers advantages such as a lower sensitivity to bulk changes, the ability to modulate the optical operating range through careful nanostructure design, and greater hardware flexibility and simplicity [20]. Technical developments in the large scale fabrication of nanoscale metallic structures have been key to the exploitation of LSPR, resulting in increased interest in LSPR sensing strategies [20, 22, 23].

In this chapter we report on the application of NPS to *in-situ* studies of the carbon-bio interface. SPR methods have found limited applications so far for the study of interfacial events at carbon surfaces in biological media because of the requirement of metal surfaces for sustaining SPR modes. Lockett *et al.* [24] demonstrated however that it is possible to sustain SPR modes at the carbon-liquid interface *via* deposition of thin carbon coatings of optimized thickness onto Au SPR sensors, a strategy that had previously proved viable for the study of interactions at polymeric surfaces [25, 26]. Metal/carbon sensing platforms have since led to SPR sensing of DNA binding [24, 27], cell binding [28], protein adsorption [12, 29, 30] and immunosensing [31] at carbon surfaces whereby the authors demonstrated that SPR is a viable method for monitoring carbon-biomolecule interactions. However, few experimental studies report a comparison of different carbon surfaces under comparable conditions, partly because of the broad variability of the optical properties of carbon materials which adds complexity to the analysis of SPR data from metal/carbon/biomolecule multilayers. Notably, Saitoh and co-workers presented a comparative SPR study of albumin adsorption at hydrogenated carbons with different chemical composition [29], but pointed out that a quantitative determination of the thickness of adsorbed layers from angle shift data using Fresnel equations is challenging due to strong correlation in the multilayer model between thickness and optical constants.

The NPS technique was combined with ellipsometry and computational methods to estimate the thickness of the protein layer at two carbon substrates

with differing optical properties. To our knowledge NPS has not been used for the study of carbon-bio interactions and in this study we use a recently reported NPS method developed by Kasemo *et al.* based on Au nanodisk sensing elements [32]. Studies of interfacial chemistry on this NPS platform have been typically carried using sensors coated with thin films of dielectrics, such as metal oxides or silica, which ensure a homogeneous surface chemistry and allow flexibility in terms of the chemical reactions under study [33]. Previous work by Cho and co-workers using biomolecules has reported a detailed study of the effect of dielectric coatings on interfacial chemistry and sensitivity [34]. Herein, the applicability of these nanostructured sensors to the study of protein adsorption at carbon surfaces in real time is demonstrated. Carbon coatings differ from typical oxide spacer layers, as their optical properties can vary significantly with electronic behavior that spans the semimetallic-semiconductor-insulator range [35]. Two types of carbon surfaces with differing composition were chosen to investigate the effect of carbon chemistry on protein adsorption: a-C, a graphitic carbon, and a-C:H, a hydrogenated, polymer-like and sp^3-rich, carbon. The two plasma proteins used, albumin and fibrinogen, were chosen because of their importance for understanding the response of biomaterials after implantation. A quantitative modelling of LSPR results was carried out using the finite difference time domain (FDTD) method for determining protein layer thickness and finally, predictions from FDTD methods were correlated to results from complementary spectroscopic and microscopic methods.

5.2 Experimental

Chemicals and Materials. Ethylene glycol (99.8%), methanol (semiconductor grade), Bovine serum albumin (BSA, ≥96%), Fibrinogen from bovine plasma (Fib, 65–85% protein) and phosphate saline buffer tablets (PBS, 0.01 M, 0.0027 KCl M and 0.137 NaCl M pH 7.4) were purchased from Sigma and used without further purification. B-doped Si wafers were purchased from MicroChemicals (5-10 Ohms) and NPS sensor chips were purchased from Insplorion AB. Millipore water was used for all experiments.

Substrate Preparation. Amorphous carbon films were prepared via DC magnetron sputtering (Torr International, Inc.) at a base pressure ≤2×10^{-6} mbar

and a deposition pressure of 7×10^{-3} mbar, as previously described in Chapter 3, page 62. Two distinct films were prepared by varying the H_2/Ar gas ratio: one type of film was sputtered using Ar and shall be referred to as a-C from here onwards, the second type of film was sputtered using 10% H_2 in Ar resulting in a hydrogen doped material which is referred to as a-C:H. For spectroscopic ellipsometry (SE) and atomic force microscopy (AFM) characterization, samples were deposited on clean Si wafers. For infrared reflectance absorbance spectroscopy (IRRAS) measurements, Si wafers were first coated with an optically thick (~450 nm) Ti layer via DC magnetron sputtering (see Chapter 4, page 81), and subsequently with either a-C or a-C:H films of approximately 70 and 40 nm thickness, respectively. For NPS measurements, sensor chips were cleaned under UV/ozone for 1 h, rinsed with methanol and dried with argon, prior to deposition of a-C and a-C:H.

Characterization Methods. Spectroscopic Ellipsometry (SE) was carried out using an alpha-SETM ellipsometer (J.A. Woolam Co.), as described in Chapter 3 (page 63). IRRAS spectra were collected on a Fourier Transform Infrared (FTIR) spectrometer (Tensor 27, Bruker) equipped with a Mercury Cadmium Telluride (MCT) detector, a specular reflectance accessory (VeeMax II), and a Zinc Selenide polarizer, following the same methodology reported in Chapter 4 (page 82). To account for differences in optical enhancement in IRRAS peaks on a-C and a-C:H, spectral intensities were normalised by the intensity of the C=O stretching absorbance of a reference 5.7 nm poly(methyl methacrylate) (PMMA) layer. PMMA films were spun from 0.2 wt% toluene solution onto 2x2 cm^2 substrates, using a spin coater: the samples were spun in open air for 60 s at the speed of 3000 rpm and 100 μL of the PMMA solution was injected on the spinning surface at the beginning of the rotation; spin coated films were dried in Ar overnight and placed in an oven at 90°C for 2 h for removing residual toluene and for annealing the polymer films [36, 37]. UV−Vis transmission measurements of plasmon extinction spectra were obtained in air for bare and carbon coated LSPR sensors over the wavelength range 500−800 nm at 1 nm resolution (Shimadzu UV-2401 PC). Thickness and surface roughness measurements were carried out via AFM (Asylum Research) using Au-coated silicon cantilevers (NT-MDT) in tapping mode (1 Hz and 512 scan lines). X-ray photoelectron spectroscopy (XPS)

characterization was performed on a VG Scientific ESCAlab Mk II system (<2 ×10-8 mbar) with an Al Kα X-rays (1486.6 eV) source at 90° take off angle. Wide survey spectra were collected at 50 eV pass energy. All spectra were calibrated to the Ag $3d_{5/2}$ peak at 368.3 eV and analysed using a commercial software (CasaXPS™) (see Chapter 2, page 37).

Nanoplasmonic sensing (NPS). Indirect nanoplasmonic sensing (INPS) measurements of protein adsorption were conducted using an XNano instrument (Insplorion AB, Gothenburg, Sweden). Ensemble-averaged recordings of plasmonic resonance peak were collected in optical transmission mode. Glass sensor chips (Insplorion AB) with deposited gold nanodisks (50 nm radius, 20 nm thickness, 8% surface coverage) fabricated by hole-mask colloidal lithography, were coated with sputter-deposited a-C or a-C:H layers as described above and mounted in an optical flow cell for *in-situ* measurements. Sample solutions were flowed through the measurement chamber via peristaltic pump at a continuous rate of 50 μL min^{-1}; protein concentration was 7 μM, equivalent to 0.5 mg mL^{-1} and 2.5 mg mL^{-1} for BSA and Fib, respectively. The bulk refractive index of reference ethylene glycol/water solutions used for calibrations was determined using a refractometer (PAL-1, ATAGO Co., Tokyo, Japan).

Computational modelling of sensor response. The Maxwell equations were solved using the finite difference time domain (FDTD) method, as implemented in the commercial package FDTD Solutions from Lumerical. The optical response of the nanostructured sensing elements comprising the coated nanodisk and the substrate were modelled based on their complex refractive index, with values for the specific a-C and a-C:H layers being experimentally determined via spectroscopic ellipsometry.

5.3 Results and Discussion

Carbon films used in our experiments were deposited *via* magnetron sputtering using Ar and H_2/Ar as deposition gases; these films had previously been characterized via a combination of spectroscopic methods [38]. Briefly, a-C and a-C:H films consist of approximately 80% and 17% trigonally bonded carbon (sp^2 centers), respectively, as estimated *via* X-ray photoelectron spectroscopy (XPS) and Raman spectroscopy. These films also contain oxidized groups resulting

in a 7-9% O/C atomic ratio for both a-C and a-C:H, as determined via XPS. The a-C films are highly graphitic and possess good conductivity, whereas a-C:H films are insulating [38]. Spectroscopic ellipsometry was used to determine optical properties of the films. The optical constants, obtained as discussed in Chapter 3 (see section 3.3) and previous works [39, 40], were consistent with the difference in graphitic content between the two materials. The Tauc gap and absorption coefficients were E_T = (0.66 ± 0.01) eV and α(632 nm) = (77.2 ± 0.7)×10^3 cm^{-1} for a-C (95% C.I.) and E_T = (1.77 ± 0.01) eV and α(632 nm) = (5.08 ± 0.17) ×10^3 cm^{-1} for a-C:H (95% C.I.), thus indicating that a-C films are more metal-like and optically absorbing than a-C:H [35, 41]. The real part of the refractive index was also different for the two materials: n(632 nm) = 2.117 ± 0.003 for a-C (95% C.I.), which is consistent with values obtained for graphitic amorphous carbons, whereas n(632 nm) = 1.672 ± 0.003 for a-C:H (95% C.I.), consistent with a low density highly hydrogenated amorphous carbon film [35, 42].

The two types of carbon material were used for *in-situ* studies of protein adsorption using NPS methods. However, prior to the *in-situ* experiments, further characterization was needed to test that sputtered carbon can form a thin, uniform and continuous film on the NPS sensors. The thickness of the carbon coatings used for the NPS measurements was determined via AFM in tapping mode. Si wafers were sputtered with a-C or a-C:H for 5 min. under the conditions reported in Section 5.2; prior to sputtering the wafer was coated for half of its surface with a 2% solution of PMMA in anisole. After sputtering the PMMA was dissolved in acetone, thus creating a step edge on which AFM measurements were carried out yielding (10.1 ± 0.5) nm (C.I. 95%) and (12.2 ± 2.1) nm (C.I. 95%), for a-C and a-C:H respectively; the observed precision is consistent with typical uniformity of sputtered layers in the range 5-10%. Figure 5.1 shows an AFM image of the step used for a-C:H thickness determinations.

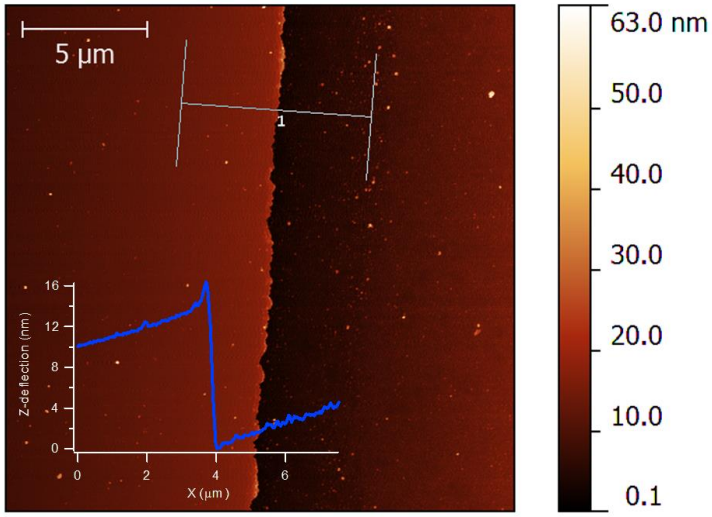

Figure 5.1. Step edge in a 5 min sputtered a-C:H layer used to measure the thickness of a-C:H coatings. Figure reproduced with permission from [43]. Copyright 2017 American Chemical Society.

Uniformity of the carbon films was tested *via* XPS. Figure 5.2 shows the survey spectra obtained for the 5 min. sputtered a-C:H layer on both a gold substrate (100 nm gold films, Evaporated Metal Films) and on NPS sensors (Insplorion). The spectra show the presence of carbon (284 eV) and oxygen (532 eV) in all of the samples. The low intensity of a doublet at 335 eV and the absence of any additional peaks for the a-C:H coated sensor indicate that the a-C:H layer uniformly covers the samples without exposing the underlying metal nanoparticles. Similar results were obtained for the a-C film.

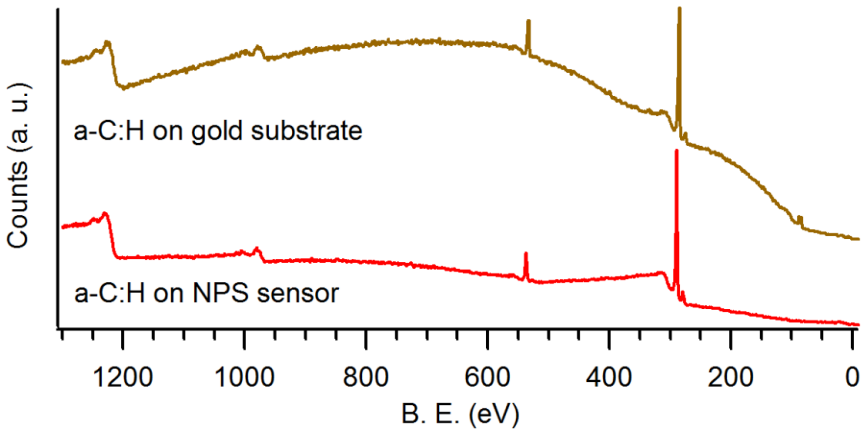

Figure 5.2. XPS survey spectra of 5 min. sputtered a-C:H coating on a gold substrate (top) and a NPS sensor (bottom). Figure reproduced with permission from [43]. Copyright 2017 American Chemical Society

After that the carbon layers were confirmed to be continuous at the thicknesses of 10 nm, for a-C, and 12 nm, for C:H, the NPS sensor chips consisting of a glass substrate with nanofabricated gold nanodisks were coated by layers of either a-C or a-C:H, as shown in the schematic in Figure 5.3a. As reported in the AFM image in Figure 5.3b, the gold nanodisks are randomly distributed on the glass substrate with 8% surface coverage [44], yielding an average disk to disk separation large enough for the discs to be considered independent of each other. The sensors were mounted in a flow cell. The plasmon excitation associated with the gold nanodisks was measured in transmittance mode and the excitation peak centre of mass monitored as a function of time during flow experiments. Figure 5.3 shows typical plasmon resonance peaks obtained in air for a bare Au sensor, and for Au/a-C and Au/a-C:H coated sensors. The presence of a ~10 nm thick carbon coating does not suppress the plasmon resonance, despite the carbon being a continuous layer, however it has an effect on both resonance peak position and full-width-at-half-maximum (fwhm), which can in turn affect the sensitivity of the LSPR modes.

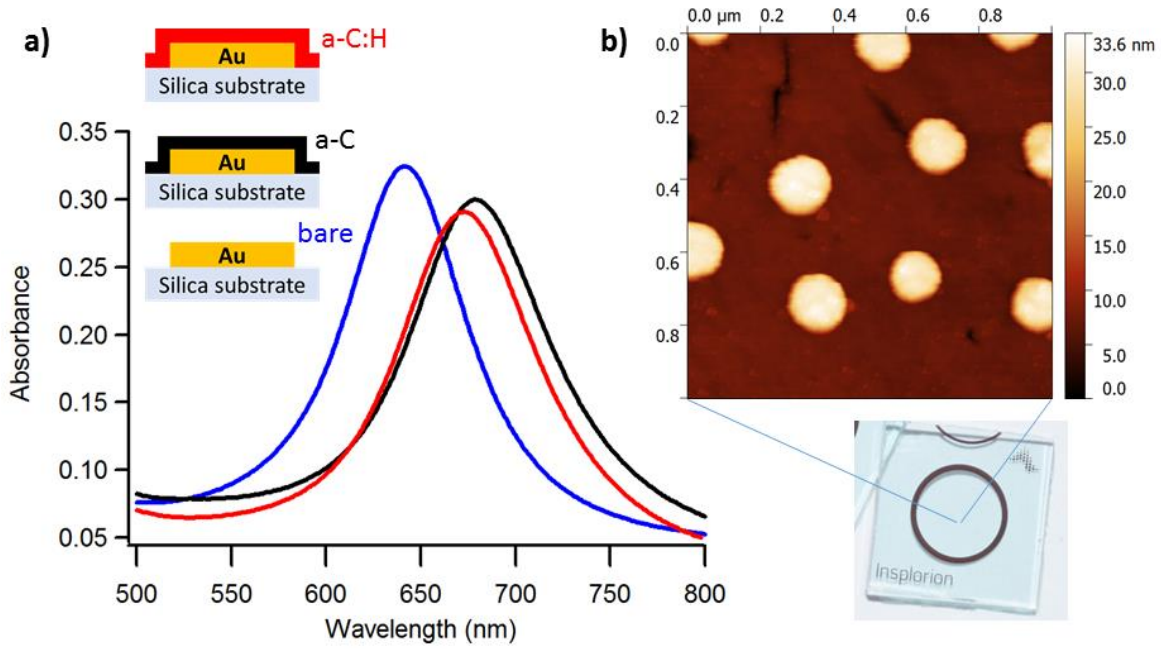

Figure 5.3. (a) Plasmon absorption in air recorded at bare (blue line), a-C (black line) and a-C:H (red line) coated sensors. The inset at the top left of the figure shows schematic of the nanodisk structures that result in the LSPR spectra. (b) AFM topography image of a a-C coated NPS sensor chip. Figure adapted with permission from [43]. Copyright 2017 American Chemical Society.

The effect of carbon coatings on the sensitivity of LSPR chips was investigated using a combination of computational and experimental methods. The wavelength of maximum absorption, λ_{max}, and the fwhm are sensitive to changes in the dielectric properties of the medium at the nanodisk interface. FDTD simulations were carried out in collaboration with Prof. Louise Bradley's group and results are presented, courtesy of Dr. Karanikolas. Simulations were used to calculate the plasmon absorption of coated Au nanodisks: the geometry used in the simulations is as shown in Figure 5.3, with the Au nanodisk possessing 50 nm radius and 20 nm thickness. Due to the low surface coverage it is assumed that nanodisks are effectively decoupled, and a single nanodisk element was thus considered in all simulations. This assumption was found to be satisfactory as will be discussed below. The carbon coating was considered as a conformal, uniform layer of 10 nm and 12 nm for a-C and a-C:H, respectively, which corresponds to the experimentally determined thickness for each layers. The optical constants for Au were obtained from Johnson and Christy [45], the refractive index for the glass substrate was real and constant at 1.459 over the wavelength range explored, and those of a-C and a-C:H films were obtained from experimental ellipsometry results (see SE characterization of carbon films in Chapter 3). Figure 5.4a and b show the logarithm of the absolute value of the total field distribution on the xz-plane, for a single nanodisk coated with a-C and a-C:H, respectively. The exciting electromagnetic field is normally incident on the top of the nanostructure and the excitation wavelengths are chosen to coincide with the maxima of the LSPR absorption in each case. We observe that the field is enhanced by up to two orders of magnitude at the edges of the Au nanodisk. The field around the Au nanodisk extends further beyond the carbon coating for a-C:H, compared to a-C, in agreement with the imaginary part of the refractive index being higher for a-C than for a-C:H. A simulation of the effect of carbon coating thickness on position and shape of the plasmon absorption shows that the presence of both carbon coatings leads to a red shift in the plasmon position and an increase in the fwhm of the peak (see Figure 5.4). However, the peak shift and peak broadening effects are significantly more pronounced for a-C than for a-C:H, in agreement with the former being the material with higher optical losses.

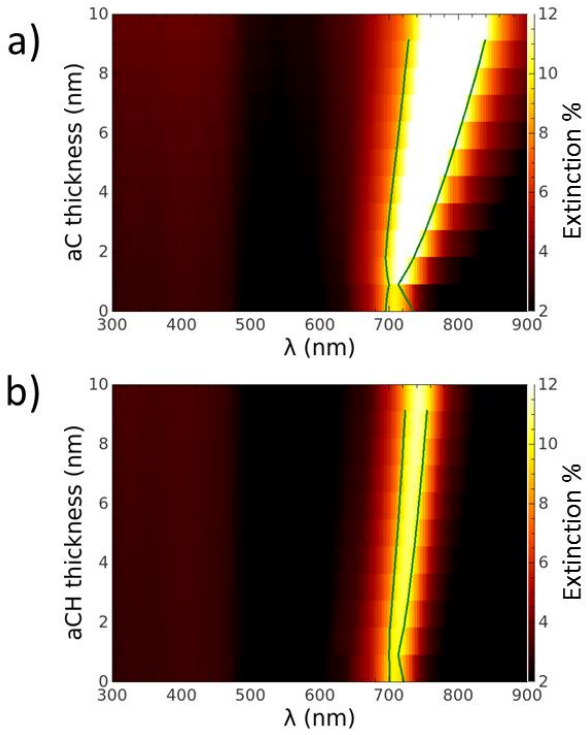

Figure 5.4. %Extinction of the sensor chip as a function of wavelength λ and carbon thickness, obtained via FDTD modelling for a-C (a) and a-C:H (b) films. The green line in the graphs corresponds to a 10%. Figure adapted with permission from [43]. Copyright 2017 American Chemical Society

The field distribution observed in Figure 5.5a and b results from plane-wave excitation of the LSPR dipole mode. The differences in field distributions observed for a-C and a-C:H coatings suggest that the sensitivity of NPS elements to adsorption/binding might be significantly modified depending on the type of carbon used to coat the sensor. A simulated calibration experiment was thus carried out, in which the resonance maximum position, $\Delta \lambda_{max}$, was calculated as a function of the refractive index in the medium surrounding the carbon (medium 1). The refractive index range explored was chosen to be identical to one that could be accessed experimentally using water/ethylene glycol solutions [34, 44]. Figure 5.5c shows the calibration plots obtained via FDTD methods for a-C and a-C:H coated sensors. The figure indicates that in both cases the LSPR at the nanodisk is sensitive to changes at the carbon/solution interface. The slopes obtained were 128.7 nm and 90.9 nm per unit change in refractive index for a-C and a-C:H, respectively, indicating that the more graphitic film results in higher sensitivity to refractive index changes.

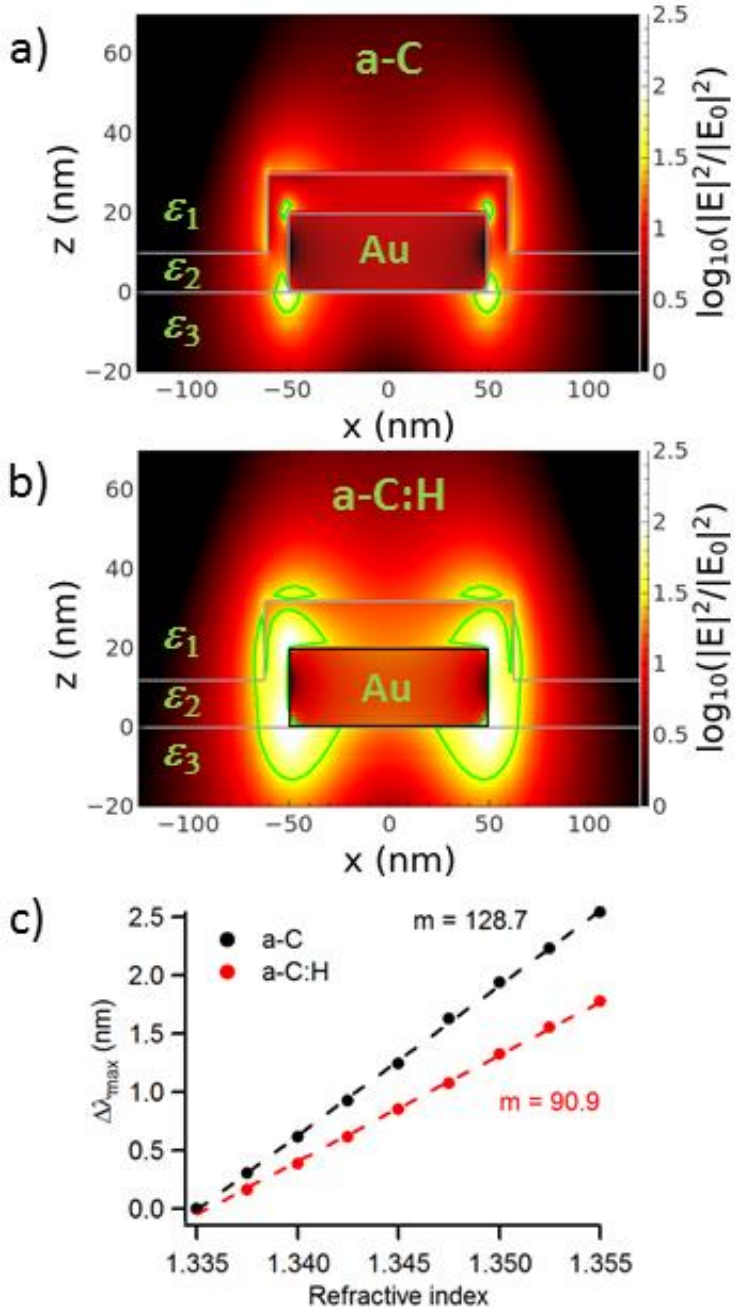

Figure 5.5. Electric field intensity distribution around isolated nanodisks immersed in PBS obtained via FDTD modelling at the wavelength corresponding to the maximum of the LSPR. The refractive index used in the simulation are reported as ε_1, ε_2 and ε_3 for the aqueous medium (ε_1=1.333), the carbon coating and the glass substrate, respectively. The green line in the graphs indicates an increment of one order of magnitude of the electric field intensity. (a) Field distribution around an isolated Au/a-C coated nanodisk at 797 nm; (b) Field distribution around an isolated Au/a-C:H coated nanodisk at 748 nm. (c) Calibration plots obtained via FDTD methods for Au/a-C (black line) and Au/a-C:H (red line) coated nanodisks.; the slope yielding the analytical sensitivity is reported next to the corresponding curve. Figure reproduced with permission from [43]. Copyright 2017 American Chemical Society

The sensitivity of carbon coated sensors was also investigated experimentally by measuring the shift $\Delta \lambda_{max}$ *vs*. refractive index of the liquid in the flow cell. Figure 5.6a shows typical dependence of $\Delta \lambda_{max}$ as a function of time obtained for a-C and a-C:H coated sensors, as water/ethylene glycol solutions of different refractive index are injected into the cell. Measured refractive indices of tested solutions are reported in Table 5.1. The staircase response was used to generate a calibration plot as shown in Figure 5.6b, which shows that the experimental $\Delta \lambda_{max}$ varies linearly with refractive index. As seen in the calibration plot, changes in the medium refractive index cause a larger peak shift in the optical extinction spectrum of a-C than of a-C:H coated sensors, in agreement with computational predictions. The average experimental slopes were found to be 130 ± 8 nm and 98 ± 12 nm per unit change in the refractive index, for a-C and a-C:H coated sensors, respectively. The experimentally determined sensitivities therefore compare very well with those obtained *via* FDTD simulations (see Figure 5.7). This further confirms that the Au nanodisks can be assumed to be decoupled.

Table 5.1. Refractive indices of the aqueous solutions used, measured at 20 ^{0}C. Table reproduced with permission from [43]. Copyright 2017 American Chemical Society

Solution	Refractive index
water	1.3329 ± 0.0003
EG 5%	1.3382 ± 0.0003
EG 10%	1.3434 ± 0.0003
EG 20%	1.3540 ± 0.0003
PBS	1.3345 ± 0.0003
BSA	1.3347 ± 0.0003
Fib	1.3349 ± 0.0003

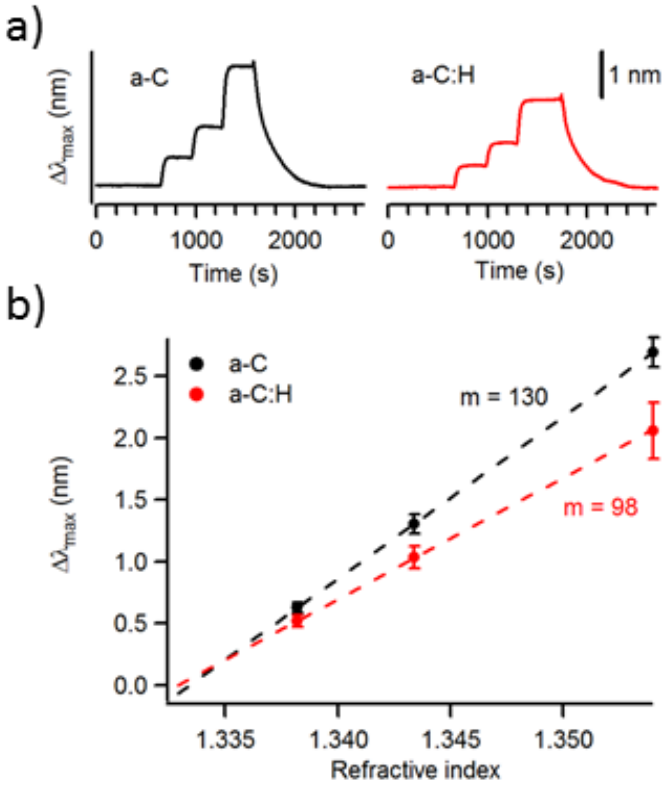

Figure 5.6. Sensitivity test obtained at a-C (black, left) and a-C:H (red, right) coated sensors. (a) LSPR shift $\Delta\lambda_{max}$ as a function of time measured after water/ethylene glycol solutions of different refractive index are injected into the cell. (b) Calibration plot of measured $\Delta\lambda_{max}$ vs. refractive index of the water/ethylene glycol solution; the slope yielding the analytical sensitivity is reported next to the corresponding curve. Error bars indicate 95% C.I. calculated from sample size n = 5 and 3 for a-C and a-C:H, respectively. Figure reproduced with permission from [43]. Copyright 2017 American Chemical Society

In Figure 5.7 is reported a comparison between the calibration plots obtained from the sensitivity test on a representative NPS sample and the one calculated by computational simulations for a-C (Figure 5.7a) and a-C:H (Figure 5.7b) coatings. As shown by the graphs, the modelling is very similar to the experimental results.

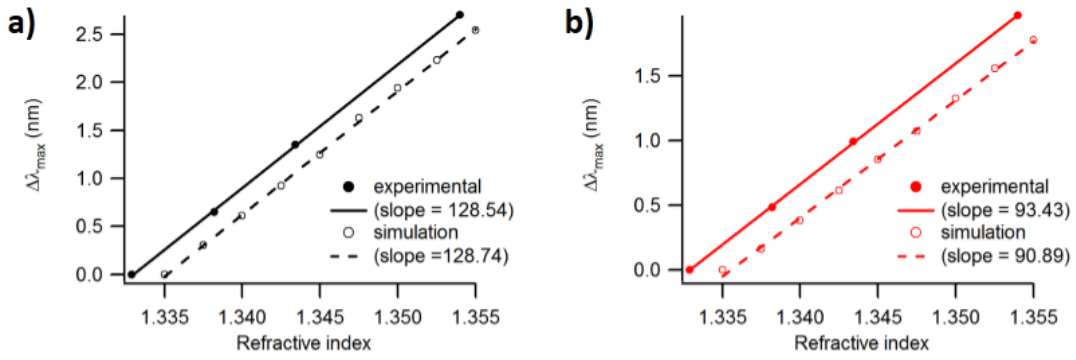

Figure 5.7. Calibration plots experimentally obtained for a representative sensor (solid line) and calculated using FDTD (dashed line) for (a) a-C, black, and (b) a-C:H, red.

In order to evaluate how proteins adsorb at different carbon substrates, both a-C and a-C:H sensors were exposed to buffered protein solutions. All sensors were mounted and calibrated in advance of all measurements using at least three water/ethylene glycol solutions. After calibration, PBS was injected first, followed by the protein solution and a final rinsing step with PBS. The calibration process was repeated at the end of each experiment to exclude any changes to the sensor sensitivity that might arise from adsorbed protein layers. An example of the full experiment is reported in Figure 5.8.

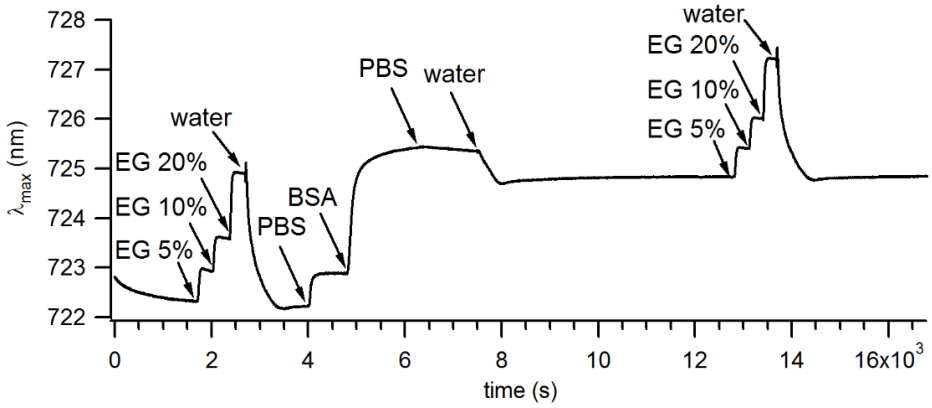

Figure 5.8. Representative BSA adsorption experiment measured using *in-situ* NPS technique. The arrows indicate the injection of different solutions in the flow cell; the first sensitivity test was carried out by injecting water, 5 vol% ethylene glycol solution (EG 5%), 10 vol% ethylene glycol solution (EG 10%), 20 vol% ethylene glycol solution (EG 20%), water; successively the phosphate-buffered saline (PBS) solution was injected, followed by the bovine serum albumin (BSA) solution and PBS again; finally a second sensitivity test was carried out as described above. This same procedure was followed for each sample analysed. Figure reproduced with permission from [43]. Copyright 2017 American Chemical Society

Figure 5.9 shows plots of $\Delta \lambda_{max}$ *vs.* time obtained on a-C and a-C:H coated sensors after the injection of protein solutions followed by injection of PBS. The exposure of carbon coated sensors to protein solutions results in a red shift of the LSPR that stabilizes to a constant value within 15 min. after the injection. Given that the refractive index of the protein solutions was statistically indistinguishable from that of the PBS solution (see Table 5.1), the wavelength shift can be unequivocally attributed to the adsorption of proteins at the carbon surface. On the other hand, the absence of any significant change in the NPS peak position after injection of protein-free buffer solution indicates that protein adsorption is irreversible at both a-C and a-C:H surfaces.

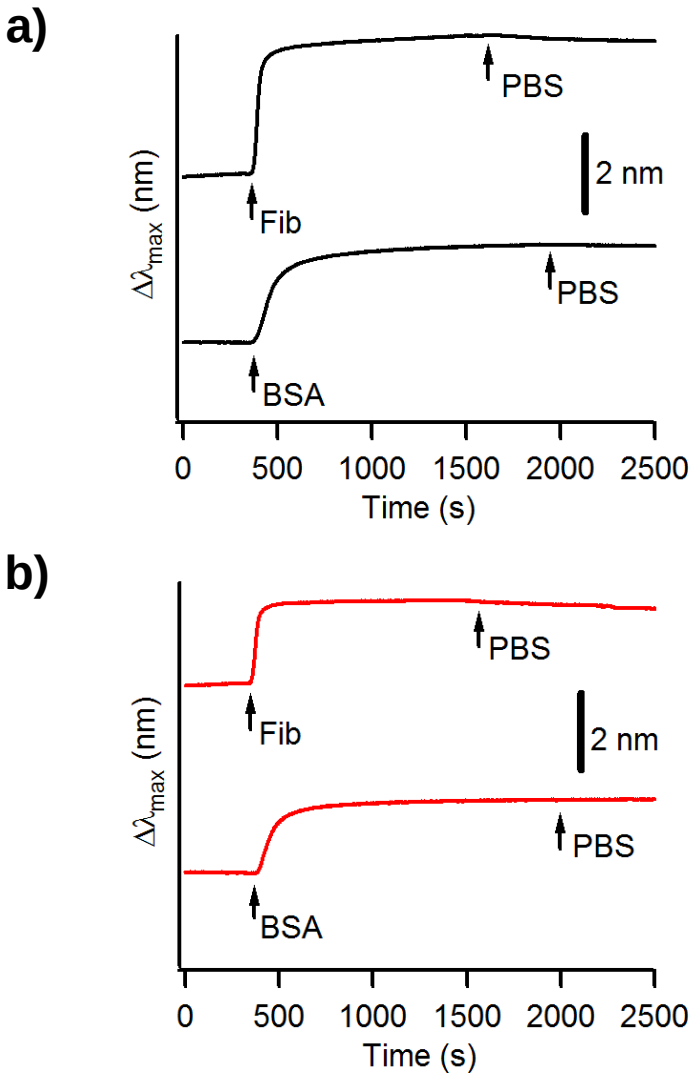

Figure 5.9. NPS wavelength shift, $\Delta\lambda_{max}$, as a function of time, measured at (a) a-C (black line) and (b) a-C:H (red line) coated sensors for in-situ protein experiments. The arrows indicate the time of the injection of BSA, Fib and PBS solutions into the flow cell. Figure adapted with permission from [43]. Copyright 2017 American Chemical Society

Moreover, the sharper steps observed in the case of Fib solutions suggests that adsorption at the carbon surface is faster for Fib than for BSA. This is also evident from a comparison of the first derivative of the curves, which show high and relatively narrow peaks in the case of Fib at both a-C and a-C:H surfaces (see Figure 5.10). Given that the bulk molar concentration is identical, the difference is a result of kinetic control, as a mass transport controlled process should be faster for BSA by a factor of ~1.7 based on reported diffusion coefficient values of 6×10^{-7} cm^2 s^{-1} and 2×10^{-7} cm^2 s^{-1} for albumin and fibrinogen, respectively [46].

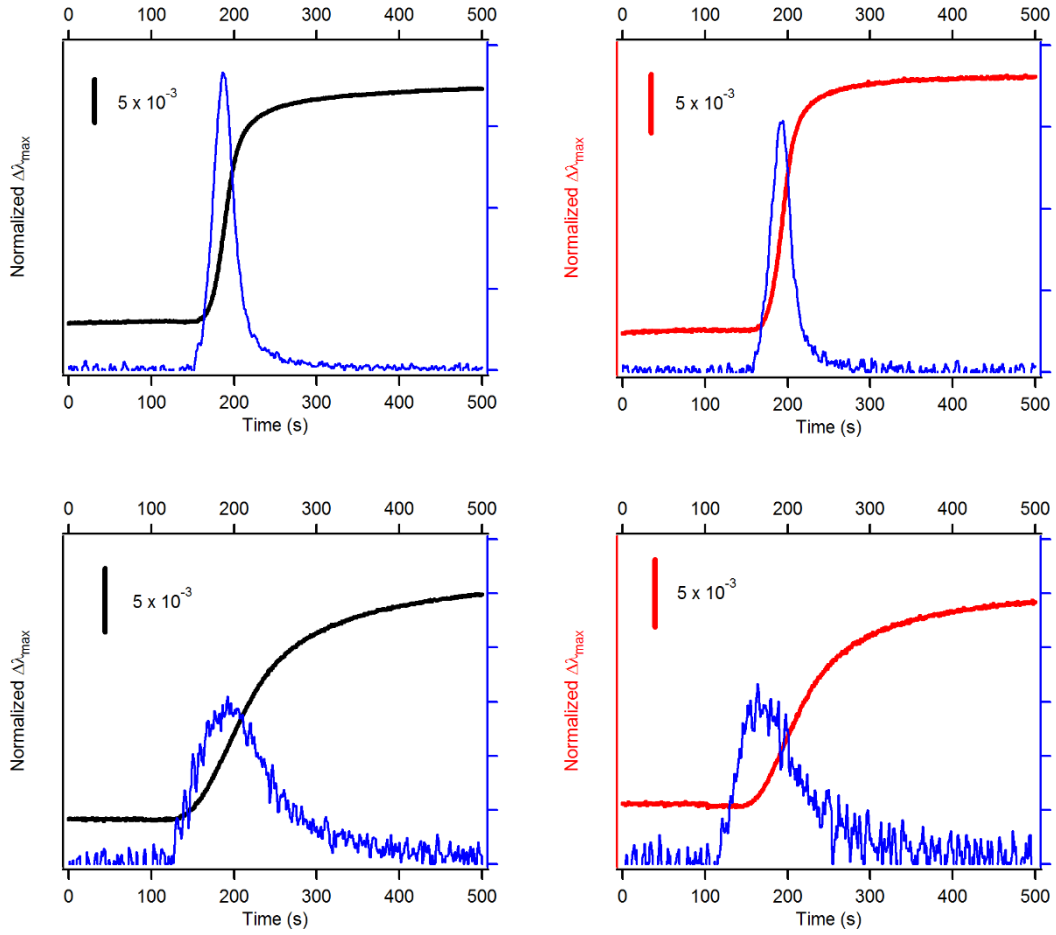

Figure 5.10. First derivative of the normalized $\Delta\lambda_{max}$ for the adsorption of BSA (bottom) and Fib (top) at a-C (left) and a-C:H (right) coated NPS sensors. Normalized $\Delta\lambda_{max}$ observed during protein adsorption at a-C (black line) and a-C:H (red line) surfaces are reported together with the first derivative (blue line). Derivative curves were smoothed to facilitate comparison. Figure reproduced with permission from [43]. Copyright 2017 American Chemical Society

The shift of the plasmon resonance is always larger for a-C than at a-C:H coated sensors when comparing adsorption from the same protein solution, however, to compare adsorption at a-C and a-C:H surfaces, the raw signal must be normalized by the experimental sensitivity. The NPS signal of each sensor was thus normalized using the slope of the calibration plot carried out as the first step in each experimental run. This normalization accounts for any differences in alignment across sensors, and for differences in sensitivity to changes in bulk refractive index that result from the two types of carbon coating. Figure 5.11 shows the normalized $\Delta \lambda_{max}$ *vs.* time calculated as $\Delta \lambda_{max}/A$, where A is the slope obtained from the initial calibration of the sensor. A summary of the average normalized $\Delta \lambda_{max}$ observed for the two carbon surfaces and the two proteins is reported in Table 5.2. After normalization, results indicate that resonance shifts are slightly greater at a-C than at a-C:H surfaces under the same conditions, thus suggesting that protein adsorption might be more pronounced at a-C than at a-C:H surfaces. For both surfaces the shift obtained for Fib is greater than that observed with BSA, which suggests greater protein adsorption from Fib solutions than from BSA solutions at the same molar concentration, in agreement with previous results obtained using *ex situ* determinations at a-C surfaces (see Chapter 4, page 89).

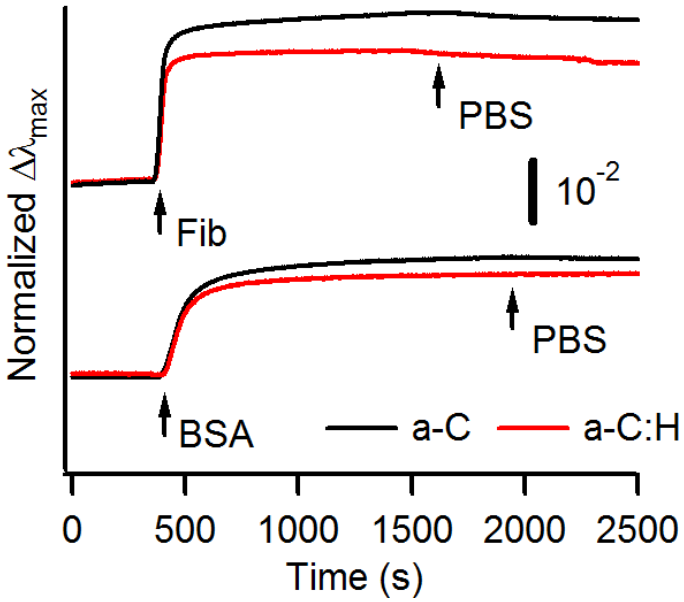

Figure 5.11. Normalized $\Delta\lambda_{max}$ as a function of time calculated using the initial calibration of the sensor at both a-C (black line) and a-C:H (red line) surfaces. The arrows indicate the time of the injection of BSA, Fib and PBS solutions into the flow cell. Figure adapted with permission from [43]. Copyright 2017 American Chemical Society

Table 5.2. Summary of results from NPS and AFM measurements. a = RMS calculated over a 100 μm^2 image; b = error represents the standard deviation of the Δz step measured after a contact mode experiment. Table reproduced with permission from [43]. Copyright 2017 American Chemical Society

Surface	Protein	Normalized $\Delta\lambda_{max}$ (x 10^{-2})	Modelled thickness (nm)	RMS[a] roughness (nm)	AFM thickness[b] (nm)
a-C	BSA	2 ± 0.5	2.3	1.05	1.0 ± 0.1
	Fib	2.8 ± 1.1	3.2	1.91	1.4 ± 0.1
a-C:H	BSA	1.4 ± 0.6	1.8	1.22	1.3 ± 0.1
	Fib	2.3 ± 0.5	3.3	2.04	1.8 ± 0.1

FDTD methods were used for the analysis of experimental LSPR shifts to obtain quantitative estimates of the protein layer thickness. The protein layer was simulated as an additional conformal layer on top of the carbon coating, with the

same geometry as in Figure 5.5a and b. The layer was modelled as a dielectric with a constant real refractive index of 1.465 [47]. The LSPR wavelength shift, $\Delta\lambda_{max}$, was simulated for both a-C and a-C:H coated sensors, at various thicknesses of the protein layer, and the normalized $\Delta\lambda_{max}$ was then calculated using the slopes of the computed calibration plots (Figure 5.5c). Figure 5.12 shows the normalized $\Delta\lambda_{max}$ calculated at different thicknesses of the protein layer. The plot shows that $\Delta\lambda_{max}$ levels off at large layer thickness. This is in agreement with expectations as the resonance shift should tend to a limit, corresponding to the value obtained for a semi-infinite medium with a refractive index equivalent to that of the protein layer. The experimental data obtained from the NPS measurements was used to estimate the thickness of the protein layer at the sensor surface *via* interpolation of the curves in Figure 5.12. The thickness estimates thus obtained are reported in Table 5.2. The protein film thicknesses obtained from *in-situ* NPS experiments using FDTD-generated calibration plots are in the range 1.8-3.3 nm; in the case of BSA the estimated adsorbed layer is thinner for a-C:H than for a-C, however, in the case of Fib, the adsorbed layer thickness is similar for both types of carbon surfaces. Given that the same refractive index was assumed for BSA and Fib layers, the thickness ratio provides a measure of relative mass density for the two proteins [48]. If we consider an adsorbed layer of thickness *d*, the adsorbed mass density *m* of a pure substance is obtained from the relationship by Cuypers *et al.* [49]:

$$m = d\frac{M}{A}\left(\frac{n^2-1}{n^2+2}\right) \tag{5.1}$$

where the mass density *m* is expressed in mg m^{-2}, the thickness *d* is expressed in nm, *M* is the molar mass, *A* is the molar refractivity and *n* is the refractive index of the adsorbed substance. The M/A ratio was assumed equivalent to 4.14, as typically reported in the case of proteins [49]. Using Cuypers one-component model, the estimated mass density for Fib is approximately 3.8 mg m^{-2} on both surfaces, whereas that of BSA is 2.1 and 2.6 mg m^{-2} on a-C:H and a-C, respectively. In the case of both carbon materials the mass density of Fib was therefore found to be higher than that of the BSA layer.

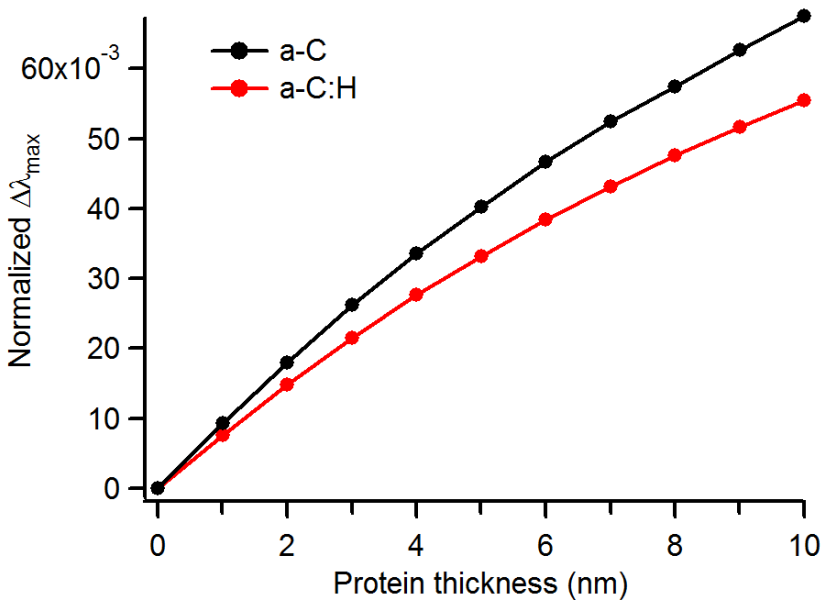

Figure 5.12. Simulated normalized $\Delta\lambda_{max}$ for a-C (black) and a-C:H (red) coated sensors calculated for various thicknesses of the protein layer using the FDTD method. Figure reproduced with permission from [43]. Copyright 2017 American Chemical Society

In situ experiments show that in the case of BSA, a globular protein, the adsorption is slightly higher on a-C vs. a-C:H surfaces. a-C:H displays lower hydrophilicity compared to a-C based on water contact angle measurements;[50] multisolvent contact angle determinations (see Chapter 3) shows that the surface free energy (SFE) of a-C:H is 58.4 mJ m^{-2}, lower than that of a-C (SFE = 63.9 mJ m^{-2}). Estimated BSA layer thicknesses in Table 5.2 are therefore consistent with both wetting and SFE comparisons, as it has been empirically observed that in the range 20-65 mJ m^{-2}, lower surface free energy translates into reduced protein adsorption.[51] It is likely however that this is not the only mechanism at the origin of the observed differences, as the adsorption of proteins at surfaces is a complex process involving long-range interactions, multiple adsorbate conformations and conformational changes at the surface over multiple timescales.[46, 52, 53] Recently, Urbassek and co-workers[54] carried out molecular dynamic simulations of insulin, a small globular protein, adsorbed at graphite surfaces, and examined the effect of immobilized ethane, a hydrocarbon, on the adsorption process. The presence of a hydrocarbon was found to significantly reduce protein-surface interaction energy values and, consequently,

protein denaturation at hydrocarbon-covered surfaces. The two surfaces used in our experiments range from a graphite-like surface (a-C) to a hydrocarbon-like surface, rich in C—H bonds (a-C:H) [38]. Based on Urbassek's results it is therefore reasonable to expect reduced protein adsorption at a-C:H compared to a-C.

In situ experiments also reveal higher protein surface coverages when using Fib compared to BSA independently of the surface examined. Fib is known to form irreversibly adsorbed layers with a wide range of surface density values, but its mechanism of adsorption is still highly debated.[55] Fib has a higher molecular weight than BSA, it possesses multiple domains and a hinged rod-like shape. Its anisotropy opens the possibility of both side-on and end-on surface approaches [52, 56], and previous experiments of Fib on Au,[56] silica,[57] polymers and mica [58] have proposed formation of mixed side-on/end-on layers. The estimated mass density for Fib of 3.8 mg m^{-2} found in our experiments is in excellent agreement with limiting coverages observed by other groups under similar conditions [55, 57]. However, it is approximately double what is expected for closed packed side-on adsorbates (1.4-2.1 mg m^{-2}) [57, 59]. This suggests that on a-C and a-C:H Fib might form mixed side-on/end-on layer as proposed for other surfaces. Minton has previously demonstrated via simulations that faster adsorption rates can be expected from end-on vs. side-on adsorbates, which are consistent with faster adsorption observed for Fib in our experiments. Relative to side-on adsorbates, end-on conformation results in weaker protein-surface interactions, which might also partially contribute to the insensitivity of the Fib thickness to the type of carbon surface chemistry. Based on the current experiments alone it is not possible to distinguish formation of mixed side-on/end-on layers from side-on multilayer formation, however experiments at lower protein concentrations, and/or using complementary techniques to probe adsorbate packing might distinguish between these two possible modes of adsorption.

The adsorbed protein layers were also characterized *via ex-situ* experiments; IRRAS technique was used to estimate the amount of protein adsorbed at carbon surfaces. Due to the different optical properties of a-C and a-C:H films (see Chapter 3), the IRRAS spectral intensities were normalized using a reference PMMA layer. PMMA was spin coated on Si, a-C and a-C:H substrates as described in the

experimental section. Determination of PMMA film thickness was carried out on Si substrates *via* SE measurements. SE data were fitted using a 3-layer model, which takes into account the Si substrate [60], the PMMA layer and the air phase, similarly to previous works [40, 61]. PMMA films were modelled as a dielectric layer, the optical constants of which were taken from the software database. The thickness of the PMMA layer was the only parameter allowed to vary, yielding a value of (5.7 ± 0.1) nm (95% C.I.). The spin coated PMMA films at a-C and a-C:H substrates were used to calibrate the optical enhancement measured for the two carbon surfaces. Figure 5.13 shows the IRRAS spectra obtained for a-C and a-C:H surfaces after spin coating with PMMA. The intensity of the C=O stretching absorbance at 1735 cm^{-1} was found to be higher for a-C:H surfaces, by a factor of 1.9 with respect to a-C, thus indicating a larger optical enhancement of the IRRAS spectral intensities in the case of a-C:H when compared to a-C coatings.

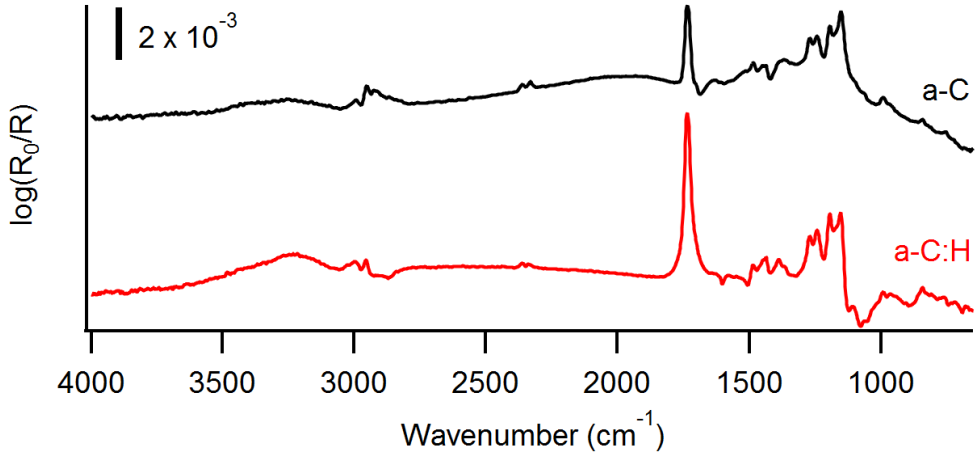

Figure 5.13. IRRAS spectra of reference 5.7 nm PMMA layer at a-C (black, top) and a-C:H (red, bottom) surfaces.

Figure 5.14 shows the baseline subtracted IRRAS spectra in the region 1900-1300 cm^{-1} of a-C and a-C:H substrates obtained after incubation with BSA and Fib protein solutions followed by rinsing. In Figure 5.14a the raw data are reported. The a-C:H spectrum was corrected for the optical enhancement using the reference 5.7 nm PMMA layer (see Figure 5.13) and normalised to be equivalent to the optical enhancement obtained at a-C substrates. This allowed for a direct comparison of peak intensities on the two optically different carbon substrates, as shown in Figure 5.14b. IRRAS Spectra exhibit the characteristic bands of amide

groups in polypeptides at ~1675 cm^{-1} and ~1540 cm^{-1}, assigned to the amide I and II modes, respectively [62]. The two strong broad peaks indicate the presence of the protein layer irreversibly adsorbed at both carbon surfaces, as previously reported by our group in the case of a-C [40]. The higher intensity obtained for amide peaks in the case of Fib is consistent with NPS results which indicate that under these conditions Fib yields thicker adsorbed layers than BSA.

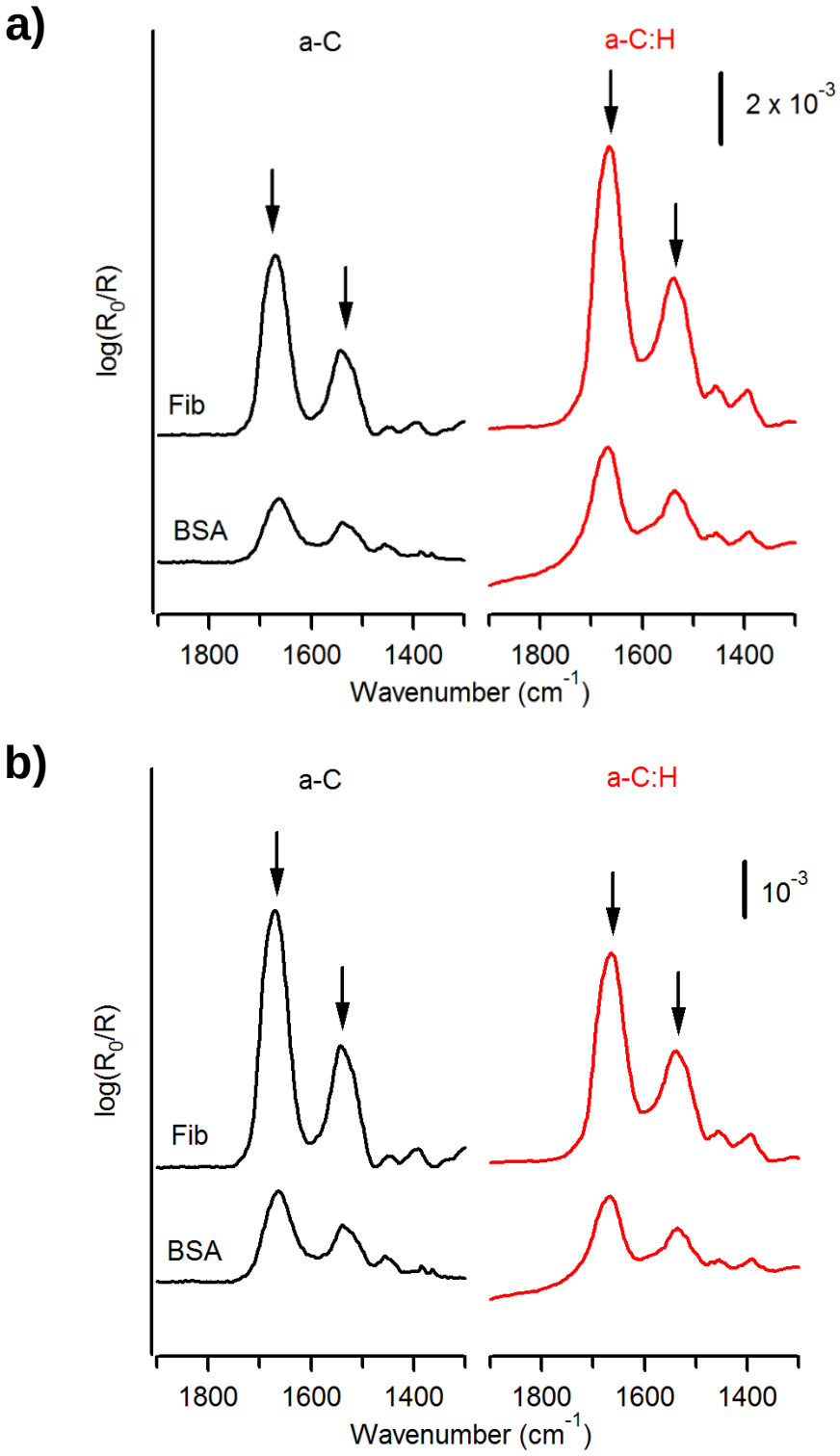

Figure 5.14. IRRAS spectra of a-C (black, left) and a-C:H (red, right) substrates after 1 h incubation with BSA (bottom) and Fib (top). The arrows indicate the peak positions of the amide I and amide II bands. Spectra were baseline corrected and a-C:H data are presented (a) before and (a) after the correction for the optical enhancement. Figure adapted with permission from [43]. Copyright 2017 American Chemical Society

AFM characterization of the films, using previously reported methods [40, 63, 64], was used to compare the morphology of protein layers obtained at the carbon surfaces and to understand whether *ex situ* and *in situ* determinations of protein layer thickness resulted in comparable results. Carbon surfaces exposed to protein solutions were first imaged in tapping mode; subsequently, a section of the film was removed by scratching the sample with the AFM tip in contact mode; finally, the step created in the organic film was imaged to determine the layer thickness through cross-section analysis. AFM images reveal that BSA tends to adsorb at both carbon substrates forming smooth layers, whereas Fib tends to form 10-30 nm thick agglomerates (Figure 5.15a and b). Roughness measurements in fact yield higher root mean square (RMS) values in the case of Fib at both a-C and a-C:H surfaces, as reported in Table 5.2. Figure 5.15c shows an example of a-C after incubation in BSA solution, imaged after the scratching process; the height profile across the step is shown in the plot underneath the image. The average height difference of protein layers was found to be in the range 1.0-1.8 nm in the case of BSA and Fib, respectively, for both a-C and a-C:H substrates (Table 5.2). These thicknesses are lower than those obtained from *in-situ* NPS measurements, but are consistent with the protein layer undergoing dehydration and compaction after sample drying prior to AFM determinations. When comparing results obtained for the two proteins, AFM measurements also show that Fib yields thicker layers than BSA (~40% thicker) at both a-C and a-C:H surfaces, in good agreement with NPS experiments.

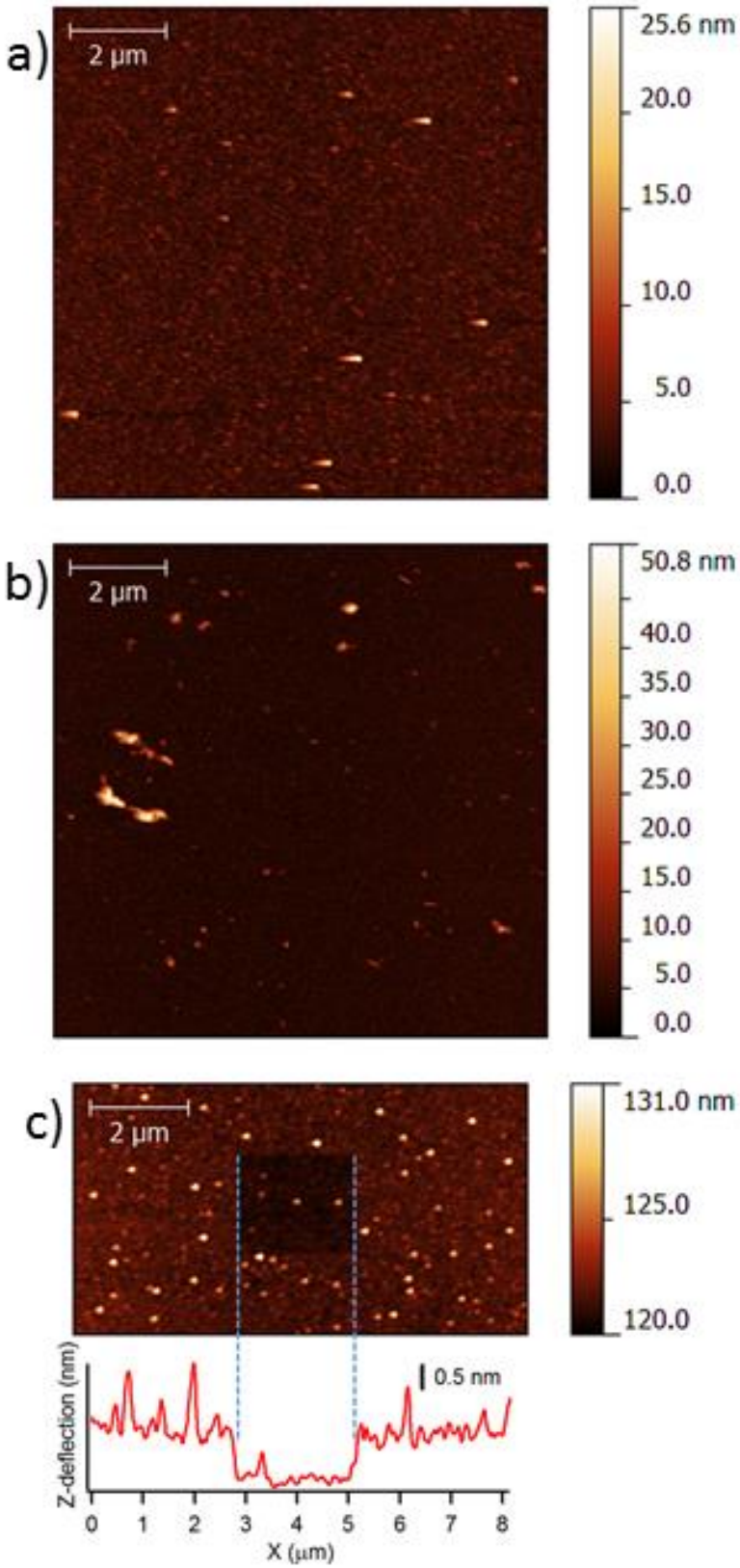

Figure 5.15. AFM topographic images of a-C:H surfaces after incubation with (a) BSA and (b) Fib solutions; thickness of (c) BSA layer adsorbed at an a-C surface. Figure reproduced with permission from [43]. Copyright 2017 American Chemical Society

5.4 Conclusions

We have studied *in-situ* adsorption of two plasma proteins at different types of carbon surfaces using an NPS methods. FDTD simulations that modelled the sensor response based on the nanodisk geometry and carbon optical constants were predictive of the analytical sensitivity. The computation model was, therefore, used to analyse protein adsorption data to determine estimated thicknesses, which were found to be consistent with results obtained via *ex-situ* spectroscopy and microscopy. Mass density estimates calculated from thickness values are in good agreement with limiting protein coverage values previously observed with other techniques. These results suggest that NPS in combination with FDTD analysis are well suited to investigating and comparing protein adsorption at carbons, even in the case of carbon materials with highly dissimilar dielectric properties. We expect the results to be important as a platform for new methodologies for the investigation of the carbon-bio interface.

5.5 References

1. Roy, R.K. and K.R. Lee, *Biomedical applications of diamond-like carbon coatings: A review.* Journal of Biomedical Materials Research Part B-Applied Biomaterials, 2007. **83B**(1): p. 72-84.
2. Stueber, M., L. Niederberger, F. Danneil, H. Leiste, S. Ulrich, A. Welle, M. Marin, and H. Fischer, *Surface topography, surface energy and wettability of magnetron-sputtered amorphous carbon (a-c) films and their relevance for platelet adhesion.* Advanced Engineering Materials, 2007. **9**(12): p. 1114-1122.
3. Sydow-Plum, G. and M. Tabrizian, *Review of stent coating strategies: clinical insights.* Materials Science and Technology, 2008. **24**(9): p. 1127-1143.
4. Anne Thomson, L., F.C. Law, N. Rushton, and J. Franks, *Biocompatibility of diamond-like carbon coating.* Biomaterials, 1991. **12**(1): p. 37-40.
5. Hauert, R., *A review of modified DLC coatings for biological applications.* Diamond and Related Materials, 2003. **12**(3-7): p. 583-589.
6. Ratner, B.D., A.S. Hoffman, F.J. Schoen, and J.E. Lemons, *Biomaterials Science*. 2nd ed. 2004, London: Elsevier Academic Press.
7. Kasemo, B., *Biological surface science.* Surface Science, 2002. **500**(1-3): p. 656-677.
8. Kasemo, B. and J. Lausmaa, *Surface properties and processes of the biomaterial-tissue interface.* Materials Science and Engineering: C, 1994. **1**(3): p. 115-119.
9. Schwartz, Z. and B.D. Boyan, *Underlying mechanisms at the bone–biomaterial interface.* Journal of Cellular Biochemistry, 1994. **56**(3): p. 340-347.
10. Thevenot, P., W. Hu, and L. Tang, *Surface Chemistry Influences Implant Biocompatibility.* Current Topics in Medicinal Chemistry, 2008. **8**(4): p. 270-280.
11. Yadav, P.K., F. McKavanagh, P.D. Maguire, and P. Lemoine, *Adsorption of bovine serum albumin on amorphous carbon surfaces studied with dip pen nanolithography.* Applied Surface Science, 2011. **258**(1): p. 361-369.
12. Takeda, A., H. Akasaka, S. Ohshio, I. Toda, M. Nakano, and H. Saitoh, *Adsorption ability comparison of plasma proteins on amorphous carbon surface.* Journal of Physics and Chemistry of Solids, 2012. **73**(11): p. 1331-1334.
13. Berlind, T., P. Tengvall, L. Hultman, and H. Arwin, *Protein adsorption on thin films of carbon and carbon nitride monitored with in situ ellipsometry.* Acta Biomaterialia, 2011. **7**(3): p. 1369-1378.
14. Lousinian, S. and S. Logothetidis, *Optical properties of proteins and protein adsorption study.* Microelectronic Engineering, 2007. **84**(3): p. 479-485.
15. Jones, M.I., I.R. McColl, D.M. Grant, K.G. Parker, and T.L. Parker, *Protein adsorption and platelet attachment and activation, on TiN, TiC, and DLC coatings on titanium for cardiovascular applications.* Journal of Biomedical Materials Research, 2000. **52**(2): p. 413-421.
16. Feng, L. and J.D. Andrade, *Protein adsorption on low temperature isotropic carbon. I. Protein conformational change probed by differential scanning calorimetry.* Journal of Biomedical Materials Research, 1994. **28**(6): p. 735-743.

17. Green, R.J., R.A. Frazier, K.M. Shakesheff, M.C. Davies, C.J. Roberts, and S.J.B. Tendler, *Surface plasmon resonance analysis of dynamic biological interactions with biomaterials.* Biomaterials, 2000. **21**(18): p. 1823-1835.
18. Kargl, R., M. Kahn, S. Köstler, M. Reischl, A. Doliška, K. Stana-Kleinschek, W. Waldhauser, and V. Ribitsch, *Deposition of silicon doped and pure hydrogenated amorphous carbon coatings on quartz crystal microbalance sensors for protein adsorption studies.* Thin Solid Films, 2011. **520**(1): p. 83-89.
19. Lousinian, S., N. Kalfagiannis, and S. Logothetidis, *Albumin and fibrinogen adsorption on boron nitride and carbon-based thin films.* Materials Science and Engineering B-Advanced Functional Solid-State Materials, 2008. **152**(1-3): p. 12-15.
20. Willets, K.A. and R.P.V. Duyne, *Localized Surface Plasmon Resonance Spectroscopy and Sensing.* Annual Review of Physical Chemistry, 2007. **58**(1): p. 267-297.
21. Yonzon, C.R., E. Jeoung, S. Zou, G.C. Schatz, M. Mrksich, and R.P. Van Duyne, *A Comparative Analysis of Localized and Propagating Surface Plasmon Resonance Sensors: The Binding of Concanavalin A to a Monosaccharide Functionalized Self-Assembled Monolayer.* Journal of the American Chemical Society, 2004. **126**(39): p. 12669-12676.
22. Hutter, E. and J.H. Fendler, *Exploitation of Localized Surface Plasmon Resonance.* Advanced Materials, 2004. **16**(19): p. 1685-1706.
23. Anker, J.N., W.P. Hall, O. Lyandres, N.C. Shah, J. Zhao, and R.P. Van Duyne, *Biosensing with plasmonic nanosensors.* Nat Mater, 2008. **7**(6): p. 442-453.
24. Lockett, M.R., S.C. Weibel, M.F. Phillips, M.R. Shortreed, B. Sun, R.M. Corn, R.J. Hamers, F. Cerrina, and L. Smith, *Carbon-on-Metal Films for Surface Plasmon Resonance Detection of DNA Arrays.* Journal Of The American Chemical Society, 2008. **130**(27): p. 8611–8613.
25. Green, R.J., J. Davies, M.C. Davies, C.J. Roberts, and S.J.B. Tendler, *Surface plasmon resonance for real time in situ analysis of protein adsorption to polymer surfaces.* Biomaterials, 1997. **18**(5): p. 405-413.
26. Green, R.J., M.C. Davies, C.J. Roberts, and S.J.B. Tendler, *Competitive protein adsorption as observed by surface plasmon resonance.* Biomaterials, 1999. **20**(4): p. 385-391.
27. Zagorodko, O., J. Spadavecchia, A.Y. Serrano, I. Larroulet, A. Pesquera, A. Zurutuza, R. Boukherroub, and S. Szunerits, *Highly Sensitive Detection of DNA Hybridization on Commercialized Graphene-Coated Surface Plasmon Resonance Interfaces.* Analytical Chemistry, 2014. **86**(22): p. 11211-11216.
28. Subramanian, P., F. Barka-Bouaifel, J. Bouckaert, N. Yamakawa, R. Boukherroub, and S. Szunerits, *Graphene-Coated Surface Plasmon Resonance Interfaces for Studying the Interactions between Bacteria and Surfaces.* ACS Applied Materials & Interfaces, 2014. **6**(8): p. 5422-5431.
29. Akasaka, H., N. Gawazawa, T. Suzuki, M. Nakano, S. Ohshio, and H. Saitoh, *Evaluation of protein adsorption on hydrogenated amorphous carbon films by surface plasmon resonance phenomenon.* Diamond and Related Materials, 2010. **19**(10): p. 1235-1239.
30. Akasaka, H., A. Takeda, T. Suzuki, M. Nakano, S. Ohshio, and H. Saitoh, *Fibrinogen and lysozyme adsorption on amorphous carbon film surface*

detected by multilayer device from the back side of the film. Diamond and Related Materials, 2011. **20**(2): p. 213-216.

31. Singh, M., M. Holzinger, M. Tabrizian, S. Winters, N.C. Berner, S. Cosnier, and G.S. Duesberg, *Noncovalently Functionalized Monolayer Graphene for Sensitivity Enhancement of Surface Plasmon Resonance Immunosensors.* Journal of the American Chemical Society, 2015. **137**(8): p. 2800-2803.
32. Larsson, E.M., C. Langhammer, I. Zorić, and B. Kasemo, *Nanoplasmonic Probes of Catalytic Reactions.* Science, 2009.
33. Langhammer, C., E.M. Larsson, B. Kasemo, and I. Zorić, *Indirect Nanoplasmonic Sensing: Ultrasensitive Experimental Platform for Nanomaterials Science and Optical Nanocalorimetry.* Nano Letters, 2010. **10**(9): p. 3529-3538.
34. Zan, G.H., J.A. Jackman, S.-O. Kim, and N.-J. Cho, *Biosensors: Controlling Lipid Membrane Architecture for Tunable Nanoplasmonic Biosensing (Small 23/2014).* Small, 2014. **10**(23): p. 4827-4827.
35. Robertson, J., *Diamond-like amorphous carbon.* Materials Science and Engineering Reports, 2002. **37**(4-6): p. 129-281.
36. Rowinska, M., S.M. Kelleher, F. Soberon, A.J. Ricco, and S. Daniels, *Fabrication and characterisation of spin coated oxidised PMMA to provide a robust surface for on-chip assays.* Journal of Materials Chemistry B, 2015. **3**(1): p. 135-143.
37. Walsh, C.B. and E.I. Franses, *Ultrathin PMMA films spin-coated from toluene solutions.* Thin Solid Films, 2003. **429**(1–2): p. 71-76.
38. Cullen, R.J., D. Jayasundara, L. Soldi, J. Cheng, G. Dufaure, and P.E. Colavita, *Spontaneous grafting of nitrophenyl groups on amorphous carbon thin films: A structure-reactivity investigation.* Chemistry of Materials, 2012. **24**(6): p. 1031-1040.
39. Behan, J.A., S.N. Stamatin, M.K. Hoque, G. Ciapetti, F. Zen, L. Esteban-Tejeda, and P.E. Colavita, *A Combined Optoelectronic and Electrochemical Study of Nitrogenated Carbon Electrodes.* submitted.
40. Zen, F., M.D. Angione, J.A. Behan, R.J. Cullen, T. Duff, J.M. Vasconcelos, E.M. Scanlan, and P.E. Colavita, *Modulation of Protein Fouling and Interfacial Properties at Carbon Surfaces via Immobilization of Glycans Using Aryldiazonium Chemistry.* Scientific Reports, 2016. **6**: p. 24840.
41. Silva, S.R.P., ed. *Properties of amorphous carbon*. 1st ed. 2003, INSPEC, Inc. The Institution of Electrical Engineers: London.
42. Schwarz-Selinger, T., A. von Keudell, and W. Jacob, *Plasma chemical vapor deposition of hydrocarbon films: The influence of hydrocarbon source gas on the film properties.* Journal of Applied Physics, 1999. **86**(7): p. 3988-3996.
43. Zen, F., V.D. Karanikolas, J.A. Behan, J. Andersson, G. Ciapetti, A.L. Bradley, and P.E. Colavita, *Nanoplasmonic Sensing at the Carbon-Bio Interface: Study of Protein Adsorption at Graphitic and Hydrogenated Carbon Surfaces.* Langmuir, 2017. **33**(17): p. 4198-4206.
44. Jackman, J.A., B. Spackova, E. Linardy, M.C. Kim, B.K. Yoon, J. Homola, and N.-J. Cho, *Nanoplasmonic ruler to measure lipid vesicle deformation.* Chemical Communications, 2016. **52**(1): p. 76-79.
45. Johnson, P.B. and R.W. Christy, *Optical Constants of the Noble Metals.* Physical Review B, 1972. **6**(12): p. 4370-4379.

46. Andrade, J.D. and V. Hlady, *Plasma Protein Adsorption: The Big Twelvea.* Annals of the New York Academy of Sciences, 1987. **516**(1): p. 158-172.
47. Goyal, D.K. and A. Subramanian, *In-situ protein adsorption study on biofunctionalized surfaces using spectroscopic ellipsometry.* Thin Solid Films, 2010. **518**(8): p. 2186-2193.
48. Vörös, J., *The Density and Refractive Index of Adsorbing Protein Layers.* Biophysical Journal, 2004. **87**(1): p. 553-561.
49. Cuypers, P.A., J.W. Corsel, M.P. Janssen, J.M. Kop, W.T. Hermens, and H.C. Hemker, *The adsorption of prothrombin to phosphatidylserine multilayers quantitated by ellipsometry.* Journal of Biological Chemistry, 1983. **258**(4): p. 2426-31.
50. Vasconcelos, J.M., F. Zen, S.N. Stamatin, J.A. Behan, and P.E. Colavita, *Determination of surface ζ-potential and isoelectric point of carbon surfaces using tracer particle suspensions.* Surface and Interface Analysis, 2017. **49**(8): p. 781-787.
51. Baier, R., *Surface behaviour of biomaterials: The theta surface for biocompatibility.* Journal of Materials Science: Materials in Medicine, 2006. **17**(11): p. 1057-1062.
52. Minton, A.P., *Adsorption of Globular Proteins on Locally Planar Surfaces. II. Models for the Effect of Multiple Adsorbate Conformations on Adsorption Equilibria and Kinetics.* Biophysical Journal, 1999. **76**(1): p. 176-187.
53. Fang, F. and I. Szleifer, *Kinetics and Thermodynamics of Protein Adsorption: A Generalized Molecular Theoretical Approach.* Biophysical Journal, 2001. **80**(6): p. 2568-2589.
54. Mücksch, C., C. Rösch, C. Müller−Renno, C. Ziegler, and H.M. Urbassek, *Consequences of Hydrocarbon Contamination for Wettability and Protein Adsorption on Graphite Surfaces.* Journal of Physical Chemistry C, 2015. **119**(22): p. 12496-12501.
55. Adamczyk, Z., J. Barbasz, and M. Cieśla, *Mechanisms of Fibrinogen Adsorption at Solid Substrates.* Langmuir, 2011. **27**(11): p. 6868-6878.
56. Dyr, J.E., I. Tichý, M. Jiroušková, P. Tobiška, R. Slavík, J. Homola, E. Brynda, M. Houska, and J. Suttnar, *Molecular arrangement of adsorbed fibrinogen molecules characterized by specific monoclonal antibodies and a surface plasmon resonance sensor.* Sensors and Actuators B: Chemical, 1998. **51**(1–3): p. 268-272.
57. Malmsten, M., *Ellipsometry Studies of Protein Layers Adsorbed at Hydrophobic Surfaces.* Journal of Colloid and Interface Science, 1994. **166**(2): p. 333-342.
58. Cieśla, M., Z. Adamczyk, J. Barbasz, and M. Wasilewska, *Mechanisms of Fibrinogen Adsorption at Solid Substrates at Lower pH.* Langmuir, 2013. **29**(23): p. 7005-7016.
59. Adamczyk, Z., J. Barbasz, and M. Cieśla, *Kinetics of Fibrinogen Adsorption on Hydrophilic Substrates.* Langmuir, 2010. **26**(14): p. 11934-11945.
60. Herzinger, C.M., B. Johs, W.A. McGahan, J.A. Woollam, and W. Paulson, *Ellipsometric determination of optical constants for silicon and thermally grown silicon dioxide via a multi-sample, multi-wavelength, multi-angle investigation.* Journal of Applied Physics, 1998. **83**(6): p. 3323-3336.
61. Behan, J.A., S.N. Stamatin, M.K. Hoque, G. Ciapetti, F. Zen, L. Esteban-Tejeda, and P.E. Colavita, *Combined Optoelectronic and Electrochemical Study of*

Nitrogenated Carbon Electrodes. The Journal of Physical Chemistry C, 2017. **121**(12): p. 6596-6604.

62. Socrates, G., *Infrared and Raman Characteristic Group Frequencies: Tables and Charts*. 2001: John Wiley & Sons.
63. Brooksby, P.A. and A.J. Downard, *Electrochemical and Atomic Force Microscopy Study of Carbon Surface Modification via Diazonium Reduction in Aqueous and Acetonitrile Solutions.* Langmuir, 2004. **20**(12): p. 5038-5045.
64. Anariba, F., S.H. DuVall, and R.L. McCreery, *Mono- and Multilayer Formation by Diazonium Reduction on Carbon Surfaces Monitored with Atomic Force Microscopy "Scratching".* Analytical Chemistry, 2003. **75**(15): p. 3837-3844.

6 Comparative *in-situ* Study of Protein Adsorption at Bare and Glycan Grafted Carbon Surfaces

In Chapter 4, ex-situ results showed that carbohydrate coatings are able to prevent unspecific protein adsorption at amorphous carbon surfaces. Herein we investigate the dynamic of albumin adsorption at bare and disaccharide modified carbon films using a combination of optical and acoustic sensing methods, consisting of nanoplasmonic sensing (NPS) and quartz crystal microbalance (QCM) measurements, respectively. In-situ results show a decrease of albumin adsorption at glycan coated surfaces with respect to bare carbon, confirming previous determinations. The relative and absolute amount of albumin adsorbed are found to be dependent on the roughness of the sensor chips. Moreover, QCM experiments indicate that protein conformation at carbohydrate layers likely differs from that at bare carbon. Finally this study emphasises the complementarity of NPS and QCM techniques, due to their differing abilities in measuring the optical mass ("dry" protein mass) and the acoustic mass (protein and coupled water mass) adsorbed at the sensors respectively.

The results presented in this chapter were obtained thanks to the collaborations with Insplorion AB for the NPS measurements and with Prof. Maria Santos-Martínez for the QCM-D measurements, which involved instrumentation loan and initial training on the use of the instruments. I carried out all the *in-situ* experiments. The electrochemist determination of the roughness of the quartz crystal electrodes was carried out by Khairul Hoque.

6.1 Introduction

Adsorption of proteins at solid surfaces is a fundamental phenomenon of extreme interest for the research community and numerous reviews and articles have been already published on the topic [1-3]. The protein-solid interaction is a crucial aspect for many applications; from the rational design of biomaterial for implants and medical devices, to the development of biological technologies, such as biosensors and biochips, and the research on antifouling surfaces in industry and marine environments [4, 5]. The adsorption of protein, in fact, occurs immediately after the introduction of any artificial material to any *in vivo* or *in vitro* biological environment [6, 7]. Thus the following interaction with cells, tissues and microorganisms are, in first instance, mediated by this adsorbed protein film. Protein aggregation, retention and structural conformation synergistically interact to promote and control biological response of biomaterials [7]. However, protein adsorption is only rudimentarily understood at the molecular level, in spite of the overwhelming amount of related studies [4]. Further progression in the comprehension of protein interactions at solid-liquid interfaces is strictly dependent on the reliability and the accuracy of the experimental method adopted. A large number of techniques based on various principles (*i.e.* optical absorption, refractive index changes, fluorescence, electromechanical microbalance, *etc.*) have been applied and are still widely used for the investigation of protein adsorption events [4]. Only few of these surface analytical techniques, however, are able to monitor dynamic interactions within a fluid environment to model likely conditions encountered *in vivo* [8]. Moreover it is necessary to obtain a broad and comparable set of data from different techniques following common protocols [4].

In this chapter we are presenting a comparative study of albumin adsorption at bare and carbohydrate coated carbon surfaces, using three *in-situ* methods: Nanoplasmonic sensing (NPS), quartz crystal microbalance (QCM) with impedance analysis and quartz crystal microbalance with dissipation (QCM-D). The first one is an optical technique based on the phenomenon of localised surface plasmon resonance (LSPR) that, together with surface plasmon resonance (SPR), it extensively used for the analysis of biological interactions at solid surfaces [8-11]. The sensing part consists in an array of gold nano-disks [12], sensitive to

changes in the refractive index close to the substrate, which occurs due to a difference between the refractive index of the adsorbed material and the bulk liquid; this technique was covered in detail in chapters 2 and 5. The other two techniques are thickness shear mode (TMS) resonators, which measure the resonance frequency of the piezoelectric acoustic wave at a quartz crystal. Quartz crystal microbalance (QCM) methods have been widely used to study the adsorption of proteins and other biological materials at different solid surfaces [5, 7, 13-20]. In QCM measurements the frequency shift (Δf) is correlated with the mass adsorbed (Δm) at the quartz crystal according to the Sauerbrey equation [21]:

$$\Delta m = -\frac{C}{n}\Delta f, \tag{6.1}$$

where C is a constant that depends on the thickness and the intrinsic properties of the quartz crystal and n is the frequency overtone number (n = 1, 3, 5…). However this relation is valid only when a rigid mass adsorbs at the quartz surface, with no slip or deformation due to the oscillatory motion. In the case of softer adsorbed layers, the dissipation contribution to the resonant frequency can be estimated by impedance analysis or free oscillation decay measurements (for QCM-D instruments [22]). Chapter 2, section 2.3.3, covers the fundamentals of QCM techniques.

In this study the dynamic interactions of bovine serum albumin (BSA) at amorphous carbon (a-C) surfaces was investigated. As reported in the Introduction, a-C is extremely interesting for biomedical applications and it is currently used as protective and biocompatible coating for prosthetics and implantable devices. Albumin, instead, is a plasma protein very relevant for biocompatibility studies. The adsorption of BSA at a-C surfaces was controlled *via* grafting of disaccharides using the aryldiazonium chemistry. As shown in our previous work [23], the carbohydrate layer is able to reduce the protein adsorption at carbon surfaces. In this chapter we used a combination of NPS and QCM *in-situ* methods in order to understand the role of the disaccharide layer in the dynamics of BSA adsorption at a-C films.

6.2 Experimental

Chemicals and Materials. Ethylene glycol (99.8%), hydrogen peroxide (30%), fluoroboric acid (48 wt.% in H_2O), sodium nitrite (≥99.0%), acetonitrile (HPLC grade), ammonia solution (ca. 35%), methanol (semiconductor grade), Bovine serum albumin (BSA, ≥96%), Fibrinogen from bovine plasma (Fib, 65–85% protein) and phosphate saline buffer tablets (PBS, 0.01 M, 0.0027 KCl M and 0.137 NaCl M pH 7.4) were purchased from Sigma and used without further purification. NPS sensor chips were purchased from Insplorion AB. Gold coated slides were purchases from EMF Corporation. MicroChemicals and 10 MHz quartz crystals were purchased from International Crystal Manufacturing. 5 MHz quartz crystals (QSX 301 Gold) were purchase from Q-Sense AB. Millipore water was used for all experiments. Precursors 4-aminophenol-β-D-lactopyranose (Lac) (see Scheme 1) were synthesized as previously reported in Chapter 4 (page 81).

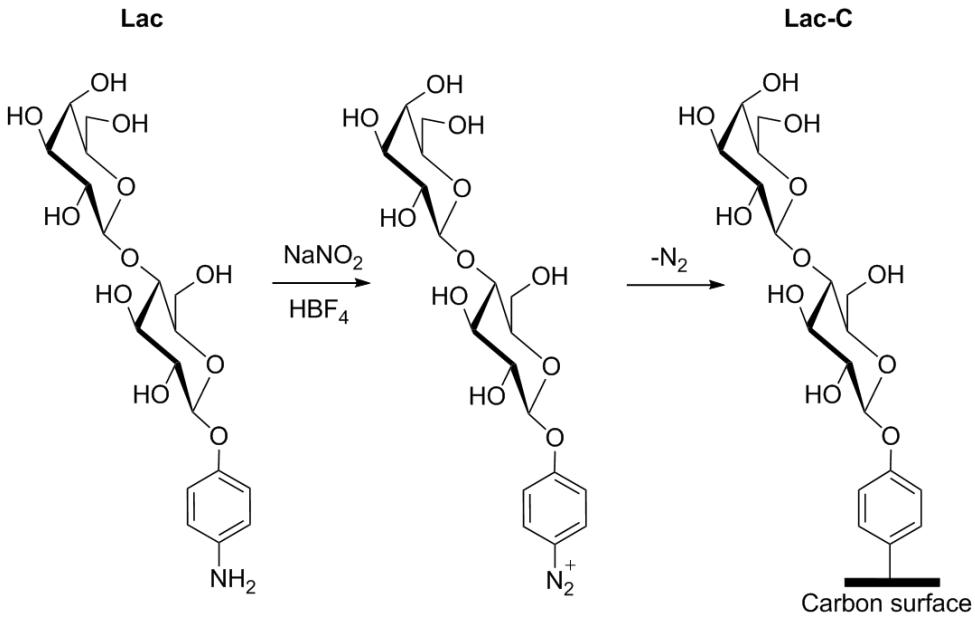

Scheme 6.1. Lac modification reaction at carbon surfaces via *in-situ* generation of aryldiazonium salts.

Substrate Preparation. Amorphous carbon films (a-C) were prepared *via* DC magnetron sputtering (Torr International, Inc.) at a base pressure ≤ 2×10^{-6} mbar and a deposition Ar pressure of 7×10^{-3} mbar, as described in the previous

chapters. For X-ray photoelectron spectroscopy (XPS) characterization, samples were deposited on clean NPS sensor chips or gold coated slides. NPS sensors were cleaned under UV/ozone for 1 h, rinsed with methanol and dried with argon, prior to deposition of a 10 nm thick a-C layer, as described in Chapter 5 (page 107). For QCM measurements, quartz crystals were coated *via* DC magnetron spattering with a 10 nm thick Ti layer (to improve the adhesion of a-C), followed by a 50 nm carbon film. Gold slides and 10 MHz crystals (International Crystal Manufacturing) were cleaned in piranha solution prior to deposition (H_2SO_4 : H_2O_2 in a 3:1 ratio – *WARNING: Piranha solution is a strong oxidant and reacts violently with organic materials and presents an explosion danger; all work should be performed under a fume hood*). 5 MHz crystals (QSX-301, Q-Sense) were cleaned prior to deposition under UV/ozone for 10 min., then immersed in 5:1:1 mixture of water, ammonia and hydrogen peroxide for 5 min. at 75 ^{0}C, rinsed with methanol, dried with argon and finally treated for other 10 min. under the UV lamp, according to the supplier specifications to avoid crystal damage and potential frequency instability.

Surface modification with carbohydrate moieties was carried out as previously reported [25], and following a protocol summarized in Scheme 1. Briefly, Lac precourse were dissolved in acid; while keeping the solution in an ice bath, $NaNO_2$ was added yielding the corresponding aryldiazonium salt *in-situ* at a final concentration of 1.0 mM. Carbon samples were immersed in the aryldiazonium salt solution for 1 h, rinsed in acetonitrile and methanol and dried under argon prior to further use. Lac grafting at a-C substrates yielded surfaces from here onwards referred to Lac-C.

Nanoplasmonic sensing (NPS). Indirect nanoplasmonic sensing (INPS) measurements of protein adsorption were conducted using an XNano instrument (Insplorion AB, Gothenburg, Sweden), as reported in Chapter 5, page 108. Ensemble-averaged recordings of the plasmonic resonance peak were collected in optical transmission mode. Glass sensor chips (Insplorion AB) with deposited gold nanodisks (50 nm radius, 20 nm thickness, 8% surface coverage) fabricated by hole-mask colloidal lithography, were coated with sputter-deposited a-C layers as described above and mounted in an optical flow cell for *in-situ* measurements. Sample solutions were flowed through the measurement chamber via peristaltic

pump at a continuous rate of 50 μL min^{-1}; BSA concentration was 7 μM, equivalent to 0.5 mg mL^{-1}. The bulk refractive index of reference ethylene glycol/water solutions used for calibrations was determined using a refractometer (PAL-1, ATAGO Co., Tokyo, Japan). X-ray photoelectron spectroscopy (XPS) was used to check that a-C and Lac-C layers were continuous on NPS sensors. XPS characterization was performed on a VG Scientific ESCAlab Mk II system (<2 ×10-8 mbar) with an Al Kα X-rays (1486.6 eV) source at 90° take off angle. Wide survey spectra were collected at 50 eV pass energy.analysed using a commercial software (CasaXPS™) (see Chapter 2, page 37).

Quartz crystal microbalance (QCM). Two types of setup were used for *in-situ* QCM measurements of protein adsorption at surfaces. The first one consists of an impedance-scanning EQCM (Gamry Instruments) and a static Teflon reaction cell; the EQCM was effectively used as a stand-alone QCM instrument and was not connected to a potentiostat. The 10 MHz crystal was clamped in the static cell with O-rings on both sides, resulting in only one face being immersed in the liquid with a geometric area of 0.205 cm^2. The cell was placed inside a home-built temperature-controlled box equipped with Peltier cooling units that maintained temperature at 20 ± 0.5 ^{0}C. The box also served as a Faraday cage in order to minimize electrical noise. PBS solution was then injected into the cell to a volume of 4.2 mL. Once the system had reached frequency stability to ≤1 Hz (approximately 3-4 h), the contents of the cell were stirred for 30 s and, immediately afterwards, 50 μL of BSA stock solution were injected to reach the final concentration of 0.5 mg mL^{-1} in the reaction cell. The above method was adopted in order to ensure mixing and minimize temperature and viscosity changes introduced by solution injections [26, 27]. Control tests carried out with only stirring or with 50 μL PBS injections showed that this procedure preserves the frequency stability of the QCM crystal. The instrument measures the series (f_s) and the parallel (f_p) resonance frequencies (see Chapter 2 for physical meaning) in real time using the acquisition Gamry Resonator software. The frequencies were recorded continuously after injection in order to monitor adsorption processes.

Dynamic QCM measurements of protein adsorption at carbon surfaces were carried out using a Q-Sense® E4 QCM-D system (Q-Sense AB, Vastra Frolunda,

Sweden). These measurements were carried out in collaboration with Prof. María J. Santos-Martínez from the School of Pharmacy. This second setup has four temperature and flow-controlled modules assembled in parallel configuration. The 5 MHz quartz crystals were mounted in the flow cells and perfused using a peristaltic microflow system (ISM 935; Ismatec SA, Glattbrugg, Switzerland). Sample solutions were flowed through the measuremnt chambers at a continuous rate of 50 μL min^{-1}; BSA solution was used at the concentration of 0.5 mg mL^{-1}. Resonance frequency (*f*) and dissipation (*D*) was monitored in real time by acquisition Q-Sense software (QSoft401).

6.3 Results

Carbon coatings used in our experiments were deposited *via* magnetron sputtering as previously described; these films had previously been characterized via a combination of spectroscopic methods [28]. Briefly, a-C films consist of approximately 80% trigonally bonded carbon (sp^2 centres) and a 7-9% oxygen content, as estimated *via* XPS and Raman spectroscopy. Modification of a-C with aryldiazonium salts was carried out as in Chapter 4 and our previous work. [23, 24], yielding Lac-functionalized surfaces, which are referred to as Lac-C. Bare and modified carbon coatings were used for *in-situ* studies of protein adsorption using a combination of NPS and QCM techniques.

6.3.1 NPS measurements

NPS methods were used for *in-situ* dynamic measurements of protein adsorption at a-C and Lac-C surfaces. a-C layers used as coating for NPS sensors were confirmed to be continuous at the thickness of (10.1 ± 0.5) nm (see Chapter 5). To test the uniformity of thin carbon coatings after sugar functionalization, XPS measurements were carried out at Lac-C samples. Figure 6.1 shows the survey spectra obtained after Lac grafting of 10 nm carbon films at NPS sensors and gold substrates. The spectra show the presence of carbon (284 eV) and oxygen (532 eV) in all of the samples. The low intensity of a doublet at 335 eV and the absence of any additional peaks for the Lac-C coated sensor indicate that the Lac-C film uniformly covers the samples without exposing the underlying metal nanoparticles.

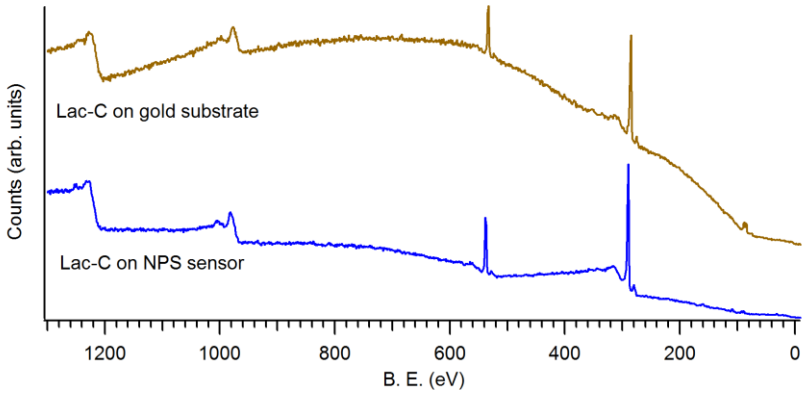

Figure 6.1. XPS survey spectra of Lac-C at gold slides (top) and a NPS sensors (bottom). Both the substrates were coated with 10 nm carbon layers, prior to the Lac-functionalization.

NPS sensors chips consist of a glass substrate with an array of nanofabricated gold nanodisks. Bare and modified coated sensors were mounted in a flow cell and the plasmon absorption, associated with the gold nanodisks, was measured in trasmittance mode. The plasmonic resonance peak is sensitive to the change in refractive index of the medium at the nanodisk interface and the wavelength at the maximum absorption, λ_{max}, was monitored as a function of time during flow experiments.

The complete procedure for each measurement was divided in three parts, as described in Chapter 5: Briefly, (i) all sensors were first calibrated using at least three water/ethylene glycol solutions; (ii) then PBS was injected, followed by the protein solution and a final rinsing step with PBS; (iii) finally, the calibration process was repeated at the end of each experiment to exclude any changes to the sensor sensitivity that might arise from adsorbed protein layers.

For the first calibration step, the sensitivity of each NPS sample was obtained by measuring the shift $\Delta\lambda_{max}$ *vs.* refractive index of the liquid in the flow cell. Figure 6.2a shows typical dependence of $\Delta\lambda_{max}$ as a function of time obtained for a-C and Lac-C sensors, as water/ethylene glycol solutions of different refractive index are injected into the cell. These results indicate that the LSPR at the nanodisk is sensitive to changes at the coating/solution interface. The staircase response was used to generate a calibration plot as shown in Figure 6.2b, which shows that the $\Delta\lambda_{max}$ varies linearly with refractive index. The slopes obtained for the two representative samples of a-C and Lac-C (123 nm and 117 nm per unit change in

refractive index, respectively) were very similar, indicating that the carbohydrate layer affects only slightly the sensitivity of coated sensors.

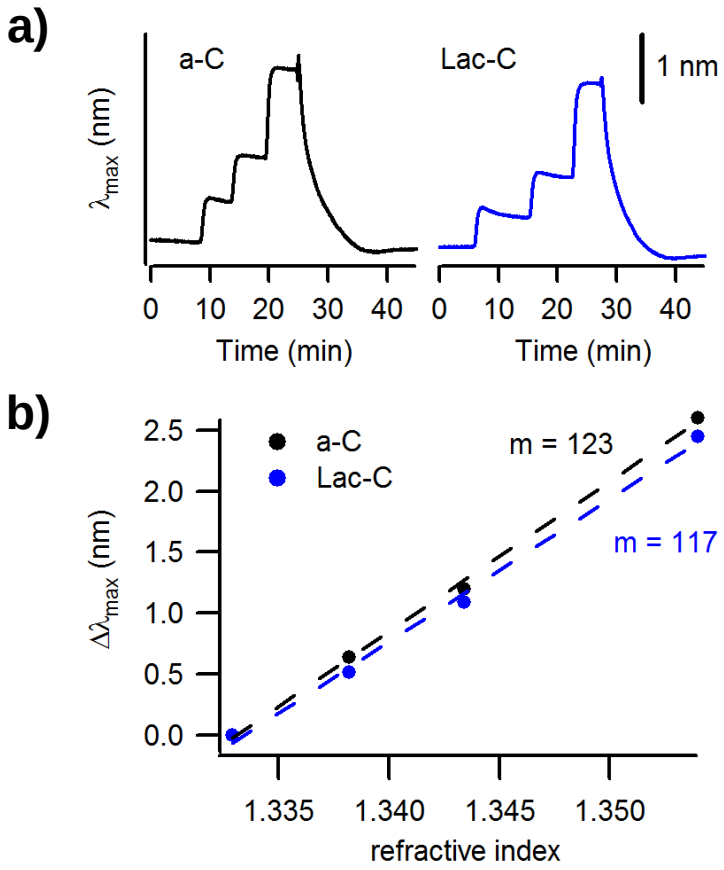

Figure 6.2. Sensitivity test obtained at a-C (black) and Lac-C (blue) sensors. (a) LSPR shift $\Delta\lambda_{max}$ as a function of time measured after water/ethylene glycol solutions of different refractive index are injected into the cell. (b) Calibration plot of measured $\Delta\lambda_{max}$ vs. refractive index of the water/ethylene glycol solution; the slope yielding the analytical sensitivity is reported next to the corresponding curve.

In order to evaluate how glycan coatings affect the carbon-protein interactions at the interface, both bare and modified carbon coated sensors were exposed to buffered BSA solutions. Figure 6.3a and b show plots of $\Delta\lambda_{max}$ *vs.* time obtained on a-C and Lac-C sensors, respectively, after the injection of BSA solutions followed by injection of PBS. The exposure of NPS sensors to the protein solution results in a red shift of the LSPR that stabilizes to a constant value within 15 min after the injection. Given that the refractive index of the protein solutions was statistically indistinguishable from that of the PBS solution (see Chapter 5, Table 6.1), the wavelength shift can be unequivocally attributed to the adsorption

of proteins at the surface. Based on the same assumption, the absence of any significant change in the LSPR peak position after injection of protein-free buffer solution indicates that BSA adsorption is irreversible at both a-C and Lac-C surfaces.

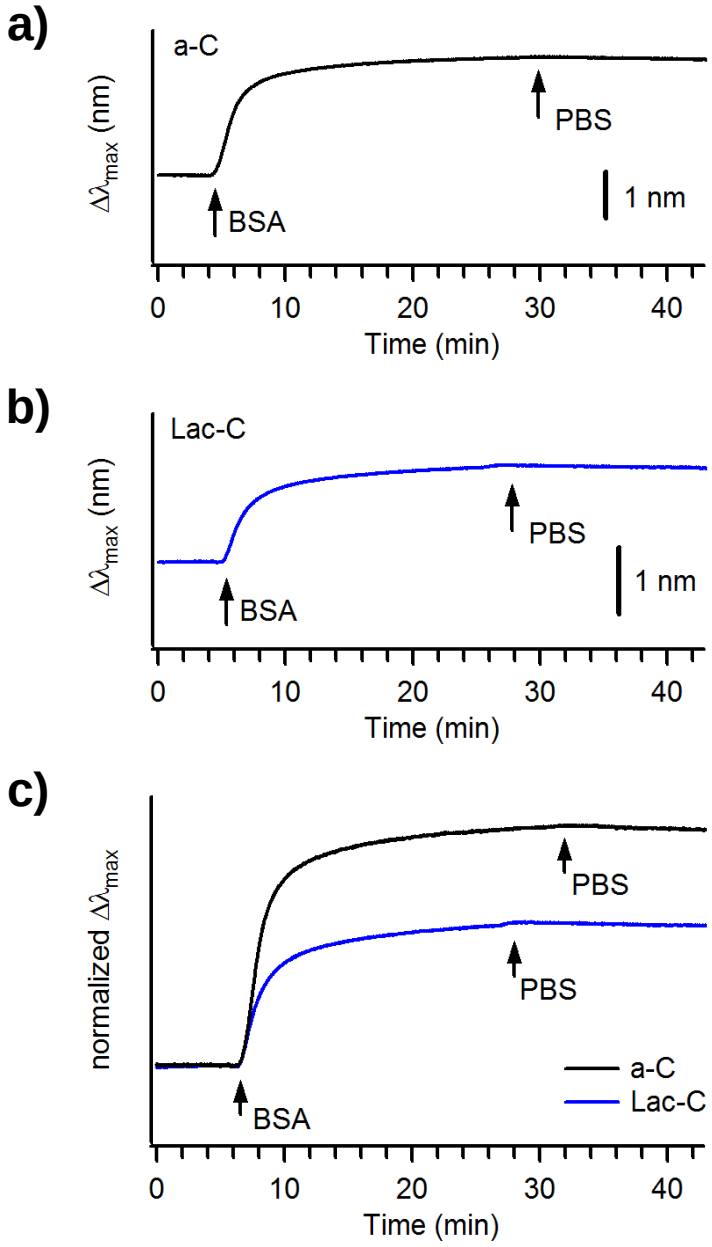

Figure 6.3. LSPR wavelength shift, $\Delta\lambda_{max}$, as a function of time, measured at (a) a-C and (b) Lac-C coated sensors for in-situ protein experiments. (c) Normalized $\Delta\lambda_{max}$ as a function of time calculated using the initial calibration of the sensor at both a-C (black line) and Lac-C (blue line) surfaces. The arrows indicate the time of the injection of BSA and PBS solutions into the flow cell.

For a comparison between different samples, the raw signal must be normalized by the experimental sensitivity, which varies slightly from sensor to sensor due to differences in setup alignment or in the coating optical properties. The NPS signal of each sensor was thus normalized using the slope of the calibration plot carried out as the first step in each experimental run, as reported in Chapter 5. Figure 6.3c shows the normalized $\Delta \lambda_{max}$ *vs.* time calculated as $\Delta \lambda_{max}/A$, where A is the slope obtained from the initial calibration of the sensor. Normalized results in the graph show that the resonant shift is significantly lower at Lac-C than at a-C surfaces, thus indicating that the disaccharide layer is able to prevent protein adsorption at carbon surfaces, as observed in our previous studies using *ex-situ* methods [23]. Over a range of at least three measurements, Lac-modification led to a 42% decrease of BSA adsorption at carbon surfaces, as reported in Table 6.1 (relative BSA adsorption = 58%). Finally, the similar shape of the two curves showed in Figure 6.3c suggests that the kinetic of protein adsorption at bare and modified carbon surfaces is very similar. Further discussions arising from the comparison with other techniques are reported is Section 6.4.

Table 6.1. Summary of LSPR results obtained at a-C and Lac-C samples: normalized $\Delta\lambda_{max}$ are measured after 15 min from the injection of the BSA solution; relative BSA adsorption at Lac-C was calculated with respect to wavelength shift measured at a-C. Errors reported are C.I. 95%.

Surface	Normalized $\Delta\lambda_{max}$ ($x10^{-3}$)	Relative BSA adsorption
a-C	20 ± 5	-
Lac-C	12 ± 3	58%

6.3.2 QCM measurements

The adsorption of BSA at bare and modified carbon surfaces was investigated using a second *in-situ* technique, based on thickness shear module (TSM) resonators. Two QCM instruments were used with different setups as described in the experimental section.

The first method reported is an EQCM interfaced to a static reaction cell, where carbon coated quartz crystals are mounted. The reaction cell is then filled with buffered solution and the impedance spectrum over the range of ~20 kHz centred at the QCM resonance frequency is monitored in real time. The acquisition software records the frequencies at the minimum (f_s) and the maximum (f_p) of the impedance spectrum, which are the series and the parallel resonance frequencies, respectively. Changes of f_s and f_p are correlated with the amount of mass adsorbed at the crystal surfaces and to the energy dissipative contribution, which is expressed by the quality factor Q (see Chapter 2). Figure 6.4a reports the shift in the series resonance frequency Δf_s as a function of time after the injection of BSA, for a-C and Lac-C coated quartz crystals. As shown in the graph, the exposure of the samples to the protein solution results in a decrease of the f_s that is associated with BSA adsorption at the carbon surfaces. For both the a-C and Lac-C, a Δf_s of ~350 Hz was recorded immediately after the injection of BSA. However, whereas for the bare carbon surface the f_s remains roughly constant for the following 60-70 min, in the case of the Lac-modified surfaces, the resonance frequency increases again by ~150 Hz within 15 min. To check if this frequency rise is accompanied by changes in the rigidity and packaging of the protein layer at the carbohydrate coating, a simplified expression of the quality factor was obtain from the relationship:

$$Q_r = \frac{f_s + f_p}{2(f_p - f_s)} \tag{6.2}$$

where Q_r is known as reduced quality factor and provides only a relative estimation of the energy dissipated during the oscillation of the quartz crystal. Thus Q_r was not used as an absolute parameter, but rather for the comparison of measurements carried out with the EQCM setup. The percentage quality factor ($\%Q_r$) versus time is plotted in Figure 6.4b for both the surfaces. In the case of a-C, the $\%Q_r$ drops to a value of ~97% after the BSA injection and it remains constant for the rest of the experiment, similarly to the trend observed for the resonance frequency. Differently for Lac-C, the $\%Q_r$ falls quickly to 95% and gradually increases, reaching the value measured at the a-C sample. This behaviour indicates a higher dissipative contribution for Lac-C surfaces at the initial stage of protein adsorption. We speculated that BSA at carbohydrate layers undergoes

conformational changes, which results in the displacement/desorption of albumin molecules (associated with an increase of f_s) and an increment of the protein layer rigidity (correlated with higher Q_r). Notably, the $\%Q_r$s measured for the two samples reach the same value at the end of the experiment, allowing a direct comparison of the amount of BSA adsorbed at a-C and Lac-C surfaces. Assuming similar dissipative contributions, relative BSA adsorption at carbohydrate layers was calculated with respect to the bare carbon. Results obtained over a range of at least three measurements show a reduction of 46% of the BSA adsorbed at Lac-C surfaces compared to a-C (see Table 6.2).

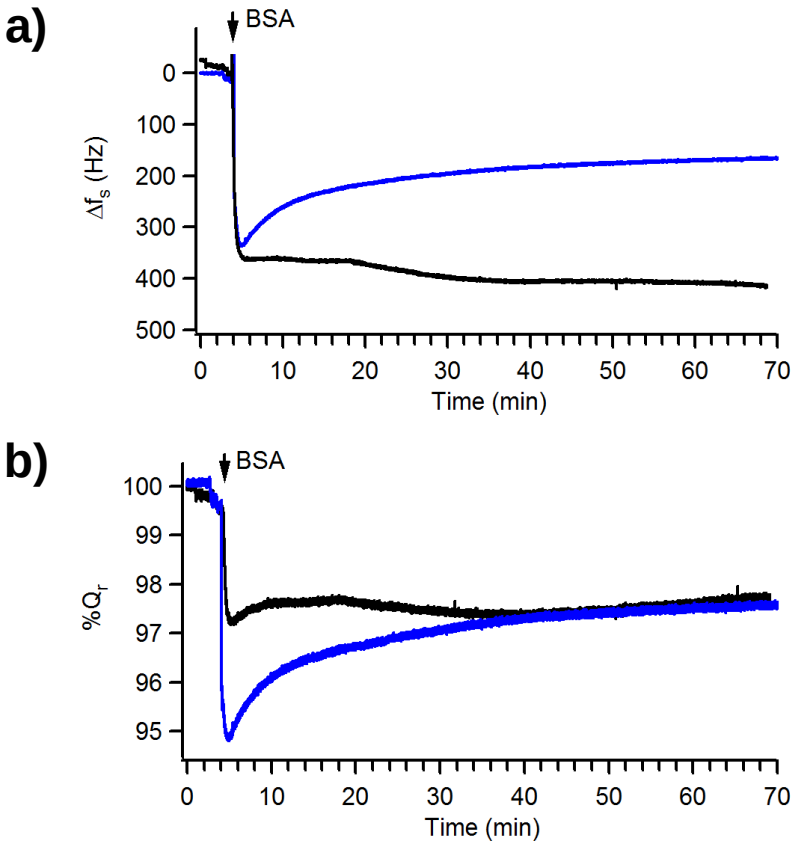

Figure 6.4. Impedance QCM protein experiment obtained for two representative samples of a-C and Lac-C coated crystals. (a) Δf_s and (b) $\%Q_r$ are reported as function of time for both a-C (black line) and Lac-C (blue line) surfaces. The arrows indicate the time of the injection of the BSA stock solution in the static cell.

Table 6.2. Summary of impedance QCM results obtained at a-C and Lac-C surfaces: frequency shift Δf_s and percent variation of the reduced quality factor measured at time = 60min with respect to the initial resonance frequency at time = 0 min; percentage variation of Q_r at the initial stage, $\%Q_r$(in), and measured after 60 min, $\%Q_r$(fin); mass of adsorbed BSA Δm_{ads} calculated from the Sauerbrey equation relative BSA adsorption was calculated with respect to the Δf_s measured at bare a-C. Errors reported are C.I. 95%.

Surface	Δf_s (Hz)	$\%Q_r$(in)	$\%Q_r$(fin)	Δm_{ads} (μg cm^{-2})	Relative BSA adsorption
a-C	520 ± 250	96 ± 4	96.9 ± 2.7	2.3 ± 1.1	-
Lac-C	280 ± 170	95.3 ± 1.3	97.4 ± 0.3	1.3 ± 0.7	54%

In the second setup, a QCM-D instrument was used to carry out dynamic experiments of BSA adsorption at a-C and Lac-C surfaces. With this technique the resonance frequency *f* and the time of free oscillation decay of the quartz crystal is recorded in real time. The decay time, indicative of the energy dissipated during the oscillation, is expressed as the dissipation factor *D*, which is equivalent to the inverse of the quality factor $Q = 1/D$ [13] (see Chapter 2). Bare and Lac-modified carbon-coated crystals were mounted in the flow chamber and perfused with PBS at the constant flow until stabilization of the *f* and *D* signals. The samples were then exposed to BSA solution at the same flow rate for another 30 min. At this time, the peristaltic pump was stopped to observe the D-QCM response in the static regime. The pump was switched on again after 20 min to let the protein solution flow for 10 min, before the final injection of PBS. The results obtained for a-C and Lac-C surfaces are shown in Figure 6.5a and b, respectively: resonant frequency (*f*) and dissipation (*D*) from the third overtone are plotted versus time. For both bare and modified coating we observe a drop of *f*, accompanied by an increase of *D*, after the injection of protein solution. The two signals stabilize after few minutes and they maintain constant values for the following 50-60 min with no appreciable effect due to the static regime. The injection of PBS causes a small increment of *f* and decrease of *D*, which are more evident in the case of Lac-C. The dissipation shifts measured at both the surfaces were very low, as observed for

small globular proteins (*i.e*. albumin) in other studies [4, 5]. Therefore we can use the Sauerbrey equation for deriving the amount of protein adsorbed at the coated crystals, assuming that the dissipation contribution is not affecting the frequency shift. In Figure 6.5c, the adsorbed mass calculated using the Sauerbrey equation for the third overtone is plotted versus time. As shown in the graph, BSA adsorbs less at Lac-C surfaces compared to a-C, confirming previous results. The mass decrease at the injection of the PBS suggests that a small amount of BSA desorbs from the surface. This effect is observed in particular in the case of Lac-C, indicating that the carbohydrate layer might favour reversible BSA adsorption. The mass change recorded at the adsorption and desorption of BSA during the experiment is reported in Table 6.3. Results repeated in duplicates shows that carbohydrate layers can reduce BSA adsorption by ~69% compared to bare a-C (see Table 6.3). These values are significantly higher than those reported above for the other two *in-situ* techniques, but similar to *ex-situ* results obtained in previous work [23]. A comparison between the three methods used is reported in the next section.

Table 6.3. Summary of QCM-D results obtained at a-C and Lac-C surfaces: frequency shift Δf and dissipation D measured after injection of BSA; mass of BSA adsorbed Δm_{ads} and desorbed Δm_{des} calculated from the Sauerbrey equation; relative BSA adsorption calculated with respect to the bare a-C. The results obtained in duplicates are reported as (value from exp.1) – (value from exp. 2).

Surface	Δf (Hz)	D (1E-6)	Δm_{ads} (ng cm^{-2})	Δm_{des} (ng cm^{-2})	Relative BSA adsorption
a-C	42 – 47	2.0 – 3.5	745 – 820	6 – 0	-
Lac-C	9 – 18	1.0 – 1.1	165 - 315	20 – 16	31%

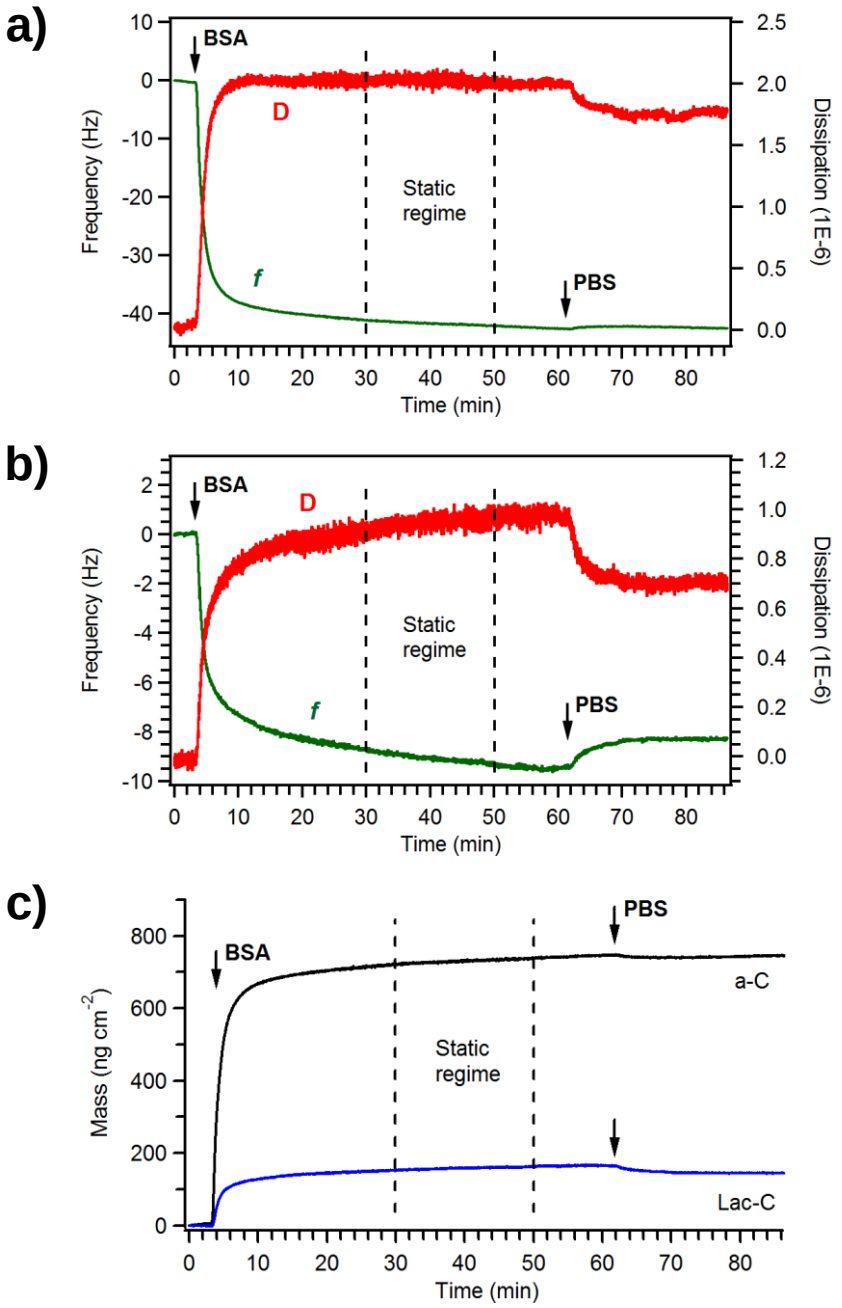

Figure 6.5. QCM-D frequency *f* (green line) and dissipation *D* (red line) shifts from the third overtone measured at (a) a-C and (b) Lac-C surfaces for in-situ protein experiments. (c) Adsorbed mass *Δm* as a function of time, calculated using the Sauerbrey equation, at both a-C (black line) and Lac-C (blue line) surfaces. The arrows indicate the time of the injection of BSA and PBS solutions into the flow cell, whereas the dotted lines delimited the time when the instrument was measuring in static conditions.

6.4 Discussion

In this section we present a comparison among the three *in-situ* methods used for the study of BSA adsorption at bare and Lac-modified carbon surfaces. Table 6.4 shows a summary of the main outputs obtained from the different techniques. In addition, the *ex-situ* results obtained under similar conditions in a previous work [23] are also reported in the table. The most obvious information that we can deduce from these studies is the relative adsorption of BSA at Lac-C surfaces compared to the bare a-C. According to our previous works [23-25], carbohydrate coatings are able to prevent protein fouling at carbon surfaces. These observations are confirmed here *via in-situ* measurements, which show a decrease of adsorbed BSA at Lac-modified surfaces: relative BSA adsorption of 58% and 54% were found using NPS and impedance QCM methods, respectively, while a lower 31% was obtained *via* QCM-D determinations. These values are considerably higher than *ex-situ* results, however differences are to be expected as the samples transition from wet/*in-situ* to dry/*ex-situ* conditions. The reason behind the differences among *in-situ* determinationsare not yet fully understood. In the case of impedance QCM under static conditions, the reproducibility of the mixing process may be an issue; the errors reported for the frequency shift are, in fact, roughly 50% of the averaged values. Such a high variability in the results can be a consequence of the challenges involved in accurately mixing the BSA stock solution with the PBS solution in the static cell; this would result in a protein concentration gradient in the static cell that increases the complexity of the interpretation. We speculated that differences in the local concentration of BSA in the surroundings of the quartz crystal might alter adsorption events and/or result in variation of the solution viscosity, which ultimately affect the QCM response.

A possible explanation for the diversity of the relative BSA adsorption observed in the *in-situ* results is the topography variability among the substrates used in the three techniques. Roughness measurements of the QCM gold electrodes were carried out electrochemically, yielding ratio values of microscopic area to geometric area equivalent to 1.2 and 7.2 in the case of QCM-D and impedance QCM, respectively. NPS samples are relatively rough due to the 20x100 nm disks as topographic features. These values of roughness correlate well with the enhanced Lac antifouling effect observed for smooth QCM-D sensor chips,

while carbohydrate coatings appear to be less effective in preventing BSA adsorption for rough surfaces, as in the case of impedance QCM and NPS measurements.

The surface finish influences also the absolute values of protein adsorption: proteins are likely to adsorb more at rougher substrates due to the higher microscopic area exposed. Moreover, the liquid trapped in surface cavities results in an additional mass component, which is detected by QCM measurements. These contributions account for the difference of the absolute value of BSA adsorption calculated using the Sauerbrey equation (see Table 6.2 and Table 6.3). The Δm_{ads} obtained *via* impedance QCM measurements were found to be higher by a factor of 3 than QCM-D results, in agreement with roughness determinations at quartz crystals.

Table 6.4. Comparison of main observation deduced from the analysis of BSA adsorption at a-C and Lac-C surfaces using different *in-situ* and *ex-situ* methods. Results from *ex-situ* measurements were taken from a previous work [23].

Properties/behaviour observed	*in-situ*			*ex-situ*	
	NPS	**EQCM**	**QCM-D**	**IRRAS**	**QCM**
Relative BSA adsorption (Lac-C/a-C)	58%	54%	31%	16%	10%
Rate of BSA desorption at PBS perfusion	No desorption	-	<1% (a-C) ~10%(Lac-C)	-	-
Viscoelastic properties of BSA layer	-	Relative determination from Q_r	Absolute deamination from D	-	-

NPS and QCM-D experiments both consist in a dynamic flow setup, which permits the analysis of adsorption/desorption events upon injection of a full cell volume of the buffered solution into the sample compartment. As reported in Table 6.3 and Table 6.4, QCM-D measurements show very little BSA desorption at

a-C surfaces, whereas roughly 10% of the protein adsorbed at the Lac-C is removed after PBS injection. This indicates that BSA layers formed at the carbohydrate coating can be partially removed by rinsing with PBS, which may also explain why relative BSA adsorption values at Lac-C were smaller in *ex-situ* determinations. On the other hand, NPS results do not show any desorption after the injection of PBS, which may be due to limitations in the sensitivity of the instrument.

Finally, qualitative considerations on the viscoelastic properties of the protein adsorbed layer can be deduced from QCM-D analysis. We already saw that very small dissipation was measured for the BSA adsorption at both a-C and Lac-C. However, an alternative presentation of the QCM data is reported in Figure 6.6, where the dissipation is plotted versus the change in frequency. In this form we eliminate the time as an explicit parameter, but we are able to compare directly the D/f ratio, which is the induced energy dissipation per coupled unit mass [15]. The D/f ratio expresses the influence of the protein adsorption on the viscoelastic damping of the crystals resonance and thus infer viscoelastic properties of the adsorbed layer [15]. For instance, it was already observed that low D/f value indicates mass addition without significant dissipation increase, characteristic of a fairly rigid layer; while a large D/f value signals a soft, dissipative film [5, 7, 15]. From Figure 6.6, we observe higher values of D/f ratio for Lac-C, which indicates the formation of a softer and less packed BSA layer. This is in good agreement with impedance QCM analysis results, which show a higher variation of $\%Q_r$ for Lac-C at the initial stages of protein adsorption (see Figure 6.4b). The formation of a less rigid and compact BSA film at carbohydrate coatings might be at the origin of the antifouling effect observed. As reported by Dolastshahi-Pirouz [17], QCM measurements are affected also by the contribution of water molecules coupled to the protein film. The high D/f ratio obtained at Lac-C surfaces suggests the presence of trapped water at the carbohydrate-protein layer, which is in excellent agreement with the increasing of hydrophilicity at carbon surfaces due to the sugar functionalization, as previously reported [23].

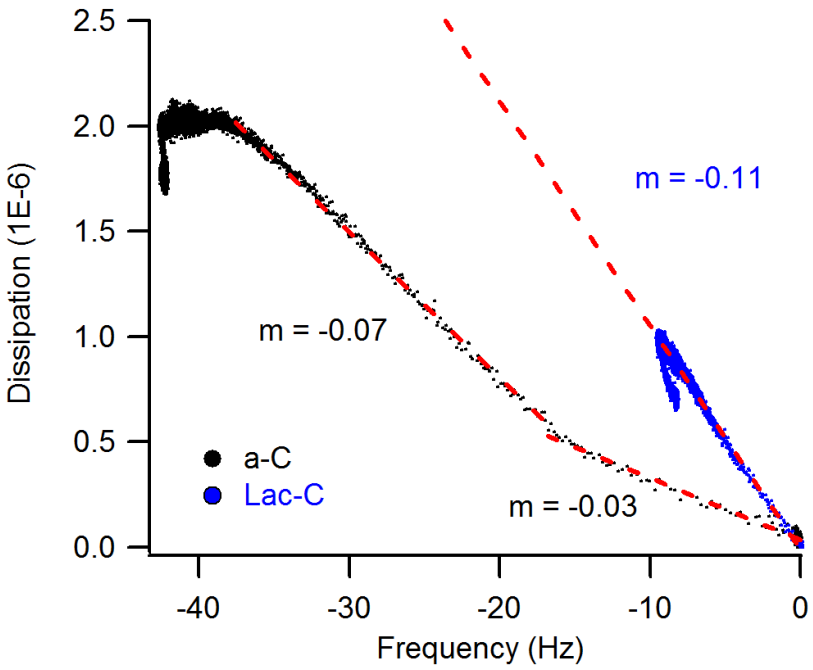

Figure 6.6. Dissipation (D) as function of the resonance frequency shift (Δf) measured during the protein experiment at a-C (black dots) and Lac-C (blue dots) *via* QDM-D measurements. Data points were fitted using linear regression and obtained slope were reported next to the corresponding curve.

6.5 Conclusions

In this chapter we studied the dynamics of BSA adsorption at a-C and Lac-C surfaces using a combinations of NPS and QCM techniques. The *in-situ* results confirmed previous observations [23], which state that carbohydrate coatings are able to prevent protein adsorption at carbon surfaces. The relative BSA adsorption at Lac-C surfaces vs. bare surfaces was found to differ for the three *in situ* methods examined. These deviations are correlated with the topography of the sensor chips: Lac layer shows better antifouling properties in the case of smooth surfaces. The roughness effect was observed also for the absolute values of BSA adsorption obtained from the Sauerbrey equation in QCM measurements: adsorbed mass at quartz crystals with large microscopic area to geometric area ratio were found to be higher than that at smoother surfaces. QCM-D measurements showed differences in the rigidity of protein layers formed at Lac-C and at a-C, suggesting

a possible reason of the antifouling effect observed. Testing other types of proteins (i.e. fibrinogen and lysozyme, which possess different shape, dimension and physical properties) may help in the investigations of conformational changes of protein layers and experimental limitations of the techniques. Qualitative analysis also shows divergences in the results: NPS spectroscopy didn't show any different in the kinetic of BSA adsorption, while both QCM methods indicate a conformational change in the protein layer adsorbed at saccharide coatings. This may be due to the different phenomena observed with the two types of measurements. In fact, while NPS spectroscopy is sensitive only to the "dry" mass of the film, QCM methods measure also the part of the solvent that is coupled to the adsorbed film and thus oscillates along with the sensor crystal [17]. Another difference was observed in BSA desorption after the injection of PBS, which wasn't registered by NPS measurements, perhaps due to the sensitive limit of the technique. In conclusion, this study illustrates some of the advantages and disadvantages as well as the complementarity of NPS and QCM methods.

6.6 References

1. Gray, J.J., *The interaction of proteins with solid surfaces.* Current Opinion in Structural Biology, 2004. **14**(1): p. 110-115.
2. Claesson, P.M., E. Blomberg, J.C. Fröberg, T. Nylander, and T. Arnebrant, *Protein interactions at solid surfaces.* Advances in Colloid and Interface Science, 1995. **57**: p. 161-227.
3. Jones, M.I., I.R. McColl, D.M. Grant, K.G. Parker, and T.L. Parker, *Protein adsorption and platelet attachment and activation, on TiN, TiC, and DLC coatings on titanium for cardiovascular applications.* Journal of Biomedical Materials Research, 2000. **52**(2): p. 413-421.
4. Höök, F., J. Vörös, M. Rodahl, R. Kurrat, P. Böni, J.J. Ramsden, M. Textor, N.D. Spencer, P. Tengvall, J. Gold, and B. Kasemo, *A comparative study of protein adsorption on titanium oxide surfaces using in situ ellipsometry, optical waveguide lightmode spectroscopy, and quartz crystal microbalance/dissipation.* Colloids and Surfaces B: Biointerfaces, 2002. **24**(2): p. 155-170.
5. Dolatshahi-Pirouz, A., K. Rechendorff, M.B. Hovgaard, M. Foss, J. Chevallier, and F. Besenbacher, *Bovine serum albumin adsorption on nano-rough platinum surfaces studied by QCM-D.* Colloids and Surfaces B: Biointerfaces, 2008. **66**(1): p. 53-59.
6. Kasemo, B., *Biological surface science.* Surface Science, 2002. **500**(1-3): p. 656-677.
7. Molino, P.J., M.J. Higgins, P.C. Innis, R.M.I. Kapsa, and G.G. Wallace, *Fibronectin and Bovine Serum Albumin Adsorption and Conformational Dynamics on Inherently Conducting Polymers: A QCM-D Study.* Langmuir, 2012. **28**(22): p. 8433-8445.
8. Green, R.J., R.A. Frazier, K.M. Shakesheff, M.C. Davies, C.J. Roberts, and S.J.B. Tendler, *Surface plasmon resonance analysis of dynamic biological interactions with biomaterials.* Biomaterials, 2000. **21**(18): p. 1823-1835.
9. Green, R.J., J. Davies, M.C. Davies, C.J. Roberts, and S.J.B. Tendler, *Surface plasmon resonance for real time in situ analysis of protein adsorption to polymer surfaces.* Biomaterials, 1997. **18**(5): p. 405-413.
10. Anker, J.N., W.P. Hall, O. Lyandres, N.C. Shah, J. Zhao, and R.P. Van Duyne, *Biosensing with plasmonic nanosensors.* Nat Mater, 2008. **7**(6): p. 442-453.
11. Yonzon, C.R., E. Jeoung, S. Zou, G.C. Schatz, M. Mrksich, and R.P. Van Duyne, *A Comparative Analysis of Localized and Propagating Surface Plasmon Resonance Sensors: The Binding of Concanavalin A to a Monosaccharide Functionalized Self-Assembled Monolayer.* Journal of the American Chemical Society, 2004. **126**(39): p. 12669-12676.
12. Larsson, E.M., C. Langhammer, I. Zorić, and B. Kasemo, *Nanoplasmonic Probes of Catalytic Reactions.* Science, 2009. **326**(5956): p. 1091-1094.
13. Eike, L., H. Alexander, K. Katja, S. Claudia, R. Björn, W. Joachim, P. Bruno, and J. Andreas, *Adhesion of liposomes: a quartz crystal microbalance study.* Measurement Science and Technology, 2003. **14**(11): p. 1865.
14. Esmeryan, K.D., C.E. Castano, M. Abolghasemibizaki, and R. Mohammadi, *An artful method for in-situ assessment of the anti-biofouling potential of*

various functional coatings using a quartz crystal microbalance. Sensors and Actuators B: Chemical, 2017. **243**: p. 910-918.
15. Feiler, A.A., A. Sahlholm, T. Sandberg, and K.D. Caldwell, *Adsorption and viscoelastic properties of fractionated mucin (BSM) and bovine serum albumin (BSA) studied with quartz crystal microbalance (QCM-D).* Journal of Colloid and Interface Science, 2007. **315**(2): p. 475-481.
16. Lord, M.S., D. Pasqui, R. Barbucci, and B.K. Milthorpe, *Protein Adsorption on Derivatives of Hyaluronan.* Macromolecular Symposia, 2008. **266**(1): p. 17-22.
17. Macakova, L., E. Blomberg, and P.M. Claesson, *Effect of Adsorbed Layer Surface Roughness on the QCM-D Response: Focus on Trapped Water.* Langmuir, 2007. **23**(24): p. 12436-12444.
18. Santos-Martinez, M.J., I. Inkielewicz-Stepniak, C. Medina, K. Rahme, D. Arcy, D. Fox, J.D. Holmes, H. Zhang, and M.W. Radomski, *The use of quartz crystal microbalance with dissipation (QCM-D) for studying nanoparticle-induced platelet aggregation.* International Journal of Nanomedicine, 2012. **7**: p. 243-255.
19. Shen, Z., M. Huang, C. Xiao, Y. Zhang, X. Zeng, and P.G. Wang, *Nonlabeled Quartz Crystal Microbalance Biosensor for Bacterial Detection Using Carbohydrate and Lectin Recognitions.* Analytical Chemistry, 2007. **79**(6): p. 2312-2319.
20. Wang, X., G. Herting, I. Odnevall Wallinder, and E. Blomberg, *Adsorption of bovine serum albumin on silver surfaces enhances the release of silver at pH neutral conditions.* Physical Chemistry Chemical Physics, 2015. **17**(28): p. 18524-18534.
21. Sauerbrey, G.Z., *Use of quartz vibration for weighing thin films on a microbalance.* J. Physik, 1959. **155**: p. 206-212.
22. Rodahl, M., F. Höök, A. Krozer, P. Brzezinski, and B. Kasemo, *Quartz crystal microbalance setup for frequency and Q ‐factor measurements in gaseous and liquid environments.* Review of Scientific Instruments, 1995. **66**(7): p. 3924-3930.
23. Zen, F., M.D. Angione, J.A. Behan, R.J. Cullen, T. Duff, J.M. Vasconcelos, E.M. Scanlan, and P.E. Colavita, *Modulation of Protein Fouling and Interfacial Properties at Carbon Surfaces via Immobilization of Glycans Using Aryldiazonium Chemistry.* Scientific Reports, 2016. **6**: p. 24840.
24. Angione, M.D., T. Duff, A.P. Bell, S.N. Stamatin, C. Fay, D. Diamond, E.M. Scanlan, and P.E. Colavita, *Enhanced Antifouling Properties of Carbohydrate Coated Poly(ether sulfone) Membranes.* ACS Applied Materials & Interfaces, 2015. **7**(31): p. 17238-17246.
25. Jayasundara, D.R., T. Duff, M.D. Angione, J. Bourke, D.M. Murphy, E.M. Scanlan, and P.E. Colavita, *Carbohydrate Coatings via Aryldiazonium Chemistry for Surface Biomimicry.* Chemistry of Materials, 2013. **25**(20): p. 4122-4128.
26. Jayasundara, D.R., R.J. Cullen, and P.E. Colavita, *In Situ and Real Time Characterization of Spontaneous Grafting of Aryldiazonium Salts at Carbon Surfaces.* Chemistry of Materials, 2013. **25**(7): p. 1144-1152.
27. Jayasundara, D.R., R.J. Cullen, L. Soldi, and P.E. Colavita, *In Situ Studies of the Adsorption Kinetics of 4-Nitrobenzenediazonium Salt on Gold.* Langmuir, 2011. **27**(21): p. 13029–13036.

28. Cullen, R.J., D. Jayasundara, L. Soldi, J. Cheng, G. Dufaure, and P.E. Colavita, *Spontaneous grafting of nitrophenyl groups on amorphous carbon thin films: A structure-reactivity investigation.* Chemistry of Materials, 2012. **24**(6): p. 1031-1040.

7 Further Work and Preliminary Results

In the previous chapters we explored how proteins adsorb at amorphous carbon surfaces depending on their surface properties. However, for a better understanding of bio-carbon interfacial events, the interaction of other biomolecules at carbon surfaces must be considered. A brief overview of phospholipid adsorption studies, obtained in our group, were summarized here. Further works of this project will include the investigation of competitive adsorption of phospholipids and proteins at amorphous carbon surfaces in relation to carbon surface properties.

In this chapter, some preliminary results obtained by myself and my colleague Joana Vasconcelos are reported. Specifically, Joana Vasconcelos curried out the phospholipids adsorption experiments; I collected the IR spectra of bare surfaces before and after the incubation in protein solutions; finally we both contributed to the competitive adsorption studies of proteins and phospholipids at carbon surfaces.

7.1 The role of phospholipids

The adsorption of proteins at macroscopic surfaces is thought to be one of the first events happening at the surface after implantation of a host material in biological media. It is believed that a protein layer forms a conditioning film that influence further events at the biomaterial interface, such as cell adhesion and tissue interaction [1]. However, as mentioned in the introduction, a straightforward correlation between protein adsorption and carbon bioresponse was not found yet [2-4]. Other biomolecules present in the bodily fluids might play an important role in determining biological response to carbon materials. Lipids are good candidates due to their abundance in the biological environment: the concentration of lipids such as triglycerides and fatty acids is indeed comparable to that of albumin and other proteins in blood plasma (see Table 2 in the Introduction) [5, 6]. Several studies have already pointed out at the importance of lipid interfacial interactions in determining biomaterial performances [7-10] and how lipid corona formation affects protein adsorption [11-14]. However, apart from few reports in literature [15-19], very little is known about lipid adsorption at carbon coatings and how this adsorption can be monitored with control over carbon surface properties. In our group, the interfacial interactions of phospholipid liposomes at amorphous carbon surfaces were investigated in a work carried out by Joana M. Vasconcelos. This class of lipids is usually found in cell membranes as aggregates and covers a principal role as a structural component and for the transport of other lipids [20-22]. One of the simplest model lipid aggregates consists in a vesicle formed by phospholipid bilayer; in this work a mixture of zwitterionic phosphatidylcholine (PC) and anionic phosphatidylserine (PS), called PC/PS liposome, was used [23, 24]. The adsorption of PC/PS liposomes was studied at bare and oxidised amorphous carbon surfaces, which shall refer to as a-C and ox-C, respectively. Amorphous carbon surface preparation and characterization are described in Chapter 3. Briefly, a-C was deposited *via* DC magnetron sputtering, bearing approximately 80% sp^2 content and 7-9% O/C atomic ratio in the film. The water contact angle (CA) and surface free energy (SFE) were found to be 35° and 63.7 mJ m^{-2}, respectively [25]. Oxidation of the carbon films was performed by exposition under UV/ozone for 2 h, yielding ox-C surfaces. UV/ozone oxidation, is commonly

used for the modification of carbon nanomaterials [26, 27] and for the modulation of cell adhesion at diamond and amorphous carbon surfaces [28-30]. The oxidation process led to increasing of the O/C atomic ratio to ~20% and to higher hydrophilicity (water CA <5°), as shown from XPS and CA measurements reported in Chapter 3. ζ-potential measurements of a-C and ox-C yielded values of -51 ± 2 mV and -62 ± 4 mV, respectively, in PBS pH =7.4 and 1.8 ± 0.15 mM ionic strength (data collected by J. M. Vasconcelos); thus suggesting that the density of negatively charged groups at ox-C surfaces is higher than that at a-C. Infrared reflectance absorbance spectroscopy (IRRAS) measurements were used to confirm the presence of negatively charged groups at ox-C surfaces. In Figure 7.1, the broad band in the region 1890-1670 cm^{-1} is attributed to C=O stretching modes from carbonyl and carboxylic acid groups [31] formed at the surface after exposure to the UV lamp. Two additional peaks are also visible at ~1630 cm^{-1} and ~1390 cm^{-1} that can be associated to the C=O stretching modes of carboxylate groups [31]. This assignment is confirmed by the effect of immersion in PBS buffer: immersion in pH 7.4 solution should change the proportion of protonated and deprotonated carboxylic acid groups. Change in the peak intensities is shown in Figure 7.1b after 1h immersion in buffer solution; the two peaks due to the carboxylate group are more intense, pointing to a higher concentration of negative carboxylate ions at the surface. These observations are confirmed by surface free energy determinations using the vOGC method, which show an increase of ~40% of the Lewis basic component in ox-C films when compared to a-C (see Chapter 3).

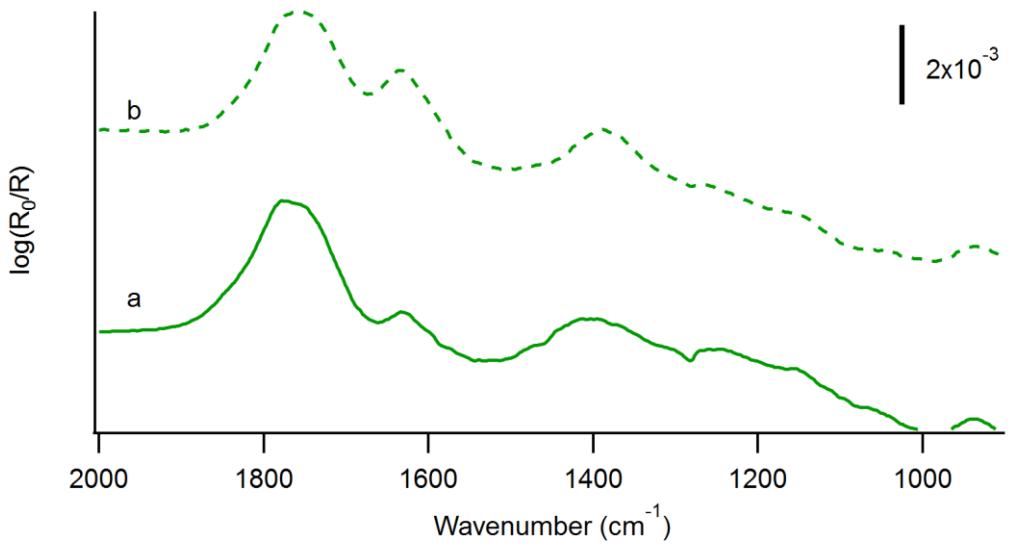

Figure 7.1. IRRAS spectra of ox-C (a, solid line) and ox-C after 1 h immersion in the buffer solution at pH=7.4 (b, dashed line).

PC/PS liposome adsorption at a-C and ox-C surfaces was studied using a combination of spectroscopic and microscopic techniques. Figure 7.1 shows IRRAS spectra in the region 3000-2700 cm^{-1} of a-C and ox-C coated surfaces after 1h incubation with 1mM suspension of phospholipids (80:20 molar ratio PC/PS) in PBS and PBS, $CaCl_2$ buffers. IR spectra of a-C surfaces after liposome adsorption in both PBS and PBS.$CaCl_2$ buffers exhibit two main characteristic peaks due to stretching modes of CH_2 groups in the lipids tails [32, 33]; while no peaks were observed in the IRRAS spectrum of ox-C after liposome incubation when PBS was utilized. On the other hand, the introduction of Ca^{2+} on the phosphate buffer results in the adsorption of phospholipids as indicated by the two main peaks of CH_2 stretching modes in the IRRAS spectrum. Similar results were obtained using fluorescence and atomic force microscopy (AFM) techniques. These findings are in agreement with the literature, according to which hydration interactions are thought to prevent liposome adsorption at highly hydrophilic surfaces, such as ox-C [34], while the introduction of a di-cation favourites formation of a liposome bilayer at the solid surface [35].

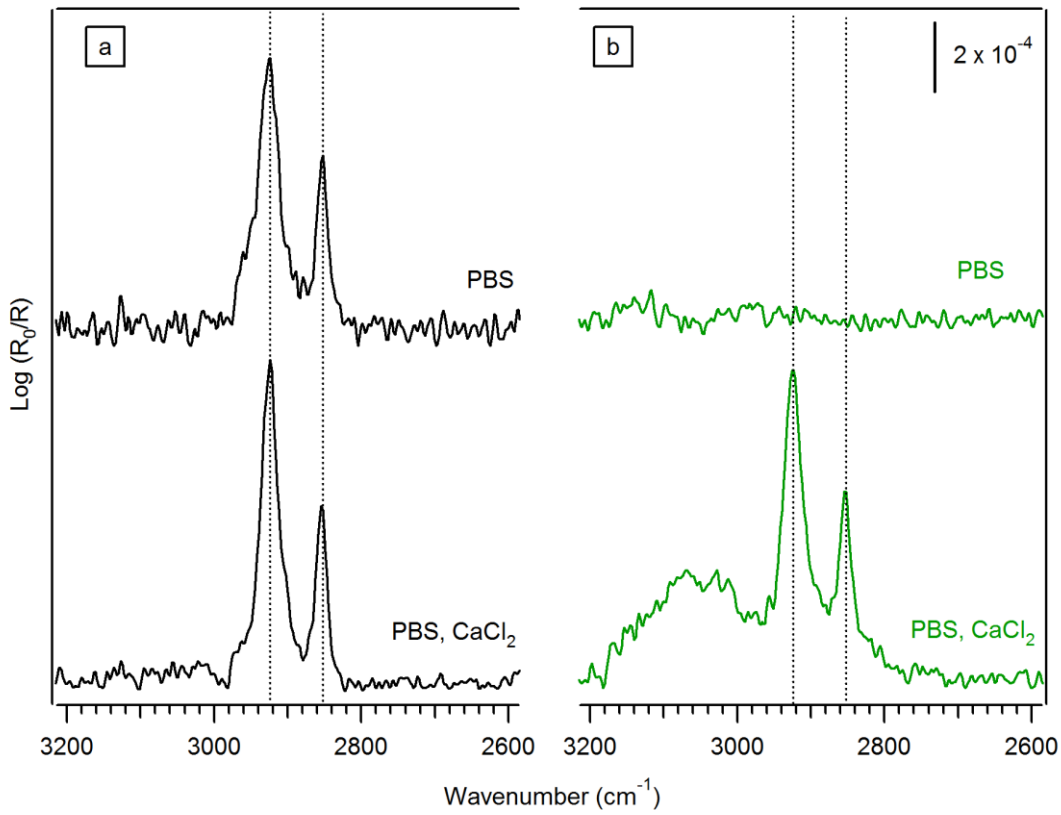

Figure 7.2. IRRAS spectra in the region 3000-2700 cm^{-1} of a-C (a, black line) and ox-C (b, green line) surfaces after 1 h incubation of liposomes suspended in PBS (top) and PBS, $CaCl_2$ (bottom) (pH 7.4). The position of CH_2- stretching bands is indicated with dot lines. With the courtesy of J. M. Vasconcelos.

7.2 Protein adsorption at oxidised carbon surfaces

The effect of the oxidation treatment at carbon surfaces was also investigated in relation to the protein adsorption. a-C and ox-C substrates were exposed to Bovine Serum Albumin (BSA), Lysozyme (Lyz) and Fibrinogen (Fib) buffered solutions at different concentrations and analysed by IRRAS, as described in Chapter 4. The same semi-quantitative method previously used was applied and the amount of protein adsorbed at the surfaces was estimated from the net absorbance of the amide I band. Figure 7.3 summarises the results obtained for a-C and ox-C after incubation with 30mM BSA, 7μM and 30mM Lyz and 7μM Fib buffered solutions. As shown in the bar graph, ox-C surfaces display protein adsorption comparable to bare a-C in the case of BSA and Fib solutions, and higher for Lyz solutions. Interestingly, a highly hydrophilic surface of comparable SFE to Lac-C (see Chapter 4 and 6), but possessing less bulky groups, such as ox-C, does

not display good resistance to protein adsorption. Moreover in the case of ox-C, it is important to consider a further contribution: contrary to the case of saccharide-coated carbon and bare carbon, ox-C possesses acid groups that impart a surface charge to the carbon. As proved from the spectra shown in Figure 7.1, carboxylate negative ions are present at the surface determining a net negative charge on ox-C. This negative charge influences the protein-surface interaction, for instance, by attracting positively charged molecules. This is the case of Lyz, which bears a net positive charge at pH 7.4, due to its high isoelectric point of pI=11.35 [36]. Attractive coulombic interactions are likely to be at the origin of the enhanced adsorption of Lyz at ox-C with respect to a-C surfaces, as shown in Figure 7.3.

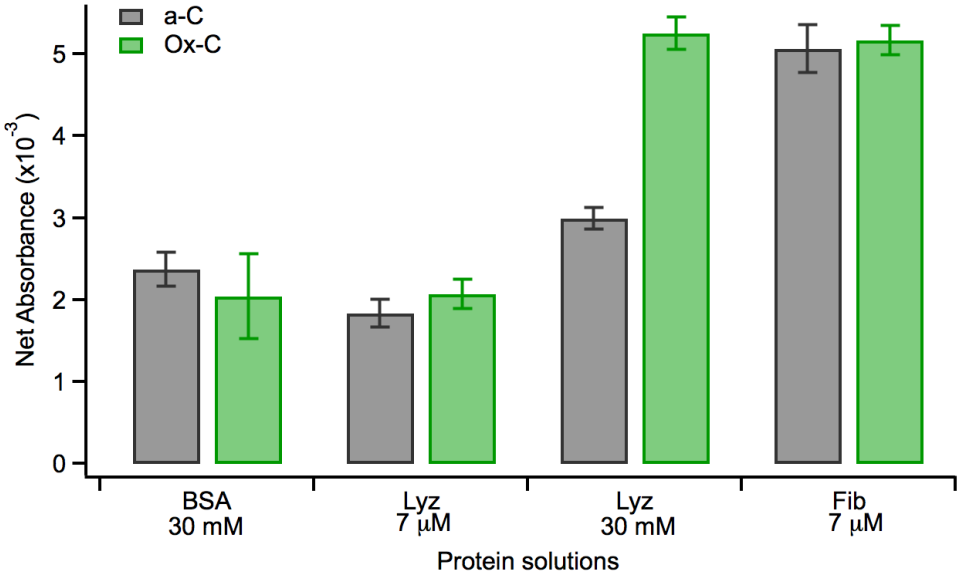

Figure 7.3. Bar-graph representing the amount of protein adsorbed on a-C (grey bars) and ox-C (green bars) after 1 h immersion of the substrate in protein solution. The solutions used are reported on the *x*-axe. On the *y*-axe is reported the net absorbance of amide I band.

7.3 Further work: competitive adsorption of proteins and phospholipids

Further works will involve the investigation of competitive adsorption of proteins and liposomes at bare and modified amorphous carbon surfaces. Moreover, the influence of Ca^{+} ions will be tested when proteins are added to the phospholipid buffered solution. Preliminarily results show no effect of the phospholipids to protein adsorption at bare carbon surfaces: Figure 7.4 shows the

IRRAS spectra of a-C substrates after 1h incubation with 7μM BSA and Fib solutions in both PBS and PBS, Ca^{2+}. The intensity of the Amide I peak at ~1675 cm^{-1} indicates that more Fib adsorbs at carbon surfaces in the present of the Ca^{2+} ions, compared to the simple buffered solutions; while no changes due to introduction of the di-cation were observed in the case of BSA adsorption. The following 1h incubation with 1mM PC/PS liposome solutions did not affect the adsorbed protein layers as shown from the very similar IRRAS spectra obtained in Figure 7.4. More experiments will employ fluorescence and AFM *ex-situ* measurements. Furthermore, the dynamic of protein and phospholipid adsorption will be studied using *in-situ* QCM and LSPR techniques.

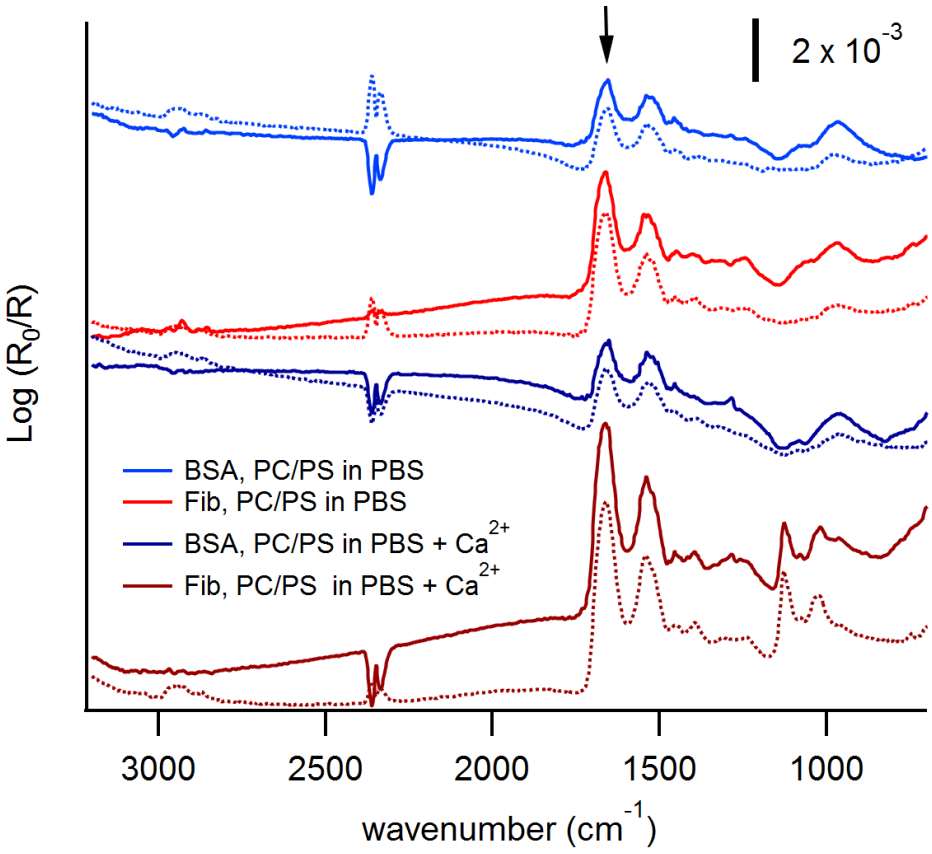

Figure 7.4. IRRAS spectra of a-C after 1 h immersion in 7μM BSA (red line) and Fib (blue line) solutions reported in dashed lines, followed by the 1 h PC/PS liposome incubation in solid lines. Solutions were prepared in both PBS (light line) and PBS, Ca^{2+} (dark line). The position of the amide I band is indicated with an arrow.

7.4 References

1. Kasemo, B., *Biological surface science.* Surface Science, 2002. **500**(1-3): p. 656-677.
2. Forti, S., L. Lunelli, C.D. Volpe, S. Siboni, L. Pasquardini, A. Lui, R. Canteri, L. Vanzetti, C. Potrich, M. Vinante, C. Pederzolli, and M. Anderle, *Hemocompatibility of pyrolytic carbon in comparison with other biomaterials.* Diamond and Related Materials, 2011. **20**(5-6): p. 762-769.
3. Feng, L. and J.D. Andrade, *Protein adsorption on low-temperature isotropic carbon. 1.Protein conformational change probed by differential scanning calorimetry.* Journal of Biomedical Materials Research, 1994. **28**(6): p. 735-743.
4. Ratner, B.D., A.S. Hoffman, F.J. Schoen, and J.E. Lemons, *Biomaterials Science*. 2nd ed. 2004, London: Elsevier Academic Press.
5. Kratz, A., M. Ferraro, P.M. Sluss, and K.B. Lewandrowski, *Normal Reference Laboratory Values.* New England Journal of Medicine, 2004. **351**(15): p. 1548-1563.
6. Quehenberger, O., A.M. Armando, A.H. Brown, S.B. Milne, D.S. Myers, A.H. Merrill, S. Bandyopadhyay, K.N. Jones, S. Kelly, R.L. Shaner, C.M. Sullards, E. Wang, R.C. Murphy, R.M. Barkley, T.J. Leiker, C.R.H. Raetz, Z. Guan, G.M. Laird, D.A. Six, D.W. Russell, J.G. McDonald, S. Subramaniam, E. Fahy, and E.A. Dennis, *Lipidomics reveals a remarkable diversity of lipids in human plasma.* Journal of Lipid Research, 2010. **51**(11): p. 3299-3305.
7. Lorentz, H. and L. Jones, *Lipid deposition on hydrogel contact lenses: How history can help us today.* Optometry and Vision Science, 2007. **84**(4): p. 286-295.
8. McHenry, M.M., E.A. Smeloff, W.Y. Fong, G.E. Miller Jr, and P.M. Ryan, *Critical obstruction of prosthetic heart valves due to lipid absorption by Silastic.* Journal of Thoracic and Cardiovascular Surgery, 1970. **59**(3): p. 413-425.
9. Nel, A.E., L. Madler, D. Velegol, T. Xia, E.M.V. Hoek, P. Somasundaran, F. Klaessig, V. Castranova, and M. Thompson, *Understanding biophysicochemical interactions at the nano-bio interface.* Nature Materials, 2009. **8**(7): p. 543-557.
10. Hellstrand, E., I. Lynch, A. Andersson, T. Drakenberg, B. Dahlbäck, K.A. Dawson, S. Linse, and T. Cedervall, *Complete high-density lipoproteins in nanoparticle corona.* FEBS Journal, 2009. **276**(12): p. 3372-3381.
11. Malmsten, M., *Ellipsometry Studies of Protein Adsorption at Lipid Surfaces.* Journal of Colloid and Interface Science, 1994. **168**(1): p. 247-254.
12. Malmsten, M. and B. Lassen, *Competitive protein adsorption at phospholipid surfaces.* Colloids and Surfaces B: Biointerfaces, 1995. **4**(3): p. 173-184.
13. Gasser, M., B. Rothen-Rutishauser, H. Krug, P. Gehr, M. Nelle, B. Yan, and P. Wick, *The adsorption of biomolecules to multi-walled carbon nanotubes is influenced by both pulmonary surfactant lipids and surface chemistry.* Journal of Nanobiotechnology, 2010. **8**(1): p. 31.
14. Kendall, M., L. Brown, and K. Trought, *Molecular Adsorption at Particle Surfaces: A PM Toxicity Mediation Mechanism.* Inhalation Toxicology, 2004. **16**(s1): p. 99-105.
15. Marco Diociaiuti, Agnese Molinari, Irene Ruspantini, Maria Cristina Gaudiano, Rodolfo Ippoliti, Eugenio Lendaro, Federico Bordi, Pietro

Chistolini, and Giuseppe Arancia, *P-glycoprotein inserted in planar lipid bilayers formed by liposomes opened on amorphous carbon and Langmuir-Blodgett monolayer.* Biochimica et Biophysica Acta, 2002. **1559**: p. 21-31.
16. Yang, W., F.Z. Cui, and X. Qing, *Behavior of phosphatidylcholine adsorption on CNx coated PTFE films.* Current Applied Physics, 2006. **6**(5): p. 827-832.
17. Tsuzuki, K., Y. Okamoto, S. Iwasa, R. Ishikawa, A. Sandhu, and R. Tero, *Reduced Graphene Oxide as the Support for Lipid Bilayer Membrane.* Journal of Physics: Conference Series, 2012. **352**: p. 012016.
18. Tero, R., *Substrate Effects on the Formation Process, Structure and Physicochemical Properties of Supported Lipid Bilayers.* Materials, 2012. **5**(12): p. 2658-2680.
19. Okamoto, Y., K. Tsuzuki, S. Iwasa, R. Ishikawa, A. Sandhu, and R. Tero, *Fabrication of Supported Lipid Bilayer on Graphene Oxide.* Journal of Physics: Conference Series, 2012. **352**: p. 012017.
20. Castellana, E.T. and P.S. Cremer, *Solid supported lipid bilayers: From biophysical studies to sensor design.* Surface Science Reports, 2006. **61**(10): p. 429-444.
21. Hussain, M.M., *A proposed model for the assembly of chylomicrons.* Atherosclerosis, 2000. **148**: p. 1-15.
22. Kurt W. Miller and Donald M. Smalls, *Surface-to-Core and Interparticle Equilibrium Distributions of Triglyceride-rich Lipoprotein Lipids.* The Journal of Biological Chemistry, 1983. **258**(22): p. 13772-13784.
23. Sessa, G. and G. Weissmann, *Phospholipid spherules (liposomes) as a model for biological membranes.* J Lipid Res, 1968. **9**(3): p. 310-8.
24. Akbarzadeh, A., R. Rezaei-Sadabady, S. Davaran, S. Joo, N. Zarghami, Y. Hanifehpour, M. Samiei, M. Kouhi, and K. Nejati-Koshki, *Liposome: classification, preparation, and applications.* Nanoscale Research Letters, 2013. **8**(1): p. 1-9.
25. Zen, F., M.D. Angione, J.A. Behan, R.J. Cullen, T. Duff, J.M. Vasconcelos, E.M. Scanlan, and P.E. Colavita, *Modulation of Protein Fouling and Interfacial Properties at Carbon Surfaces via Immobilization of Glycans Using Aryldiazonium Chemistry.* Scientific Reports, 2016. **6**: p. 24840.
26. Morales-Lara, F., M.J. Pérez-Mendoza, D. Altmajer-Vaz, M. García-Román, M. Melguizo, F.J. López-Garzón, and M. Domingo-García, *Functionalization of Multiwall Carbon Nanotubes by Ozone at Basic pH. Comparison with Oxygen Plasma and Ozone in Gas Phase.* The Journal of Physical Chemistry C, 2013. **117**(22): p. 11647-11655.
27. Simmons, J.M., B.M. Nichols, S.E. Baker, M.S. Marcus, O.M. Castellini, C.S. Lee, R.J. Hamers, and M.A. Eriksson, *Effect of Ozone Oxidation on Single-Walled Carbon Nanotubes.* The Journal of Physical Chemistry B, 2006. **110**(14): p. 7113-7118.
28. Hernandez, M.R., E.N. Towns, T.C. Ng, B.C. Walsh, R. Osibanjo, A.N. Parikh, and D.P. Land, *Use of attenuated total reflectance Fourier transform infrared spectroscopy to monitor the development of lipid aggregate structures.* Appl Opt, 2012. **51**(15): p. 2842-6.
29. Nistor, P.A., P.W. May, F. Tamagnini, A.D. Randall, and M.A. Caldwell, *Long-term culture of pluripotent stem-cell-derived human neurons on diamond – A substrate for neurodegeneration research and therapy.* Biomaterials, 2015. **61**: p. 139-149.

30. Regan, E.M., A. Taylor, J.B. Uney, A.D. Dick, P.W. May, and J. McGeehan, *Spatially Controlling Neuronal Adhesion and Inflammatory Reactions on Implantable Diamond.* IEEE Journal on Emerging and Selected Topics in Circuits and Systems, 2011. **1**(4): p. 557-565.
31. Socrates, G., *Infrared and Raman Characteristic Group Frequencies: Tables and Charts*. 2001: John Wiley & Sons.
32. Sovago, M., G.W.H. Wurpel, M. Smits, M. Müller, and M. Bonn, *Calcium-Induced Phospholipid Ordering Depends on Surface Pressure.* Journal of the American Chemical Society, 2007. **129**(36): p. 11079-11084.
33. Hull, M.C., L.R. Cambrea, and J.S. Hovis, *Infrared spectroscopy of fluid lipid bilayers.* Anal Chem, 2005. **77**(18): p. 6096-9.
34. Isono, T., H. Tanaka, and T. Ogino, *Effect of Chemical Modification of the Substrate Surface on Supported Lipid Bilayer Formation.* e-Journal of Surface Science and Nanotechnology, 2007. **5**: p. 99-102.
35. Seantier, B. and B. Kasemo, *Influence of Mono- And Divalent Ions on the Formation of Supported Phospholipid Bilayers via Vesicle Adsorption.* Langmuir, 2009. **25**(10): p. 5767-5772.
36. Kim, S.K., J.B. Lee, J.Y. Koak, S.J. Heo, K.R. Lee, L.R. Cho, and S.S. Lee, *An abutment screw loosening study of a Diamond Like Carbon-coated CP titanium implant.* Journal of Oral Rehabilitation, 2005. **32**(5): p. 346-350.

8 Conclusions

The goal of this project is the understanding of carbon interfacial interactions with biological fluids and how these interactions may impact on host response towards this family of biomaterials. My thesis takes part in this final aim by studying protein adsorption at carbon surfaces and how the modulation of interfacial properties influence protein-carbon interactions.

For this purpose, a variety of different types of carbon film were prepared in this work. DC magnetron sputtering technique was used to deposit highly graphitic amorphous carbon (a-C) layers. Wettability of a-C surfaces was modified *via* immobilization of mono- and di-saccharides using the spontaneous aryldiazonium reaction. Bulk properties of carbon layers were changed by introduction of H_2 during sputtering bearing hydrogen doped amorphous carbon (a-C:H) films with low graphitic content and high optical transparency.

Investigation of protein adsorption at bare and modified a-C surfaces was carried out using both *ex-situ* and *in-situ* measurements. Results show that carbohydrate coatings are able to prevent the adsorption of different types of protein at both high and low concentrations. The antifouling effect observed for these phenyglycoside layers is associated with the increasing of hydrophilicity and Lewis basicity measured at carbon surfaces after sugar functionalization.

The dynamic of protein adsorption at the carbon-liquid interface was investigated using a combination of label-free techniques: optical and acoustic biosensors enable complementary study of interfacial processes occurring at surfaces in real-time. Optical methods based on nanoplasmonic sensing, in combination with computational simulations, were shown to be a valuable platform for comparing protein adsorption at carbon coated sensors, even in the case of a-C and a-C:H films with highly dissimilar dielectric properties. Acoustic sensors consisting in quartz crystal microbalance provides additional information about the rigidity and the hydration fraction of the protein layers, by measuring the biomolecular and coupled water mass adsorbed at bare and modified carbon surfaces. Results show differences in the dynamic of protein conformation at

carbohydrate surfaces from that at the bare carbon, which likely contribute to the antifouling effect observed for the phenyglycoside layers.

This thesis elucidated how surfaces properties can affect both the amount and the dynamic of protein adsorption at carbon surfaces. We expect these results to be important to understand the role of proteins in affecting the interactions between carbon and other bio-molecules (*i.e.* phospholipids), with the final aim of rationalizing the host response to biomedical and implantable carbon coated devices.

Published Works

During the course of this PhD research project, a number of peer-reviewed articles have been published on the work presented in this thesis, together with other co-authored works. They are listed here for reference. The first two articles are presented in original copy at the end of this thesis.

- Zen, F.; Angione, M.D.; Behan, J.A.; Cullen, R.J.; Duff, T.; Vasconcelos, J.M.; Scanlan, E.M.; Colavita, P.E. Modulation of Protein Fouling and Interfacial Properties at Carbon Surfaces via Immobilization of Glycans at Carbon Surfaces. *Scientific Reports* **2016**, 24840.
- Zen, F.; Karanikolas, V.D.; Behan; J.A.; Andersson, J.; Ciapetti, G.; Bradley, A.L.; Colavita, P.E. Nanoplasmonic Sensing Studies of Protein Adsorption at Graphitic and Hydrogenated Carbon Surfaces. *Langmuir* **2017**, DOI: 10.1021/acs.langmuir.7b00612.
- Vasconcelos, J.M.; Zen, F.; Stamatin, S.N; Behan, J.A.; Colavita, P.E. Determination of surface ζ-potential and isoelectric point of carbon surfaces using tracer particle suspensions. *Surface and Interface Analysis* **2017**, DOI: 10.1002/sia.6223.
- Behan, J.A.; Stamatin, S.N.; Hoque, Md. K.; Ciapetti, G.; Zen, F.; Esteban-Tejeda, L.; Colavita, P.E. Combined optoelectronic and electrochemical study of nitrogenated carbon electrodes. *Journal of Physical Chemistry C* **2017**, 121 (12), pp 6596–6604.

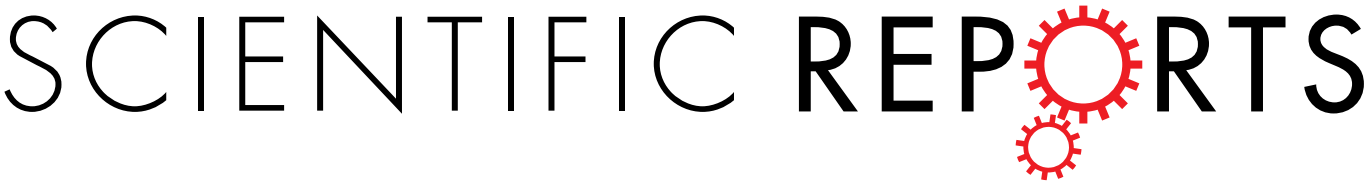

OPEN

Modulation of Protein Fouling and Interfacial Properties at Carbon Surfaces via Immobilization of Glycans Using Aryldiazonium Chemistry

Received: 22 January 2016
Accepted: 05 April 2016
Published: 25 April 2016

Federico Zen, M. Daniela Angione, James A. Behan, Ronan J. Cullen, Thomas Duff, Joana M. Vasconcelos, Eoin M. Scanlan & Paula E. Colavita

Carbon materials and nanomaterials are of great interest for biological applications such as implantable devices and nanoparticle vectors, however, to realize their potential it is critical to control formation and composition of the protein corona in biological media. In this work, protein adsorption studies were carried out at carbon surfaces functionalized with aryldiazonium layers bearing mono- and di-saccharide glycosides. Surface IR reflectance absorption spectroscopy and quartz crystal microbalance were used to study adsorption of albumin, lysozyme and fibrinogen. Protein adsorption was found to decrease by 30–90% with respect to bare carbon surfaces; notably, enhanced rejection was observed in the case of the tested di-saccharide vs. simple mono-saccharides for near-physiological protein concentration values. ζ-potential measurements revealed that aryldiazonium chemistry results in the immobilization of phenylglycosides without a change in surface charge density, which is known to be important for protein adsorption. Multisolvent contact angle measurements were used to calculate surface free energy and acid-base polar components of bare and modified surfaces based on the van Oss-Chaudhury-Good model: results indicate that protein resistance in these phenylglycoside layers correlates positively with wetting behavior and Lewis basicity.

Much effort towards the design and fabrication of biomaterials and medical devices is dedicated to the attainment of desirable surface chemistry and surface physical properties, as these can often determine the biological response to materials *in vivo*[1]. There is therefore a strong interest in investigating surface modification strategies that enable a degree of control over interfacial biointeractions. Protein-surface interactions are thought to be of particular importance due to the abundance of these molecules in tissues and biological fluids and due to the central role of peptides and proteins in cell adhesion and signalling. Depending on the specific biomaterial and its application (e.g. biosensor, implant) it might be desirable to either promote protein adsorption or repel protein build-up in order to modulate performance[2–5]. Therefore, much effort has been devoted to developing surface modification strategies to modulate protein-surface interactions.

Various forms of carbon find multiple applications as biomaterials; coatings such as pyrocarbon and amorphous carbons (e.g. a-C, a-C:Si, a-C:H, ta-C)[6,7], are promising for biomedical applications because of their frictional and mechanical properties, their corrosion resistance and chemical inertness, and their bio- and hemocompatibility. Carbon nanomaterials, such as nanotubes and nanodiamonds, have also received much attention as delivery agents for *in vivo* imaging and sensing[8,9]. Finally, materials such as diamond electrodes, carbon coatings and carbon nanofibers are routinely used for *in vivo* and *in vitro* bioanalytical chemistry[10,11]. For all of these applications it is critical to achieve control over interfacial interactions of the carbon solid surface with proteins in solution, to avoid unspecific adsorption that might result in undesirable cell-surface events, or in blocking of sensing/binding sites[12–15].

School of Chemistry and Centre for Research on Adaptive Nanostructures and Nanodevices (CRANN), Trinity College Dublin, College Green, Dublin 2, Ireland. Correspondence and requests for materials should be addressed to E.M.S. (email: eoin.scanlan@tcd.ie) or P.E.C. (email: colavitp@tcd.ie)

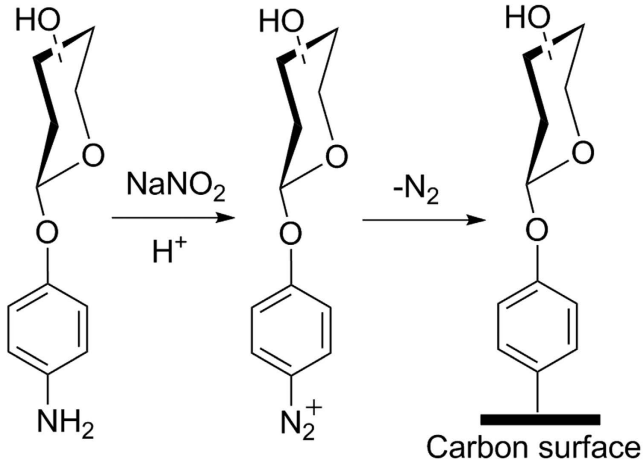

Figure 1. Surface modification reaction for carbon surfaces via *in situ* generation of aryldiazonium salts.

Several surface modification methods have been investigated in order to control and minimize protein fouling at surfaces: cationic polymers, enzymes or peptides are effective but costly and often present problems of leaching and durability[16]. Poly and oligo (ethylene glycol) (PEG, OEG) coatings have been shown to successfully minimize protein adsorption[12,17]; however, PEG/OEGs can easily oxidize, losing their antifouling properties[16]. This problem has prompted a search for alternative antifouling coatings with enhanced chemical stability. In an effort to mimic biological antifouling strategies, work has focused on the use of immobilized carbohydrates, given the presence of these molecules in the antiadhesive glycocalyx that surrounds certain cells[18,19]. Research shows, in fact, that oligo- and polysaccharide coatings can control fouling and protein adsorption, while being extremely stable to oxidation[20–26].

The use of aryldiazonium salt chemistry for the immobilization of simple carbohydrates on carbon surfaces was recently reported by our group[27]. Aryldiazonium chemistry offers a versatile route for surface immobilization with key advantages for carbon applications: (a) functionalization can be carried out from solution, (b) it occurs under mild conditions without the use of multistep reactions, and (c) it leads to the formation of robust functional layers via formation of strong C—C covalent bonds between R-Ph groups and carbon substrates[28]. This is a desirable property that imparts chemical and thermal stability to carbohydrate adlayers under a variety of conditions thus preventing interfacial exchange between the layer and biomolecules in solution. The ability to solution process surfaces also makes it intrinsically scalable and thus relevant for widespread applications. We have recently shown that immobilized phenylglycosides bearing mono-saccharide groups obtained via aryldiazonium chemistry can reduce the unspecific adsorption of Bovine Serum Albumin (BSA) at carbon surfaces[27]. However, it remains unclear whether antifouling properties can be observed with other proteins and whether specific carbohydrate structural properties are responsible for the antifouling behavior. Interestingly, we have also identified that phenyl-lactosides are more effective than mono-saccharide glycosides at preventing adsorption on polymer surfaces[20].

Herein, we report a study of protein adsorption at phenylglycoside-modified and bare amorphous carbon surfaces using five different glycosides, four bearing mono-saccharide moieties and one being a phenyl-lactoside. We use three proteins with different levels of structural complexity and isoelectric points to understand the generality of protein adsorption trends. Importantly, we investigate the relationship between protein adsorption at phenylglycoside layers and surface free energy, charge and glycoside structure with the aim of improving our current understanding of key properties that result in antifouling activity of aryldiazonium carbohydrate layers.

Results

Protein adsorption studies. Amorphous carbon (a-C) films used in our experiments were deposited via magnetron sputtering. These films had previously been characterized via a combination of spectroscopic methods[29]. Briefly, they consist of approximately 80% trigonally bonded carbon (sp^2 centers), as estimated via X-ray photoelectron spectroscopy (XPS) and Raman spectroscopy. The films also contain oxidized groups resulting in a 9% O/C atomic ratio as determined via XPS.

Modification of a-C with aryldiazonium salts was carried out as in our previous work (Fig. 1), via diazoniation of 4-aminophenyl glycoside precursors *in situ*. Precursor glycosides bearing glucose (Glc), galactose (Gal), mannose (Man), rhamnose (Rha) and lactose (Lac) groups (compounds **1–5**, Fig. 2), yielded surfaces from here onwards referred to as Glc-C, Gal-C, Man-C, Rha-C and Lac-C, respectively. Figure 3 shows examples of IR reflectance absorption spectroscopy (IRRAS) of Gal-C, a monosaccharide-modified surface, and of Lac-C, a disaccharide-modified surface, obtained from precursors **2** and **5**, respectively. Both IRRAS spectra show the characteristic infrared absorbances of glycosides in the region 1290–950 cm^{-1} due to C–O stretching modes arising from the carbohydrate ring[27,30]. Peaks in the region 1550–1500 cm^{-1} arise from C–C skeletal vibrations of phenyl rings[30]; in particular, it was possible to observe in all spectra the presence of a peak at 1508 cm^{-1} which can be attributed to the strong 19a stretching mode of phenyl rings[27]. Similar IRRAS spectra were obtained for Glc-C, Man-C and Rha-C surfaces.

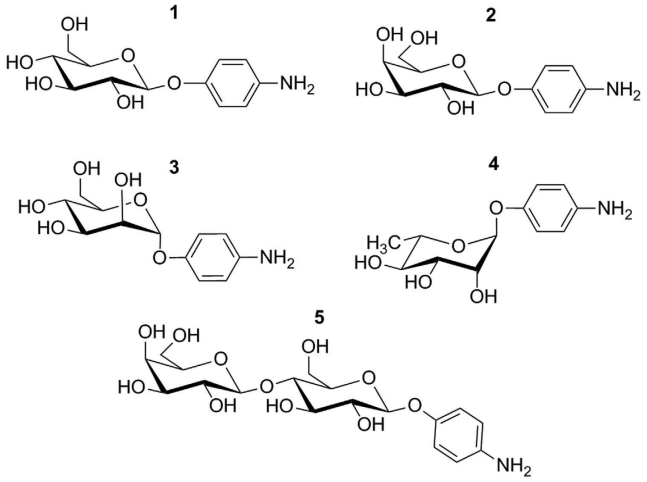

Figure 2. 4-aminophenyl glycosides synthesized as precursors for the preparation of carbohydrate layers via aryldiazonium chemistry: 4-aminophenol-β-D-glucopyranose (**1**), 4-aminophenol-β-D-galactopyranose (**2**), 4-aminophenol-α-D-mannopyranose (**3**), 4-aminophenol-α-L-rhamnopyranose (**4**) and 4-aminophenol-β-D-lactopyranose (**5**).

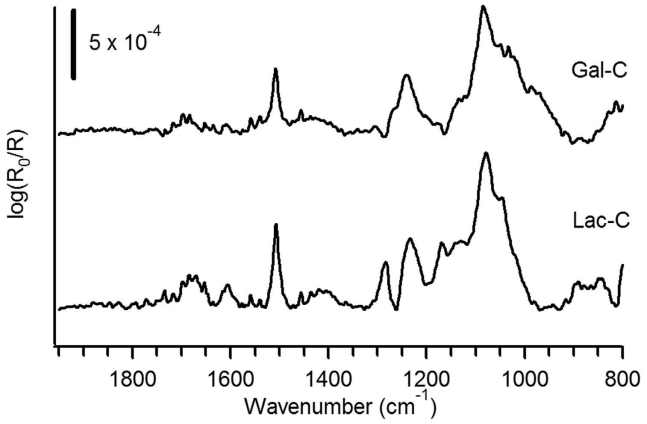

Figure 3. IRRAS spectra of a-C surfaces after modification with Gal (Gal-C) and Lac monosaccharides (Lac-C).

The thickness of phenylglycoside layers was characterized via atomic force microscopy (AFM) using previously reported methods[31,32]. Briefly, phenylglycoside-modified surfaces were first imaged in tapping mode; subsequently, a section of the film was removed by scratching the sample with the AFM tip in contact mode; finally, the step created in the organic film was imaged in tapping mode. Figure 4 shows an example of a Lac-C surface imaged after the scratching process and of a height profile across the step. Height profiles were used to obtain an average thickness which was found to be 0.8 ± 0.1 nm in the case of both Gal-C and Lac-C layers. These thickness values are slightly lower than estimates of molecular length of 1.0 nm and 1.5 nm for phenyl-β-galactoside and benzyl-β-lactoside conformers, respectively, obtained from optimized glycoside geometries[33,34]. Thickness results therefore indicate that layers prepared via aryldiazonium chemistry using both mono- and di-saccharide groups reach a surface coverage of at most 1 monolayer, as expected based on the presence of bulky terminal groups such as Lac and Gal glycans[35].

In order to evaluate the antifouling properties of glycosylated interfaces, both unmodified and modified a-C substrates were incubated in buffered protein solutions for 1 h and analyzed by IRRAS *ex situ*. Three proteins with different properties were chosen for our studies: BSA, lysozyme (Lyz) and fibrinogen (Fib); a summary of their main physical properties is reported in Table 1[36–38]. Figure 5 shows IRRAS spectra in the region 1900–1300 cm^{-1} of bare a-C, Gal-C and Lac-C surfaces after incubation in BSA, Lyz and Fib solutions at two different concentrations; dotted lines in the central and right hand panel show the IRRAS spectra of Gal-C and Lac-C surfaces prior to protein adsorption in the same spectral region. After adsorption, spectra exhibit the characteristic bands of amide groups in polypeptides: the two strong, broad peaks at ~1675 cm^{-1} and ~1540 cm^{-1} are assigned to the amide I and II modes, respectively[30]. Noticeably, the sharp peak at ~1510 cm^{-1} assigned to the aromatic ring appears in all of the spectra, thus confirming that the phenyl groups used for surface modification are strongly bound to the surface and are not displaced by adsorbed proteins. Similar results were obtained in the case of Man-C, Glc-C and Rha-C surfaces.

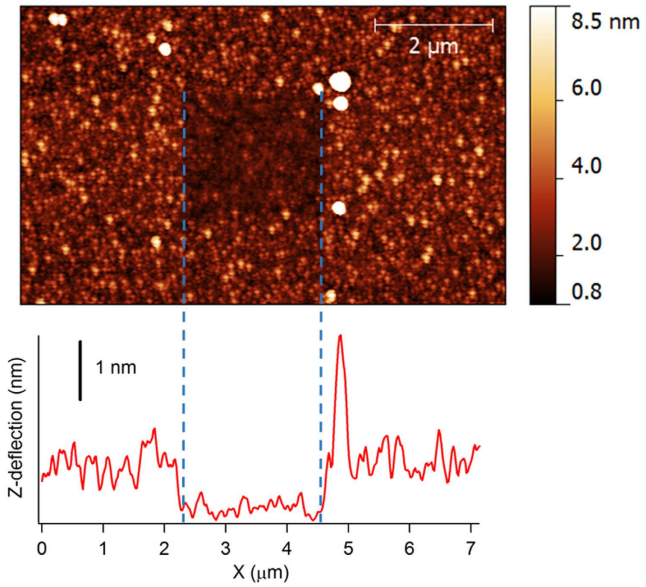

Figure 4. AFM topographic image of a Lac-C surface (top) after removal of a portion of the film with the AFM tip. The height profile (bottom) shows a step edge with a height equivalent to the thickness of the phenyl-lactoside layer.

	Mass (kDa)	Amino acids	Size (nm^3)	Isoelectric point
BSA	66	583	$8 \times 8.7 \times 6$	4.7–4.9
Lyz	14	129	$4.5 \times 3 \times 3$	11.35
Fib	340	3620	$45 \times 9 \times 6$	5.8

Table 1. Main properties of proteins used for adsorption studies; molar mass, number of amino acids and isoelectric point are provided by the manufacturer, except for the isoelectric point of Fib which is taken from ref. 36 and sizes which are taken from refs 37 and 38.

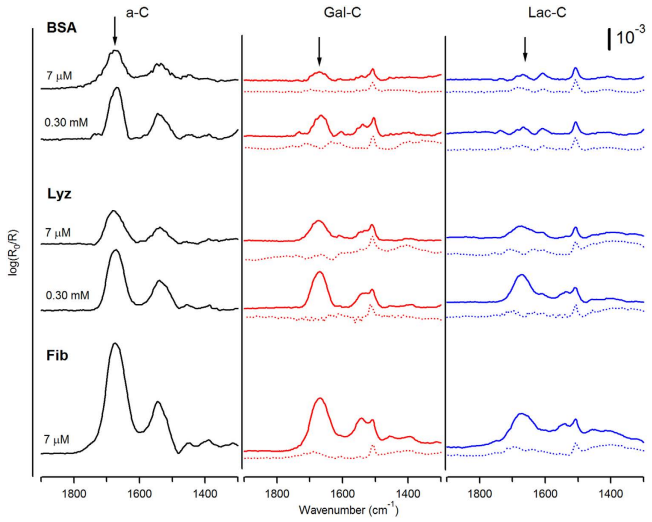

Figure 5. IRRAS spectra in the amide I/II region of bare a-C (black), Gal-C (red) and Lac-C (blue) surfaces after functionalization (dotted lines) and after incubation in buffered solutions of BSA, Lyz and Fib at different concentrations (solid lines). The position of the amide I band is indicated with an arrow.

The relative amounts of protein adsorbed at bare and saccharide-modified surfaces can be estimated from the net absorbance of amide bands in IRRAS spectra, under the assumption of no preferential orientation of peptide

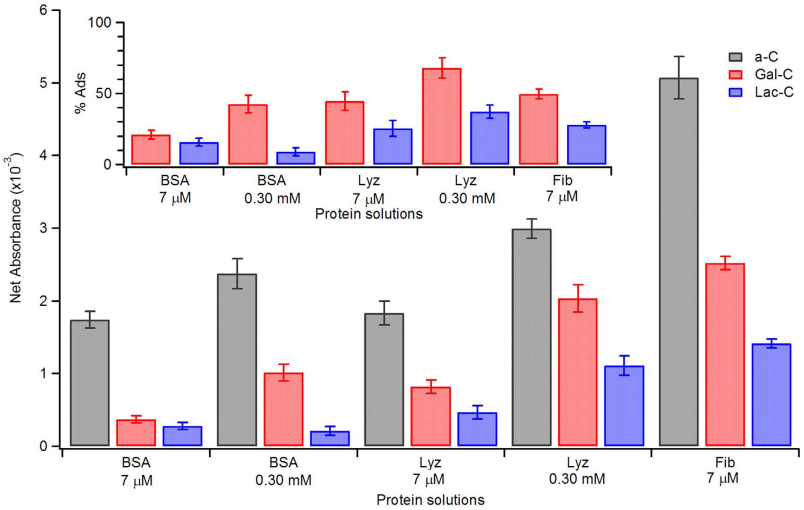

Figure 6. Comparison of amide I net absorbance values at a-C, Gal-C and Lac-C surfaces after incubation in solutions of BSA, Lyz and Fib. Inset shows adsorbed amounts relative to bare a-C surfaces.

Surface	Adsorbed BSA (μg cm^{-2})	Relative BSA Mass	Relative Amide I peak absorbance
a-C	1.02 ± 0.27	–	–
Gal-C	0.35 ± 0.22	34%	21%
Lac-C	0.10 ± 0.11	9.8%	16%

Table 2. BSA adsorption measurements at a-C, Gal-C and Lac-C surfaces, carried out using 7 μM solutions. The table reports absolute adsorbed mass values determined via *ex situ* QCM, relative adsorbed masses calculated with respect to adsorption at bare a-C and relative adsorbed values determined via IRRAS under the same experimental conditions.

bonds at the carbon surface. Net absorbance values of amide I peaks at bare a-C, and phenylglycoside-modified carbon are reported in Fig. 6, where the inset shows the same results as percentage adsorption with respect to the bare surface. Values in Fig. 6 were obtained from adsorption experiments carried out at two different molar concentrations: 7 μM, equivalent to 0.5, 0.1 and 2.5 g L^{-1} for BSA, Lyz and Fib, respectively, and 0.30 mM, equivalent to 20 and 4.3 g L^{-1} for BSA and Lyz, respectively. These two concentrations are relevant for understanding the behavior of surfaces in physiological conditions since molar concentrations of 7 μM are in the normal range for Fib in plasma, while a 0.30 mM concentration is close to that of albumin in serum[39]. Fib could not be studied at the higher concentration because it falls beyond its solubility limit[40].

IRRAS results indicate that at bare a-C surfaces, adsorption increases with increasing molar concentration for the same protein. Fib solutions yielded the strongest adsorption among all protein solutions tested. These observed trends are in general agreement with previous reports of adsorption isotherms of human albumin and fibrinogen at isotropic carbon surfaces by Feng and Andrade[41]. Adsorption values on monosaccharide-modified surfaces were significantly lower than at bare a-C for all three proteins at all concentrations studied. Similar results were obtained for surfaces modified with Glc, Man and Rha units: only small differences were observed in protein resistance among the four monosaccharides used in our studies. The amount of protein adsorbed at Lac-C was however found to be significantly lower than at either bare a-C, or monosaccharide-modified surfaces, thus indicating that Lac-C surfaces are better at resisting protein adsorption.

In order to obtain quantitative estimates of protein adsorption at mono- and disaccharide modified surfaces, Quartz Crystal Microbalance (QCM) measurements of protein mass were also carried out *ex situ*. Upon incubation in 7 μM BSA for 1 h, bare a-C surfaces reported a mass increase of 1.02 ± 0.27 μg cm^{-2}, whereas Gal-C and Lac-C surfaces yielded increases of only (0.35 ± 0.22) and (0.10 ± 0.11) μg cm^{-2} (C.I. 95%), respectively. The above estimates likely constitute upper boundaries for BSA adsorption at the three surfaces, given that *ex situ* QCM also measures contributions from the mass of water trapped within the BSA layer. Table 2 summarizes BSA mass densities and relative adsorption mass values measured via *ex situ* QCM, together with the corresponding adsorption estimates obtained from amide I peak absorptions in IRRAS spectra. The comparison between the spectroscopic and gravimetric determination of protein adsorption was found to be satisfactory, thus indicating that amide I peak intensities are proportional to surface mass density of proteins on these surfaces. Also, gravimetric analysis confirms that Lac-C layers perform better than Gal-C layers in terms of protein rejection.

Surface contact angle and surface free energy studies. Surface free energy (SFE) and wettability play an important role in defining the extent to which a surface can resist biofouling. The SFE of unmodified and modified a-C substrates was determined via contact angle (CA) measurements of multiple solvents using the sessile

Test liquids	γ_L	γ_L^{LW}	γ_L^+	γ_L^-
Water	72.8	21.8	25.5	25.5
Glycerol	63.3	34	3.92	57.4
Diiodomethane	50.8	50.8	0	0

Table 3. Total surface tensions (γ_L), dispersive (γ_L^{LW}), electron donating γ_L^- and accepting (γ_L^+) components (mJ m^{-2}) of test liquids used for contact angle measurements and vOCG analysis[43,45].

Surface	Contact Angles (degrees)			SFE components (mJ m^{-2})				
	θ_W	θ_G	θ_{DM}	γ^{LW}	γ^+	γ^-	γ_{tot}	ζ-potential (mV)
a-C	35.3 ± 1.4	22.2 ± 1.4	11.9 ± 0.9	49.7	1.79	27.4	63.7	−55 ± 3
Glc-C	20.2 ± 0.3	16.4 ± 1.2	5.4 ± 0.4	50.6	1.38	38.7	65.2	–
Gal-C	26.1 ± 1.1	17.1 ± 0.4	7.5 ± 0.4	50.4	1.61	34.2	65.2	−56.3 ± 1.9
Man-C	22.9 ± 0.6	15.9 ± 1.3	4.9 ± 0.1	50.6	1.52	36.5	65.5	–
Rha-C	25.0 ± 0.5	20.3 ± 0.6	6.2 ± 0.2	50.4	1.30	36.3	64.2	–
Lac-C	11.8 ± 0.4	16.9 ± 0.7	4.2 ± 0.3	50.7	1.11	43.9	64.6	−58.0 ± 2.6

Table 4. Summary of experimentally determined properties of bare and modified carbon surfaces: measured contact angles using water (θ_W), glycerol (θ_G) and diiodomethane (θ_{DM}); surface free energy or total surface tension (γ_{tot}), its dispersive (γ^{LW}), electron accepting (γ^+) and donating (γ^-) components determined from vOCG analysis; surface ζ-potential values obtained using polystyrene tracer particles in 1 mM NaCl at pH 9.2.

drop method. In order to obtain the SFE, we used the model of van Oss, Chaudhury and Good (vOCG)[42,43]. This model assumes that the total surface tension results from additive contributions of apolar, or Lifshitz-van der Waals (γ^{LW}), and polar forces (γ^{AB}):

$$\gamma = \gamma^{LW} + \gamma^{AB} \tag{1}$$

where γ^{AB} includes contributions γ^- and γ^+ from electron donor-acceptor interactions, respectively, also called Lewis base-acid interactions. The model assumes that the work of adhesion at the solid-liquid interface, W_{SL}, can be approximated by geometric means as below:

$$W_{SL} = 2\left(\sqrt{\gamma_S^{LW}\gamma_L^{LW}} + \sqrt{\gamma_S^-\gamma_L^+} + \sqrt{\gamma_S^+\gamma_L^-}\right) \tag{2}$$

where the subscripts "*L*" and "*S*" indicate components of the liquid and solid, respectively. vOCG is considered to be a suitable model for describing the asymmetric nature of polar interactions when hydrogen bonding contributions are present[42,43]: electron donating and accepting groups must interact "reciprocally" to contribute to surface tension, as reflected by mixed donating/accepting products in Equation (2). Equation (2), in combination with the Young-Dupre equation results in:

$$\sqrt{\gamma_S^{LW}\gamma_L^{LW}} + \sqrt{\gamma_S^-\gamma_L^+} + \sqrt{\gamma_S^+\gamma_L^-} = \frac{\gamma_L}{2}(1 + \cos\theta) \tag{3}$$

which can be used to obtain γ_S^{LW}, γ_S^- and γ_S^+ by measuring the CA of three liquids with known surface tension components γ_L^{LW}, γ_L^- and γ_L^+.

Carbon films used for CA measurements were deposited on Si wafers and were found to display low rms roughness before and after modification (see Supporting Information). Surface tension components of the three test liquids at 20 °C are taken from van Oss's data compilation[43] and are reported in Table 3; the choice of liquids was based on the analysis of solvent triplets by Della Volpe *et al*[44]. γ_S^{LW} was first calculated using eq. (3) and the CA of diiodomethane, a liquid with $\gamma_L^+ = \gamma_L^- = 0$. CAs of water and glycerol were then used to set a system of two linear equations that were solved for $\sqrt{\gamma_S^+}$ and $\sqrt{\gamma_S^-}$[45]; positive values were obtained from our calculations thus confirming that all surfaces yield physical solutions for γ_S^+ and γ_S^-.

CA values and surface tension components for all surfaces examined in this work are reported in Table 4. Bare a-C displayed a water CA of 35.3°, total SFE $\gamma_S = 63.7$ mJ m^{-2} and components $\gamma_S^{LW} = 49.7$ mJ m^{-2} and $\gamma_S^{AB} = 14.0$ mJ m^{-2}. These values are in good agreement with those reported by Leezenberg *et al.*[46] for sputtered a-C films, but the polar component and total surface energy are higher than those obtained by Zebda *et al.*[45] via vOCG analysis. Differences in components and total SFE could arise due to variations in material properties (e.g. sp^2/sp^3 or O-content) or film history[46]. Surface modification with saccharides leads to a significant decrease in water CA for all saccharide units tested, with the lowest CA observed for Lac-C surfaces. The total SFEs of phenylglycoside layers are slightly higher than that of bare a-C (<3% difference), with negligible differences observed among saccharides. Similarly, the apolar γ^{LW} contribution does not change significantly with surface treatment, remaining approximately constant across all surfaces (<3% difference). The most striking differences among surface modifications were observed in the acid-base components. The vOCG model does not permit to directly

compare the solid acid/base contributions of a solid surface[44]; however, as discussed by Della Volpe *et al.*[44], using the same solvent triplet it is possible to examine relative changes in acid and basic character brought upon by the surface modifications studied. Bare a-C displays the minimum γ_S^- value; modification with monosaccharides increases surface basicity by 30–40%, and a further and significant increase is observed when the disaccharide Lac is used. This result is surprising as carbohydrate units are typically classified as hydrogen bond donors and thus would not be expected to increase the Lewis basicity of a surface; possible explanations for these findings are included in the Discussion section.

Surface charge density at bare and modified carbon surfaces. Electrostatic interactions can play an important role in protein adsorption phenomena given that proteins and most surfaces possess ionizable groups whose charge is dependent on pH. To investigate whether electrostatic interactions could contribute to observed changes in protein adsorption upon carbon modification, we carried out ζ-potential measurements using standard solutions of tracer particles. Table 4 summarizes ζ-potential results obtained for a-C, Gal-C and Lac-C surfaces in 1 mM NaCl solutions at pH 9.2. The ζ-potential of a-C was found to be -55 ± 3 mV, whereas surface modification with phenylglycosides led to ζ-potential values for Gal-C and Lac-C of -56.3 ± 1.9 mV and -58.0 ± 2.6 mV, respectively.

These results indicate that surface modification via aryldiazonium chemistry results in negligible changes in ζ-potential with respect to that of the bare a-C substrate. This indicates that that functionalisation with phenylglycosides via this methodology offers a route for increasing the wettability of carbon surfaces without the introduction of significant changes in electrostatic charge, as is often the case with other modifications (e.g. oxidation). The implications of these results for understanding the origin of protein antifouling properties of aryldiazonium carbohydrate layers and for the design of carbohydrate coatings with enhanced antifouling properties will be discussed in the following section.

Discussion

Protein adsorption studies on phenylglycoside layers obtained via aryldiazonium chemistry show that this functionalisation strategy leads to the formation of glycoside adlayers that impart resistance to protein adsorption. Spectroscopic and gravimetric studies carried out *ex situ*, all indicate that coated surfaces adsorb less protein than the unmodified carbon, with phenyl-lactoside groups appearing to be particularly effective at reducing unspecific adsorption.

Solvation/hydration forces have been identified as important for determining protein adsorption trends, given that solvation and desolvation processes play a key role in protein adsorption[47]. Many studies[1,7,21,47–50] have in fact concluded that highly hydrophilic surfaces tend to prevent unspecific protein adsorption, whereas hydrophobic surfaces are more likely to favor protein adsorption because they are easier to dehydrate and because they can maximize their interactions with protein hydrophobic groups through changes in protein secondary structure upon adsorption[51]. In the case of aryldiazonium carbohydrate layers, CA measurements indicate that modification results in greater hydrophilicity; this correlates well with the reduction in protein adsorption that was observed in general, for all the three proteins at both concentration ranges examined. Lac-C surfaces were found to be the most effective carbohydrate-modified surfaces in terms of repelling protein fouling, and the ones with the lowest water CA in agreement with trends that positively correlate wettability with protein resistance.

The contributions of polar and dispersive interactions resulting in the observed wettability were obtained from a multisolvent determination and analysis of Surface Free Energies (SFE). Carbohydrate surfaces obtained via aryldiazonium chemistry possess SFEs that are <3% higher than that of a-C. However the analysis based on the vOCG model suggests that large differences are introduced in the polar contributions to the total SFE, via modification of carbon with phenylglycosides. The solid-water interfacial SFE can be estimated from the data in Table 4, according to $\gamma_{SL} = \gamma_S + \gamma_L - 2\left(\sqrt{\gamma_S^{LW}\gamma_L^{LW}} + \sqrt{\gamma_S^-\gamma_L^+} + \sqrt{\gamma_S^+\gamma_L^-}\right)$, which yields values of 4.3, −0.2 and −6.6 mJ m^{-2} for a-C, Gal-C and Lac-C surfaces, respectively. The observation of decreasing fouling in the order a-C > Gal-C > Lac-C is therefore consistent with expectations based on values of γ_{SL} calculated from CA results.

Analysis of SFE components also indicates that surface modification via aryldiazonium phenyl-glycosides increases the Lewis basicity of the carbon surface: Glc-C, Man-C, Gal-C and Rha-C have 30–40% greater γ_S^- values than that of bare a-C, while phenyl-lactoside immobilization leads to a 60% increase. This is somewhat surprising as carbohydrate units are typically classified as hydrogen bond donors and, thus, would not be expected to increase the Lewis basicity of a surface. Evidence from studies on alkylthiols indicates that the presence of groups that are polar, neutral and hydrogen-bond acceptors promotes fouling resistance[21,52]. Carbohydrates have been identified as exceptions to the hydrogen-acceptor requirement, however vOCG results suggest that this might not be the case and that once carbohydrates are immobilized they can actually enhance the hydrogen-acceptor character of surfaces. We speculate that saccharide-saccharide and saccharide-water intermolecular bonding within a dense glycan layer, might result in the basicity displayed by phenylglycoside layers. It is likely that engagement of hydroxyl groups in intra-layer hydrogen bonding modulates the hydrogen bonding properties displayed by the saccharide layer at the interface.

Çarçabal *et al.*[33] carried out experimental and computational work on Man, Gal and Glc phenylglycosides and on benzyl-β-lactoside in the gas phase, showing that hydration leads to the formation of extended intra- and intermolecular hydrogen bond networks. The effect of hydration was greater in the case of benzyl-β-lactoside which was found to effectively lock into conformation through cooperative hydrogen bonding. It appears therefore likely that the water shroud associated with saccharide units would create a barrier to dehydration, and contributes to the protein resistance of carbohydrate aryldiazonium coatings. Further studies that directly probe

hydrogen bonding within aryldiazonium layers would be desirable, to determine whether trends observed for phenylglycosides in the gas phase also translate to thin films of surface-immobilized groups.

Finally, the surface-blocking effect and the steric hindrance of the saccharide moiety in phenylglycoside layers is likely to also contribute to preventing adsorption of proteins, given that coatings displaying bulky groups can screen protein-substrate interactions. Molecular density however might play a role beyond blocking access to the carbon surface, by also regulating the observed basicity of saccharide layers through intermolecular interactions within the adlayer. Thus it would be important in future studies to identify whether the observed basicity and protein resistance behavior vary significantly with molecular surface density, given the same carbohydrate motif. Conversely, carbohydrate structure might be leveraged to enhance or reduce hydrogen bonding by selecting units with different propensity to engage in inter/intra molecular hydrogen bonding. Studies of layers prepared with oligosaccharide moieties that display predominantly inter- or intra-chain bonding might reveal more about the role of inter and intra-chain interactions in determining basicity and protein fouling resistance in phenylglycoside layers.

Conclusions

We have investigated the adsorption of three proteins at carbon surfaces modified with phenylglycoside layers prepared via aryldiazonium chemistry; layers bearing both monosaccharides and a di-saccharide, lactose, were prepared and compared in their properties and protein resistance to bare carbon surfaces. Results indicate that these coatings display good protein resistance and that judicious choice of synthetic phenylglycosides can be used to optimize resistance. This is an important finding from a practical standpoint because aryldiazonium covalent immobilization is a versatile method for the functionalization of carbons and nanocarbons. Furthermore, it is known to work with a wide range of substrate materials beyond carbon and it is applicable under mild conditions from dip, spray and contact deposition methods. Thus, the methodology offers a versatile route to imparting antifouling properties onto surfaces of complex, mixed material devices, e.g. for biosensing, implantation, blood contacting applications.

A study of interfacial physical properties revealed that the protein resistance of these layers correlates well with their hydrophilic character when compared to the bare carbon material. An increase in wettability with respect to bare carbon is achieved without a significant change in surface charge density. Interestingly, we notice that mono and di-saccharides increase the Lewis basicity of the surface, contrary to expectations from typical reactivity patterns of carbohydrates in solution. This finding is consistent with empirical rules on the type of properties that lead to protein fouling resistance of thin-organic layers. We propose that the observed basicity might arise from inter- and intra- molecular hydrogen bonding networks, which could alter the acid-base properties of units exposed at the surface. Further studies would be desirable for understanding the correlation between Lewis basicity and inter- and intra-molecular hydrogen bonding in the phenylglycoside layer. The vast number of existing carbohydrate structural motifs offers an exciting landscape for exploring the potential of these layers to leverage structural variability and achieve tunable fouling resistance.

Experimental Methods

Chemicals and Materials. Diiodomethane (99%), glycerol ($\geq$99.5%), sulfuric acid (95–97%), hydrochloric acid (37%), hydrogen peroxide (30%), fluoroboric acid (48 wt.% in H_2O), sodium nitrite ($\geq$99.0%), acetonitrile (HPLC grade) and methanol (semiconductor grade) were purchased from Sigma and used without further purification. B-doped Si wafers were purchased from MicroChemicals and 10 MHz quartz crystals were purchased from International Crystal Manufacturing. Bovine Serum Albumin (BSA, $\geq$96%), Lysozyme from chicken egg white (Lyz), Fibrinogen from bovine plasma (Fib, 65–85% protein) and phosphate saline buffer tablets (PBS, 0.01 M, 0.0027 KCl and 0.137 NaCl pH 7.4) were purchased from Sigma. Millipore water was used for all experiments. Precursors 4-aminophenol-β-D-glucoopyranose (**1**), 4-aminophenol-β-D-galactopyranose (**2**), 4-aminophenol-α-D-mannopyranose (**3**), 4-aminophenol-α-L-rhamnopyranose (**4**) and 4-aminophenol-β-D-lactopyranose (**5**) (see Fig. 2) were synthesized as previously reported[20,27].

Substrate preparation. Amorphous carbon films (a-C) with thickness 73.6 ± 0.6 nm (C.I. 95%) were prepared via DC magnetron sputtering (Torr International, Inc.) at a base pressure $\leq 2 \times 10^{-6}$ mbar and a deposition Ar pressure of 7×10^{-3} mbar, as previously described[29]. Silicon wafers were cleaned in piranha solution prior to deposition (H_2SO_4 : H_2O_2 in a 3:1 ratio – *WARNING: Piranha solution is a strong oxidant and reacts violently with organic materials and presents an explosion danger; all work should be performed under a fume hood*). For infrared reflectance absorbance spectroscopy (IRRAS) measurements, Si wafers were coated prior to a-C deposition, with an optically thick (449 ± 29) nm (C.I. 95%) Ti layer via DC magnetron sputtering. Surface modification with carbohydrate moieties was carried out as previously reported[27], and following a protocol summarized in Fig. 1. Briefly, 4-aminophenyl glycosides were dissolved in acid; while keeping the solution in an ice bath, $NaNO_2$ was added yielding the corresponding aryldiazonium salt *in situ* at a final concentration of 1.0 mM. Carbon samples were immersed in the aryldiazonium salt solution for 1 h, rinsed in acetonitrile and methanol and dried under argon prior to further use.

Characterization Methods. Static contact angles (CA) were measured on a CA analyzer (FTA) under ambient conditions of temperature and humidity; samples were rinsed in methanol immediately prior to CA characterization[45] and a minimum of three CA measurements were obtained for each surface. Spectroscopic Ellipsometry (SE) was carried out using an alpha-SETM ellipsometer (J.A. Woolam Co.). a-C films were deposited on clean Si wafers and measured at 65°, 70°, 75° incidence angle over the 370–900 nm range; SE data was then fitted using the CompleteEASE® software package using a three layer model to account for Si, a-C and air phases (see Supporting Information). ζ-potential measurements were carried out using a Malvern Zetasizer

Nano-ZS equipped with a surface ζ-potential cell; standard 300 nm latex tracer particle suspensions, NaCl 1 mM, at pH 9.2 (Malvern, DTS1235) were used in all experiments. IRRAS was carried out on a Fourier Transform Infrared (FTIR) spectrometer (Tensor 27, Bruker) equipped with a Mercury Cadmium Telluride (MCT) detector, a specular reflectance accessory (VeeMax II), and a ZnSe polarizer. Spectra were taken at 80° incidence using p-polarized light; 100 spectra were collected at 4 cm^{-1} resolution using a bare substrate as background. All spectra reported in this work were baseline corrected using commercial FTIR software (WinFIRST). Quartz Crystal Microbalance (QCM) measurements were carried out *ex situ* following a previously reported procedure[27]. The resonant frequency of a carbon coated QCM crystal was measured in air before and after protein adsorption, and the difference was used to calculate the mass change at the crystal via the Sauerbrey equation[53]. Measurements were carried out in a home-built chamber at the same temperature before and after modification; in the case of lactose-modified surfaces it was necessary to introduce a dessicant (Drierite®) in the measurement chamber in order to achieve frequency stability, likely due to water adsorption by surface-bound disaccharide units. Thickness and surface roughness measurements were carried out via Atomic Force Microscopy (AFM, Asylum Research) using silicon catilevers.

Protein adsorption experiments. BSA, Lyz and Fib were dissolved in 0.01 M PBS buffer (pH 7.4) at different concentrations for each protein: 0.5 and 20 mg/mL for BSA, 0.1 and 4.3 mg/mL for Lyz and 2.5 mg/mL for Fib. Carbohydrate-coated and bare a-C surfaces were incubated in buffered protein solutions for 1 h at ambient temperature (20 °C). Substrates were rinsed, immersed for 10 min in water, and finally dried under argon prior to characterization.

References

1. Ratner, B. D., Hoffman, A. S., Schoen, F. J. & Lemons, J. E. *Biomaterials Science*. 2nd edn, (Elsevier Academic Press, 2004).
2. Andrade, J. D., Hlady, V., Feng, L. & Tingey, K. In *Interfacial phenomena and bioproducts Bioprocess Technology* (eds J. L. Brash & P. W. Wojciechowski) Ch. 2, 19–55 (Marcel Dekker, 1996).
3. Monopoli, M. P., Aberg, C., Salvati, A. & Dawson, K. A. Biomolecular coronas provide the biological identity of nanosized materials. *Nat Nano* **7,** 779–786 (2012).
4. Aggarwal, P., Hall, J. B., McLeland, C. B., Dobrovolskaia, M. A. & McNeil, S. E. Nanoparticle interaction with plasma proteins as it relates to particle biodistribution, biocompatibility and therapeutic efficacy. *Adv. Drug Delivery Rev*. **61,** 428–437 (2009).
5. Cifuentes-Rius, A., de Puig, H., Kah, J. C. Y., Borros, S. & Hamad-Schifferli, K. Optimizing the Properties of the Protein Corona Surrounding Nanoparticles for Tuning Payload Release. *ACS Nano* **7,** 10066–10074 (2013).
6. Roy, D. Surface Plasmon Resonance Spectroscopy of Dielectric Coated Gold and Silver Films on Supporting Metal Layers: Reflectivity Formulas in the Kretschmann Formalism. *Appl. Spectrosc.* **55,** 1046–1052 (2001).
7. Stueber, M. *et al.* Surface topography, surface energy and wettability of magnetron-sputtered amorphous carbon (a-c) films and their relevance for platelet adhesion. *Adv. Eng. Mater.* **9,** 1114–1122 (2007).
8. Lu, F. *et al.* Advances in Bioapplications of Carbon Nanotubes. *Adv. Mater.* **21,** 139–152 (2009).
9. Mochalin, V. N., Shenderova, O., Ho, D. & Gogotsi, Y. The properties and applications of nanodiamonds. *Nat Nano* **7,** 11–23 (2012).
10. McCreery, R. L. Advanced Carbon Electrode Materials for Molecular Electrochemistry. *Chem. Rev.* **108,** 2646–2687 (2008).
11. Lockett, M. R. & Smith, L. M. Carbon Substrates: A Stable Foundation for Biological Arrays. *Annu. Rev. Anal. Chem.* **8,** 17.11–17.23 (2015).
12. Clare, T. L., Clare, B. H., Nichols, B. M., Abbott, N. L. & Hamers, R. J. Functional Monolayers for Improved Resistance to Protein Adsorption: Oligo (ethylene glycol)-Modified Silicon and Diamond Surfaces. *Langmuir* **21,** 6344–6355 (2005).
13. Trouillon, R., O'Hare, D. & Einaga, Y. Effect of the doping level on the biological stability of hydrogenated boron doped diamond electrodes. *Phys. Chem. Chem. Phys.* **13,** 5422–5429 (2011).
14. Mu, Q. *et al.* Chemical Basis of Interactions Between Engineered Nanoparticles and Biological Systems. *Chem. Rev.* **114,** 7740–7781 (2014).
15. Harrison, C. Nanotechnology: Biological proteins knock nanoparticles off target. *Nat Rev Drug Discov* **12,** 264–264 (2013).
16. Banerjee, I., Pangule, R. C. & Kane, R. S. Antifouling Coatings: Recent Developments in the Design of Surfaces That Prevent Fouling by Proteins, Bacteria, and Marine Organisms. *Adv. Mater.* **23,** 690–718 (2011).
17. Ostuni, E. *et al.* Self-assembled monolayers that resist the adsorption of proteins and the adhesion of bacterial and mammalian cells. *Langmuir* **17,** 6336–6343 (2001).
18. Hilkens, J., Ligtenberg, M. J. L., Vos, H. L. & Litvinov, S. V. Cell membrane-associated mucins and their adhesion-modulating property. *Trends Biochem. Sci.* **17,** 359–363 (1992).
19. Sumiyoshi, M. *et al.* Antiadhesive Character of Mucin O-glycans at the Apical Surface of Corneal Epithelial Cells. *Invest. Ophthalmol. Vis. Sci.* **49,** 197–203 (2008).
20. Angione, M. D. *et al.* Enhanced antifouling properties of carbohydrate coated poly (ether sulfone) membranes. *ACS Appl. Mater. Interfaces* **7,** 17238–17246 (2015).
21. Ederth, T. *et al.* Resistance of Galactoside-Terminated Alkanethiol Self-Assembled Monolayers to Marine Fouling Organisms. *ACS Appl. Mater. Interfaces* **3,** 3890–3901 (2011).
22. Österberg, E. *et al.* Comparison of polysaccharide and poly (ethylene glycol) coatings for reduction of protein adsorption on polystyrene surfaces. *Colloids Surf A Physicochem Eng Asp.* **77,** 159–169 (1993).
23. Holland, N. B., Qiu, Y. X., Ruegsegger, M. & Marchant, R. E. Biomimetic engineering of non-adhesive glycocalyx-like surfaces using oligosaccharide surfactant polymers. *Nature* **392,** 799–801 (1998).
24. Perrino, C., Lee, S., Choi, S. W., Maruyama, A. & Spencer, N. D. A Biomimetic Alternative to Poly (ethylene glycol) as an Antifouling Coating: Resistance to Nonspecific Protein Adsorption of Poly (l-lysine)-graft-dextran. *Langmuir* **24,** 8850–8856 (2008).
25. Lord, M. S., Pasqui, D., Barbucci, R. & Milthorpe, B. K. Protein Adsorption on Derivatives of Hyaluronan. *Macromol. Symp.* **266,** 17–22 (2008).
26. Mussard, W., Kebir, N., Kriegel, I., Estève, M. & Semetey, V. Facile and Efficient Control of Bioadhesion on Poly (dimethylsiloxane) by Using a Biomimetic Approach. *Angew. Chem. Intl. Ed.* **50,** 10871–10874 (2011).
27. Jayasundara, D. R. *et al.* Carbohydrate Coatings via Aryldiazonium Chemistry for Surface Biomimicry. *Chem. Mater.* **25,** 4122–4128 (2013).
28. Barriere, F. & Downard, A. J. Covalent modification of graphitic carbon substrates by non-electrochemical methods. *J. Solid State Electrochem.* **12,** 1231–1244 (2008).
29. Cullen, R. J. *et al.* Spontaneous grafting of nitrophenyl groups on amorphous carbon thin films: A structure-reactivity investigation. *Chem. Mater.* **24,** 1031–1040 (2012).
30. Socrates, G. *Infrared and Raman Characteristic Group Frequencies: Tables and Charts*. (John Wiley & Sons, 2001).

31. Brooksby, P. A. & Downard, A. J. Electrochemical and Atomic Force Microscopy Study of Carbon Surface Modification via Diazonium Reduction in Aqueous and Acetonitrile Solutions. *Langmuir* **20,** 5038–5045 (2004).
32. Anariba, F., DuVall, S. H. & McCreery, R. L. Mono- and Multilayer Formation by Diazonium Reduction on Carbon Surfaces Monitored with Atomic Force Microscopy "Scratching". *Anal. Chem.* **75,** 3837–3844 (2003).
33. Çarçabal, P. *et al.* Hydrogen Bonding and Cooperativity in Isolated and Hydrated Sugars: Mannose, Galactose, Glucose, and Lactose. *J. Am. Chem. Soc.* **127,** 11414–11425 (2005).
34. Jockusch, R. A. *et al.* Probing the Glycosidic Linkage: UV and IR Ion-Dip Spectroscopy of a Lactoside. *J. Am. Chem. Soc.* **126,** 5709–5714 (2004).
35. Combellas, C., Jiang, D.-e., Kanoufi, F., Pinson, J. & Podvorica, F. I. Steric Effects in the Reaction of Aryl Radicals on Surfaces. *Langmuir* **25,** 286–293 (2009).
36. Wasilewska, M., Adamczyk, Z. & Jachimska, B. Structure of Fibrinogen in Electrolyte Solutions Derived from Dynamic Light Scattering (DLS) and Viscosity Measurements. *Langmuir* **25,** 3698–3704 (2009).
37. Höök, F. *et al.* A comparative study of protein adsorption on titanium oxide surfaces using *in situ* ellipsometry, optical waveguide lightmode spectroscopy, and quartz crystal microbalance/dissipation. *Colloids Surf., B* **24,** 155–170 (2002).
38. Pasche, S., Vörös, J., Griesser, H. J., Spencer, N. D. & Textor, M. Effects of Ionic Strength and Surface Charge on Protein Adsorption at PEGylated Surfaces. *J. Phys. Chem. B* **109,** 17545–17552 (2005).
39. Kratz, A., Ferraro, M., Sluss, P. M. & Lewandrowski, K. B. Normal Reference Laboratory Values. *N. Engl. J. Med.* **351,** 1548–1563 (2004).
40. Rampling, M. W. The solubility of fibrinogen in solutions containing dextrans of various molecular weights. *Biochem. J.* **143,** 767–769 (1974).
41. Feng, L. & Andrade, J. D. Protein adsorption on low temperature isotropic carbon: III. Isotherms, competitivity, desorption and exchange of human albumin and fibrinogen. *Biomaterials* **15,** 323–333 (1994).
42. Van Oss, C. J., Chaudhury, M. K. & Good, R. J. Interfacial Lifshitz-van der Waals and polar interactions in macroscopic systems. *Chem. Rev.* **88,** 927–941 (1988).
43. van Oss, J. C. *Interfacial Forces in Aqueous Media*. 1st edn, (Marcel Dekker, 1994).
44. Della Volpe, C., Maniglio, D., Brugnara, M., Siboni, S. & Morra, M. The solid surface free energy calculation: I. In defense of the multicomponent approach. *J. Colloid Interface Sci.* **271,** 434–453 (2004).
45. Zebda, A., Sabbah, H., Ababou-Girard, S., Solal, F. & Godet, C. Surface energy and hybridization studies of amorphous carbon surfaces. *Appl. Surf. Sci.* **254,** 4980–4991 (2008).
46. Leezenberg, P. B., Johnston, W. H. & Tyndall, G. W. Chemical modification of sputtered amorphous-carbon surfaces. *J. Appl. Phys.* **89,** 3498–3507 (2001).
47. Kasemo, B. Biological surface science. *Surf. Sci.* **500,** 656–677 (2002).
48. Kirschner, C. M. & Brennan, A. B. Bio-Inspired Antifouling Strategies. *Annu. Rev. Mater. Res.* **42,** 211–229 (2012).
49. Morra, M. *Water in Biomaterials Surface Science* (John Wiley & Sons, Baffins Lane, Chichester, 2001).
50. Ham, H. O., Park, S. H., Kurutz, J. W., Szleifer, I. G. & Messersmith, P. B. Antifouling Glycocalyx-Mimetic Peptoids. *J. Am. Chem. Soc.* **135,** 13015–13022 (2013).
51. Feng, L. & Andrade, J. D. Protein adsorption on low temperature isotropic carbon. 1. Protein conformational change probed by differential scanning calorimetry. *J. Biomed. Mater. Res.* **28,** 735–743 (1994).
52. Ostuni, E., Chapman, R. G., Holmlin, R. E., Takayama, S. & Whitesides, G. M. A Survey of Structure−Property Relationships of Surfaces that Resist the Adsorption of Protein. *Langmuir* **17,** 5605–5620 (2001).
53. Sauerbrey, G. Z. Use of quartz vibration for weighing thin films on a microbalance. *J. Physik* **155,** 206–212 (1959).

Acknowledgements

The authors would like to thank Dr. B. Ramesh and T. Woods for access to contact angle instrumentation, and S. Mills for AFM assistance. This publication has emanated from research conducted with the financial support of Science Foundation Ireland (SFI) under Grant Number 12/IP/1273. MDA and TD acknowledge support from Enterprise Ireland Grant Number CF/2012/2634; JAB acknowledges support from grant GOIPG/2014/399.

Author Contributions

F.Z. carried out the majority of the experimental work and data analysis and wrote the manuscript together with PEC. M.D.A. assisted with protein adsorption measurements; T.D. synthesized compounds; J.A.B. and R.J.C. contributed with ellipsometry and AFM measurements; J.M.V. developed protocols for electrokinetic measurements. E.M.S. and P.E.C. led the work and contributed to experimental design. All authors reviewed the manuscript.

Additional Information

Competing financial interests: The authors declare no competing financial interests.

How to cite this article: Zen, F. *et al.* Modulation of Protein Fouling and Interfacial Properties at Carbon Surfaces via Immobilization of Glycans Using Aryldiazonium Chemistry. *Sci. Rep.* **6**, 24840; doi: 10.1038/srep24840 (2016).

LANGMUIR

Article

pubs.acs.org/Langmuir

Nanoplasmonic Sensing at the Carbon-Bio Interface: Study of Protein Adsorption at Graphitic and Hydrogenated Carbon Surfaces

Federico Zen,[†] Vasilios D. Karanikolas,[‡] James A. Behan,[†] Jenny Andersson,[§] Guido Ciapetti,[†] A. Louise Bradley,[‡] and Paula E. Colavita*[,†]

[†]School of Chemistry and AMBER Research Centre and [‡]School of Physics and CRANN, Trinity College Dublin, College Green, Dublin, Ireland

[§]Insplorion AB, Medicinaregatan 8A, 413 90 Göteborg, Sweden

Supporting Information

ABSTRACT: Various forms of carbon are known to perform well as biomaterials in a variety of applications and an improved understanding of their interactions with biomolecules, cells, and tissues is of interest for improving and tailoring their performance. Nanoplasmonic sensing (NPS) has emerged as a powerful technique for studying the thermodynamics and kinetics of interfacial reactions. In this work, the in situ adsorption of two proteins, bovine serum albumin and fibrinogen, were studied at carbon surfaces with differing chemical and optical properties using nanoplasmonic sensors. The carbon material was deposited as a thin film onto NPS surfaces consisting of 100 nm Au nanodisks with a localized plasmon absorption peak in the visible region. Carbon films were fully characterized by X-ray photoelectron spectroscopy, atomic force microscopy, and spectroscopic ellipsometry. Two types of material were investigated: amorphous carbon (a-C), with high graphitic content and high optical absorptivity, and hydrogenated amorphous carbon (a-C:H), with low graphitic content and high optical transparency. The optical response of the Au/carbon NPS elements was modeled using the finite difference time domain (FDTD) method, yielding simulated analytical sensitivities that compare well with those observed experimentally at the two carbon surfaces. Protein adsorption was investigated on a-C and a-C:H, and the protein layer thicknesses were obtained from FDTD simulations of the expected response, yielding values in the 1.8−3.3 nm range. A comparison of the results at a-C and a-C:H indicates that in both cases fibrinogen layers are thicker than those formed by albumin by up to 80%.

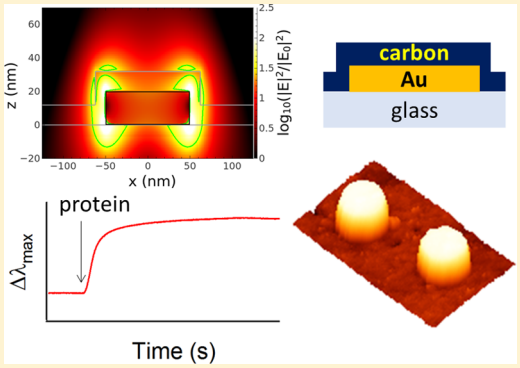

INTRODUCTION

Carbon coatings, such as amorphous carbon (a-C) and hydrogen-doped carbon (a-C:H), have emerged as good biomaterials and have been integrated into several biodevices like catheters, stents, sensors, medical guidewires, surgical needles, orthopedic implants, and prostheses.[1−3] The success of carbon coatings in biological applications is partly due to a combination of physical/chemical properties that underpins their good performance, such as chemical inertness, low frictional coefficient, and high wear resistance.[4,5] However, the durability, functionality, and bioresponse of artificial materials in vivo are limited by their interaction with blood and tissue.[2,6] The competitive adsorption of plasma proteins (such as albumin and fibrinogen) occurring at an early stage after implantation, is considered to have a crucial effect in determining the response of the host when in contact with biomaterials.[6−10] For this reason, much effort has been dedicated to the description of protein adsorption and/or binding at carbon surfaces with different physical and chemical properties by using both in situ and ex situ methods.[11−16] However, only a few of the techniques applied to these studies are able to monitor dynamic interactions in situ, within a fluid environment that may be tailored to model likely conditions encountered in vivo.[17]

Surface plasmon resonance (SPR)[14,17−19] has been recognized as a powerful and advantageous label-less method for studying the thermodynamics and kinetics of interfacial interactions in situ.[17] SPR modes are hybrid modes of the free electrons of a metal and the electromagnetic field. These modes are confined at a metal−dielectric interface, propagate along it, and are extremely sensitive to interfacial changes in dielectric properties, such as those that arise from adsorption, binding, or cell adhesion events. Thin metal films are necessary to support surface plasmons in sensing applications, and the majority of commercial instruments currently used for quantitative analysis and screening rely on this type of sensing element. More recently, nanoplasmonic sensing (NPS) based on the physical phenomenon of localized surface plasmon resonance (LSPR) has emerged as a valuable alternative. In LSPR modes, light interacts with particles much smaller than

Received: February 22, 2017
Revised: April 6, 2017
Published: April 11, 2017

DOI: 10.1021/acs.langmuir.7b00612
Langmuir 2017, 33, 4198−4206

the incident wavelength, leading to a hybrid confined mode with a characteristic resonant frequency that depends on optical properties of the metal and dielectric and on nanoparticle geometry.[20−23] LSPR can be leveraged for biological and chemical sensing by monitoring the wavelength shifts of the characteristic resonance, which take place in response to changes in the local refractive index.[20,21] Compared to conventional SPR, NPS offers advantages such as a lower sensitivity to bulk changes, the ability to modulate the optical operating range through careful nanostructure design, and greater hardware flexibility and simplicity.[20] Technical developments in the large-scale fabrication of nanoscale metallic structures have been key to the exploitation of LSPR, resulting in increased interest in LSPR sensing strategies.[20,22,23]

This work describes the application of NPS to in situ studies of the carbon−bio interface. SPR methods have found limited applications so far for the study of interfacial events at carbon surfaces in biological media because of the requirement of metal surfaces for sustaining SPR modes. Lockett et al.[24] demonstrated, however, that it is possible to sustain SPR modes at the carbon−liquid interface via deposition of thin carbon coatings of optimized thickness onto Au SPR sensors, a strategy that had previously proven viable for the study of interactions at polymeric surfaces.[25,26] Metal/carbon sensing platforms have since led to SPR sensing of DNA binding,[24,27] cell binding,[28] protein adsorption,[12,29,30] and immunosensing[31] at carbon surfaces, whereby the authors demonstrated that SPR is a viable method for monitoring carbon−biomolecule interactions. However, few experimental studies report a comparison of different carbon surfaces under comparable conditions, partly because of the broad variability of the optical properties of carbon materials, which adds complexity to the analysis of SPR data from metal/carbon/biomolecule multilayers. Notably, Saitoh and co-workers presented a comparative SPR study of albumin adsorption at hydrogenated carbons with different chemical composition[29] but pointed out that a quantitative determination of the thickness of adsorbed layers from angle shift data using Fresnel equations is challenging due to strong correlation in the multilayer model between thickness and optical constants.

In this work, NPS was used in combination with ellipsometry and computational methods to estimate the thickness of the protein layer at two carbon substrates with differing optical properties. To our knowledge NPS has not been used for the study of interactions at carbon coatings; herein, we apply a recently reported NPS method developed by Kasemo et al. based on Au nanodisk sensing elements.[32−34] Studies of interfacial chemistry on this NPS platform have been typically carried out using sensors coated with thin films of dielectrics, such as metal oxides or silica, which ensure a homogeneous surface chemistry and allow flexibility in terms of the chemical reactions under study.[35] Previous work by Cho and co-workers using biomolecules has reported a detailed study of the effect of dielectric coatings on interfacial chemistry and sensitivity.[34] In this work, the applicability of these nanostructured sensors to the study of protein adsorption at carbon surfaces in real time is demonstrated. Carbon coatings differ from typical oxide spacer layers, as their optical properties can vary significantly with electronic behavior that spans the semimetallic semiconductor−insulator range.[36] Two types of carbon with differing composition were chosen to investigate the effect of carbon chemistry on protein adsorption: a-C, a graphitic carbon, and a-C:H, a hydrogenated, polymer-like, and sp^3-rich carbon. The two plasma proteins used, albumin and fibrinogen, were chosen because of their importance for understanding the response of biomaterials after implantation. A quantitative modeling of NPS results was carried out using the finite difference time domain (FDTD) method for determining protein layer thickness, and finally, predictions from FDTD methods were correlated to results from complementary spectroscopic and microscopic methods.

EXPERIMENTAL METHODS

Chemicals and Materials. Ethylene glycol (99.8%), methanol (semiconductor grade), bovine serum albumin (BSA, ≥96%), fibrinogen from bovine plasma (Fib, 65−85% protein), and phosphate saline buffer tablets (PBS, 0.01 M, 0.0027 M KCl and 0.137 M NaCl, pH 7.4) were purchased from Sigma and used without further purification. B-doped Si wafers were purchased from MicroChemicals (5−10 Ohms), and NPS sensor chips were purchased from Insplorion AB. Millipore water was used for all experiments.

Substrate Preparation. Amorphous carbon films were prepared via DC magnetron sputtering (Torr International, Inc.) at a base pressure $\lesssim 2 \times 10^{-6}$ mbar and a deposition pressure of 7×10^{-3} mbar as previously described.[37] Two distinct films were prepared by varying the H_2/Ar gas ratio: one type of film was sputtered using Ar and shall be referred to as a-C from here onward; the second type of film was sputtered using 10% H_2 in Ar, resulting in a hydrogen-doped material referred to as a-C:H. Silicon wafers were cleaned in piranha solution prior to deposition (H_2SO_4/H_2O_2 in a 3:1 ratio; ***Warning!*** *Piranha solution is a strong oxidant and reacts violently with organic materials and presents an explosion danger; all work should be performed under a fume hood*). For spectroscopic ellipsometry (SE) and atomic force microscopy (AFM) characterization, samples were deposited on clean Si wafers. For infrared reflectance absorbance spectroscopy (IRRAS) measurements, Si wafers were first coated with an optically thick (~450 nm) Ti layer via DC magnetron sputtering,[38] and subsequently with either a-C or a-C:H films of approximately 70 and 40 nm thickness, respectively. For NPS measurements, sensor chips were cleaned under UV/ozone for 1 h, rinsed with methanol, and dried with argon prior to deposition of a-C and a-C:H; the thickness of the layers was determined to be (10.1 ± 0.5) nm and (12.2 ± 2.1) nm for a-C and a-C:H (95% C.I.), respectively (see Supporting Information).

Characterization Methods. Spectroscopic ellipsometry (SE) was carried out using an alpha-SETM ellipsometer (J.A. Woolam Co.). Carbon films were deposited on clean Si wafers and measured at 65°, 70°, and 75° incidence angles over the 370−900 nm range; SE data was then fitted using the CompleteEASE software package using a three layer model to account for Si, carbon, and air phases (see Supporting Information).[38,39] IRRAS spectra were collected on a Fourier transform infrared (FTIR) spectrometer (Tensor 27, Bruker) equipped with a mercury cadmium telluride (MCT) detector, a specular reflectance accessory (VeeMax II), and a zinc selenide polarizer. Spectra were taken at 80° incidence using p-polarized light; 100 spectra were collected at 4 cm^{-1} resolution using a bare substrate as background. All spectra reported in this work were baseline corrected using commercial FTIR software (WinFIRST). To account for differences in optical enhancement in IRRAS peaks on a-C and a-C:H, spectral intensities were normalized by the intensity of the C═O stretching absorbance of a reference 5.7 nm poly(methyl methacrylate) (PMMA) layer. UV−vis transmission measurements of plasmon extinction spectra were obtained in air for bare and carbon-coated NPS sensors over the wavelength range 500−800 at 1 nm resolution (Shimadzu UV-2401 PC). Thickness and surface roughness measurements were carried out via AFM (Asylum Research) using Au-coated silicon cantilevers (NT-MDT) in tapping mode (1 Hz and 512 scan lines).

Nanoplasmonic Sensing (NPS). Measurements of protein adsorption were conducted using an XNano instrument (Insplorion AB, Gothenburg, Sweden). Ensemble-averaged recordings of the resonance peak were collected in optical transmission mode. Glass

DOI: 10.1021/acs.langmuir.7b00612
Langmuir 2017, 33, 4198−4206

sensor chips (Insplorion AB) with deposited gold nanodisks (50 nm radius, 20 nm thickness, 8% surface coverage) fabricated by hole-mask colloidal lithography were coated with sputter-deposited a-C or a-C:H layers as described above and mounted in an optical flow cell for in situ measurements. Sample solutions were flowed through the measurement chamber via a peristaltic pump at a continuous rate of 50 μL min^{-1}; the protein concentration was 7 μM, equivalent to 0.5 and 2.5 mg mL^{-1} for BSA and Fib, respectively. The bulk refractive index of reference ethylene glycol/water solutions used for calibrations was determined using a refractometer (PAL-1, ATAGO Co., Tokyo, Japan).

Computational Modeling of Sensor Response. The Maxwell equations were solved using the finite difference time domain (FDTD) method, as implemented in the commercial package FDTD Solutions from Lumerical. The optical response of the nanostructured sensing elements comprising the coated nanodisk and the substrate were modeled based on their complex refractive index with values for the specific a-C and a-C:H layers being experimentally determined via spectroscopic ellipsometry.

RESULTS AND DISCUSSION

Carbon films used in our experiments were deposited via magnetron sputtering using Ar and H_2/Ar as deposition gases; these films had previously been characterized via a combination of spectroscopic methods.[37] Briefly, a-C and a-C:H films consist of approximately 80 and 17% trigonally bonded carbon (sp^2 centers), respectively, as estimated via X-ray photoelectron spectroscopy (XPS) and Raman spectroscopy. These films also contain oxidized groups resulting in a 7−9% O/C atomic ratio for both a-C and a-C:H, as determined via XPS. The a-C films are highly graphitic and possess good conductivity, whereas a-C:H films are insulating.[37] Spectroscopic ellipsometry was used to determine optical properties of the films. The optical constants, obtained as discussed in the Supporting Information and previous work,[38] were consistent with the difference in graphitic content between the two materials. The Tauc gap and absorption coefficients were E_T = 0.66 ± 0.01 eV and α(632 nm) = (77.2 ± 0.7) × 10^3 cm^{-1} for a-C (95% C.I.) and E_T = 1.77 ± 0.01 eV and α(632 nm) = (5.08 ± 0.17) × 10^3 cm^{-1} for a-C:H (95% C.I.), thus indicating that a-C films are more metal-like and optically absorbing than a-C:H.[36,40] The real part of the refractive index was also different for the two materials: n(632 nm) = 2.117 ± 0.003 for a-C (95% C.I.), which is consistent with values obtained for graphitic amorphous carbons, whereas n(632 nm) = 1.672 ± 0.003 for a-C:H (95% C.I.), consistent with a low density highly hydrogenated amorphous carbon film.[36,41]

The two types of carbon materials were used for in situ studies of protein adsorption using NPS methods. Sensor chips consisting of a glass substrate with nanofabricated gold nanodisks were coated by layers of either a-C or a-C:H, as shown in the schematic in Figure 1; the carbon layers were confirmed to be continuous at the thicknesses of (10.1 ± 0.5) nm and (12.2 ± 2.1) nm used for NPS experiments (see Supporting Information). The gold nanodisks are randomly distributed on the glass substrate with 8% surface coverage,[33] yielding an average disk-to-disk separation large enough for the discs to be considered independent from each other. The sensors were mounted in a flow cell, and the plasmon excitation associated with the gold nanodisks was measured in transmittance mode; the center of mass of the excitation peak was monitored as a function of time during flow experiments. Figure 1 shows typical plasmon resonance peaks obtained in air for a bare Au sensor and for Au/a-C- and Au/a-C:H-coated sensors. The presence of an ∼10 nm thick carbon coating does not suppress the plasmon resonance despite the carbon being a continuous layer; however, it has an effect on both resonance peak position and full-width-at-half-maximum (fwhm), which can in turn affect the sensitivity of the LSPR modes.

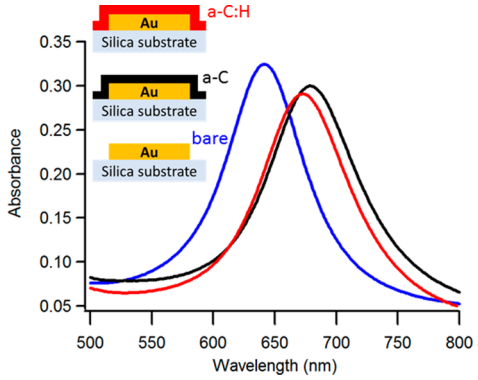

Figure 1. Plasmon absorbance spectrum in air recorded at bare (blue line) and a-C (black line)- and a-C:H (red line)-coated sensors. The inset at the top left of the figure shows schematics of the nanodisk structures that result in the LSPR spectra.

The effect of carbon coatings on the sensitivity of LSPR chips was investigated using a combination of computational and experimental methods. The wavelength of maximum extinction, λ_{max}, and the fwhm are sensitive to changes in the dielectric properties of the medium at the nanodisk interface. FDTD simulations were used to calculate the plasmon extinction of coated Au nanodisks: the geometry used in the simulations is as shown in Figure 1 with the Au nanodisk possessing 50 nm radius and 20 nm thickness. Because of the low surface coverage, it is assumed that nanodisks are effectively decoupled, and a single nanodisk element was thus considered in all simulations. This assumption was found to be satisfactory as will be discussed below. The carbon coating was considered as a conformal, uniform layer of 10 and 12 nm for a-C and a-C:H, respectively, which corresponds to the experimentally determined thickness for each layer. The optical constants for Au were obtained from Johnson and Christy;[42] the refractive index for the glass substrate was real and constant at 1.459 over the wavelength range explored, and those of the a-C and a-C:H films were obtained from experimental ellipsometry results (see Supporting Information). Panels a and b in Figure 2 show the logarithm of the absolute value of the total field distribution in the xz-plane for a single nanodisk coated with a-C and a-C:H, respectively. The exciting electromagnetic field is normally incident on the top of the nanostructure, and the excitation wavelengths are chosen to coincide with the maxima of the LSPR extinction in each case. We observe that the field is enhanced by up to 2 orders of magnitude at the edges of the Au nanodisk. The field around the Au nanodisk extends further beyond the carbon coating for a-C:H compared to that for a-C, in agreement with the imaginary part of the refractive index for a-C being higher than for a-C:H. A simulation of the effect of carbon coating thickness on the position and shape of the plasmon extinction shows that the presence of both carbon coatings leads to a red shift in the plasmon position and an increase in the fwhm of the peak (see Supporting Information). However, the peak shift and peak broadening effects for a-C are significantly more pronounced than for a-C:H, in agreement with the former being the material with higher optical losses. The field distribution observed in Figure 2a and b results from plane-wave excitation of the LSPR dipole mode. The

DOI: 10.1021/acs.langmuir.7b00612
Langmuir 2017, 33, 4198−4206

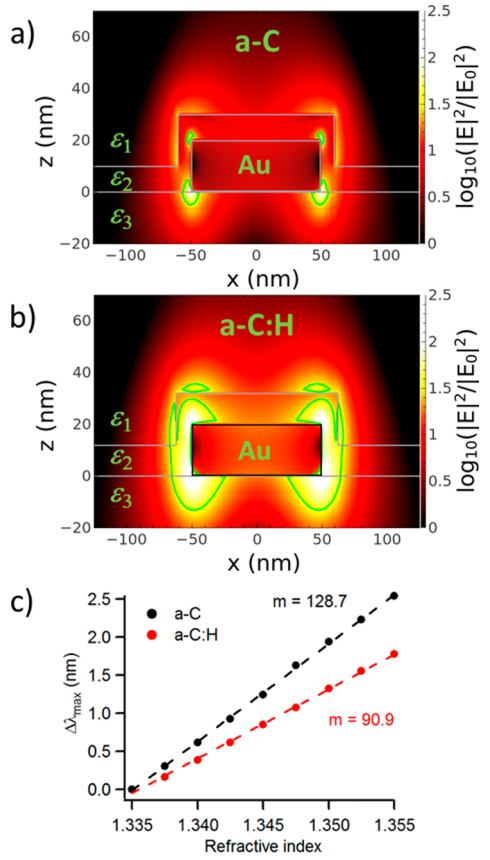

Figure 2. Electric field intensity distribution around isolated nanodisks immersed in PBS obtained via FDTD modeling at the wavelength corresponding to the maximum of the LSPR. The refractive indices used in the simulation are reported as ε_1, ε_2, and ε_3 for the aqueous medium (ε_1 = 1.333), the carbon coating, and the glass substrate, respectively. The green line in the graphs indicates a factor of 30 increase in the electric field intensity. (a) Field distribution around an isolated Au/a-C-coated nanodisk at 797 nm. (b) Field distribution around an isolated Au/a-C:H-coated nanodisk at 748 nm. (c) Calibration plots obtained via FDTD methods for Au/a-C (black line)- and Au/a-C:H (red line)-coated nanodisks; the slope yielding the analytical sensitivity is reported next to the corresponding curve.

differences in field distributions observed for a-C and a-C:H coatings suggest that the sensitivity of NPS elements to adsorption/binding might be significantly affected depending on the type of carbon used to coat the sensor. A simulated calibration experiment was thus carried out in which the resonance maximum position, $\Delta\lambda_{max}$, was calculated as a function of the refractive index in the medium surrounding the carbon (medium 1). The refractive index range explored was chosen to be identical to one that could be accessed experimentally using water/ethylene glycol solutions.[33,34] Figure 2c shows the calibration plots obtained via FDTD methods for a-C- and a-C:H-coated sensors. The figure indicates that in both cases the LSPR at the nanodisk is sensitive to changes at the carbon−solution interface. The slopes obtained were 128.7 and 90.9 nm per unit change in refractive index for a-C and a-C:H, respectively, indicating that the more graphitic film results in higher sensitivity to refractive index changes.

The sensitivity of carbon-coated sensors was also investigated experimentally by measuring the shift $\Delta\lambda_{max}$ relative to the refractive index of the liquid in the flow cell. Figure 3a shows

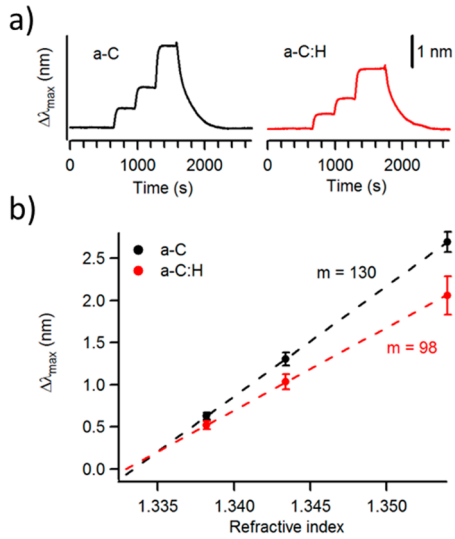

Figure 3. Sensitivity test obtained at a-C (black, left)- and a-C:H (red, right)-coated sensors. (a) NPS shift $\Delta\lambda_{max}$ as a function of time measured after water/ethylene glycol solutions of different refractive indices are injected into the cell. (b) Calibration plot of measured $\Delta\lambda_{max}$ vs refractive index of the water/ethylene glycol solution; the slope yielding the analytical sensitivity is reported next to the corresponding curve. Error bars indicate 95% C.I. calculated from sample size n = 5 and 3 for a-C and a-C:H, respectively.

the typical dependence of $\Delta\lambda_{max}$ as a function of time obtained for a-C- and a-C:H-coated sensors as water/ethylene glycol solutions of different refractive indices are injected into the cell. The staircase response was used to generate a calibration plot as shown in Figure 3b, which shows that the experimental $\Delta\lambda_{max}$ varies linearly with refractive index. As seen in the calibration plot, changes in the medium refractive index cause a larger peak shift in the optical extinction spectrum of a-C- than of a-C:H-coated sensors, in agreement with computational predictions. The average experimental slopes were found to be 130 ± 8 and 98 ± 12 nm per unit change in the refractive index for a-C- and a-C:H-coated sensors, respectively. The experimentally determined sensitivities therefore compare very well with those obtained via FDTD simulations. This further confirms that the Au nanodisks can be assumed to be decoupled.

To evaluate how proteins adsorb at different carbon substrates, both a-C and a-C:H sensors were exposed to buffered protein solutions. All sensors were mounted and calibrated in advance of all measurements using at least three water/ethylene glycol solutions. After calibration, PBS was injected first, followed by the protein solution and a final rinsing step with PBS. The calibration process was repeated at the end of each experiment to exclude any changes to the sensor sensitivity that might arise from adsorbed protein layers. Panels a and b in Figure 4 show plots of $\Delta\lambda_{max}$ vs time obtained on a-C- and a-C:H-coated sensors, respectively, after the injection of protein solutions followed by injection of PBS. The full experiment, including the calibration steps, is reported in the Supporting Information. The exposure of carbon-coated sensors to protein solutions results in a red shift of the LSPR that stabilizes to a constant value within 15 min after the injection. Given that the refractive index of the protein solutions was statistically indistinguishable from that of the PBS solution (see Supporting Information), the wavelength shift can be unequivocally attributed to the adsorption of

DOI: 10.1021/acs.langmuir.7b00612
Langmuir 2017, 33, 4198−4206

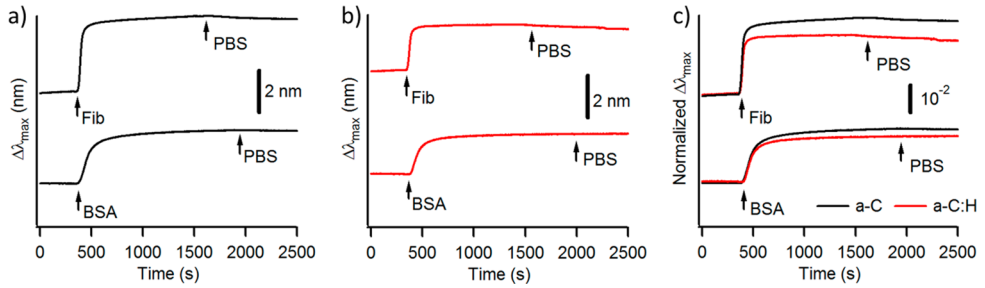

Figure 4. NPS wavelength shift, $\Delta\lambda_{max}$, as a function of time measured at (a) a-C- and (b) a-C:H-coated sensors for in situ protein experiments. (c) Normalized $\Delta\lambda_{max}$ as a function of time calculated using the initial calibration of the sensor at both a-C (black line) and a-C:H (red line) surfaces. The arrows indicate the time of the injection of BSA, Fib, and PBS solutions into the flow cell.

proteins at the carbon surface. The sharper step observed in the case of Fib solutions suggests that adsorption at the carbon surface is faster for Fib than for BSA; this is also evident from a comparison of the first derivative of the curves (see Supporting Information). Given that the bulk molar concentration is identical, the difference is a result of kinetic control, as a mass transport-controlled process should be faster for BSA by a factor of ~1.7 based on reported diffusion coefficient values of 6×10^{-7} and 2×10^{-7} cm^2 s^{-1} for albumin and fibrinogen, respectively.[43] Moreover, the absence of any significant change in $\Delta\lambda_{max}$ after injection of protein-free buffer solution indicates that protein adsorption is irreversible at both a-C and a-C:H surfaces.

The shift of the plasmon resonance is always larger at a-C- than at a-C:H-coated sensors when comparing adsorption from the same protein solution; however, to compare adsorption at a-C and a-C:H surfaces, the raw signal must be normalized by the experimental sensitivity. The NPS signal of each sensor was thus normalized using the slope of the calibration plot obtained as the first step in each experimental run. This normalization accounts for any differences in alignment across sensors and for differences in sensitivity to changes in bulk refractive index that result from the two types of carbon coating. Figure 4c shows the normalized $\Delta\lambda_{max}$ vs time calculated as $\Delta\lambda_{max}/A$, where A is the slope obtained from the initial calibration of the sensor. A summary of the average normalized $\Delta\lambda_{max}$ observed for the two carbon surfaces and the two proteins is reported in Table 1.

Table 1. Summary of Results from NPS and AFM Measurements

surface	protein	normalized $\Delta\lambda_{max}$ ($\times 10^{-2}$)	modeled thickness (nm)	RMS[a] roughness (nm)	AFM[b] thickness (nm)
a-C	BSA	2.0 ± 0.5	2.3	1.05	1.0 ± 0.1
	Fib	2.8 ± 1.1	3.2	1.91	1.4 ± 0.1
a-C:H	BSA	1.4 ± 0.6	1.8	1.22	1.3 ± 0.1
	Fib	2.3 ± 0.5	3.3	2.04	1.8 ± 0.1

[a]RMS calculated over a 100 μm^2 image. [b]Error represents the standard deviation of the Δz step measured after a contact mode experiment.

After normalization, results indicate that resonance shifts are slightly greater at a-C than at a-C:H surfaces under the same conditions, thus suggesting that protein adsorption might be more pronounced at a-C than at a-C:H surfaces. For both surfaces, the shift obtained for Fib is greater than that observed with BSA, which suggests greater protein adsorption from Fib solutions than from BSA solutions at the same molar concentration in agreement with previous results obtained using ex situ determinations at a-C surfaces.[38]

FDTD methods were used for the analysis of experimental LSPR shifts to obtain quantitative estimates of the protein layer thickness. The protein layer was simulated as an additional conformal layer on top of the carbon coating with the same geometry as in Figure 2a and b. The layer was modeled as a dielectric with a constant real refractive index of 1.465.[44] The LSPR wavelength shift, $\Delta\lambda_{max}$, was simulated for both a-C- and a-C:H-coated sensors at various thicknesses of the protein layer, and the normalized $\Delta\lambda_{max}$ was then calculated using the slopes of the computed calibration plots (Figure 2c). Figure 5 shows

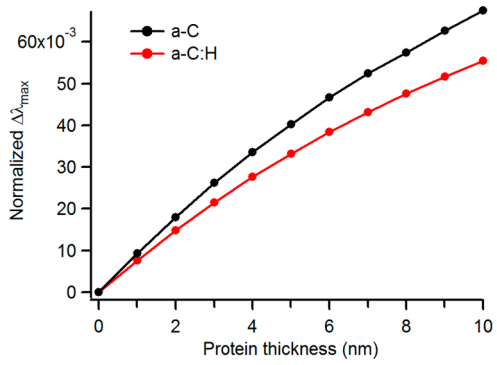

Figure 5. Simulated normalized $\Delta\lambda_{max}$ for a-C (black)- and a-C:H (red)-coated sensors calculated for various thicknesses of the protein layer using the FDTD method.

the normalized $\Delta\lambda_{max}$ calculated at different thicknesses of the protein layer. The plot shows that $\Delta\lambda_{max}$ levels off at large layer thicknesses. This is in agreement with expectations as the resonance shift should tend to a limit, corresponding to the value obtained for a semi-infinite medium with a refractive index equivalent to that of the protein layer. The experimental data obtained from the NPS measurements was used to estimate the thickness of the protein layer at the sensor surface via interpolation of the curves in Figure 5. The thickness estimates thus obtained are reported in Table 1. The protein film thicknesses obtained from in situ NPS experiments using FDTD-generated calibration plots are in the range 1.8−3.3 nm. In the case of BSA, the estimated adsorbed layer is thinner for a-C:H than for a-C; however, in the case of Fib, the adsorbed layer thickness is similar for both types of carbon surfaces. Given that the same refractive index was assumed for BSA and Fib layers, the thickness ratio provides a measure of relative mass density for the two proteins.[45] Using a ratio of molar mass to molar refractivity of 4.14 typical of proteins and Cuypers

DOI: 10.1021/acs.langmuir.7b00612
Langmuir 2017, 33, 4198−4206

one-component model,[46] the estimated mass density for Fib is approximately 3.8 mg m^{-2} on both surfaces, whereas that of BSA is 2.1 and 2.6 mg m^{-2} on a-C:H and a-C, respectively. In the case of both carbon materials, the mass density of Fib was therefore found to be higher than that of the BSA layer.

In situ experiments show that, in the case of BSA, a globular protein, the adsorption is slightly higher on a-C vs a-C:H surfaces. a-C:H displays lower hydrophilicity compared to that of a-C based on water contact angle measurements;[47] multisolvent contact angle determinations (see Supporting Information) show that the surface free energy of a-C:H is 58.4 mJ m^{-2}, which is lower than that of a-C. Estimated BSA layer thicknesses in Table 1 are therefore consistent with both wetting and surface free energy comparisons, as it has been empirically observed that, in the range 20−65 mJ m^{-2}, lower surface free energy translates into reduced protein adsorption.[48] It is likely however that this is not the only mechanism at the origin of the observed differences, as the adsorption of proteins at surfaces is a complex process involving long-range interactions, multiple adsorbate conformations, and conformational changes at the surface over multiple time scales.[43,49,50] Recently, Urbassek and co-workers[51] carried out molecular dynamic simulations of insulin, a small globular protein adsorbed at graphite surfaces, and examined the effect of immobilized ethane, a hydrocarbon, on the adsorption process. The presence of a hydrocarbon was found to significantly reduce protein−surface interaction energy values and, consequently, protein denaturation at hydrocarbon-covered surfaces. The two surfaces used in our experiments range from a graphite-like surface (a-C) to a hydrocarbon-like surface rich in C−H bonds (a-C:H).[37] On the basis of Urbassek's results, it is therefore reasonable to expect protein adsorption at a-C:H to be reduced compared to that at a-C.

In situ experiments also reveal higher protein surface coverages when using Fib compared to BSA independent of the surface examined. Fib is known to form irreversibly adsorbed layers with a wide range of surface density values, but its mechanism of adsorption is still highly debated.[52] Fib has a higher molecular weight than BSA; it possesses multiple domains and a hinged rodlike shape. Its anisotropy opens the possibility of both side-on and end-on surface approaches,[49,53] and previous experiments of Fib on Au,[53] silica,[54] polymers, and mica[55] have proposed the formation of mixed side-on/end-on layers. The estimated mass density for Fib of 3.8 mg m^{-2} found in our experiments is in excellent agreement with limiting coverages observed by other groups under similar conditions.[52,54] However, it is approximately double what is expected for closed packed side-on adsorbates (1.4−2.1 mg m^{-2}).[54,56] This suggests that, on a-C and a-C:H, Fib might form a mixed side-on/end-on layer as proposed for other surfaces. Minton has previously demonstrated via simulations that faster adsorption rates can be expected from end-on vs side-on adsorbates, which are consistent with faster adsorption observed for Fib in our experiments. Relative to side-on adsorbates, the end-on conformation results in weaker protein−surface interactions, which might also partially contribute to the insensitivity of the Fib thickness to the type of carbon surface chemistry. On the basis of the current experiments alone, it is not possible to distinguish the formation of mixed side-on/end-on layers from side-on multilayer formation; however, experiments at lower protein concentrations and/or using complementary techniques to probe adsorbate packing might distinguish between these two possible modes of adsorption.

The adsorbed protein layers were also characterized via ex situ experiments; Figure 6 shows IRRAS spectra in the region

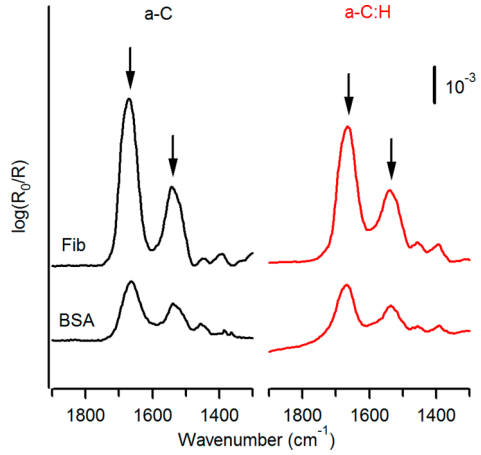

Figure 6. IRRAS spectra of a-C (black, left) and a-C:H (red, right) substrates after 1 h incubation with BSA (top) and Fib (bottom) solutions. The arrows indicate the peak positions of the amide I and II bands. Spectra were baseline corrected, and a-C:H peaks were corrected for optical enhancement, as indicated in the Experimental Methods, to facilitate comparison of peak intensities.

1900−1300 cm^{-1} of a-C and a-C:H surfaces after incubation in BSA and Fib solutions followed by rinsing. Spectra exhibit the characteristic bands of amide groups in polypeptides at ∼1675 and ∼1540 cm^{-1} assigned to the amide I and II modes, respectively.[57] The two strong broad peaks indicate the presence of the protein layer irreversibly adsorbed at both carbon surfaces, as previously reported by our group in the case of a-C.[38] The higher intensity obtained for amide peaks in the case of Fib is consistent with NPS results, which indicate that under these conditions Fib yields thicker adsorbed layers than BSA. AFM characterization of the films using previously reported methods[38,58,59] was used to compare the morphology of protein layers obtained at the carbon surfaces and to understand whether ex situ and in situ determinations of protein layer thickness resulted in comparable results. Carbon surfaces exposed to protein solutions were first imaged in tapping mode; subsequently, a section of the film was removed by scratching the sample with the AFM tip in contact mode. Finally, the step created in the organic film was imaged to determine the layer thickness through cross-section analysis. AFM images reveal that BSA tends to adsorb at both carbon substrates forming smooth layers, whereas Fib tends to form 10−30 nm thick agglomerates (Figure 7a and b). Roughness measurements in fact yield higher root-mean-square (rms) values in the case of Fib at both a-C and a-C:H surfaces as reported in Table 1. Figure 7c shows an example of a-C after incubation in BSA solution imaged after the scratching process; the height profile across the step is shown in the plot underneath the image. The average height difference of protein layers was found to be in the range 1.0−1.8 nm in the case of BSA and Fib, respectively, for both a-C and a-C:H substrates (Table 1). These thicknesses are lower than those obtained from in situ NPS measurements but are consistent with the protein layer undergoing dehydration and compaction after sample drying prior to AFM determinations. When comparing results obtained for the two proteins, AFM measurements also show that Fib yields thicker layers than BSA (∼40% thicker) at

DOI: 10.1021/acs.langmuir.7b00612
Langmuir 2017, 33, 4198−4206

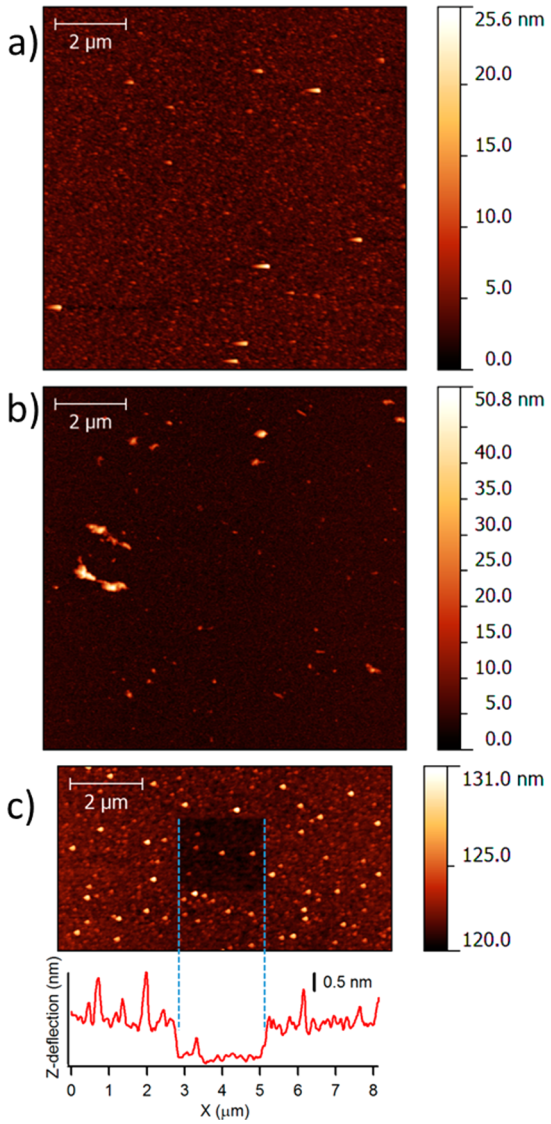

Figure 7. AFM topographic images of a-C:H surfaces after incubation with (a) BSA and (b) Fib solutions; thickness of (c) BSA layer adsorbed at an a-C surface.

both a-C and a-C:H surfaces in good agreement with NPS experiments.

CONCLUSIONS

We have studied in situ adsorption of two plasma proteins at different types of carbon surfaces using an NPS method. FDTD simulations that modeled the sensor response based on the nanodisk geometry and carbon optical constants were predictive of the analytical sensitivity. The computation model was therefore used to analyze protein adsorption data to determine estimated thicknesses, which were found to be consistent with results obtained via ex situ spectroscopy and microscopy. Mass density estimates calculated from thickness values are in good agreement with limiting protein coverage values previously observed with other techniques. These results suggest that NPS in combination with FDTD analysis are well suited to investigating and comparing protein adsorption at carbons, even in the case of carbon materials with highly dissimilar dielectric properties. We expect the results to be important as a platform for new methodologies for the investigation of the carbon–bio interface.

ASSOCIATED CONTENT

Supporting Information

The Supporting Information is available free of charge on the ACS Publications website at DOI: 10.1021/acs.langmuir.7b00612.

Spectroscopic ellipsometry analysis; AFM determinations of coating thickness; XPS characterization of coated sensors; extended plots of NPS data in real time; refractive index of solutions used in experiments; additional comparison of experimental and simulated analytical sensitivity of carbon-coated sensors; and raw data of IRRAS measurements (PDF)

AUTHOR INFORMATION

Corresponding Author

*E-mail: colavitp@tcd.ie.

ORCID

Paula E. Colavita: 0000-0003-1008-2874

Author Contributions

The manuscript was written mainly by F.Z. and P.E.C. with contributions from all authors; F.Z. and J.A. designed and carried out NPS experimental work; J.A.B. contributed with ellipsometric determinations; G.C. contributed with XPS data collection; F.Z. carried out all ex situ characterizations; A.L.B. and V.K. contributed the FDTD simulations. All authors have given approval to the final version of the manuscript.

Notes

The authors declare the following competing financial interest(s): One of the authors is an employee of a company that manufactures NPS elements. However, none of the authors have a financial interest in results or conclusions reported in this manuscript.

ACKNOWLEDGMENTS

This publication has resulted from research conducted with the financial support of Science Foundation Ireland (SFI) Grant 12/IP/1273. J.A.B. acknowledges support from the Irish Research Council through Grant GOIPG/2014/399; G.C. acknowledges support from SFI Grant 13/CDA/2213. A.L.B. and V.D.K. acknowledge support from Science Foundation Ireland (SFI) under Grant 10/IN.1/12975. The authors are grateful to S. Mills and Prof. J. Boland for access to AFM instrumentation. The authors also thank Olof Andersson and Patrik Bjöörn for their generous support through access to NPS instrumentation.

REFERENCES

(1) Roy, R. K.; Lee, K. R. Biomedical applications of diamond-like carbon coatings: A review. *J. Biomed. Mater. Res., Part B* **2007**, *83B* (1), 72–84.

(2) Stueber, M.; Niederberger, L.; Danneil, F.; Leiste, H.; Ulrich, S.; Welle, A.; Marin, M.; Fischer, H. Surface topography, surface energy and wettability of magnetron-sputtered amorphous carbon (a-c) films and their relevance for platelet adhesion. *Adv. Eng. Mater.* **2007**, *9* (12), 1114–1122.

(3) Sydow-Plum, G.; Tabrizian, M. Review of stent coating strategies: clinical insights. *Mater. Sci. Technol.* **2008**, *24* (9), 1127–1143.

DOI: 10.1021/acs.langmuir.7b00612
Langmuir 2017, 33, 4198–4206

(4) Anne Thomson, L.; Law, F. C.; Rushton, N.; Franks, J. Biocompatibility of diamond-like carbon coating. *Biomaterials* **1991**, *12* (1), 37−40.
(5) Hauert, R. A review of modified DLC coatings for biological applications. *Diamond Relat. Mater.* **2003**, *12* (3−7), 583−589.
(6) Ratner, B. D.; Hoffman, A. S.; Schoen, F. J.; Lemons, J. E. *Biomaterials Science*, 2nd ed.; Elsevier Academic Press: London, 2004.
(7) Kasemo, B. Biological surface science. *Surf. Sci.* **2002**, *500* (1−3), 656−677.
(8) Kasemo, B.; Lausmaa, J. Surface properties and processes of the biomaterial-tissue interface. *Mater. Sci. Eng., C* **1994**, *1* (3), 115−119.
(9) Schwartz, Z.; Boyan, B. D. Underlying mechanisms at the bone−biomaterial interface. *J. Cell. Biochem.* **1994**, *56* (3), 340−347.
(10) Thevenot, P.; Hu, W.; Tang, L. Surface Chemistry Influences Implant Biocompatibility. *Curr. Top. Med. Chem.* **2008**, *8* (4), 270−280.
(11) Yadav, P. K.; McKavanagh, F.; Maguire, P. D.; Lemoine, P. Adsorption of bovine serum albumin on amorphous carbon surfaces studied with dip pen nanolithography. *Appl. Surf. Sci.* **2011**, *258* (1), 361−369.
(12) Takeda, A.; Akasaka, H.; Ohshio, S.; Toda, I.; Nakano, M.; Saitoh, H. Adsorption ability comparison of plasma proteins on amorphous carbon surface. *J. Phys. Chem. Solids* **2012**, *73* (11), 1331−1334.
(13) Berlind, T.; Tengvall, P.; Hultman, L.; Arwin, H. Protein adsorption on thin films of carbon and carbon nitride monitored with in situ ellipsometry. *Acta Biomater.* **2011**, *7* (3), 1369−1378.
(14) Lousinian, S.; Logothetidis, S. Optical properties of proteins and protein adsorption study. *Microelectron. Eng.* **2007**, *84* (3), 479−485.
(15) Jones, M. I.; McColl, I. R.; Grant, D. M.; Parker, K. G.; Parker, T. L. Protein adsorption and platelet attachment and activation, on TiN, TiC, and DLC coatings on titanium for cardiovascular applications. *J. Biomed. Mater. Res.* **2000**, *52* (2), 413−421.
(16) Feng, L.; Andrade, J. D. Protein adsorption on low temperature isotropic carbon. 1. Protein conformational change probed by differential scanning calorimetry. *J. Biomed. Mater. Res.* **1994**, *28* (6), 735−743.
(17) Green, R. J.; Frazier, R. A.; Shakesheff, K. M.; Davies, M. C.; Roberts, C. J.; Tendler, S. J. B. Surface plasmon resonance analysis of dynamic biological interactions with biomaterials. *Biomaterials* **2000**, *21* (18), 1823−1835.
(18) Kargl, R.; Kahn, M.; Köstler, S.; Reischl, M.; Doliška, A.; Stana-Kleinschek, K.; Waldhauser, W.; Ribitsch, V. Deposition of silicon doped and pure hydrogenated amorphous carbon coatings on quartz crystal microbalance sensors for protein adsorption studies. *Thin Solid Films* **2011**, *520* (1), 83−89.
(19) Lousinian, S.; Kalfagiannis, N.; Logothetidis, S. Albumin and fibrinogen adsorption on boron nitride and carbon-based thin films. *Mater. Sci. Eng., B* **2008**, *152* (1−3), 12−15.
(20) Willets, K. A.; Van Duyne, R. P. Localized Surface Plasmon Resonance Spectroscopy and Sensing. *Annu. Rev. Phys. Chem.* **2007**, *58* (1), 267−297.
(21) Yonzon, C. R.; Jeoung, E.; Zou, S.; Schatz, G. C.; Mrksich, M.; Van Duyne, R. P. A Comparative Analysis of Localized and Propagating Surface Plasmon Resonance Sensors: The Binding of Concanavalin A to a Monosaccharide Functionalized Self-Assembled Monolayer. *J. Am. Chem. Soc.* **2004**, *126* (39), 12669−12676.
(22) Hutter, E.; Fendler, J. H. Exploitation of Localized Surface Plasmon Resonance. *Adv. Mater. (Weinheim, Ger.)* **2004**, *16* (19), 1685−1706.
(23) Anker, J. N.; Hall, W. P.; Lyandres, O.; Shah, N. C.; Zhao, J.; Van Duyne, R. P. Biosensing with plasmonic nanosensors. *Nat. Mater.* **2008**, *7* (6), 442−453.
(24) Lockett, M. R.; Weibel, S. C.; Phillips, M. F.; Shortreed, M. R.; Sun, B.; Corn, R. M.; Hamers, R. J.; Cerrina, F.; Smith, L. Carbon-on-Metal Films for Surface Plasmon Resonance Detection of DNA Arrays. *J. Am. Chem. Soc.* **2008**, *130* (27), 8611−8613.
(25) Green, R. J.; Davies, J.; Davies, M. C.; Roberts, C. J.; Tendler, S. J. B. Surface plasmon resonance for real time in situ analysis of protein adsorption to polymer surfaces. *Biomaterials* **1997**, *18* (5), 405−413.
(26) Green, R. J.; Davies, M. C.; Roberts, C. J.; Tendler, S. J. B. Competitive protein adsorption as observed by surface plasmon resonance. *Biomaterials* **1999**, *20* (4), 385−391.
(27) Zagorodko, O.; Spadavecchia, J.; Serrano, A. Y.; Larroulet, I.; Pesquera, A.; Zurutuza, A.; Boukherroub, R.; Szunerits, S. Highly Sensitive Detection of DNA Hybridization on Commercialized Graphene-Coated Surface Plasmon Resonance Interfaces. *Anal. Chem.* **2014**, *86* (22), 11211−11216.
(28) Subramanian, P.; Barka-Bouaifel, F.; Bouckaert, J.; Yamakawa, N.; Boukherroub, R.; Szunerits, S. Graphene-Coated Surface Plasmon Resonance Interfaces for Studying the Interactions between Bacteria and Surfaces. *ACS Appl. Mater. Interfaces* **2014**, *6* (8), 5422−5431.
(29) Akasaka, H.; Gawazawa, N.; Suzuki, T.; Nakano, M.; Ohshio, S.; Saitoh, H. Evaluation of protein adsorption on hydrogenated amorphous carbon films by surface plasmon resonance phenomenon. *Diamond Relat. Mater.* **2010**, *19* (10), 1235−1239.
(30) Akasaka, H.; Takeda, A.; Suzuki, T.; Nakano, M.; Ohshio, S.; Saitoh, H. Fibrinogen and lysozyme adsorption on amorphous carbon film surface detected by multilayer device from the back side of the film. *Diamond Relat. Mater.* **2011**, *20* (2), 213−216.
(31) Singh, M.; Holzinger, M.; Tabrizian, M.; Winters, S.; Berner, N. C.; Cosnier, S.; Duesberg, G. S. Noncovalently Functionalized Monolayer Graphene for Sensitivity Enhancement of Surface Plasmon Resonance Immunosensors. *J. Am. Chem. Soc.* **2015**, *137* (8), 2800−2803.
(32) Larsson, E. M.; Langhammer, C.; Zorić, I.; Kasemo, B. Nanoplasmonic Probes of Catalytic Reactions. *Science* **2009**, *326* (5956), 1091−1094.
(33) Jackman, J. A.; Spackova, B.; Linardy, E.; Kim, M. C.; Yoon, B. K.; Homola, J.; Cho, N.-J. Nanoplasmonic ruler to measure lipid vesicle deformation. *Chem. Commun.* **2016**, *52* (1), 76−79.
(34) Zan, G. H.; Jackman, J. A.; Kim, S.-O.; Cho, N.-J. Biosensors: Controlling Lipid Membrane Architecture for Tunable Nanoplasmonic Biosensing. *Small* **2014**, *10* (23), 4827−4827.
(35) Langhammer, C.; Larsson, E. M.; Kasemo, B.; Zorić, I. Indirect Nanoplasmonic Sensing: Ultrasensitive Experimental Platform for Nanomaterials Science and Optical Nanocalorimetry. *Nano Lett.* **2010**, *10* (9), 3529−3538.
(36) Robertson, J. Diamond-like amorphous carbon. *Mater. Sci. Eng., R* **2002**, *37* (4−6), 129−281.
(37) Cullen, R. J.; Jayasundara, D.; Soldi, L.; Cheng, J.; Dufaure, G.; Colavita, P. E. Spontaneous grafting of nitrophenyl groups on amorphous carbon thin films: A structure-reactivity investigation. *Chem. Mater.* **2012**, *24* (6), 1031−1040.
(38) Zen, F.; Angione, M. D.; Behan, J. A.; Cullen, R. J.; Duff, T.; Vasconcelos, J. M.; Scanlan, E. M.; Colavita, P. E. Modulation of Protein Fouling and Interfacial Properties at Carbon Surfaces via Immobilization of Glycans Using Aryldiazonium Chemistry. *Sci. Rep.* **2016**, *6*, 24840.
(39) Behan, J. A.; Stamatin, S. N.; Hoque, M. K.; Ciapetti, G.; Zen, F.; Esteban-Tejeda, L.; Colavita, P. E. A Combined Optoelectronic and Electrochemical Study of Nitrogenated Carbon Electrodes. *J. Phys. Chem. C* **2017**, *121* (12), 6596−6604.
(40) Silva, S. R. P. *Properties of amorphous carbon*, 1st ed.; INSPEC, Inc., The Institution of Electrical Engineers: London, 2003.
(41) Schwarz-Selinger, T.; von Keudell, A.; Jacob, W. Plasma chemical vapor deposition of hydrocarbon films: The influence of hydrocarbon source gas on the film properties. *J. Appl. Phys.* **1999**, *86* (7), 3988−3996.
(42) Johnson, P. B.; Christy, R. W. Optical Constants of the Noble Metals. *Phys. Rev. B* **1972**, *6* (12), 4370−4379.
(43) Andrade, J. D.; Hlady, V. Plasma Protein Adsorption: The Big Twelvea. *Ann. N. Y. Acad. Sci.* **1987**, *516* (1), 158−172.
(44) Goyal, D. K.; Subramanian, A. In-situ protein adsorption study on biofunctionalized surfaces using spectroscopic ellipsometry. *Thin Solid Films* **2010**, *518* (8), 2186−2193.

DOI: 10.1021/acs.langmuir.7b00612
Langmuir 2017, 33, 4198−4206

(45) Vörös, J. The Density and Refractive Index of Adsorbing Protein Layers. *Biophys. J.* **2004**, *87* (1), 553−561.
(46) Cuypers, P. A.; Corsel, J. W.; Janssen, M. P.; Kop, J. M.; Hermens, W. T.; Hemker, H. C. The adsorption of prothrombin to phosphatidylserine multilayers quantitated by ellipsometry. *J. Biol. Chem.* **1983**, *258* (4), 2426−31.
(47) Vasconcelos, J. M.; Zen, F.; Stamatin, S. N.; Behan, J. A.; Colavita, P. E. Determination of surface ζ-potential and isoelectric point of carbon surfaces using tracer particle suspensions. *Surf. Interface Anal.* **2017**, DOI: 10.1002/sia.6223.
(48) Baier, R. Surface behaviour of biomaterials: The theta surface for biocompatibility. *J. Mater. Sci.: Mater. Med.* **2006**, *17* (11), 1057−1062.
(49) Minton, A. P. Adsorption of Globular Proteins on Locally Planar Surfaces. II. Models for the Effect of Multiple Adsorbate Conformations on Adsorption Equilibria and Kinetics. *Biophys. J.* **1999**, *76* (1), 176−187.
(50) Fang, F.; Szleifer, I. Kinetics and Thermodynamics of Protein Adsorption: A Generalized Molecular Theoretical Approach. *Biophys. J.* **2001**, *80* (6), 2568−2589.
(51) Mücksch, C.; Rösch, C.; Müller-Renno, C.; Ziegler, C.; Urbassek, H. M. Consequences of Hydrocarbon Contamination for Wettability and Protein Adsorption on Graphite Surfaces. *J. Phys. Chem. C* **2015**, *119* (22), 12496−12501.
(52) Adamczyk, Z.; Barbasz, J.; Cieśla, M. Mechanisms of Fibrinogen Adsorption at Solid Substrates. *Langmuir* **2011**, *27* (11), 6868−6878.
(53) Dyr, J. E.; Tichý, I.; Jiroušková, M.; Tobiška, P.; Slavík, R.; Homola, J.; Brynda, E.; Houska, M.; Suttnar, J. Molecular arrangement of adsorbed fibrinogen molecules characterized by specific monoclonal antibodies and a surface plasmon resonance sensor. *Sens. Actuators, B* **1998**, *51* (1−3), 268−272.
(54) Malmsten, M. Ellipsometry Studies of Protein Layers Adsorbed at Hydrophobic Surfaces. *J. Colloid Interface Sci.* **1994**, *166* (2), 333−342.
(55) Cieśla, M.; Adamczyk, Z.; Barbasz, J.; Wasilewska, M. Mechanisms of Fibrinogen Adsorption at Solid Substrates at Lower pH. *Langmuir* **2013**, *29* (23), 7005−7016.
(56) Adamczyk, Z.; Barbasz, J.; Cieśla, M. Kinetics of Fibrinogen Adsorption on Hydrophilic Substrates. *Langmuir* **2010**, *26* (14), 11934−11945.
(57) Socrates, G. *Infrared and Raman Characteristic Group Frequencies: Tables and Charts*; John Wiley & Sons, 2001.
(58) Brooksby, P. A.; Downard, A. J. Electrochemical and Atomic Force Microscopy Study of Carbon Surface Modification via Diazonium Reduction in Aqueous and Acetonitrile Solutions. *Langmuir* **2004**, *20* (12), 5038−5045.
(59) Anariba, F.; DuVall, S. H.; McCreery, R. L. Mono- and Multilayer Formation by Diazonium Reduction on Carbon Surfaces Monitored with Atomic Force Microscopy "Scratching". *Anal. Chem.* **2003**, *75* (15), 3837−3844.

DOI: 10.1021/acs.langmuir.7b00612
Langmuir 2017, 33, 4198−4206